

**Investigation into Device Optimisation
of Organic Solar Cells Using Narrow
Bandgap Polymer and the Role of
Acceptor Material**

Author: Soheil Komilian

**A thesis submitted in partial fulfilment of the requirement of
Staffordshire University for the degree of Doctor of Philosophy**

August 2019

Abstract

Organic solar cells (OSCs) based on PBDTTT-EFT copolymer as the electron donor material have shown promising power conversion efficiencies (PCE) when blended with fullerene derivative acceptor materials in bulk heterojunction structures. The properties of blended donor and acceptor material and their compatibility plays a critical role in the device performance of OSCs. Therefore, to optimise OSCs devices based on PBDTTT-EFT, it is necessary to investigate the behaviour of the donor and acceptor materials in their pristine and blended form. Based on the literature, the role of donor: acceptor [D:A] blend ratio is amongst the critical aspects for optimising the active layer morphology. However, for OSC devices based on PBDTTT-EFT: PC₇₁BM, the significant correlation between device performance and device physics for different D:A ratios has not yet been fully understood.

Therefore, in this research project, one of the major case studies investigated, will be on devices fabricated from PBDTTT-EFT: PC₇₁BM blends with different PC₇₁BM percentage weight ratios. Results obtained from combined optical absorption spectroscopy, structural, morphological and electrical characterisation, indicates that the best device performance belongs to D:A ratio of 1:2, achieving an average PCE of 9.56%. This is believed to stem from the change in preferred molecular orientation of PBDTTT-EFT molecules from *Face-on* to *Edge-on*, as a result of increased PC₇₁BM content within the blend. For the first time, the existence of PBDTTT-EFT molecules in *Edge-on* orientation was identified using an OOP GIXRD. Also, further evidence of the GIXRD analysis indicates that the highest vertical stacking of PC₇₁BM molecules occurs at D:A blend ratio of 1:2, which is favourable for charge transport and extraction.

The other major investigation on PBDTTT-EFT based OSC devices is on the impact of different fullerene derivative materials to be used as the acceptor, such as PC₆₁BM and IC₆₁BA. IC₆₁BA, in particular, was chosen, as it has higher levels of LUMO compared to PC₇₁BM. Therefore, the V_{oc} of devices fabricated from PBDTTT-EFT: IC₆₁BA is expected to be higher than PBDTTT-EFT: PC₇₁BM. Although device enhancement of some OSCs has been reported by employing IC₆₁BA instead of PCBM

[1], using IC₆₁BA as the acceptor material in a blend with BDT-based low bandgap polymers has shown the opposite effect [2]. As an example, it has been reported that devices fabricated using blend of PBDTTT-C-T: IC₆₁BA will show poor device performance compared to PBDTTT-C-T: PC₆₁BM, despite achieving higher V_{oc} values when employing IC₆₁BA as the acceptor [2]. It was suggested that poor ‘network’ formation between the donor and acceptor material within the blend causes the problem in reduced device performance, however very little detail is provided as to what is the exact issue. Therefore, investigating PBDTTT-EFT: IC₆₁BA devices has also been the focus of this PhD project. Devices fabricated from PBDTTT-EFT: IC₆₁BA blends resulted in averaged PCE of 5.86%, with V_{oc} value just under 1V.

However, the J_{sc} and FF parameters are reduced when compared to devices fabricated from PCBM (C₆₁ or C₇₁). From the analysed GIXRD results, it was evident that IC₆₁BA has a very low vertical segregation and stacking, which is detrimental for electron charge transport and extraction. Also, it has been noticed that IC₆₁BA molecules had the least impact on the change in molecular orientation of the PBDTTT-EFT molecule. The mobility measurements further provide evidence to unbalance charge transport mechanism in PBDTTT-EFT: IC₆₁BA devices compared to PBDTTT-EFT: PC₇₁BM devices.

Photoluminescence spectroscopy indicates that thin films composed of PBDTTT-EFT: IC₆₁BA have a higher recombination rate compared to PBDTTT-EFT: PC₇₁BM blend. Thus, when compiled with the analysis of GIXRD results from the blend films, it is concluded that the morphology between PBDTTT-EFT molecules and IC₆₁BA is poor, and their phase domain separation is significant. The recombination analysis elucidates that the inadequate vertical segregation of IC₆₁BA molecules (due to the nature of the molecule shape) results in weak charge dissociation and transport. Therefore, high recombination rates will take place within the active layer, mainly governed by the trap-assisted mechanism.

Acknowledgement

Firstly, I would like to thank my principal supervisor Professor Torfeh Sadat-Shafai, who has provided me with the opportunity to work under his supervision. I appreciate his valuable support and guidance during tough times that I had to go through in my life and really appreciate his encouragement, training and motivation; most importantly, not giving up on me.

I would also like to thank my parents, friends and family for supporting me throughout my PhD period and giving the energy to carry on during hard times.

I would also like to acknowledge the technical team in the school of engineering and science at Staffordshire University for providing generous support and assistance in various areas.

Moreover, I would like to thank Staffordshire University for offering me a partial scholarship and the facilities to conduct and complete my PhD and research.

Publications

A list of journal publications co-authored during this PhD program.

Komilian, S., Oklobia, O. and Sadat-Shafai, T., 2018. Controlling intercalations of PBDTTT-EFT side chain to initiate suitable network for charge extraction in PBDTTT-EFT: PC₇₁BM blended bulk heterojunction solar cell. *Solar Energy Materials and Solar Cells*, 175, pp.35-40.

Komilian, S., Oklobia, O. and Sadat-Shafai, T., 2018. Data related to the PC₇₁BM loading and its impact on nanostructuring for blend of PBDTTT-EFT: PC₇₁BM bulk heterojunction solar cell. *Data in brief*, 16, pp.506-510.

Oklobia, O., **Komilian, S.** and Sadat-Shafai, T., 2018. Impedance spectroscopy and Capacitance-voltage measurements analysis: Impact of charge carrier lifetimes and mapping vertical segregation in Bulk heterojunction P3HT: PCBM solar cells. *Organic Electronics*, 61, pp.276-281.

Content

Abstract	i
Acknowledgement	iii
Publications	iv
Content	v
List of Figures	viii
List of Tables	xii
List of Equations	xiv
List of Abbreviations	xvii
Chapter 1 - Introduction	1
1.1 Introduction	1
1.2 Types of Solar Cells	4
1.2.1 Type-I	4
1.2.2 Type-II	5
1.2.3 Type-III	5
1.3 The architecture of organic solar cells	7
1.3.1 Single Layer	7
1.3.2 Bi-layer	8
1.3.3 Blended structure	10
1.4 Challenges	11
1.5 Aim of this research project	11
1.6 Objectives	12
Chapter 2 - Device Physics of Organic Solar Cells	13
2.1 Introduction	13
2.2 Organic Semiconductor Properties	14
2.2.1 Conjugated Polymers	14
2.3 Charge Transport in Organic Semiconductors	16
2.3.1 Electrode – Semiconductor interface	17
2.3.2 Ohmic and SCL Conductivity in Organic Semiconductors	19
2.4 Operation mechanism of Organic Solar Cells	20
2.4.1 Equivalent circuit model of organic solar cells	22
2.4.2 Exciton Dissociation	26
2.4.3 Recombination Mechanism: Geminate and Bimolecular	30

2.4.4 Trapped recombination mechanism	32
2.5 Summary	34
Chapter 3 - Materials for Organic Solar Cells.....	35
3.1 Introduction.....	35
3.2 Donor Material	38
3.2.1 Polythiophenes Polymers and Its Derivatives.....	38
3.2.2 Polymers based on 2,1,3-Benzothiadiazole.....	40
3.2.3 Pyrrolo[3,4-c]pyrrole-1,4-dione (DPP) Derivative Polymers	42
3.2.4 Polymers based on Benzo[1,2-b;4,5-b`]dithiophene	43
3.3 Acceptor Materials	49
3.3.1 PCBM derivatives	49
3.3.2 Indene-C _x Bisadduct derivatives	51
3.4 Buffer layers.....	52
3.5 Summary	54
Chapter 4 - Experimental Procedures & Methodology	55
4.1 Introduction.....	55
4.2 Experimental Procedures	55
4.2.1 Device architecture.....	56
4.2.2 Substrates	56
4.2.3 Sample preparation.....	58
4.2.4 Sample Fabrication (Spin Coating).....	59
4.2.5 Thermal Vacuum deposition of Electrodes	60
4.2.6 Solar Simulator.....	62
4.3 DC – Characteristics	64
4.4 AC – Characteristics	65
4.5 Optical Absorption.....	66
4.6 Raman & Photoluminescence Spectroscopy.....	68
4.7 Grazing incident X-ray diffraction.....	71
4.8 Atomic Force Microscopy.....	76
4.9 Cyclic Voltammetry Measurements.....	80
4.10 Thin Film Thickness measurements.....	81
4.11 Mobility measurement of charge carriers.....	81
4.12 Summary	82
Chapter 5 - Results & Discussions.....	83
5.1 Introduction.....	83
5.2 Thin Film Material characteristics	84

5.2.1 Cyclic voltammetry	84
5.2.2 Optical absorption	85
5.2.3 Photoluminescence.....	88
5.2.4 Raman Spectroscopy	90
5.2.5 Molecular structure (GIXRD)	94
5.3 Device Performance Enhancement	99
5.3.1 Active Layer Film Thickness	100
5.3.2 Post-thermal Annealing.....	101
5.3.3 Solution Ageing	104
5.3.4 Solution Concentration.....	105
5.3.5 Active layer drying technique	106
5.3.6 Solvent Additive.....	109
5.3.7 Active Layer Surface Washing	112
5.3.8 Co-solvents.....	114
5.3.9 Optimising Donor: Acceptor ratio	116
5.3.10 Fullerene Derivative Acceptor Materials	130
5.4 Summary	156
Chapter 6 - Conclusion & Future Work.....	157
References.....	161

List of Figures

Chapter 1

Figure 1.1: Illustrates the chart of approximated Global ...	2
Figure 1.2: Annual global electricity generated from PV ...	3
Figure 1.3: Best research solar cell efficiencies in the ...	4
Figure 1.4: Some of the significant advances in the development ...	7
Figure 1.5: Schematic of single layer OSC device, (1) photon absorption ...	8
Figure 1.6: Structure of bi-layer architecture OSC ...	9
Figure 1.7. Structure of BHJ device architecture, with ...	10

Chapter 2

Figure 2.1: Energy band diagram illustrating different levels ...	13
Figure 2.2: Representation of conjugated organic polymeric ...	14
Figure 2.3: Schematics illustration of ethylene ...	15
Figure 2.4: Molecular orbital interactions presented ...	16
Figure 2.5: Schematic of Schottky barrier junction ...	17
Figure 2.6. Schematic of energy band diagram after ...	18
Figure 2.7: Schematic of Energy band diagram for BHJ system ...	19
Figure 2.8: Operation mechanism of BHJ OSCs under illumination ...	21
Figure 2.9: J-V characteristic curves of an ideal solar cell ...	22
Figure 2.10: J-V and P-V curves for an ideal solar cell under illumination ...	23
Figure 2.11: Equivalent circuit model of a solar cell with R_s and R_{sh} incorporated ...	24
Figure 2.12: Impact of change in the R_{sh} and R_s on the J-V ...	25
Figure 2.13: Determination of R_s and R_{sh} from a J-V curve plot under ...	25
Figure 2.14. (a) D-A interface energy diagram illustrating ...	27
Figure 2.15: Energy diagram of dissociation probability of electron-hole pairs ...	29
Figure 2.16: Schematic diagram illustrating bimolecular recombination ...	31
Figure 2.17: Schematic of SRH recombination stages: ...	32

Chapter 3

Figure 3.1: Schematic of the chemical structure of P3HT ...	36
Figure 3.2: Absorption spectra for pristine PC ₆₁ BM film ...	36
Figure 3.3: Few possible derivatives of Polythiophene: 2D-PT ...	39
Figure 3.4: Chemical structure of copolymers based on dithiophene and ...	40
Figure 3.5: Chemical structure of DTBT-based polymers: ...	41
Figure 3.6: Chemical structure of DPP-based polymers: DPP, PDPP, ...	42
Figure 3.7: Chemical structure illustrating the synthesis of ...	44

Figure 3.8: Chemical structure of eight BDT-based polymers ...	44
Figure 3.9: The molecular structure of BDT-based copolymers ...	46
Figure 3.10: The molecular structure of PBDTTT-EFT, ...	47
Figure 3.11: Parameters of PBDTTT-EFT. (a) optical absorption ...	47
Figure 3.12: Bar chart representation published work on PBDTTT-EFT per year ...	48
Figure 3.13: The molecular structure of PC ₆₁ BM and PC ₇₁ BM ...	49
Figure 3.14: Optical absorption of PC ₆₁ BM and PC ₇₁ BM, ...	50
Figure 3.15: Molecular structure of IC ₆₁₍₇₁₎ BM and IC ₆₁₍₇₁₎ BA ...	51
Figure 3.16: The molecular structure of PEDOT: PSS ...	53

Chapter 4

Figure 4.1: Schematic illustration of the ITO substrate Etching process ...	56
Figure 4.2: N ₂ Glovebox system at R117 Thin Film Laboratory ...	57
Figure 4.3: Pictures and diagram of Active solution preparation stages ...	59
Figure 4.4: Schematic of Spin coating technique ...	59
Figure 4.5: Plot of ω against d . Random Data generated using ...	60
Figure 4.6: (a) schematic diagram of AUTO-500 ...	61
Figure 4.7: Picture of Intellemetric IL-150 Quartz crystal growth monitor ...	62
Figure 4.8: Photos of three deferent samples each with ...	62
Figure 4.9: Pictures of Left: LOT-LSO104 Solar simulator, ...	63
Figure 4.10. The plot of solar light against Spectral irradiance ...	63
Figure 4.11: Pictures of a) Newport 91150V reference cell, ...	64
Figure 4.12: Picture of KEITHLEY 2400 source-meter ...	64
Figure 4.13. Pictures of the OSC device test station, ...	65
Figure 4.14. (a) Impedance plot (vector diagram representation) ...	66
Figure 4.15. A typical Cole-Cole plot for IS data obtained in ...	66
Figure 4.16. Schematic of Varian Cary bio 50 UV – Vis ...	67
Figure 4.17. Schematic diagram of incident light and ...	68
Figure 4.18. Schematic diagram of a Raman microscope ...	69
Figure 4.19: Schematic diagram of PL spectrometer setup ...	70
Figure 4.20: Schematic diagram of Bragg's law in vector form ...	72
Figure 4.21: Schematics of Out-of-Plane (OOP), ...	73
Figure 4.22: Picture of Bruker D8 Advance GIXRD with ...	74
Figure 4.23: Schematic diagram of s polymer orientation, ...	75
Figure 4.24: Surface composition detection schematic of AFM probe ...	76
Figure 4.25: A schematic illustration of an AC-AFM operation ...	77
Figure 4.26: Cantilever under resonant oscillation, ...	78
Figure 4.27: (a) Schematic of cantilever force F_c applied on different ...	79
Figure 4.28: (a) Picture of Agilent 5500 AFM electrochemistry station, ...	80
Figure 4.29: A measured step height profile of a thin film ...	81

Figure 4.30: Example architecture configuration for a ...	82
---	----

Chapter 5

Figure 5.1: Cyclic voltammograms of pristine PBDTTT-EFT and ...	84
Figure 5.2: UV-Vis spectra of pristine PBDTTT-EFT, PC ₇₁ BM, PC ₆₁ BM, IC ₆₁ BA, ...	86
Figure 5.3: UV-Vis Spectrum of PBDTTT-EFT, and ...	87
Figure 5.4: UV-Vis spectra of PBDTTT-EFT blended with ...	87
Figure 5.5: PL spectra of pristine PBDTTT-EFT, PC ₇₁ BM, PC ₆₁ BM, and ...	88
Figure 5.6: Normalised PL spectrum of pristine PBDTTT-EFT, and ...	89
Figure 5.7: UV-Vis spectra of pristine materials with Raman excitation ...	91
Figure 5.8: Raman spectrum of pristine PBDTTT-EFT under ...	92
Figure 5.9: Raman spectra of pristine PC ₇₁ BM, PC ₆₁ BM, and IC ₆₁ BA under ...	94
Figure 5.10: OOP GIXRD diffractograms of pristine ...	95
Figure 5.11: OOP GIXRD diffractograms of pristine PC ₇₁ BM film coated onto ...	95
Figure 5.12: OOP GIXRD of the pristine PC ₇₁ BM thin film after background ...	96
Figure 5.13: OOP GIXRD diffractogram of pristine PBDTTT-EFT ...	96
Figure 5.14: OOP GIXRD diffractogram of pristine acceptor material films and ...	97
Figure 5.15: Schematic diagram of the d_{200} plane for ...	98
Figure 5.16: Extracted d_{200} curves from the computer-generated ...	99
Figure 5.17: Schematic workflow diagram of experiments ...	99
Figure 5.18: PBDTTT-EFT: PC ₇₁ BM J-V characteristics of ...	100
Figure 5.19: J-V characteristics of averaged OSC devices ...	102
Figure 5.20: UV-Vis spectra of PBDTTT-EFT: PC ₇₁ BM upon post thermal annealing ...	103
Figure 5.21: J-V characteristics of averaged PBDTTT-EFT: PC ₇₁ BM, ...	104
Figure 5.22: J-V characteristics of PBDTTT-EFT: PC ₇₁ BM with different ...	105
Figure 5.23: Schematic diagram of different active layer drying techniques: ...	107
Figure 5.24: J-V characteristics of PBDTTT-EFT: PC ₇₁ BM devices with ...	107
Figure 5.25: UV-Vis spectra of PBDTTT-EFT: PC ₇₁ BM active ...	108
Figure 5.26: Average J-V characteristics curves of ...	110
Figure 5.27: UV-Vis spectra of PBDTTT-EFT: PC ₇₁ BM, As-cast (red), ...	111
Figure 5.28: Schematic diagram of the active layer surface washing ...	112
Figure 5.29: Averaged J-V characteristic curves for ...	113
Figure 5.30: UV-Vis spectra of As-cast, Methanol, and ...	114
Figure 5.31: Averaged J-V characteristic curves for PBDTTT-EFT: PC ₇₁ BM ...	115
Figure 5.32: Averaged J-V characteristic curves for ...	117
Figure 5.33: (a) UV-Vis spectra profile and ...	118
Figure 5.34: PL Quenching efficiency (Q.E.) as a function of D:A ...	119
Figure 5.35: Correlation graph between FF and R_{sh} as a ...	120
Figure 5.36: AFM morphology images for PBDTTT-EFT: PC ₇₁ BM ...	121
Figure 5.37: Schematic diagram of PC ₇₁ BM cluster formation on ...	123

Figure 5.38: 3D representation of OOP GIXRD diffractograms for ...	124
Figure 5.39: Raman spectrum of pristine PBDTTT-EFT and its ...	127
Figure 5.40: The FWHM for P1 – P4 assigned on the Raman spectrum ...	128
Figure 5.41: Schematic diagram of PBDTTT-EFT: PC ₇₁ BM blend ...	129
Figure 5.42: J-V characteristic curves of PBDTTT-EFT: PC ₇₁ BM, ...	131
Figure 5.43: (a) PL spectra profile of pristine EFT, PC ₇₁ BM, PC ₆₁ BM, ...	132
Figure 5.44: Correlation graph between Q.E. and FF as a function of ...	133
Figure 5.45: AFM images: (a-c) Topography images of pristine ...	133
Figure 5.46: OOP GIXRD diffractograms of PBDTTT-EFT: PC ₇₁ BM, ...	134
Figure 5.47: (a) Raman spectra profile for PBDTTT-EFT: acceptor blends ...	136
Figure 5.48: Correlation graph between FWHM of ...	137
Figure 5.49: Dark J-V plot of electron-only devices for ...	139
Figure 5.50: Dark J-V plot of the hole only devices for pristine ...	139
Figure 5.51: Correlation plots between (a) d_{100} / d_{010} intensity and μ_e / μ_h , ...	141
Figure 5.52: Log-Log graph of photocurrent (J_{ph}) against effective applied ...	143
Figure 5.53: Correlation graphs for PBDTTT-EFT based devices blended with ...	145
Figure 5.54: Correlation graphs for PBDTTT-EFT based OSC devices ...	149
Figure 5.55: V_{oc} as a function of light intensity for PBDTTT-EFT ...	152
Figure 5.56: (a) Impedance spectra of PBDTTT-EFT blended with ...	153
Figure 5.57: Workflow diagram for pilot study experiments in chapter 5, ...	156

List of Tables

Chapter 1

Table 1.1: Global renewable energies available with...	2
--	---

Chapter 3

Table 3.1: OSC device characteristics of BT based copolymers blended with PC ₆₁ BM...	41
Table 3.2: OSC device characteristics for DPP-based polymers blended with PC ₆₁ BM...	43
Table 3.3: OSC device characteristics for BDT-based polymers blended with...	45
Table 3.4: Electrical characteristic parameters extracted from different...	52

Chapter 4

Table 4.1: Summation of materials and chemicals used in this project...	55
Table 4.2: Summary of solution preparation in this project...	58

Chapter 5

Table 5.1: HOMO and LUMO parameters of materials...	85
Table 5.2: OOP GIXRD parameters extracted from the computer-generated...	98
Table 5.3: Spin coating speeds corresponding to film thickness for a fixed period of time...	100
Table 5.4: Electrical parameters extracted from averaged J-V curves for samples with...	101
Table 5.5: Electrical characteristic parameters extracted from averaged J-V...	102
Table 5.6: Electrical characteristic parameters extracted from averaged J-V...	104
Table 5.7: Electrical characteristic parameters extracted from averaged J-V...	106
Table 5.8: Electrical parameters extracted from averaged J-V curves for...	108
Table 5.9: Electrical parameters extracted from averaged J-V curves for As-Cast and...	110
Table 5.10: Electrical parameters extracted from the averaged J-V curves for...	113
Table 5.11: Electrical parameters extracted from the averaged J-V curves...	115
Table 5.12: Electrical parameters extracted from the averaged J-V curves for different...	117
Table 5.13: Surface roughness (S_q), an absolute difference of surface roughness between...	122
Table 5.14: OOP GIXRD parameters extracted from the curve fits for PBDTTT-EFT...	125
Table 5.15: Dihedral angle ψ and d_{010} spacing for PBDTTT- based polymer...	126
Table 5.16: Raman spectrum profile peak analysis for samples with different D:A ratios...	127
Table 5.17: Extracted electrical parameters from the averaged J-V characteristic...	130
Table 5.18: Surface roughness of blended films and pristine acceptor ...	134
Table 5.19: Extracted parameters from GIXRD computer model curve fits ...	135
Table 5.20: FWHM parameters for identified Raman peaks ...	137
Table 5.21: Charge mobility measurement parameters ...	140
Table 5.22: Summary of PV parameters for PBDTTT-EFT based devices ...	144

Table 5.23: Recombination parameters calculated for EFT: PC ₇₁ BM, ...	146
Table 5.24: Recombination decay constant rate parameters calculated for ...	148
Table 5.25: Extracted parameters from the equivalent circuit models used to ...	154

List of Equations

$$eV_{bi} = e\Phi_m - e\Phi_s \dots\dots\dots(1)$$

$$e\Phi_B = e\Phi_m - e\chi_s \dots\dots\dots(2)$$

$$W = \left(\frac{2\varepsilon(V_{bi} \pm V)}{eN_d} \right)^{\frac{1}{2}} \dots\dots\dots(3)$$

$$J = (p, n)\mu_{p(n)}q \frac{V}{d} \dots\dots\dots(4)$$

$$J = \frac{9}{8} \varepsilon \mu_{p(n)} \frac{V^2}{d^3} \dots\dots\dots(5)$$

$$J = \left(\frac{\mu_{p(n)}N_{cv}}{q} \right) \left(\frac{\varepsilon}{N_{Th(e)}} \cdot \frac{1}{l+1} \right)^l \left(\frac{2l+1}{l+1} \right)^{l+1} \frac{V^{l+1}}{d^{2l+1}} \dots\dots\dots(6)$$

$$E (eV) = \frac{hc}{\lambda} \dots\dots\dots(7)$$

$$J = J_s \left[\exp\left(\frac{qV}{k_B T}\right) - 1 \right] \dots\dots\dots(8)$$

$$J = J_s \left[\exp\left(\frac{qV}{k_B T}\right) - 1 \right] - J_{sc} \dots\dots\dots(9)$$

$$V_{oc} = \frac{k_B T}{q} \ln \left(\frac{J_{sc}}{J_s} + 1 \right) \dots\dots\dots(10)$$

$$PCE (\%) = \frac{P_{out}}{P_{in}} \times 100 \dots\dots\dots(11)$$

$$P_{out} = J_{sc} V_{oc} \dots\dots\dots(12)$$

$$PCE (\%) = FF \times \frac{J_{sc} V_{oc}}{P_{in}} \times 100 \dots\dots\dots(13)$$

$$FF = \frac{J_{max} V_{max}}{J_{sc} V_{oc}} \dots\dots\dots(14)$$

$$J = J_{sc} - J_s \left[\exp\left(\frac{q(V - JR_s)}{nk_B T}\right) - 1 \right] - \frac{V - JR_s}{R_{sh}} \dots\dots\dots(16)$$

$$E (J) = \frac{q^2}{4\pi\varepsilon a} \dots\dots\dots(16)$$

$$V_{oc} = \frac{1}{q} (\text{HOMO}_D - \text{LUMO}_A) - 0.3V \dots\dots\dots(17)$$

$$r_c = \frac{q^2}{4\pi\varepsilon k_B T} \dots\dots\dots(18)$$

$$P(E, T) = \left(1 + \frac{qr_c E}{2k_B T}\right) \exp\left(\frac{-r_c}{a}\right) \dots\dots\dots (19)$$

$$P(E, T) = \frac{k_D(E)}{k_F + k_D(E)} \dots\dots\dots (20)$$

$$R_B = B_L(np - n_i p_i) \dots\dots\dots (21)$$

$$n_i p_i = N_{CV} \exp\left(\frac{-E_g}{k_B T}\right) = n_i^2 \dots\dots\dots (22)$$

$$R_B = B_L(n \times p) \dots\dots\dots (23)$$

$$B_L = \frac{q}{\epsilon} (\mu_h + \mu_e) \dots\dots\dots (24)$$

$$B_L = \frac{q}{\epsilon} \langle \mu_h + \mu_e \rangle \dots\dots\dots (25)$$

$$B_L = \frac{q}{\epsilon} \min(\mu_h, \mu_e) \dots\dots\dots (26)$$

$$R_{SRH} = B_{SRH}(np - n_i p_i) \dots\dots\dots (27)$$

$$B_{SRH} = \frac{C_p C_n N_{Te}}{[C_n(n+n_i) + C_p(p+p_i)]} \dots\dots\dots (28)$$

$$V_{oc} = \frac{E_g}{q} - \frac{k_B T}{q} \ln\left(\frac{[1-P(E, T)] B_L N_{CV}^2}{P(E, T) G(E, T)}\right) \dots\dots\dots (29)$$

$$V_{oc} = \frac{E_g}{q} - \frac{k_B T}{q} \ln\left(\frac{[1-P(E, T)] B_T N_{CV}^2}{P(E, T) G(E, T)}\right) \dots\dots\dots (30)$$

$$C_p = \frac{q}{\epsilon} \mu_h \dots\dots\dots (31)$$

$$C_n = \frac{q}{\epsilon} \mu_e \dots\dots\dots (32)$$

$$R_{SRH} = B_{SRH}(n, p) \dots\dots\dots (33)$$

$$B_{SRH} = \frac{C_p C_n N_{Te}}{(C_n n) + (C_p p)} \dots\dots\dots (34)$$

$$R_{SRH} = C_p N_{Te} p \dots\dots\dots (35)$$

$$R_{SRH} = C_n N_{Te} n \dots\dots\dots (36)$$

$$d(nm) = k\omega^\alpha \dots\dots\dots (37)$$

$$Z = R + jX = |Z| \angle \theta^\circ \dots\dots\dots (38)$$

$$A = \log_{10}\left(\frac{I_0}{I_T}\right) = -\log_{10} T \dots\dots\dots (39)$$

$$n\lambda = 2d \sin \theta \dots\dots\dots (40)$$

$$L_{hkl} = \frac{k\lambda}{\beta \cos \theta} \dots\dots\dots (41)$$

$$F_c = A_0 \sin(\omega_0 t + \Phi) \dots\dots\dots(42)$$

$$E_{HOMO} = -e(\Phi_p^{on} + 4.39) \dots\dots\dots(43)$$

$$E_{LUMO} = -e(\Phi_n^{on} + 4.39) \dots\dots\dots(44)$$

$$E_g^{opt} (eV) = \frac{h.c}{\lambda_{on}} \dots\dots\dots(45)$$

$$G(E, T) = G_{max}P(E, T) \dots\dots\dots(46)$$

$$J_{sat} = qG_{max}l \dots\dots\dots(47)$$

$$J_{ph} = qG_{max}P(E)l \dots\dots\dots(48)$$

$$P(E) = \frac{J_{ph}}{J_{sat}} \dots\dots\dots(49)$$

$$k_D(E) = [\max(n, p) \text{ or } \langle n + p \rangle] \times B_L \dots\dots\dots(50)$$

$$k_F = \left(\frac{k_D(E)}{P(E)} \right) - k_D(E) \dots\dots\dots(51)$$

$$k_D(E) = \max(n, p) \times B_L \dots\dots\dots(52)$$

$$k_D(E) = \langle n + p \rangle \times B_L \dots\dots\dots(53)$$

$$\tau_{avg} = R_{rec}C_{eq} \dots\dots\dots(54)$$

List of Abbreviations

AFM	Atomic force microscopy
Al	Aluminium
BHJ	Bulk heterojunction
C ₆₀	Buckminsterfullerene
CO ₂	Carbon dioxide
D/A	Donor/Acceptor
EFT	PBDTTT-EFT molecule
E _g	Energy bandgap
eV	Electron Volt
FF	Fill Factor
FWHM	Full width at half maximum
GIXRD	Grazing Incidence X-ray Diffraction
GPIB	General-purpose interface bus
HOMO	Highest occupied molecular orbital
ITO	Indium tin oxide
J _{sc}	Short circuit current density
LCD	Liquid crystal displays
LCR	Inductor, capacitor, resistance
LUMO	Lowest unoccupied molecular orbital
OFET	Organic field-effect transistor
OLED	Organic light-emitting diode
OSC	Organic solar cell
OTFT	Organic thin-film transistor
ϕ	Work function
P3HT	Poly (3-hexylthiophene)
PCBM	[6, 6] phenyl-C61-butyric acid methyl ester
PCE	Power conversion efficiency
PL spectra	Photoluminescence spectra
PV	Photovoltaic
Q.E.	Quenching efficiency
SCLC	Space charge limited current
Si-based	Silicon-based
TOF	Time of Flight
UV	Ultra-violet
V _{bi}	Built - in potential
V _{oc}	Open circuit voltage

CHAPTER 1

Introduction

1.1 Introduction

It is predicted that by 2100, the human global population will reach around 9.5 billion [3]. With such an increase, four major areas: Food, Water, Urbanisation and Energy will significantly be challenged in society [3]. To address these, research communities are working to find appropriate solutions to these challenges. Most of the energy usage has been in the form of heat conversion into other forms of energy, mainly by burning fossil fuels to convert the energy into electrical or mechanical energy. However, burning fossil fuel and coal over the years has had a severe impact on the environment and climate. With serious concerns about CO₂ emissions, global warming and low reserves of fossil fuels, our energy requirements have never been more important. In 2016 nations across the globe gathered in Paris (France) and decided to act and contribute efforts to combat the climate change. They agreed to reduce the carbon emission and to use more renewable energy sources to meet the demand for global energy. This became to be known as the *Paris agreement*.

New sustainable clean renewable energy sources such as Wind, Hydroelectric, Geothermal, and Solar can be excellent replacements for current energy production methods. There are two primary forms of energy usage when it comes to fossil fuels,

one is as fuel (vehicle and transportations), and the other is to generate electricity. It seems that the usage of electricity as a source of energy is the future with electric vehicles for transportation. The total renewable energies available globally reported by Sandia National Laboratories, are summarised in Table 1.1 [4].

Table 1.1: Global renewable energies available with technical powers calculated for solar electricity, the theoretical value is at 1.5 hrs of sunshine [4].

Energy Resources	Theoretical Power (TW)	Technical Power (TW)	Extractable Power (TW)
Ocean Surface current	8.1	2	0.012
Ocean Tidal	2.4	0.6	0.037
Ocean Wave	34	8.5	0.62
Hydropower	12	3.5	1.2
Geothermal	44	2.8	1.9
Wind Power	1,000	250	14
Solar Electricity	89,000	25,091	5,018

Based on the information provided in Table 1.1, solar energy by far has the highest theoretical energy source (about 89,000 TW in about 1.5hrs) [4]. However, if taking into account, the land/water ratio of earth, the technical power of solar harvesting will decrease to about 25,091 TW [4]. PV technology is the process of generating electricity directly from sunlight by converting solar energy into electrical energy; this process is done using solar cells [5].

The global electricity production and consumption in 2018 were about 25,592 TWh and 22,016 TWh, respectively [6], [7]. Figure 1.1 illustrates the total electricity production by the end of 2018, which includes the proportion of generation from renewable energies.

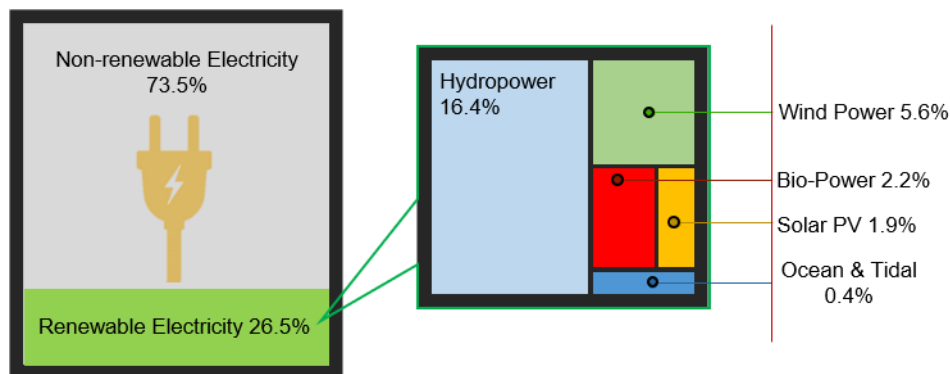


Figure 1.1: Illustrates the chart of approximated Global electricity generation and its renewable energy share [8].

From Figure 1.1, the global electricity generated from PV was only about 1.9% REN21 [8]. Figure 1.2 illustrates the global electricity generated from PV systems per year in the past decade.

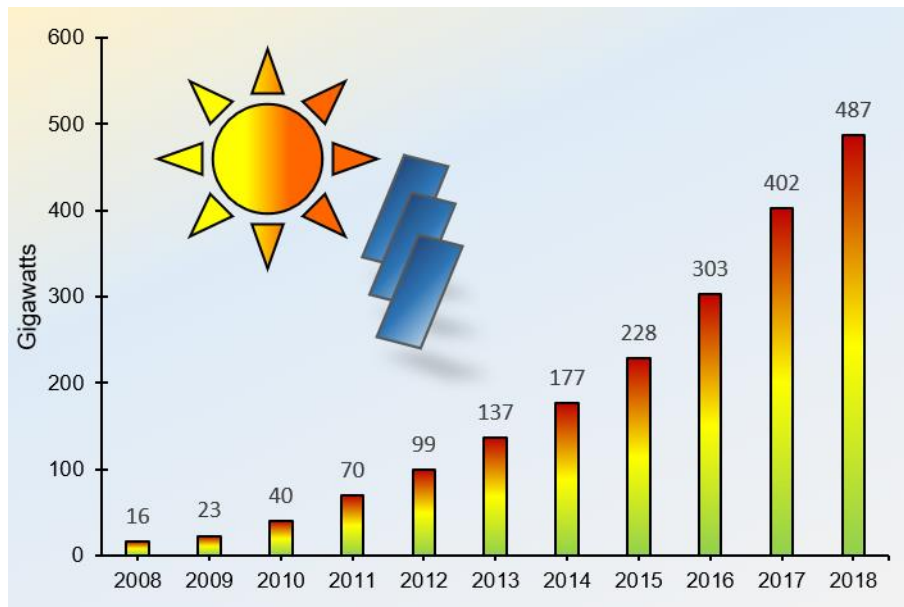


Figure 1.2: Annual global electricity generated from PV technology [8].

In the past few decades, there has been a great deal of investment in the development and enhancement of PV technology. Electricity generated by PV systems is clean and has no noise pollution. Since their primary fuel is sunshine, PV systems do not release any toxic air or water pollution into the environment, deplete natural resources, or endanger animal or human health. PV cells were initially designed for space use, where repairs are costly, if not impossible. To date, the primary source of electricity generation in the space is via PV cells because they operate reliably for long periods with virtually no maintenance. Small-scale solar plants can take advantage of unused space on rooftops of existing buildings, and large-scale solar farms can generate electricity for grid connection. Hence, electricity generated from solar cells reduces the environmental impacts and reduces dependency on fossil fuels [9]. PV systems can be installed to harvest solar energy as a stand-alone unit or for grid connection by building solar farms.

With all the advantages PV cells have, there are some drawbacks to this technology. Electricity generated from solar energy is to some extent more expensive to produce than using conventional sources of energy. This is due to the high cost of

manufacturing PV devices, DC-DC / DC-AC converters and energy storage systems such as batteries. As the manufacturing costs and price of kWh continue to decrease, PV panels become increasingly cost-competitive with conventional fuels [9]. The recent developments on the enhancement of PV cell power conversion efficiencies can be summarised in Figure 1.3 produced by National Renewable Energy Lab, USA [10].

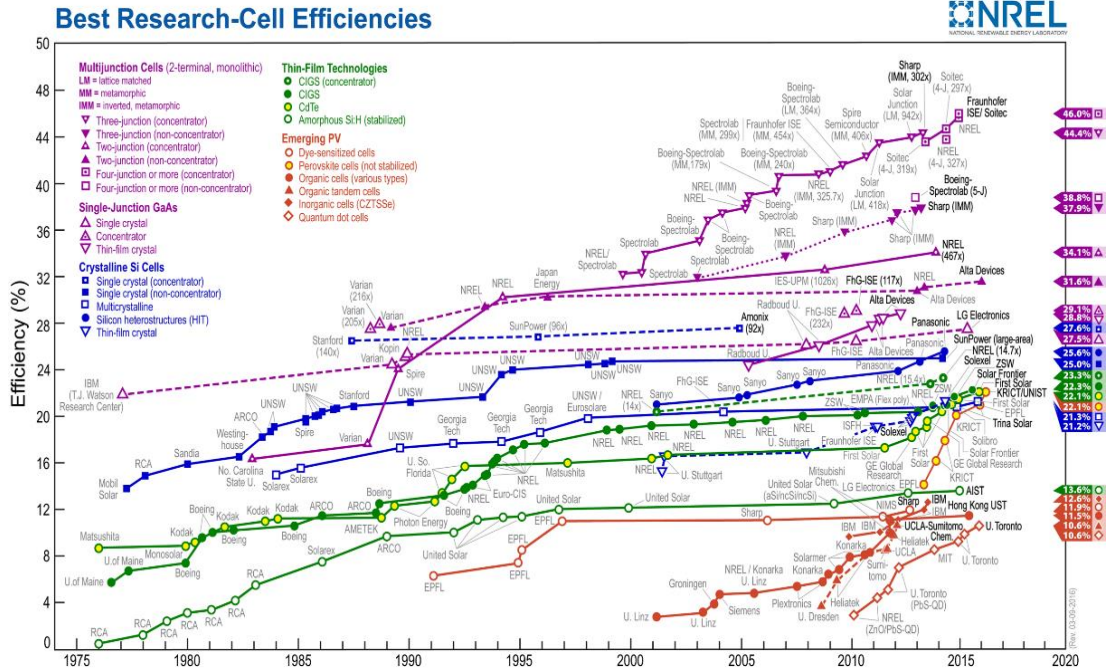


Figure 1.3: Best research solar cell efficiencies in the world, Timeline produced by National Renewable Energy Laboratory USA.

1.2 Types of Solar Cells

As is evident in Figure 1.3, solar cells, have been developing significantly in the past four decades, and their power conversion efficiency (PCE) has been significantly enhanced. Solar cells can be generally divided into three types, which are described briefly in the following subsections.

1.2.1 Type-I

Type-I (**T-I**) solar cells are single P-N junction mono/poly-crystalline silicon-based solar cells. Mono-crystalline cells are created from a single continuous silicon crystal structure wafer, whereas poly-crystalline cells are produced from fragments of silicon

that are merged together to form a wafer [11], [12]. These solar cells are the most commercially available in the current global market, with average PCE of 18-20 % [12]–[15]. Solar cells are generally evaluated based on their performance, which is measured as their PCE. The work of W. Shockley and H. Queissier showed that the maximum theoretical PCE of a single junction solar cell is about 33 % [16]. Majority of solar cells that use polycrystalline silicon have PCEs of around 15-20 % [13]–[15]. However, mono-crystalline silicon solar cells have fewer defects in silicon lattice and usually have greater PCEs, with highest recorded efficiency of 25 % [17]. **T-I** solar cells have reasonably high PCEs and long lifetime; however, their production and manufacturing costs are relatively expensive.

1.2.2 Type-II

Type-II (**T-II**) solar cells were developed to reduce the manufacturing and material costs of **T-I** solar cells; since **T-I** cells predominantly relied on the use of silicon wafers. According to work done by Shaheen & Ginley, in the past decade, there has been an immense amount of research conducted on the production of more cost-effective **T-II** thin-film solar cells [18]. These solar cells are based on amorphous silicon, Cadmium telluride Cds / CdTe, and Cu (In, Ga) Se₂. They are produced by methods such as sputtering, plasma-enhanced chemical vapour deposition and physical vapour deposition. **T-II** cells tend to have lower PCEs than **T-I** (based on crystalline silicon) due to less crystallised structure and presence of impurities. The highest record of PCE for Thin Film Technology solar cells are 21.1 – 23.3 %, certified by National Renewable Energy Laboratory USA, shown in Figure 1.3 [10], [19]. The advantages of **T-II** solar cells compared to **T-I** cells can be summarised as: ease of manufacturing, faster production and lower material/manufacturing costs. Cheaper production cost allows **T-II** cells to be an excellent competitor to **T-I** type solar cells.

1.2.3 Type-III

Type-III (**T-III**) solar cells are the new and emerging technologies which bring a new era to the solar cell industry. They vary in design and consist of multi-junction cells, dye-sensitized cells (DSCs), organic solar cells (OSCs) and perovskite cells. Like **T-II** cells, these devices introduce an alternative approach to the manufacturing of solar

cells as well as making solar energy economically possible. Multi-junction solar cells have the highest PCEs amongst all of the types of solar cells; in fact, they hold the highest record, with PCE of 44% for a device made from GaInP/GaAs/GaInNAs [17]. These devices are made of multi-level cells constructed into one unit to harvest solar energy at different wavelengths to maximise their efficiency [20]. Each cell with different semiconductor material has a different energy bandgap to maximise the percentage of absorption from the solar spectrum. A stack of cells matching the solar spectrum can exceed the Shockley and Queissier PCE limit. For a multi-junction solar cell, the theoretical efficiency can reach up to 66% [20]. The main aim of multi-junction solar cells is to increase the PCE. However, their PCE to cost ratio is so high that it makes these devices less economical and commercially unavailable [21]. Their main application is for space usage (i.e. satellite and space stations) where maximum PCE is essential.

Organic solar cells (also referred to as organic photovoltaics OPVs) are a branch of **T-III** photovoltaic devices that are developed to be a competitor for inorganic solar cells [22]. OSCs have become a promising energy conversion system due to their unique advantages such as: low-cost production, ease of fabrication techniques, printable on flexible surfaces, lightweight and transparent [5]. Initial investigations of OSCs began in the 1950s, where organic dyes, such as Chlorophyll and other such compounds were investigated [22], [23]. Organic solar cell investigation further developed in the 1980s, where polymers such as poly(sulphur nitride), polyacetylene and copper phthalocyanine (CuPc) were amongst the first materials to be investigated [22], [24]. However, solar cells based on pure dyes/polymer had a limited yield of PCE, generally below the value of 0.1% [22]. Some of the main advancement in solar cell time line is illustrated in Figure 1.4.

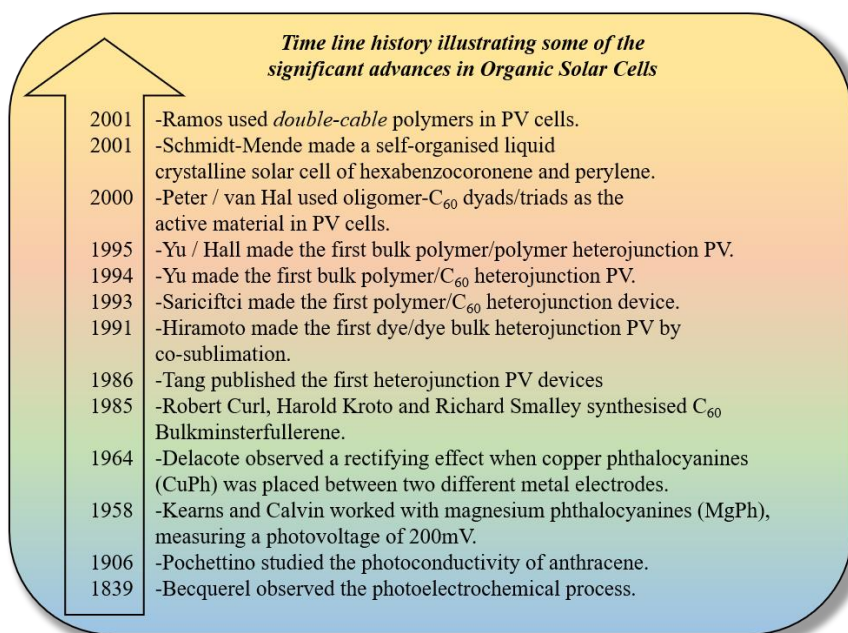


Figure 1.4: Some of the significant advances in the development of organic solar cells [22].

In 1986 Tang had a significant breakthrough in PCE of OSCs, achieving around 1% efficiency by having a donor and an acceptor material placed together to create a bi-layer and formation of heterojunction between the donor and acceptor materials [24]. Therefore, the foundation of first heterojunctions was applied to OSCs with donor-acceptor configuration such as; (dye/dye, polymer/dye, polymer/polymer, polymer/small molecule). OSCs are mainly fabricated via solution processing, where the materials used for photon absorption is dissolved in a solvent to form a solution which is then used for fabrication of OSCs.

1.3 The architecture of organic solar cells

The architecture of OSC devices can be summarised into three main categories, which are described in detail in the following subsections.

1.3.1 Single Layer

This type of OSC is constructed using only a single type of organic material polymer/small molecule. Single-layer devices operate based on the difference of work function between the two electrodes; this difference creates an electric field within the active layer. When excitons are produced, the electric field can assist the exciton pairs

in dissociating, directing electrons and holes to their respective electrodes (see Figure 1.5) [22], [25], [26]. Amongst the advantages of single-layer devices, it can be said that they use a minimal amount of material and their manufacturing process is speedy and straightforward. However, these devices do not perform well and have very low power conversion efficiencies [5], [22], [27]. The poor performance of single-layer OSC devices is mainly due to the weak electric field produced between the two electrodes to separate the generated excitons. Often these generated excitons recombine before being dissociated and transported to the electrode. Hence, they do not have high performance.

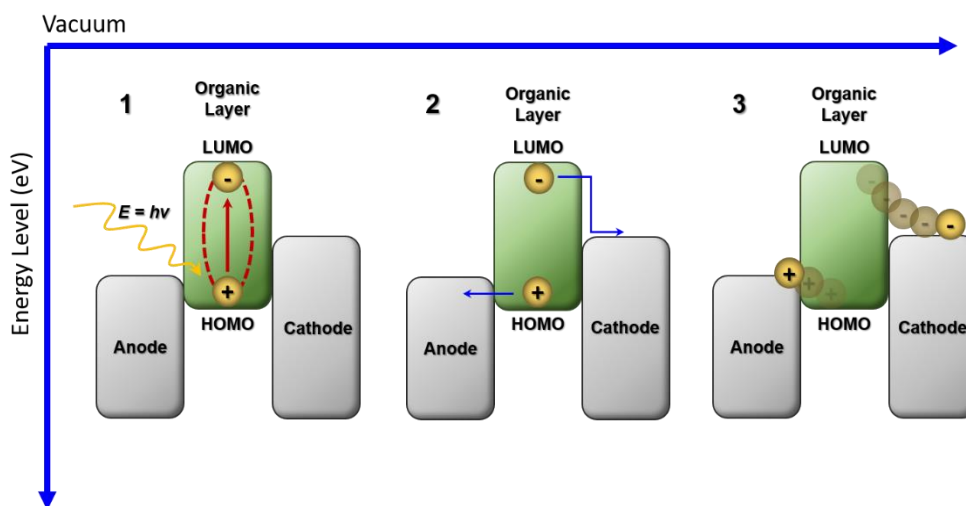


Figure 1.5: Schematic of single layer OSC device, (1) photon absorption and excitons generation, (2) exciton dissociation via electric field generated from the difference in the work function of electrodes, (3) charge collection at corresponding electrodes.

1.3.2 Bi-layer

Bi-layer OSC devices are fabricated similarly to single-layer devices, however these devices are fabricated using two layers of different organic materials to form the active layer. An active layer is a term used for layer(s) which are responsible for absorption of photons and their conversion to excitons. The active layer is sandwiched between the two electrodes. The device architecture of the bi-layer cell is illustrated in Figure 1.6.

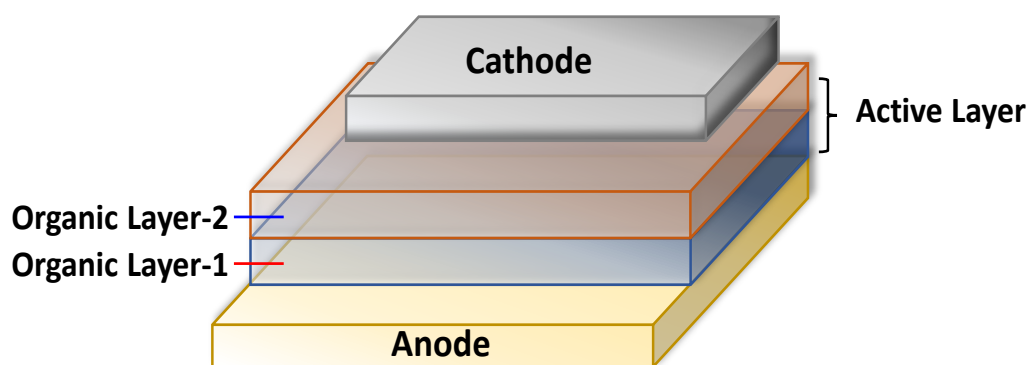


Figure 1.6: Structure of bi-layer architecture OSC sandwiched between two electrodes.

The materials used for the active layer are chosen based on their ‘electron affinity’ and ‘ionisation potential’. This creates an electrostatic force, which can dissociate the generated excitons [5], [24], [28]. Materials with significant electron affinity and ionisation potential are referred to as ‘*electron donors*’ (mainly polymers) and are used as *organic layer-1* in Figure 1.6, and materials with low electron affinity and ionisation level are referred to as ‘*electron acceptors*’ (mainly fullerene derivatives) used as *organic layer-2* in Figure 1.6. An active layer fabricated from a solution donor material and acceptor material with a D:A interface is known as a heterojunction [22], [24]–[26].

The donor layer will absorb the photon to generate excitons which travel towards the heterojunction interface, where the acceptor layer is fabricated. At this interface, if the electrochemical force between the donor and acceptor material is large enough, the coulombically bonded excitons will dissociate into free charges and travel through the corresponding layer towards the electrodes, holes toward anode and electrons toward cathode. The electrochemical energy difference between the donor and acceptor material works more efficiently than the electrode potential difference in single layer devices, and hence, bi-layer devices show better device performance and PCE. However, the main issue with this architecture is directly related to the exciton diffusion length. Since exciton distance of travel is limited to around 10 nm, they would recombine if their travelling distance is exceeded [29]. For excitons to dissociate suitably, each layer thickness must be around 10 nm [30]. Thus, an extremely thin active layer is required. As a result, absorption of photons will be limited, resulting in the inadequate generation of excitons, and therefore, the PCE of these devices are very limited [31].

1.3.3 Blended structure

The blended structure also referred to as bulk-heterojunction (BHJ) solutions are based on a blend of donor and acceptor materials in solution format. The organic materials are usually dissolved in a solvent to form the active solution which is used for fabrication of the active layer. The device structure of BHJ cells is similar to the bi-layer structure, with the difference that the active layer sandwiched between the two electrodes is fabricated from a BHJ blend. BHJ cell structure is illustrated in Figure 1.7. The main advantage of BHJ is that the donor and acceptor materials are blended together to form the active layer. Hence the limitation in *bi-layer* structure does not exist in BHJ systems. The active layer film thickness can be as thick as a few hundred nm [5], [27], [32].

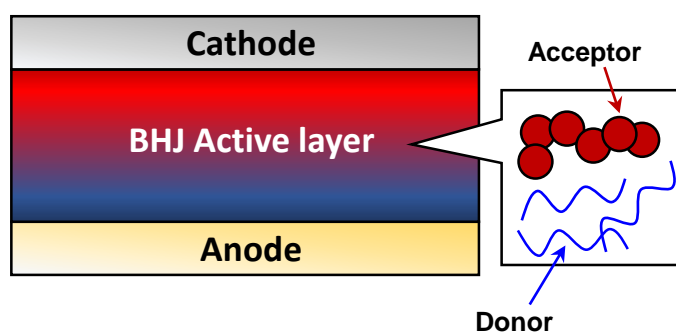


Figure 1.7. Structure of BHJ device architecture, with D:A composition illustrated on the side.

In the BHJ structure, there are nano-sized heterojunctions within the bulk of the active layer film. It is due to this unique feature that BHJ devices are the most investigated OSC structure and hold the highest PCEs [5], [27], [33], [34]. If the diffusion lengths within the active layer are close to the exciton diffusion length, the majority of the produced excitons will reach the heterojunction interface, where excitons can dissociate efficiently [35]–[37]. Electrons travel via the acceptor material to reach the cathode electrode. Similarly, holes travel via the donor material in the opposite direction to be collected by the anode electrode. The operation mechanism of BHJ OSCs will be discussed in more detail in *Chapter 2, section 2.3*.

1.4 Challenges

Despite the progress made so far in improving PCEs of OSC devices, they are hardly commercialised compared to silicon-based PVs. For OSCs to become commercially available, it is estimated that they should exhibit PCEs >10% and demonstrate long-term stability [38]. The PCE calculation of OSC is mainly dependent on the device photogenerated current density J_{sc} , open circuit voltage V_{oc} and its fill factor FF [5].

These parameters are used to assess and calculate PV performance. Improvement of these parameters is necessary for enhancing the PCE. There are several significant challenges which need to be addressed. Addressing these has been the primary driving force behind current research in this field. Some of these challenges are listed below:

- Maximising the photon absorption (using low bandgap polymers for higher photon absorption)
- Optimising the device morphology
- Increasing the charge transport within the active layer
- Finding compatible acceptor materials
- Large scale manufacturing techniques
- Use of environmentally friendly chemicals
- Stability of the fabricated OSCs in air
- Chemical solubility

1.5 Aim of this research project

The aim of this PhD project is to understand and optimise the device performance and structure of conventional BHJ solar cells based on PBDTTT-EFT polymer. PBDTTT-EFT based OSCs have been reported to yield PCE's in the range of 5 – 10 %, which are dependent on device structure (conventional/inverted), solution concentration, D:A ratio, solution preparation (choice of solvent) and fabrication techniques [39]–[43]. From the literature review, it seems that the least explored for PBDTTT-EFT based OSCs are D:A blending ratio between PBDTTT-EFT: PC₇₁BM and using different fullerene derivative acceptor materials such as IC₆₁BA or PC₆₁BM. Therefore, by identifying these gaps, it was decided that these avenues are further pursued.

Amongst these methods, D:A blend ratio and the choice of acceptor material have been the least explored methods for OSCs based on PBDTTT-EFT polymer. Most of

the published work on PBDTTT-EFT based cells are composed of BHJ blend of PBDTTT-EFT: PC₇₁BM with D:A ratio of 1:1.5. There is a limited investigation on finding the optimum blend ratio for PBDTTT-EFT: PC₇₁BM active layer. Also, there is minimal work published on investigating the impact of using IC₆₁BA as the acceptor material with PBDTTT-EFT polymer. This could be because there have been numerous published reports that IC₆₁BA does not perform well when blended with BDT-based narrow bandgap polymers [2], [44]. The lack of performance for BDT-based polymers with IC₆₁BA is not fully understood, and this research investigation is aiming to answer some of the unknown questions arising from the lack of performance in PBDTTT-EFT: IC₆₁BA solar cells. Understanding the impact and influence of acceptor material on PV performance parameters is crucial for the optimisation of the PCE. Therefore, it is necessary to provide a quantitative and qualitative evaluation on the influence of the acceptor material(s) within PBDTTT-EFT based OSC devices. Therefore, a systematic approach needs to be taken in unravelling the reasons for lack of performance when IC₆₁BA is used in a blend with PBDTTT-EFT. Before that, the optimum active blend ratio needs to be obtained and fully understood. Therefore, this research project aims to enhance the PCE of OSC devices based on BHJ in conventional architecture.

1.6 Objectives

In order to achieve the aim stated in the section above, the following objectives must be reached:

- To characterise the materials used for fabrication of the active layer of the OSC devices.
- To optimise the fabrication methods and device performance of on the PBDTTT-EFT: PC₇₁BM devices.
- To determine the optimum D:A blend ratio for PBDTTT-EFT: PC₇₁BM based OSCs.
- To investigate the impact of different fullerene derivatives (IC₆₁BA and PC₆₁BM) on the OSC device performance when used as acceptor materials to be blended with PBDTTT-EFT polymer.

The objectives listed above are an overview of what needs to be done, each bullet point is expanded into multiple tasks which are later discuss in this thesis.

CHAPTER 2

Device Physics of Organic Solar Cells

2.1 Introduction

Solid materials can be categorised into three groups, conductors, insulators and semiconductors. Generally, conductors are described as materials that pass current conduction with low resistivity, while insulators do not allow electrical current to pass through. Semiconductors are defined as materials whose electrical conductivity fall in the range of conductors and insulators ($10^3 - 10^8 \text{ S cm}^{-1}$) [38]. In solid-state physics, the valance and conduction band are the bands nearest to the Fermi level (denoted by E_F) and therefore define the electrical conductivity of the solid [45]. The valance and conduction bands are occupied and unoccupied of electrons respectively. Figure 2.1 illustrated the energy band diagram for the different types of solid materials according to the classification above.

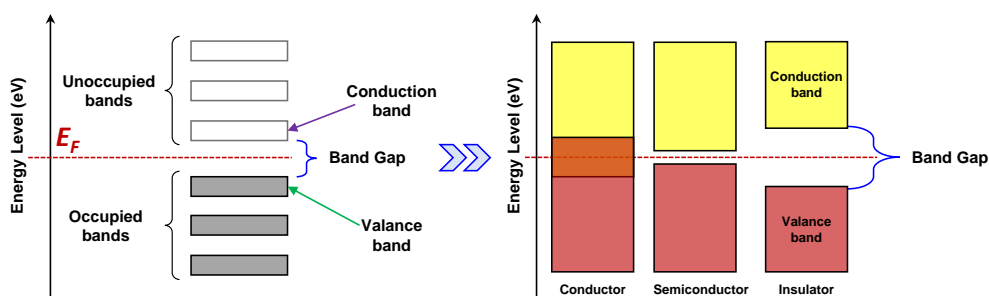


Figure 2.1: Energy band diagram illustrating different levels of valance and conduction band. Also showing the difference between conductor, semiconductor and insulator on energy band diagram.

As can be seen from Figure 2.1, conductor's valance and conduction bands edge over one another, allowing materials in this category to conduct better [46]. The larger the gap between the valance and conduction bands, the less the conductivity for that specific solid, hence, insulators have the largest bandgap [46].

2.2 Organic Semiconductor Properties

Organic semiconductors (OS) are carbon-based materials having semiconducting characteristics [47]. They are suitable for a range of electronic applications [5]. In the past decade, OS has been employed in electronic devices such as organic light emitting diodes (OLEDs), organic field effect transistors (OFETs) and organic solar cells (OSCs) [38]. Similar to inorganic semiconductors they have equivalent of valance and conduction energy bands know as Highest Occupied Molecular Orbital (HOMO) and Lowest Unoccupied Molecular Orbital (LUMO) the same as conduction band [47], [48]. Organic materials have larger bandgap as compared to their inorganic counterparts [38]. Within OS materials, conjugated polymers have been investigated over three decades for photovoltaic applications [49], [50]. They have high absorption coefficient which allows them to fabricate thin films with a thickness of <100nm and still absorb light; they have a flexible structure, solubility, low manufacturing costs (compared to silicon) and transparency [5], [27], [51], [52].

2.2.1 Conjugated Polymers

Conjugated polymers are made of alternating single and double carbon bonds which are expressed as conjugation. Their energy bands are less ordered compared to inorganic semiconductors and therefore, understanding the energy band formation of conjugated polymers is essential. Figure 2.2 illustrates the chemical structure for a simple conjugation of polymeric semiconductor, Polyacetylene.

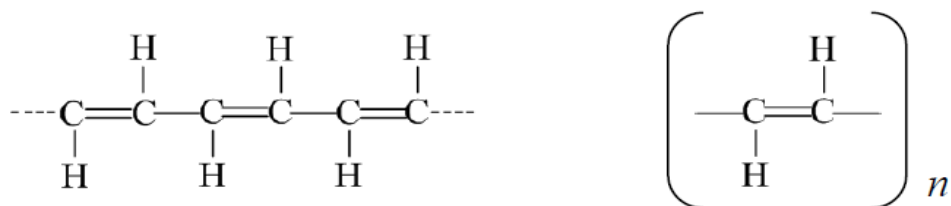


Figure 2.2: Representation of conjugated organic polymeric semiconductor, Polyacetylene [38].

Formation of energy bands in OS materials is expressed in terms of the molecular orbital interaction. There are four electrons available in a carbon atom for forming bonds; three of these bonds are considered to occupy the sp^2 hybridised orbitals and one on p_z orbital. When organic material such as ethylene (C_2H_4) is bonded, the three electrons in sp^2 orbital of the carbon form covalent bonds to their adjacent carbon and hydrogen atoms via sigma (σ) bond and the remaining electron in p_z orbital becomes available to form covalent bond via a pi (π) bond. A single bond will have a sigma bond, and it is formed from the overlap of atomic orbitals. However, a double bond has a (σ) and a (π) bond which arises due to the unhybridized p orbital above and below the sigma bond. This process is illustrated in Figure 2.3.

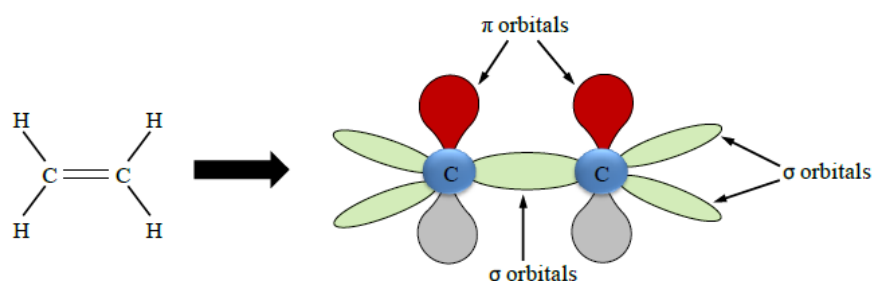


Figure 2.3: Schematics illustration of ethylene molecule and its molecular orbital bonds [38].

Therefore, the chemical bond of conjugated polymers can be described as a series of an alternating single (σ only) and double (σ and π) bonds [38]. The interaction between adjoining (p_z atomic orbitals) will result in the splitting of the π molecular orbitals into π (bonding) and π^* (antibonding) orbitals and therefore, π electrons are believed to exist in in the π band, whilst the π^* is empty at lower energy states [38], [53].

The splitting of π orbital creates a gap between the bonding and antibonding bands; as the carbon chain increase, it seems that there is a smaller splitting of the levels of discrete bonding π and antibonding π^* states, this is illustrated in Figure 2.4 [38], [53]. The π and π^* are considered as HOMO and LUMO, respectively [38]. The energy difference between HOMO and LUMO level is the energy bandgap (E_g) of the polymeric material, as shown in Figure 2.4.

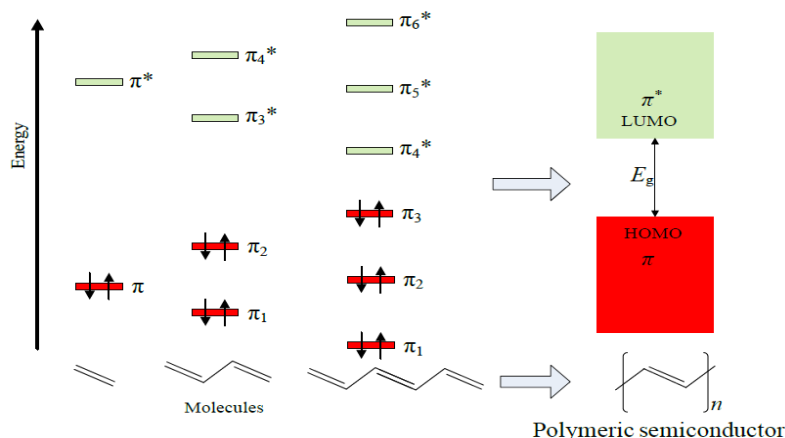


Figure 2.4: Molecular orbital interactions presented in the form of energy bands for polymers [38].

Generally speaking, the increase of conjugation length will lead to the decrease of energy difference between LUMO and HOMO. But this effect will become unnoticeable when the number of monomer units gets to a saturated value. Therefore, unlimited extension of the conjugation length is not necessary by virtue of a limited reduction of the bandgap [54]. According to *particle in a box* theory, the delocalization of the π electrons along the conjugated carbon chain shifts the energy needed for the electronic absorption down into the infra-red region, and the wavelength of the transition increases with the length of the conjugated system. A more powerful strategy to lower the bandgap and tune the electronic energy levels of the conjugated polymers is introducing an alternative structure of conjugated electron rich donor (D) and electron-deficient acceptor (A) into one polymer backbone [54].

2.3 Charge Transport in Organic Semiconductors

When no external energy is applied to the organic molecule, the HOMO is filled with electrons and LUMO is unoccupied. Charge transport to take place through the dissociation of excitons generated from the absorbed photons [38]. Due to weak intermolecular bonds in organic molecules, the delocalization of charges is not difficult compared to inorganic semiconductors. Furthermore, as a result of excitation, there is a spatial distribution of electrons in the σ orbital, resulting in changes to the molecular geometry. Therefore, OS occupy more localised charges, and their transport characteristic is regarded as hopping from molecule to molecule [38].

2.3.1 Electrode – Semiconductor interface

Electrode – semiconductor interface is an important concept in OSC devices. This interface is constructed via deposition of a metal onto the surface of the organic semiconductor to create a contact. Dependant on the work function of the metal relative to the semiconductor type (n or p), an Ohmic contact can be obtained [38]. As an example, a schematic diagram of the metal-semiconductor interface for an n -type semiconductor is illustrated in Figure 2.5, showing the energy band of the metal and the semiconducting material before and after contact.

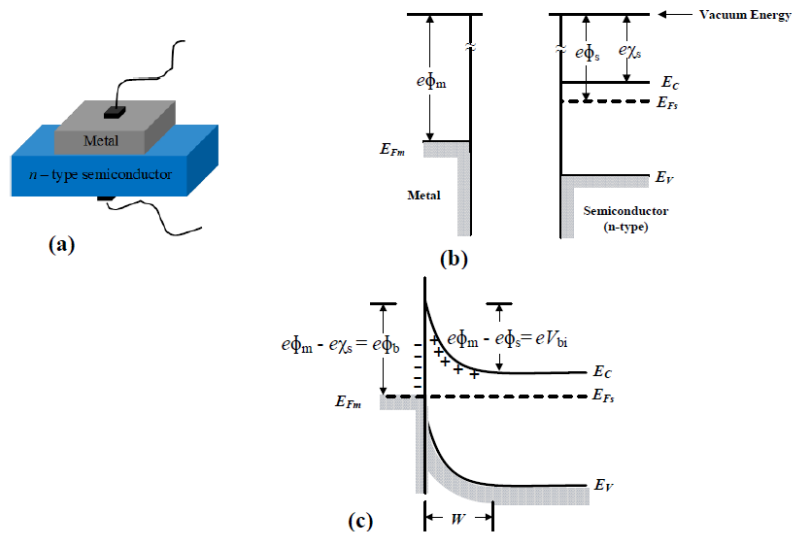


Figure 2.5: Schematic of Schottky barrier junction for n-type semiconductor and metal interface (a), energy band diagram before the interface contact (b), and energy band diagram after the interface contact under positive bias voltage (c) [38].

Where, $e\Phi_m$ and $e\Phi_s$ are the metal's and the semiconductor's work function, respectively. The difference between the metal-semiconductor work function is known as the built-in potential, eV_{bi} . Therefore, the Schottky barrier height $e\Phi_B$ can be expressed as:

$$eV_{bi} = e\Phi_m - e\Phi_s \dots \dots \dots (1)$$

$$e\Phi_B = e\Phi_m - e\chi_s \dots \dots \dots (2)$$

Where, χ_s is the electron affinity.

If $e\Phi_m > e\Phi_s$ the alignment of the Fermi level (E_{Fm}) across a junction for an n -type semiconductor will state that the electrons will travel from the semiconductor to the metal. This will induce a depletion layer with a width (W) as a function of the applied

voltage [38]. Positive charges accumulate on the semiconductor and the negative charges on the metal. W is mathematically expressed as:

$$W = \left(\frac{2\varepsilon(V_{bi} \pm V)}{eN_d} \right)^{\frac{1}{2}} \dots \dots \dots (3)$$

where, $\varepsilon = \varepsilon_0\varepsilon_r$ is the permittivity of the semiconductor material with ε_0 being vacuum permittivity and ε_r being relative permittivity of the material, N_d is the concentration of ionised donor and $\pm V$ is the forward or reverse bias voltage applied under thermal equilibrium $V = 0$ V.

By applying a positive bias voltage across the *n-type* semiconductor material, the value of $e\Phi_B$ will increase, resulting in hindering of the electron flow from the semiconductor to the metal, this is known as reverse bias condition (for *n-type*) [38]. However, if the negative bias voltage is applied across the *n-type* semiconductor material, $e\Phi_B$ will decrease and electrons can travel from the semiconductor to the metal easier, this is known as forwarding bias condition (for *n-type*) [38].

For an *n-type* semiconductor and metal, if $e\Phi_m < e\Phi_s$, an Ohmic contact will be formed at the interface junction [38]. Once this junction is formed between the semiconductor and the metal, there will be an energy band bending of the semiconductor towards the metal electrode as illustrated in Figure 2.6. If there is no potential barrier at the formed junction, electrons can travel to the metal regardless of the direction of the applied bias voltage. If the semiconducting material used is a *p-type* semiconductor, then the Ohmic contact will be formed when, $e\Phi_m > e\Phi_s$ [38].

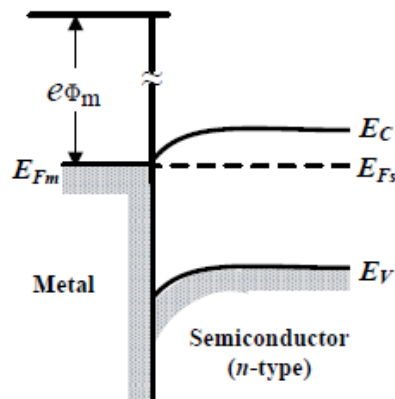


Figure 2.6. Schematic of energy band diagram after semiconductor-metal contact, forming an Ohmic contact [38].

If instead of having a single n -type or p -type semiconducting material, two semiconducting materials with different energy gaps are brought to contact, the junction formed between these materials is known as heterojunction [55]. Organic semiconducting devices such as OSCs cells have been adopting the heterojunctions [38]. The organic semiconductor materials are generally termed as a donor (electron-donating / p -type) and an acceptor (electron-accepting / n -type) materials.

Bulk-heterojunctions (BHJs) are typically produced via solution casting of donor-acceptor blends [38]. Electron donor materials are characterised similar to p -type semiconductors, with conjugated polymers being an excellent example of such materials [55], while electron accepting materials are characterised similar to n -type semiconductors and fullerene derivatives are an excellent example [56]. Energy band diagram of a Donor-Acceptor BHJ system is illustrated as a schematic in Figure 2.7.

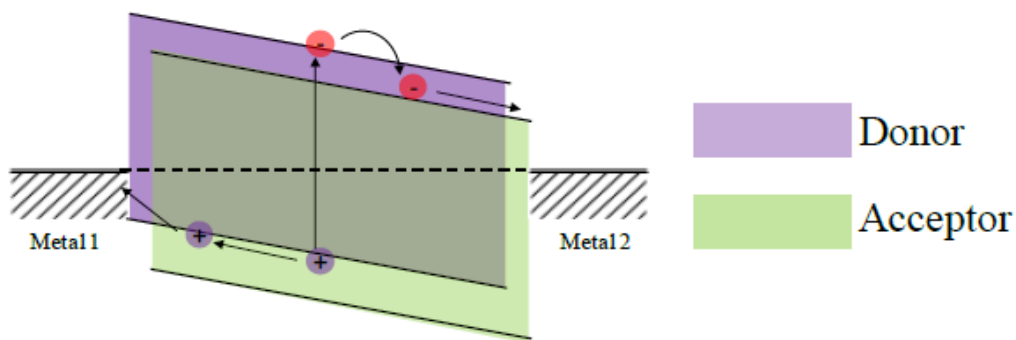


Figure 2.7: Schematic of Energy band diagram for BHJ system illustrating donor and acceptor material.

Figure 2.7 illustrates the charge transport in a BHJ organic solar cell system under illumination, where there is no applied bias voltage. Important to note that for correct charge collection of electrons and holes, the work function of metal-1 must be higher than metal-2, as this is necessary, to ensure selective charge collection at the electrodes [38].

2.3.2 Ohmic and SCL Conductivity in Organic Semiconductors

The resistance in an Ohmic contact between the semiconductor and the electrode is usually negligible compared to the bulk resistance of the semiconductor [57]. Ohmic conduction in semiconductors is mostly due to thermally generated carriers [38].

Therefore, such conduction takes place at low applied voltages due to excess thermally generated carriers relative to injected ones [38]. The current density at low voltages will obey Ohm's law and is mathematically expressed as:

$$J = (p, n)\mu_{p(n)}q \frac{V}{d} \dots \dots \dots (4)$$

where, (p, n) is the hole or electron concentration density respectively (depending on the semiconductor material p or n type), $\mu_{p(n)}$ is the hole or electron mobility respectively, q is the elementary charge, V is the applied DC bias voltage, and d is the thickness of the semiconductor layer.

It is important to note that Ohm's law is no longer obeyed within the space charge limit at the higher electric field as the injected charge carriers become denser. The electric field becomes dominant over the applied voltage, and the condition becomes space charge limited [38]. This behaviour is characterised by a quadratic dependence of current density on the applied voltage, also referred to as the Mott-Gurney relationship [58]:

$$J = \frac{9}{8} \varepsilon \mu_{p(n)} \frac{V^2}{d^3} \dots \dots \dots (5)$$

In the case of trapped charge carriers, the relationship between current density (J) and applied bias voltage (V) will no longer follow the quadratic Mott – Gurney expression. In such circumstances, Lambert and Mark power law should be used to express the relationship between J and V [59], [60]:

$$J = \left(\frac{\mu_{p(n)} N_{cv}}{q} \right) \left(\frac{\varepsilon}{N_{T_{h(e)}}} \cdot \frac{1}{l+1} \right)^l \left(\frac{2l+1}{l+1} \right)^{l+1} \frac{V^{l+1}}{d^{2l+1}} \dots \dots \dots (6)$$

where N_{cv} is the effective density of state (either in conduction or valence band), $N_{T_{h(e)}}$ is the trap density for holes or electrons, respectively [$N_{T_{h(e)}}$], and l is the exponent power greater than 2. This condition is typically met for applied bias voltage above 5V, where the J-V relationship is in a trap-filled state [58].

2.4 Operation mechanism of Organic Solar Cells

Solar radiation is emitted in the form of electromagnetic waves/particles, also known as photons. The energy of a photon E is defined by Planck – Einstein relationship:

$$E \text{ (eV)} = hv = \frac{hc}{\lambda} \dots \dots \dots (7)$$

where ν is the photon's frequency, h is Planck's constant, c is the speed of light in vacuum and λ is the photon's wavelength. When the incident photon's energy is equal to or greater than the energy bandgap (E_g) of the organic semiconductor material, excitons are generated. The operation mechanism of BHJ OSCs under illumination is illustrated as a schematic in Figure 2.8.

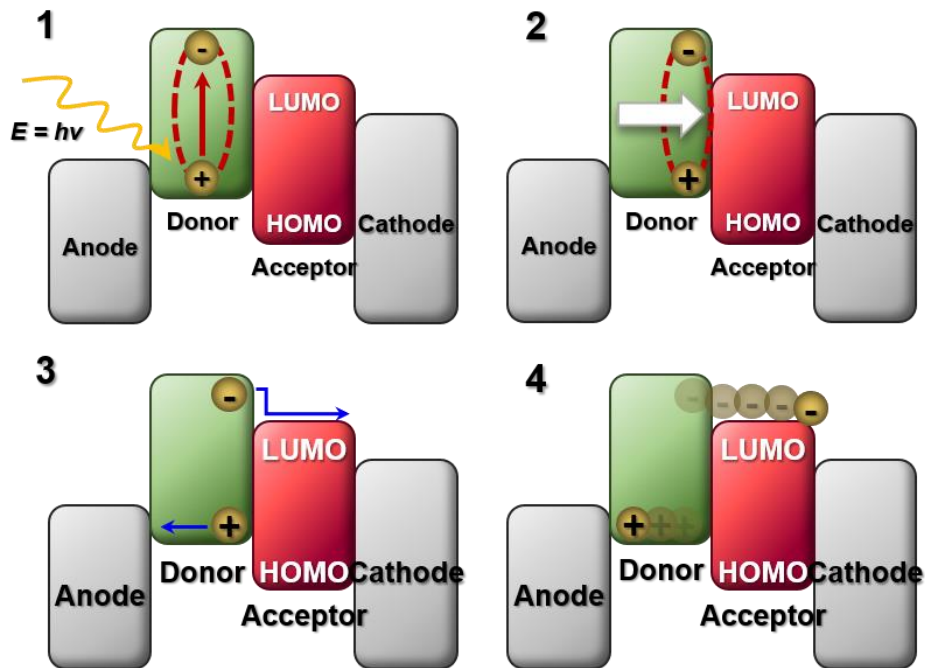


Figure 2.8: Operation mechanism of BHJ OSCs under illumination, indicating the primary four stages: Absorption, dissociation, transport, and extraction.

The operation mechanism in BHJ OSCs can be described as:

1. Photon Absorption and exciton generation: the incident photons will be absorbed by the donor material, and excitons are generated within the donor material.
2. The excitons are then transferred to the edge of the D-A interface, which is referred to as the Heterojunction.
3. The excitons will dissociate into free charge carriers at the heterojunction interface.
4. The divided free charge carriers drift to the corresponding electrodes at the opposite ends of the cell.

2.4.1 Equivalent circuit model of organic solar cells

Under dark conditions, OSCs will behave like a diode, and their J – V characteristics can be modelled similarly to an ideal p-n junction diode. This is mathematically expressed as [57]:

$$J = J_s \left[\exp\left(\frac{qV}{k_B T}\right) - 1 \right] \dots \dots \dots (8)$$

where, J_s is the saturation current density under reverse bias, q is the elementary charge, V is the applied bias voltage, k_B is Boltzmann constant, and T is the temperature (K). Solar cell under no light is characterised like a diode. However, a solar cell examined under illumination will have a different J-V characteristic. This is mathematically expressed as:

$$J = J_s \left[\exp\left(\frac{qV}{k_B T}\right) - 1 \right] - J_{sc} \dots \dots \dots (9)$$

where J_{sc} is the short circuit current density when the applied bias voltage is at zero ($V = 0$). J_{sc} generated is directly related to illumination intensity. Solar cells yield their highest voltage at open circuit condition, when $J = 0$, this is referred to as an open circuit voltage (V_{oc}) and is mathematically expressed as:

$$V_{oc} = \frac{k_B T}{q} \ln\left(\frac{J_{sc}}{J_s} + 1\right) \dots \dots \dots (10)$$

where k_B is Boltzmann constant.

It can be noted that V_{oc} has a direct logarithmic relationship with the J_{sc} . Figure 2.9 illustrated the J-V characteristic curve plots of an ideal solar cell under dark and illumination conditions.

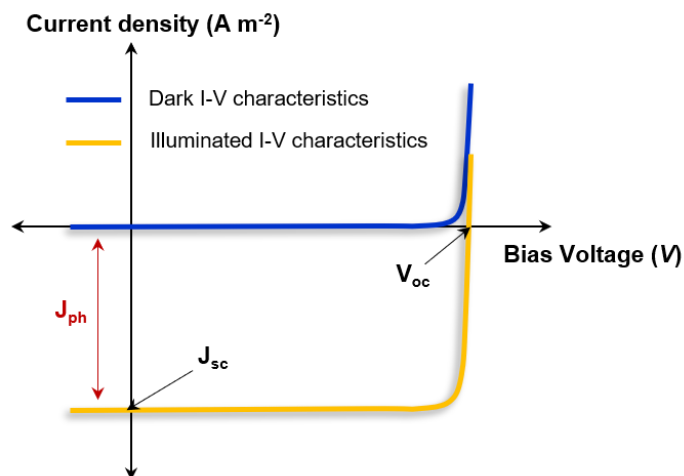


Figure 2.9: J-V characteristic curves of an ideal solar cell under dark and illumination conditions.

By plotting the J-V characteristic curve of a solar cell under illumination, the cells electrical characteristics can be determined. A typical J-V and its corresponding power density-voltage (P-V) curves for an ideal solar cell are plotted in Figure 2.10.

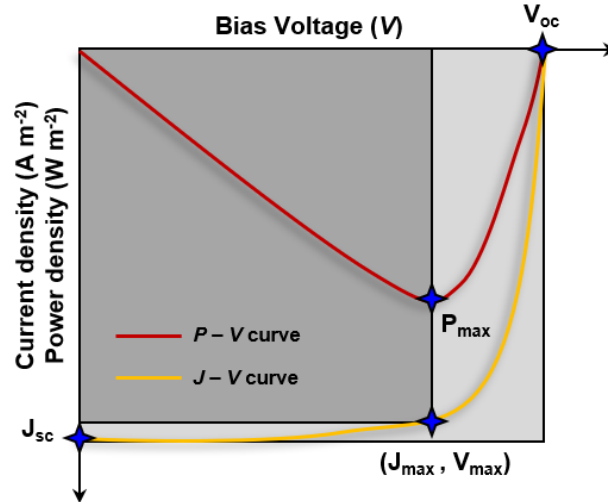


Figure 2.10: J-V and P-V curves for an ideal solar cell under illumination, indicating the J_{sc} , V_{oc} , P_{max} and its corresponding J_{max} and V_{max} .

In Figure 2.10 above, J_{max} and V_{max} are maximum current density and voltage that the device can generate. This corresponds to a maximum power output P_{max} . The power conversion efficiency of any system is stated as a ratio of its output to its input, which can be expressed as:

$$PCE (\%) = \frac{P_{out}}{P_{in}} \times 100 \dots \dots \dots (11)$$

PCE of a solar cell is also expressed in the same way. The input power is the same as the power of illumination intensity. However, the output power is determined from the generated electricity from the solar cell device. Since electrical power is expressed as the product of current and voltage, the output power density and PCE of a solar cell can be expressed as:

$$P_{out} = J_{sc} V_{oc} \dots \dots \dots (12)$$

$$PCE (\%) = FF \times \frac{J_{sc} V_{oc}}{P_{in}} \times 100 \dots \dots \dots (13)$$

where FF in the equation above is referred to as the fill factor of the device. This parameter defines the quality of the device; an ideal solar cell device will have an FF of unity. FF can be mathematically expressed as:

$$FF = \frac{J_{max}V_{max}}{J_{sc}V_{oc}} \dots \dots \dots (14)$$

What has been described in the sections above has been for an ideal solar cell. However, in a realistic case where there are imperfections, there will be parameters which will impact the PCE of solar cells. These parameters, such as contact resistance and current leakage, can be added to the model for calculating the PCE by having their equivalent. Series and shunt resistance (R_s and R_{sh}) are the circuit equivalent of those parameters [61]. Therefore, a circuit model of a solar cell can be drawn, which is illustrated in Figure 2.11.

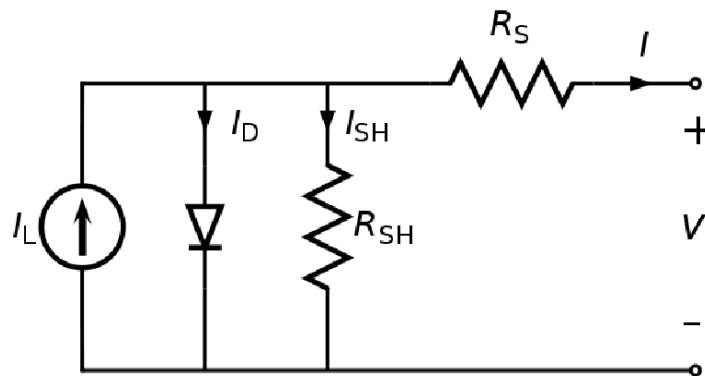


Figure 2.11: Equivalent circuit model of a solar cell with R_s and R_{sh} incorporated.

As can be seen from Figure 2.11, the circuit has resistance in series (R_s) and one in parallel. The resistance in parallel is referred to as shunt resistance R_{sh} . R_s is governed mainly by the semiconducting material and electrode interface as well as current flow within the material. Therefore, series resistance R_s value is the summation of the contact resistance and bulk of the material. On the other hand, R_{sh} is governed by the level of leakage current through the solar cell and its surrounding edges.

The power conversion efficiency of a solar cell is directly related to the value of these resistances. In an ideal solar cell, the value of R_s would be zero, and the value of R_{sh} would be infinitely high. However, in a real system this is not the case, the impact of increase and decrease of R_s and R_{sh} values respectively on J-V characteristic curves are illustrated in Figure 2.12.

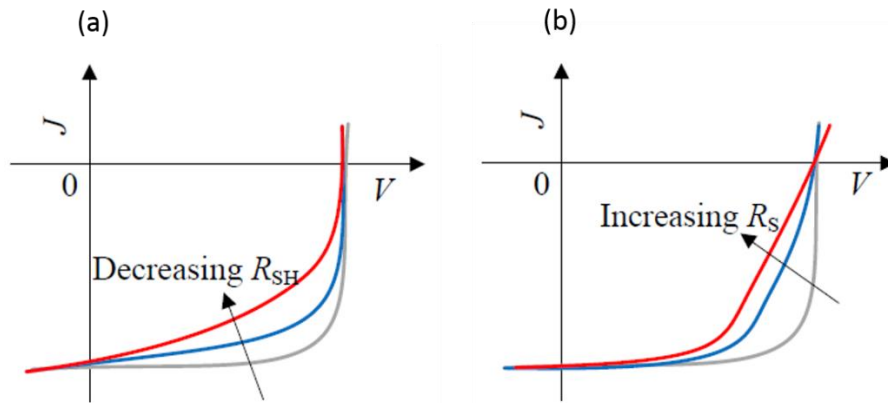


Figure 2.12: Impact of change in the R_{sh} and R_s on the J-V characteristic curve of the solar cell under illumination: (a) effect of R_{sh} decreasing, (b) effect of R_s increasing.

From Figure 2.12, it can be seen that change in R_s and R_{sh} will impact the PCE of the solar cell. As R_s and R_{sh} values increase and decrease, respectively, the J-V curve becomes less of a rectangular shape, which represents an ideal solar cell operation under illumination. As a result, such changes will reduce FF parameter resulting in lower PCEs. By incorporating R_s and R_{sh} into the J-V characteristic model, the new mathematical representation for J as a function of applied bias voltage (V) will be:

$$J = J_{sc} - J_s \left[\exp \left(\frac{q(V - JR_s)}{nk_B T} \right) - 1 \right] - \frac{V - JR_s}{R_{sh}} \dots \dots \dots (15)$$

where n is the ideality factor of the diode component shown in Figure 2.11.

As it was evident in figure 2.12, it can be seen that the impact of R_{sh} is near the J_{sc} regions and R_s is near V_{oc} regions. It has been reported in number of published work that the R_{sh} and R_s parameters can be extracted from the I-V or J-V characteristic curves by calculating the inverse slope of that curve [62]–[64]. Figure 2.13 illustrates how R_s and R_{sh} can be obtained from a J-V curve.

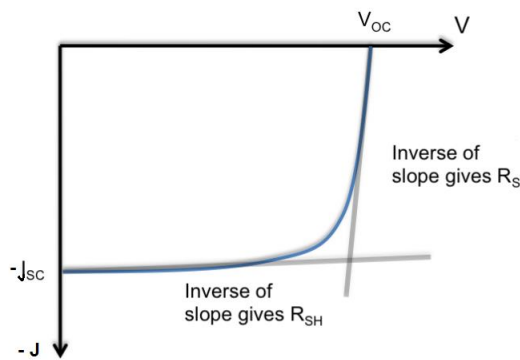


Figure 2.13: Determination of R_s and R_{sh} from a J-V curve plot under illumination for a solar cell.

2.4.2 Exciton Dissociation

Upon absorption of photons by the donor material, excitons are generated. This mechanism is different in inorganic semiconductors, where free charges are generated directly [38]. Such a difference is mainly because inorganic semiconductors have low dielectric constants and better electron-lattice interactions [47], [65]. The lower dielectric constant of inorganic semiconducting materials would mean that less energy / electric field is needed for a free charge to be generated [66]. Exciton dissociation in OS is mainly governed by a mechanism linked to the electronic energy difference of the donor-acceptor materials used [67]. In BHJ systems, successful dissociation of excitons takes place at the heterojunction of the D-A interface. Excitons do not directly dissociate into free charges at the D-A interface. Instead, they initially form a spatial electron-hole separation. At this stage, the electron-hole pair is bounded by Coulomb force; this stage is usually referred to as geminate pairs or charge transfer state (CT state) [68].

CT state is the midpoint between bounded electron-hole pairs and dissociated free charges. Successful dissociation of CT states into free charge carriers are critical and contribute to the level of photocurrent generated. Unfortunately, not all the electron-hole pairs in CT state will fully be dissociated into free charge carriers. The process that inhibits electron-hole pairs to become free charge carriers is through two recombination mechanism, known as *Geminate* and *Bimolecular* recombination. Geminate recombination takes place when the electron-hole pairs recombine before dissociation, while bimolecular recombination takes place after electron-hole pairs have been dissociated into free charges [67], [68]. For the electron-hole pairs to dissociate, they need to be separated apart by overcoming the coulomb force bounding them. As mentioned at the beginning of this section, the dissociation of excitons is governed by the energy difference at the D-A interface. Therefore, the energy required at the D-A interface to overcome the Coulomb force between electron-hole pairs can mathematically be expressed as:

$$E (J) = \frac{q^2}{4\pi\epsilon a} \dots \dots \dots (16)$$

Where ϵ is the permittivity of the semiconductor material, q is the elementary charge, and a is the spatial separation distance between electron-hole pairs.

Figure 2.14 illustrates a simple schematic diagram of exciton dissociation at the D-A interface for a typical BHJ OSC, indicating the initial dissociation and CT state.

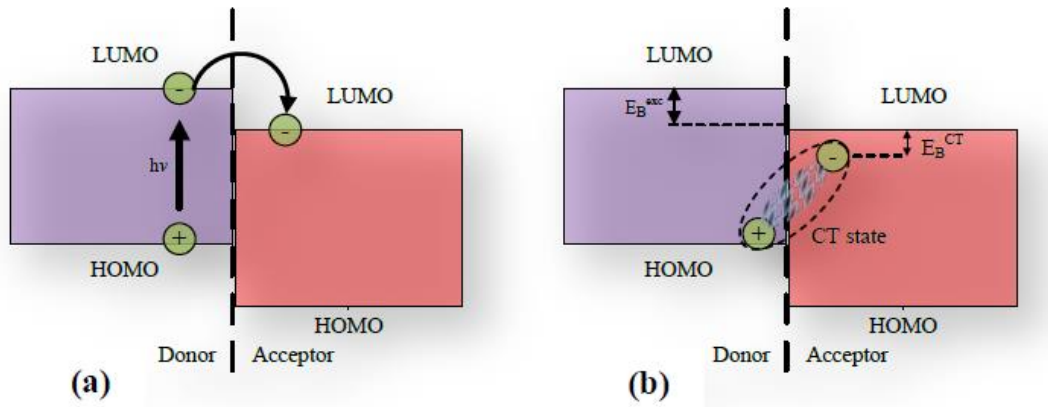


Figure 2.14. (a) D-A interface energy diagram illustrating the excited electron in the LUMO level of the donor material upon photon absorption in the donor material. (b) Formation of CT state between the electron and hole; with E_B^{exc} being the exciton binding energy, relating to the difference between the LUMO's of the donor and acceptor materials (Δ LUMO), and E_B^{CT} being the charge transfer state binding energy.

In order for the initial dissociation stage to take place, there should be a minimum energy difference between donor and acceptor LUMO levels [38]. The LUMO difference should be sufficient enough to exceed the E_B^{exc} , which will initialise the CT stage [38]. Because the D-A interfaces are confined to each other, this initial electron transfer stage will transfer into a spatial separation between the electron and hole (CT state). This separation distance is usually around the same dimension of the molecule size (0.5 – 1 nm) [38]. By applying these distances (a) into the equation above, Columbic energies in the region of 0.1 – 0.5 eV is estimated. This is referred to as the CT binding energy (E_B^{CT}) as shown in Figure 2.14b. By comparing the degree of Columbic energy to thermal energy ($k_B T \sim 0.025$ eV), it can be stated that there is a significant difference between them and that thermal energy is not sufficient enough to dissociate excitons. Heeger et al. [69] evaluated that the origin of V_{oc} for BHJ OSC is related to the difference between the HOMO of the donor and LUMO of the acceptor material. Based on their investigation, it was empirically deduced that a minimum LUMO difference of 0.3 eV between the LUMO of acceptor and donor is required for sufficient exciton dissociation [65]. They reported that the V_{oc} could be determined using the following equation [65]:

$$V_{oc} = \frac{1}{q}(\text{HOMO}_D - \text{LUMO}_A) - 0.3V \dots \dots \dots (17)$$

The exciton dissociation process at the D-A interface for BHJ OSCs has been revolved around the Onsager model, which offers a measurable description of the exciton dissociation efficiency affected by an electric field [68]. The main reasons for incomplete exciton dissociation in BHJ OSCs are low dielectric constants and charge carrier mobilities of conjugated polymers. If charges in CT state are not dissociated within their lifetime, they will have a geminate recombination.

Geminate recombination was firstly reported and explained by Onsager [68]. The probability of recombination for ion-pairs separated by a distance was the focus of Onsager's work. The established theory laid the groundwork for the application of Onsager's Theory to be applied successfully on numerous conjugated semiconducting systems [38]. Onsager was able to estimate the probability of escaping recombination for oppositely charged ion – pairs while undergoing Brownian motion and the impact of Coulombic attraction and external electric field. The proposed model suggested that localised holes and thermalized electrons are being generated upon absorption of photons. Due to the excess thermal energy it possesses, the electron thermalizes after undergoing a rapid motion [38]. The thermalization occurs at a distance (a), from the localized hole.

This distance of separation between the thermalized electron and the localized hole is referred to as the thermalization length (as illustrated in Figure 2.15) [38]. The model proposed by Onsager also defines a Coulombic capture radius, which is known as Onsager radius (r_c). Since the distance of the Coulombic attraction energy can be represented by the thermal energy $k_B T$, then Onsager radius (r_c) can be determined using:

$$r_c = \frac{q^2}{4\pi\epsilon k_B T} \dots \dots \dots (18)$$

From the Onsager model, the CT state will be fully dissociated if $a > r_c$. However, if $a < r_c$, CT states can dissociate into free charges with a dissociation probability $[P(E,T)]$ taken into account. Geminate recombination, takes place with a probability of $1 - P(E,T)$. Dissociation probability is dependent on the strength of the electric field (E) and the temperature (T), electron-hole separation distance (a) [70]. When there is no electric field ($E = 0$), $P(E,T)$ becomes proportional to the negative reciprocal of the electron-hole distance a . Therefore, the probability of dissociation is mathematically expressed as [70]:

$$P(E, T) = \left(1 + \frac{qr_c E}{2k_B T}\right) \exp\left(\frac{-r_c}{a}\right) \dots \dots \dots (19)$$

A schematic diagram has been drawn to illustrate the functionality of the equation above. This is illustrated in Figure 2.15.

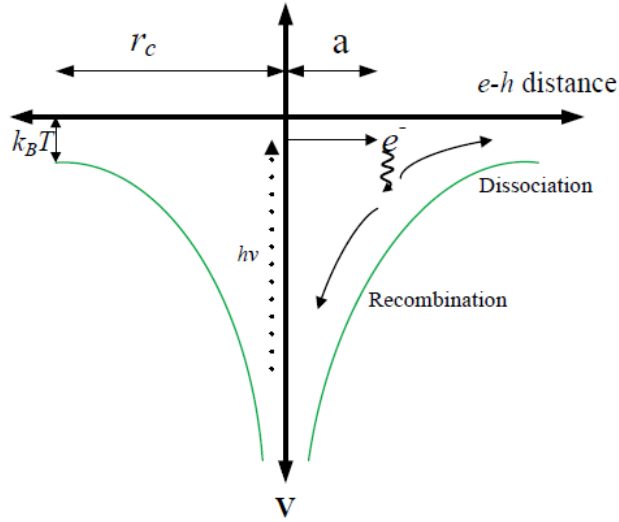


Figure 2.15: Energy diagram of dissociation probability of electron-hole pairs escaping Coulombic attraction forces, leading into free charge carriers, based on Onsager theory [38].

Braun further modified Onsager’s model to highlight the importance of CT states lifetime [71]. Braun noticed that CT states have a limited lifetime, which is dependent on the electron-hole distance (a) [67]. By modifying Onsager’s model which is related to the electric field, he calculated the electron-hole distance to be in the range of 2.5 – 3 nm, although these values are more significant than the usual CT state length (~ 1 nm).

Braun’s modification of the Onsager model, states that produced CT states at the D-A interface, have a limited lifetime, and therefore, they will have to undergo one of the following cases:

1. Recombine back to the ground state with a decay constant rate k_F .
2. Split into free charges dependent on the electric field with a constant rate of $k_D(E)$.

In case 2, the free charges, could possibly form an electron-hole pair along the way and recombine with a constant rate k_D [72]. The significant difference between Braun’s modified Onsager model is that re-captured free charges into electron-hole pairs can still be dissociated within their lifetime. Therefore, the dissociation probability can be re-written from the modifications made by Braun in terms of case 1 and 2 above. This is mathematically represented as:

$$P(E, T) = \frac{k_D(E)}{k_F + k_D(E)} = \dots \dots \dots (20)$$

Where, $P(E, T)$ is the probability of escape (dependent on temperature and electric field), k_D is the is electric field dependent decay rate constant of separated free charge carriers (decay rate constant of bimolecular recombination), and k_F is geminate decay rate constant of electron-hole pairs back to ground state [248]. In the following sections, different types of recombination mechanisms are described in detail.

2.4.3 Recombination Mechanism: Geminate and Bimolecular

Between the generation of excitons and free charge carriers, either geminate recombination will occur or bimolecular recombination.

- Geminate recombination – where electron-hole pairs in CT state recombine after exciton dissociation.
- Bimolecular recombination – where dissociated free charges recombine.

In either case, these recombination processes will cause a substantial reduction in the performance of BHJ OSCs [73]. Minimising these recombination processes is essential in enhancing the PCE of BHJ OSCs. Bimolecular recombination rate can be expressed mathematically as:

$$R_B = B_L(np - n_i p_i) \dots \dots \dots (21)$$

where, B_L is Langevin recombination constant, $n(p)$ are the density of free electron(hole) respectively, and $n_i p_i$ is an intrinsic concentration in the material. $n_i p_i$ can be expressed as:

$$n_i p_i = N_{cv} \exp\left(\frac{-E_g}{k_B T}\right) = n_i^2 \dots \dots \dots (22)$$

where N_{cv} is the effective density of state in conduction or valence band, and E_g is the energy bandgap of the material. Since the intrinsic concentration is much smaller than the free charge density ($np \gg n_i p_i$), n_i^2 can be ignored in bimolecular recombination rate. Therefore, the bimolecular recombination rate can be simplified and expressed as:

$$R_B = B_L(n \times p) \dots \dots \dots (23)$$

Langevin recombination constant B_L , for pristine material was initially proposed by Langevin and is mathematically expressed as [74], [75]:

$$B_L = \frac{q}{\epsilon} (\mu_h + \mu_e) \dots \dots \dots (24)$$

Where μ_h and μ_e are hole and electron mobility, respectively. Equation 24, includes both μ_h and μ_e due to both charges being free to travel. This would mean that the quickest charge carrier would dominate the recombination rate constant. However, for a system with two different materials (blend) such as BHJ, the electrons and holes are restricted to acceptor and donor phase, respectively. Therefore, the recombination takes place at the D-A interface. This process has been illustrated as a schematic in Figure 2.16.

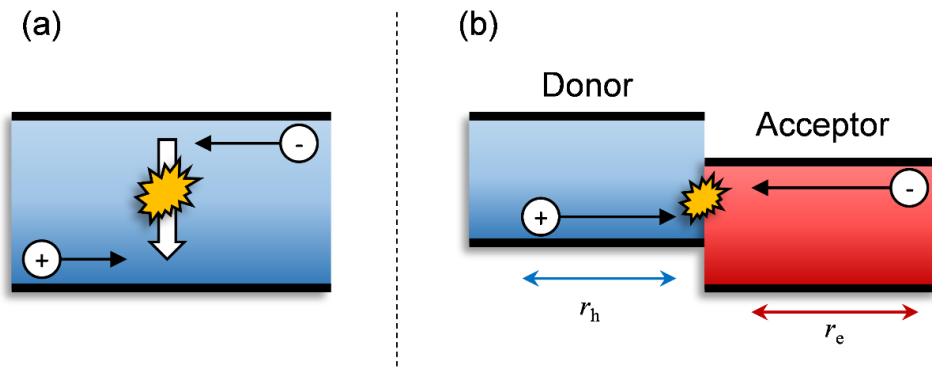


Figure 2.16: Schematic diagram illustrating bimolecular recombination for (a) a pristine semiconducting material, (b) a D-A phase in a BHJ system.

Therefore, the Langevin recombination constant was modified by Braun to balance the mobility difference. Langevin-Braun recombination constant can be expressed mathematically as the spatial average sum of μ_h and μ_e [71]:

$$B_L = \frac{q}{\epsilon} \langle \mu_h + \mu_e \rangle \dots \dots \dots (25)$$

Where, $\langle \dots \rangle$ denotes spatial average.

However, in an intermixed system such as BHJ, holes, and electrons must travel a distance before reaching the interface. Therefore, if hypothetically $\mu_e \gg \mu_h$, then electrons will reach the interface much quicker than holes. However, the time taken for holes to reach the interface will be much longer. Therefore, it can be concluded that for BHJ OSCs, bimolecular recombination is governed by the slowest charge carrier mobility [73]. Therefore, the Langevin recombination constant equation is further modified to compensate for this effect, and it is expressed as:

$$B_L = \frac{q}{\epsilon} \min(\mu_h, \mu_e) \dots \dots \dots (26)$$

Where ‘min’ is the slowest mobility, either μ_h or μ_e .

2.4.4 Trapped recombination mechanism

Within the band gap of semiconductors, there may be one or more localized energy levels due to the presence of impurities [38]. Exchange of charges can take place between these levels and the HOMO (or LUMO) [38]. These energy levels can trap free charges (electrons or holes), by initially attracting either a hole or an electron and subsequently the opposite charge. These levels are known to act as traps and considered as trap centres [57]. The operation mechanism of these trap levels will result in recombination. In 1952 Schokley and Read referred to this recombination as *trap-assisted recombination* [76]. The rate of trap-assisted recombination is determined by the quantity of the trap centres in the blend and how fast the free carrier can find the respective trapped carrier [38]. The model developed in 1952, for inorganic semiconductors by Schokley – Read – Hall known as SHR recombination, is also used for organic semiconductors, such as BHJ OSC systems [77], [78]. Four stages can exist in the SRH recombination process, which is illustrated in Figure 2.17.

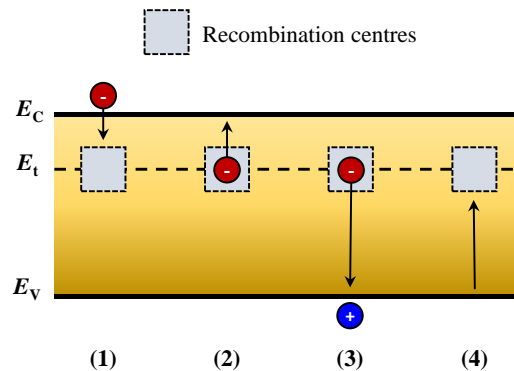


Figure 2.17: Schematic of SRH recombination stages: (1) capture of electron, (2) emission of an electron, (3) capture of hole, (4) emission of the hole.

Valence band (E_V), trapping energy level (E_t), and conduction band (E_C) can be seen in the schematic above. The four stages mentioned earlier for the SRH recombination process is as follows:

1. Capturing an electron into a neutral trap centre at a rate determined by the electron capture coefficient (C_n), C_n is the probability per unit time that an electron in the conduction band can be captured when the trap centre is empty [79].
2. The trapped electron in stage 1 can be excited back to the conduction band.

3. The trapped electron in stage 1 can be caught by a hole at a rate determined by the hole capture coefficient (C_p), therefore leaving an empty trap centre. C_p is the probability per unit time that a hole can be captured when the trap centre is filled with an electron, and a hole is captured [79].
4. An electron can be captured from the valence band via the neutral trap centre.

If there is a thermal equilibrium between the stages above, the model for the SRH recombination rate can be mathematically expressed as:

$$R_{\text{SRH}} = B_{\text{SRH}}(np - n_i p_i) \dots \dots \dots (27)$$

where B_{SRH} is SRH recombination constant and it is expressed as:

$$B_{\text{SRH}} = \frac{C_p C_n N_{T_e}}{[C_n(n + n_i) + C_p(p + p_i)]} \dots \dots \dots (28)$$

Where C_n and C_p are electron and hole capture coefficient respectively, and N_{T_e} is the electron trap density. Determining the capture coefficients (C_n and C_p) has been reported by Kuik et al. in 2011, where they explored the light intensity dependence of the open circuit voltage (V_{oc}) for an organic light-emitting diode (OLED) [79]. They noted that V_{oc} reaction to different light intensities would follow the following mathematical model:

$$V_{\text{oc}} = \frac{E_g}{q} - \frac{k_B T}{q} \ln \left(\frac{[1 - P(E, T)] B_L N_{\text{CV}}^2}{P(E, T) G(E, T)} \right) \dots \dots \dots (29)$$

where B_L is Langevin recombination constant and G is the exciton generation rate. When plotting V_{oc} against light intensity (in logarithm scale), the resultant slope of the plot should be equal to $\frac{k_B T}{q}$ when there are no traps and Langevin recombination is dominant. However, if there are SRH recombination processes taking place in the device, then the slope of the plot will be higher than $\frac{k_B T}{q}$ [79]. Therefore, in such a case, the relationship between V_{oc} and light intensity will be expressed as:

$$V_{\text{oc}} = \frac{E_g}{q} - \frac{k_B T}{q} \ln \left(\frac{[1 - P(E, T)] B_T N_{\text{CV}}^2}{P(E, T) G(E, T)} \right) \dots \dots \dots (30)$$

where B_T is a combination of SRH and Langevin recombination constants ($B_T = B_{\text{SRH}} + B_L$) [78]. Kuik et al. further explored their model and managed to establish a mathematical expression to determine capture coefficients C_p and C_n are:

$$C_p = \frac{q}{\epsilon} \mu_h \dots \dots \dots (31)$$

$$C_n = \frac{q}{\varepsilon} \mu_e \dots \dots \dots (32)$$

Therefore, to summarise the calculations for SRH recombination, it can be said that when C_p and C_n are within the same order of magnitude R_{SRH} is expressed as:

$$R_{SRH} = B_{SRH}(n.p) \dots \dots \dots (33)$$

With SRH recombination constant B_{SRH} to be expressed as:

$$B_{SRH} = \frac{C_p C_n N_{Te}}{(C_n \cdot n) + (C_p \cdot p)} \dots \dots \dots (34)$$

However, in the case where $C_p \ll C_n$ and $n \sim p$, R_{SRH} is expressed as:

$$R_{SRH} = C_p N_{Te} p \dots \dots \dots (35)$$

And when $C_n \ll C_p$ and $n \sim p$, R_{SRH} is expressed as:

$$R_{SRH} = C_n N_{Te} n \dots \dots \dots (36)$$

Both of these equations are very similar to the bimolecular recombination equation, with B_L being replaced with either C_p or C_n .

2.5 Summary

In this chapter, an overview of semiconductor physics with application in BHJ OSCs was presented, and it can be briefly summarised into the following points:

- Brief descriptions of the energy bands formation in OS materials with regards to the interaction of molecular orbitals. Defining what the (HOMO) and (LUMO) concerning inorganic semiconductors valence and conduction bands, respectively is.
- Charge transport within OS materials through *hopping mechanism*.
- Electrode – semiconductor interface: Schottky barrier junction, Ohmic contact and Space charge limited conductivity (SCLC), and mobility mechanism.
- The operation mechanism of OSCs: Circuit modelling and the difference between ideal and conventional devices, with taking series and shunt resistance into account.
- Exciton dissociation and recombination processes, such as Bimolecular and SRH recombination and the significance in minimising them in BHJ OSC devices.

CHAPTER 3

Materials for Organic Solar Cells

3.1 Introduction

In this chapter, the materials used for organic solar cells (OSCs) are introduced and discussed. Starting with the existing materials for the active layer as Donor and Acceptor, followed by the materials used as a buffer layer (hole/electron transport layers). The architecture of BHJ OSCs was briefly described in section 1.3.3, where it was mentioned that a photoactive layer composed of a blend of the donor (conjugated polymers) and acceptor (mainly fullerene derivatives) is sandwiched between two electrodes and buffer layers. The conjugated polymer donor and fullerene derivative acceptor are the primary materials for OSCs. Therefore, photovoltaic materials with ideal properties are essential for material design in OSCs. As it was mentioned before, BHJ architecture has been the most successful photoactive layer design in the fabrication of OSCs [80]. This is due to the bi-continuous phase separation of D-A formation [81].

Amongst the D-A materials used for OSC applications, P3HT: PC₆₁BM is the most commonly used materials and have been under investigation by researchers for the past two decades [5], [27], [32], [38]. Figure 3.1 illustrates the chemical structure of P3HT and PC₆₁BM.

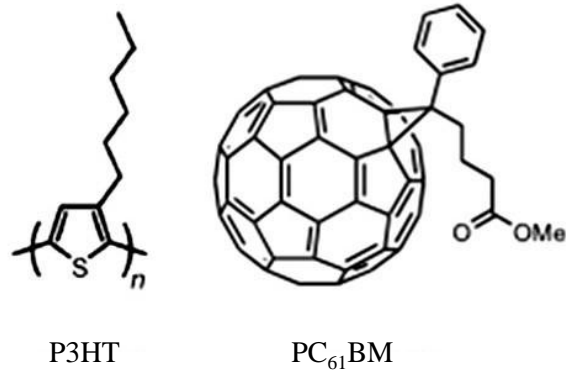


Figure 3.1: Schematic of the chemical structure of P3HT (Poly(3-hexylthiophene-2,5-diyl) Regioregular) and PC₆₁BM ([6,6]-Phenyl C₆₁ butyric acid methyl ester).

The photo-absorption of P3HT: PC₆₁BM blend covers the range of 380 – 670 nm (Figure 3.2), which means excitons are generated when photons with an energy of 2.0 – 3.3 eV are absorbed by the active layer [82], [83]. However, the PCE of such blend is around 2 – 4 %. This is due to the photocurrent generation limitation, with J_{sc} around 9 – 10 mA cm⁻² and V_{oc} of around 0.4 – 0.6 V [78], [79].

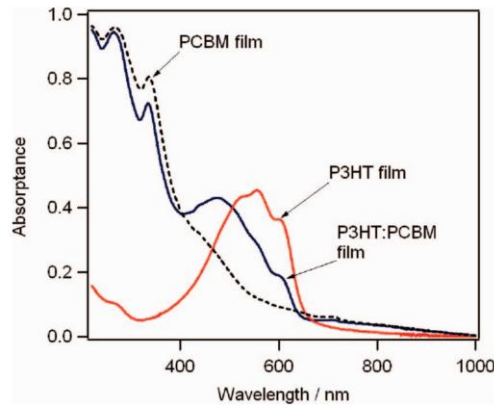


Figure 3.2: Absorption spectra for pristine PC₆₁BM film, pristine P3HT film and a blend of P3HT: PC₆₁BM (1:2 w/w) [84].

The photocurrent generation is directly proportional to the optical bandgap of the donor material (P3HT), and the V_{oc} is proportional to the difference of the HOMO level of the donor material and the LUMO level of the acceptor. The energy bandgap of P3HT is around 2 eV, which is considered to be a wide, compared to inorganic

semiconductor such as silicon ($E_g \sim 1.14$ eV) [84], [85]. Since the LUMO and the HOMO of P3HT is higher than that of PCBM; the excitons will separate into positive and negative charges at the interface of the P3HT phase and PCBM phase. The negative charge will transport through the LUMO of PCBM, and the positive charge will transport through the HOMO of P3HT, and then the charges can be collected by the electrodes [86]. Also, to get efficient charge separation, HOMO and LUMO of the donor material should be 0.2–0.3 eV higher than that of the acceptor material, respectively. If the offset is too small, it would be hard to get efficient charge separation; and if the offset is too big, much energy loss would be happened [86].

In order to make better utilization of the sunlight, active layer materials with broad absorption band range are required, and for this purpose, more and more low bandgap (LBG) polymers have been developed, and significant successes have been made in the past decade [86]. Furthermore, the charge carrier mobility of the donor and the acceptor materials is also an important factor for organic photovoltaic materials. In comparison with inorganic semiconductors, organic semiconducting materials exhibit much lower mobilities. Therefore, improving hole and/or electron mobility of organic photovoltaic materials becomes one of the critical objectives in molecular design of materials. For organic semiconducting material, both inter- and intra-molecular charge transfer properties are very important. The relationship between intra-molecular charge transfer property and molecular structure is still unclear [86]. Enhancing the inter-molecular stacking has been proven to be an effective way to improve charge transportation [83]. For examples, the hole mobility of regio-regular P3HT is 2–3 orders higher than regioregular P3HT due to the stronger pi–pi stacking [87].

Besides absorption band, molecular energy levels (HOMO and LUMO) and charge transport mobilities, there are still many other issues like solubility in different solvents and chemical stability, which should be considered in the molecular design of OSC materials [86]. Therefore, the right balance of these parameters is required to achieve ideal OS materials for OSC applications. In the following sections of this chapter, several broadly used material systems will be introduced to provide a general profile of molecular structure design of OSC materials, amongst which the ideal materials are selected for the use in this project.

3.2 Donor Material

Various donor materials, such as polymers have been designed in the past decade for OSC applications. The list to categorise these materials is vast. Therefore, in this section, some of the low bandgap polymers synthesised are reviewed for identifying an ideal candidate to be chosen as the primary donor material in this research project.

3.2.1 Polythiophenes Polymers and Its Derivatives

Poly(3-alkyl thiophene) (P3AT) is used as an electron donor material in OSCs. As it was mentioned in the introduction section, P3HT has the best device performance for OSCs applications in the P3AT category. P3ATs can be synthesised, over different methods. The repeating units of P3ATs were asymmetric. Therefore, three possible orientations exist when two *thiophene* rings connect between the head and tail position [33]. Therefore, these possible orientations are as follow:

- Head-to-Tail (HT) connection
- Head-to-Head (HH) connection
- Tail-to-Tail (TT) connection

The HT–HT configurations of *Polythiophenes* are considered as Regioregular, and the other three configurations are considered as regiorandom. Hence, the HT–HT isomer percentage within the polymers is known as the *Regioregularity*. Regioregular *poly(3-substituted thiophene)* can obtain a low-energy planar structure, which can result in well-conjugated polymers. Increase in torsion angles between *thiophene* rings will increase the polymer band-gap, decrease of conductivity. Therefore, the *Regioregularity* level is an essential parameter in the characterisation of *Polythiophenes*. Hence, P3HT with *Regioregularity* level of 98% used as the donor material in BHJ OSCs results in high performance [33]. Although P3HT has shown notable photovoltaic property. However, the absorption band (500 – 650 nm) of this polymer is not broad enough to harvest the desired solar spectrum.

On the other hand, two-dimensional conjugated *Polythiophenes* (2D-PTs) possess a much broader absorption band [88]. 2D-PT molecule absorption band is configured from two parts located at short wavelength direction from the conjugated side chain, and long-wavelength direction from the conjugated main chain [33], [88]. By altering the conjugate length of the side chain, the absorption peak position of short wavelength

direction can be tuned, and by altering the $m:n$ ratio (see Figure 3.3, 2D-PD structure), a broad and strong absorption band can be obtained [33]. 2D-PTs show faster hole mobilities than P3ATs family. In some cases, hole mobilities have been 2-3 orders of magnitude higher for some 2D-PTs [89]. By replacing the alkyl side groups from P3ATs to alkoxy groups, reduction in the energy band gap of *Polythiophenes* can be achieved [33].

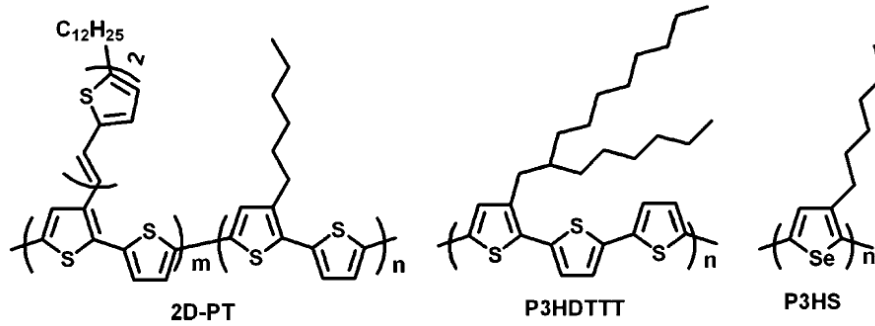


Figure 3.3: Few possible derivatives of Polythiophene: 2D-PT, P3HD TTT, and P3HS [33].

For example, *Poly(3-alkoxythiophene)s* (P3AOTs) have an energy band gap of 1.55 eV, which is far lower than P3ATs. However, P3AOTs are not suitable as donor material because of their high HOMO levels. This is because alkoxy as a side chain has a higher electron-donating ability than alkyl, which impacts the HOMO level. Therefore, the HOMO levels of *Polythiophenes* can be tuned by reduction of alkyl side chains, which can result in obtaining higher HOMO levels. P3HD TTT (see Figure 25) has been designed based on this idea. For P3HT molecules, each *thiophene* unit is linked to an alkyl side chain; however, for P3HD TTT, for every three *thiophene* units, only one alkyl is lined as a side chain.

Therefore, resulting in a deeper HOMO level for P3HD TTT molecules. Hence, a higher V_{oc} (0.84 V) can be obtained when the active layer of P3HD TTT: PC₆₁BM blend is employed to fabricate OSCs devices [90]. Ballantyne et al. designed and synthesised Regioregular *Poly(3-hexylselenophene)*, (rr-P3HS), where the bandgap of the molecule was reduced to 1.60 eV [91]. They are achieving a PCE of 2.7% when blended with PC₆₁BM.

3.2.2 Polymers based on 2,1,3-Benzothiadiazole

Polymers based on 2,1,3-Benzothiadiazole (BT) have been used as electron reducing building block to design conjugated polymers [33]. This category of donor materials has been widely studied in the field of OSCs, and it has exhibited great performances (see Table 2 for such copolymers). It is known that *thiophene* rings are electron filled units with weak aromatic properties. Therefore *thiophene* derivatives can be used as the main electron-donating blocks in designing conjugated polymers as donor materials [33]. Few copolymers designed on dithiophene derivatives and BT units are illustrated in Figure 3.4.

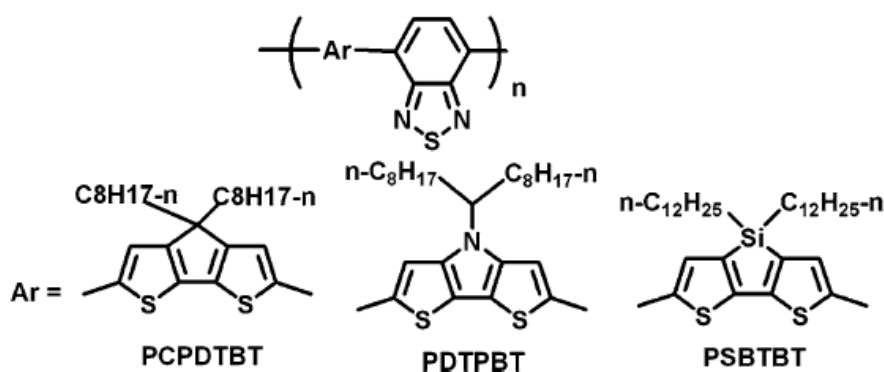


Figure 3.4: Chemical structure of copolymers based on dithiophene and BT units: PCPDTBT, PDTPBT, and PSBTBT [33].

As it can be seen from Figure 3.4, dithiophene derivatives have a well planar configuration, with atoms like Si, C, or N linked between them. PCPDTBT was amongst the first low bandgap donor polymers synthesised for applications in BHJ OSCs [92], [93]. PCPDTBT absorption band corresponds to an energy band gap of 1.50 eV. PCPDTBT also displayed relatively high hole mobility, ($1 \times 10^{-3} \text{ cm}^2 \text{ V}^{-1} \text{ s}^{-1}$) obtained via field effect transistor (FET) method [94]. The initial PCEs of PCPDTBT: PC₆₁BM blends were in the region of 3.2 % [92].

However, the active layer morphology was optimised by employing 1,8-Diiodooctane (DIO) or 1,8-dithiol-octane (ODT) as a solvent additive during the spin-coating process. This modification enhanced the PCE to 5 % [95]. It has been reported that the solubility of PC₆₁BM in DIO is higher than the polymer; also, DIO has much lower vapour pressure than the regularly used solvents such as o-dichlorobenzene and chlorobenzene [96]. Therefore during fabrication of OSCs when DIO is present, the

polymer can crystallise while PC₆₁BM has a longer time to dry [96]. The use of solvent additive has been reported to be a successful way for enhancement of OSCs performance for another polymer: PC₆₁BM blends [33]. These enhancements using such methods indicates that the morphology control of the active layer blend is of importance. Table 3.1 presents the device performance for some of the copolymers based on dithiophene and BT unit polymers which have been blended with PC₆₁BM to be used as an active layer for BHJ OSC applications.

Table 3.1: OSC device characteristics of BT based copolymers blended with PC₆₁BM.

Polymer	E _g (eV)	HOMO (eV)	LUMO (eV)	J _{sc} (mA cm ⁻²)	V _{oc} (V)	FF	PCE (%)	Refs
PCPDTBT	1.40	-5.30	-3.57	16.2	0.62	0.55	5.5	[95]
PSBTBT	1.37	-	-	17.3	0.57	0.61	5.9	[97]
PDTPBT	1.43	-4.81	-3.08	11.9	0.54	0.44	2.8	[98]
PFDTBT	-	-	-	7.70	1.00	0.54	4.2	[99]
PFSiDTBT	1.86	-5.70	-3.81	9.40	0.90	0.51	5.4	[100]
PCDTBT	1.88	-5.50	-3.60	10.6	0.88	0.66	6.1	[101]
PDTPDTBT	1.46	-5.00	-3.43	9.47	0.52	0.44	2.2	[102]
PCPDTDTBT	1.55	-	-	8.75	0.60	0.4	2.1	[103]
PBDTDTBT	1.75	-5.31	-3.44	10.7	0.92	0.57	5.7	[104]
PSiDTBT	1.53	-4.99	-3.17	10.67	0.62	0.52	3.4	[105]

The chemical structure for some of the polymers presented in Table 3.1 is illustrated in Figure 3.5.

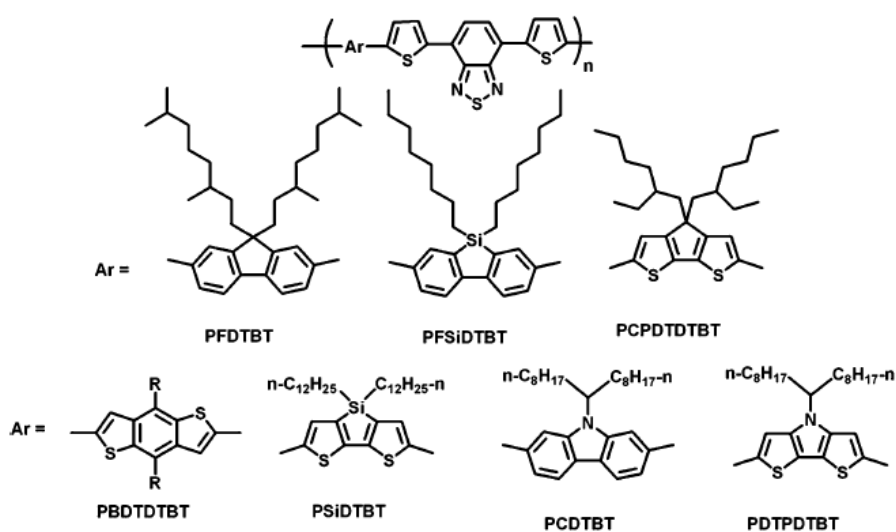


Figure 3.5: Chemical structure of DTBT-based polymers: PFDTBT, PFSiDTBT, PCPDTDTBT, PBDTDTBT, PSiDTBT, PCBTBT, and PDTPDTBT [33].

3.2.3 Pyrrolo[3,4-c]pyrrole-1,4-dione (DPP) Derivative Polymers

Pyrrolo[3,4-c]pyrrole-1,4-dione (DPP) and its derivatives have demonstrated good absorption in the visible region of the solar spectrum. *Thiophene*-based DPP molecules possess a well-structured conjugation, which is very beneficial for charge carrier mobility [33]. DPP polymers were initially designed for the organic field effect transistors (OFETs). Winnewisser et al. reported hole and electron mobilities of $0.1 \text{ cm}^2 \text{ V}^{-1} \text{ s}^{-1}$ for OFET devices based on DPP [106]. Chemical structure of few DPP derivative polymers is illustrated in Figure 3.6.

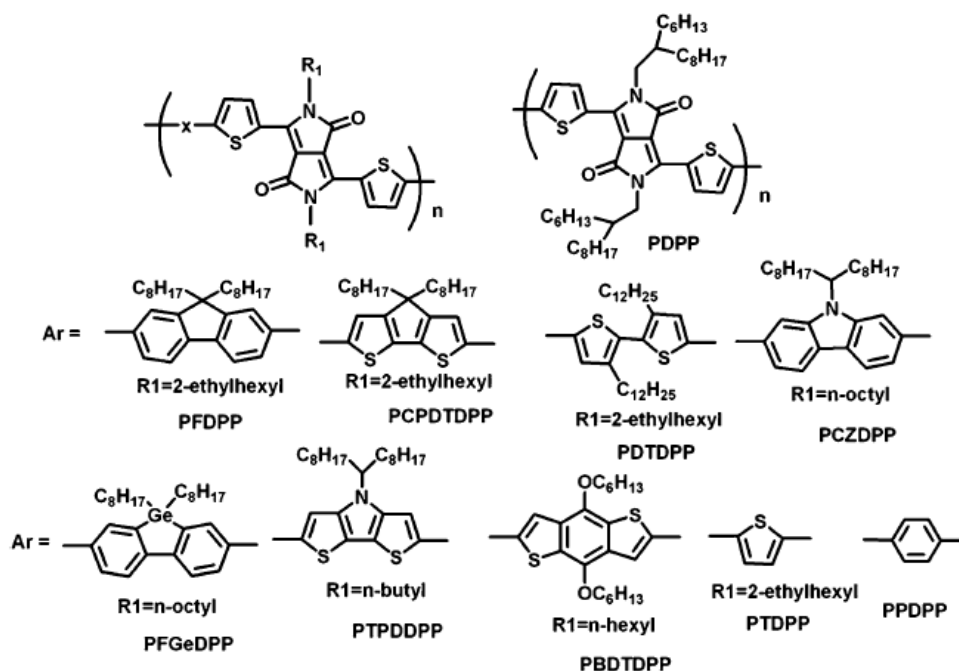


Figure 3.6: Chemical structure of DPP-based polymers: DPP, PDPP, PFDPP, PCPDTDPP, PDTDPP, PCZDPP, PFGeDPP, PTPDDPP, PBDTDPP, PTDPP, PPDPP [33].

Numerous low bandgap polymers based on DPP derivatives were designed and synthesised, as illustrated in Figure 3.5 [33]. The device characteristic of some DPP-based polymers blended with $PC_{61}BM$ for OSC applications is presented in Table 3.2.

Table 3.2: OSC device characteristics for DPP-based polymers blended with PC₆₁BM.

Polymer	E _g (eV)	HOMO (eV)	LUMO (eV)	J _{sc} (mA cm ⁻²)	V _{oc} (V)	FF	PCE (%)	Refs
PTDPP	1.30	-5.17	-3.16	11.80	0.65	0.60	4.7	[107]
PFDPP	1.77	-5.43	-3.67	2.41	0.91	0.41	0.9	[108]
PCPDTDPP	1.39	-5.25	-3.74	5.73	0.61	0.49	1.7	[108]
PPDTDPP	1.40	-5.10	-3.40	11.30	0.61	0.58	4.0	[109]
PPPDPP	1.53	-5.35	-3.53	10.80	0.80	0.65	5.5	[110]
PDPP	1.24	-5.29	-3.99	0.76	0.64	0.58	0.3	[108]
PCZDPP	1.57	-5.44	-3.92	8.60	0.80	0.47	3.2	[111]
PFGEDPP	1.63	-5.38	-3.70	4.10	0.76	0.62	1.5	[112]
PTPDDPP	1.13	-4.90	-3.63	14.90	0.38	0.48	2.7	[113]
PBDTDPP	1.43	-5.15	-3.69	6.72	0.74	0.56	2.8	[114]

As it can be seen from Table 3.2, PDPP polymer blended with PC₆₁BM exhibits poor PCE performance, despite the polymer having a low bandgap property of the polymer. Researchers assigned one of the main reasons for such low performance to the low D-A LUMO off-set (0.18 eV), which could be insufficient for charge separation [107], [115]. To expand the backbone of the polymer, a third *thiophene* ring was attached (see Figure 3.6) to produce PTDPP polymer which exhibits PCE of 4.7% with a bandgap of 1.3 eV [107]. DPP based polymers have shown promising performances for their use as donor materials in OSC application, with energy band gaps in the region of 1.5 – 1.8 eV and PCEs of over 4 % [33].

3.2.4 Polymers based on *Benzo[1,2-b;4,5-b']dithiophene*

It is reported that three types of functional groups can be used as side chains for *Benzo[1,2-b;4,5-b']dithiophene* (BDT) units to make them into soluble polymers. These functional groups are; alkyl, alkoxy, alkylthiophene [33], [116]. BDT units have a symmetrical planar conjugated structure. Therefore compact stacking is expected from BDT-based conjugated copolymers [117]. BDT-based polymers were initially developed for OFET applications in 2007, a reported polymer of such kind showed hole mobility of 0.25 cm² V⁻¹ s⁻¹ illustrated in Figure 3.7 [118].

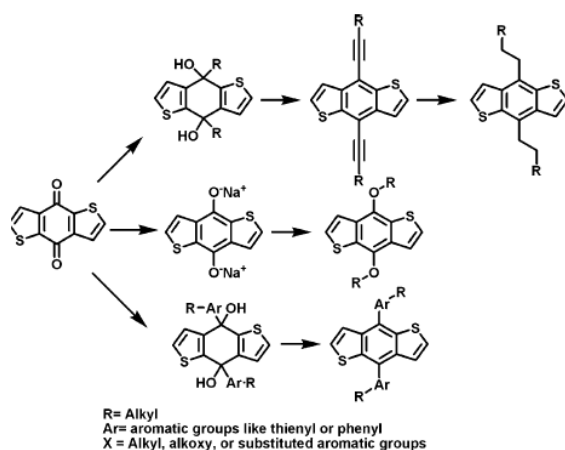


Figure 3.7: Chemical structure illustrating the synthesis of three possible substitutes of BDTs [33].

BDT-based polymers bandgap can be easily adjusted using a broad range of conjugated units/blocks with various electron-withdrawing abilities to form a copolymer. Hou et al., initially designed and synthesised eight different BDT-based polymers, to explore the correlation between conjugated backbones and the energy bandgap of the molecules [116]. The chemical structure of these polymers is illustrated in Figure 3.8.

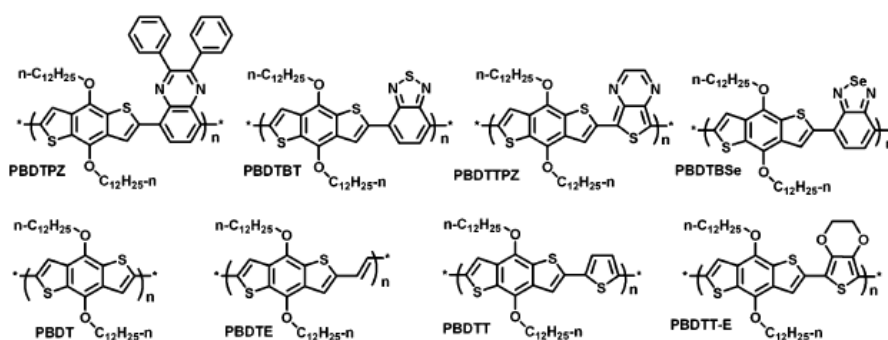


Figure 3.8: Chemical structure of eight BDT-based polymers with identical BDT units [33].

Hou et al. further explored their research into the correlation between HOMO levels, these polymers and the V_{oc} values obtained when BHJ OSCs were fabricated from the blend of these polymers: PC₆₁BM. From these studies, it was noticed that the achieved V_{oc} is directly proportional to the difference between the donor's HOMO level (H_D) and acceptor's LUMO level (L_A) [116]. A list of BDT-based polymers used in as donor material in BHJ OSCs is presented in Table 3.3. These polymers were blended with either, PC₆₁BM or PC₇₁BM to form the active layer.

Table 3.3: OSC device characteristics for BDT-based polymers blended with PC₆₁BM or PC₇₁BM.

Polymer	E _g (eV)	HOMO (eV)	LUMO (eV)	J _{sc} (mA cm ⁻²)	V _{oc} (V)	FF	PCE (%)	Refs
PBDT	2.13	-5.16	-2.67	-	-	-	-	[116]
PBDTE	2.03	-5.07	-2.86	1.16	0.56	0.38	0.3	[116]
PBDTT	2.06	-5.05	-2.69	3.78	0.75	0.56	1.6	[116]
PBDTT-E	1.97	-4.56	-2.66	2.46	0.37	0.40	0.4	[116]
PBDTPZ	1.63	-4.78	-3.28	1.54	0.60	0.26	0.2	[116]
PBDTBT	1.70	-5.10	-3.19	2.97	0.68	0.44	0.9	[116]
PBDTTPZ	1.05	-4.65	-3.46	1.41	0.22	0.35	0.1	[116]
PBDTBS _e	1.52	-4.88	-3.33	1.05	0.55	0.32	0.2	[116]
PBDTTT-C	1.61	-5.12	-3.35	14.70	0.70	0.64	6.6	[119]
PBDTTT-CT	1.58	-5.11	-3.25	17.48	0.74	0.59	7.6	[120]
PBDTTT-CF	1.60	-5.22	-3.45	15.20	0.76	0.67	7.7	[121]
PBDTTT-EF	1.63	-5.12	-3.13	14.50	0.74	0.69	7.4	[122]
PBDTTT-EFT	1.58	-5.24	-3.66	16.17	0.78	0.68	8.6	[123]
PBDTTTPD	1.73	-5.40	-	11.50	0.85	0.70	6.8	[124]
PBDTFTAZ	2.00	-5.36	-3.05	11.80	0.79	0.73	6.8	[125]
PBDTDTffBT	1.70	-5.54	-3.33	12.91	0.91	0.61	7.2	[126]

As it can be seen from Table 3.3, PBDTTPZ is a good example where strong and broad absorption band of 1.05 eV exist; however, the V_{oc} of PBDTTPZ: PC₆₁BM device is around 0.2 V, primarily due to a high level of the HOMO value. Therefore, the correct balance between the energy band gap and the HOMO level of the donor polymer is required when designing efficient donor materials. In the past decade, there have been numerous BDT-based polymers designed and synthesised for the application BHJ OSCs, amongst which some of the best performance till date are presented in Figure 3.9.

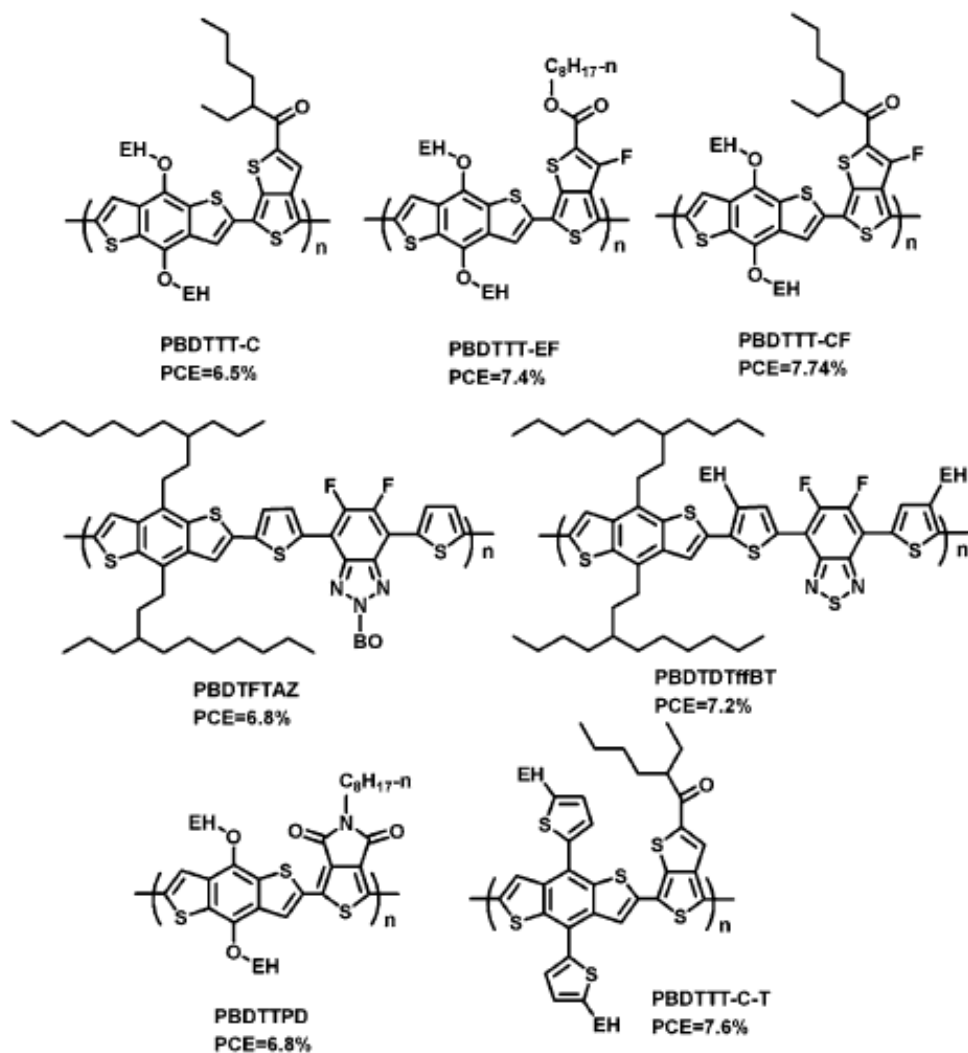


Figure 3.9: The molecular structure of BDT-based copolymers [33].

Amongst the BDT-based polymers mentioned in Table 3.3, the highest performance polymer is PBDTTT-EFT, which exhibits the highest PCE of 8.6%, with J_{sc} of 16.17 mA cm^{-2} , V_{oc} of 0.78 V and FF of 0.68 [123]. Chemical structure of PBDTTT-EFT molecule is illustrated in Figure 3.10.

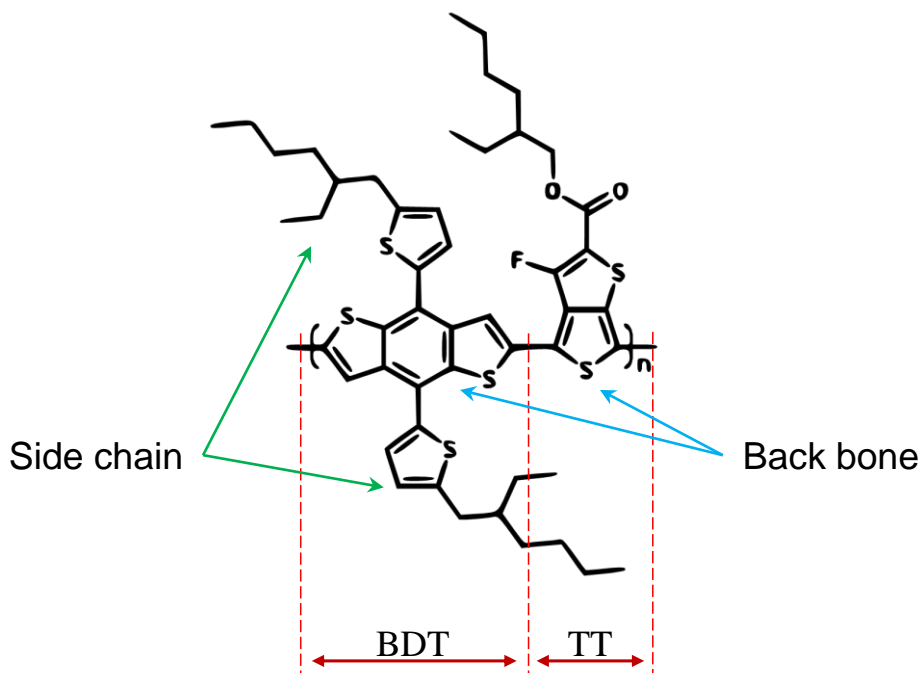


Figure 3.10: The molecular structure of PBDTTT-EFT, indicating BDT and TT unit attachment as the building block of the molecule.

PBDTTT-EFT low bandgap polymer incorporates the *2-ethylhexyl-thienyl* group into the BDT unit to improve the co-planarity of the main chain so that the absorption band can be extended and lower bandgap to be achieved. Also, by advancing the fluorine-substituted TT unit (F-TT) with the *2-ethylhexyl carboxylate* group, the higher HOMO level can be obtained. It has been reported in the literature that PCEs of over 9 % can be achieved using BDT-based polymer as the donor material for BHJ OSC devices [49], [127]. Therefore, PBDTTT-EFT seems to be the ideal candidate to be used as the donor material for this project. Some of the characteristic parameters for this polymer are presented in Figure 3.11.

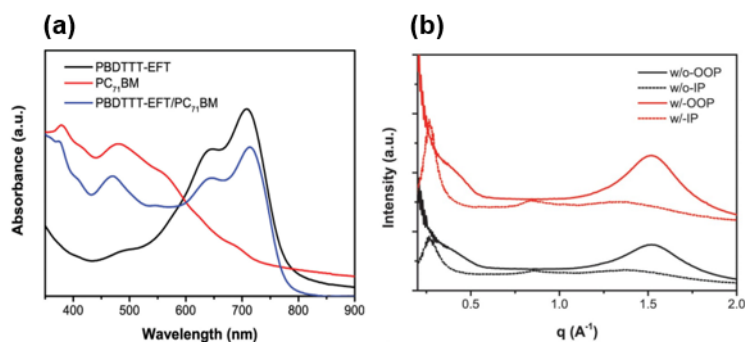


Figure 3.11: Parameters of PBDTTT-EFT. (a) optical absorption of pristine PBDTTT-EFT, PC₇₁BM and their blend, (b) out-of-plane (OOP) and in-plane (IP) 2D GIWAXS line profile of pristine PBDTTT-EFT [128].

From Figure 3.11a, the optical on-set of pristine PBDTTT-EFT is ~ 780 nm which corresponds to E_g of ~ 1.58 eV and Figure 3.11b showing the in-plane and out-of-plane line diffractogram of pristine PBDTTT-EFT [128]; indicating a broad peak is observed along the out-of-plane direction at $q = 1.52 \text{ \AA}^{-1}$. This peak corresponds to π - π stacking, indicating that PBDTTT-EFT is predominately stacking in a face-on orientation [128]. The π - π spacing between polymer backbones is calculated from the peak position of out-of-plane to be 0.41 nm. In the in-plane direction, an intense (100) reflection centred at $q = 0.27 \text{ \AA}^{-1}$ is observed, indicating that the spacing of PBDTTT-EFT lamellae from the backbone to backbone across alkyl side chains is 2.33 nm [128].

A basic statistical survey was done to investigate the number of publications using PBDTTT-EFT polymer keyword over the years, using ‘Google scholar’ website. A simple bar chart in Figure 3.12 illustrates the number of journals/papers published with the phrase “PBDTTT-EFT” involved in them against completed years; hence, 2019 is not included in the data.

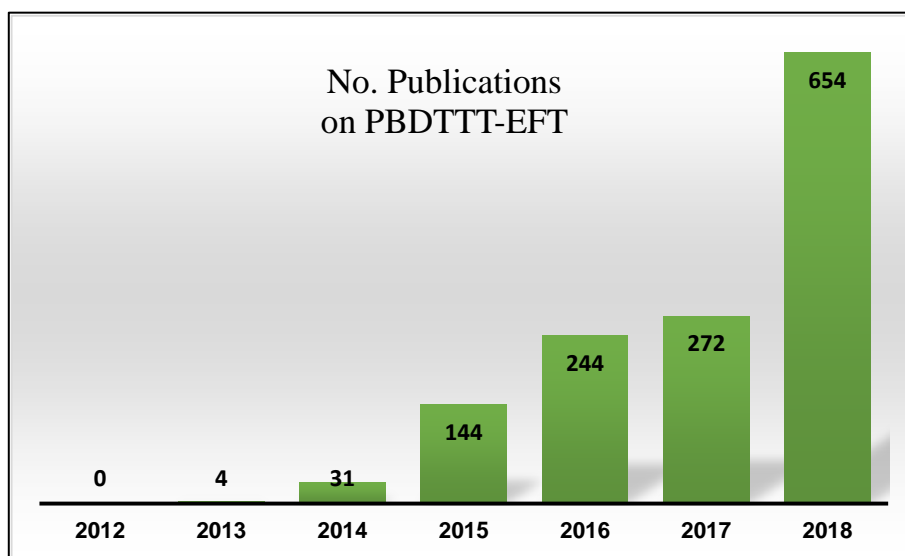


Figure 3.12: Bar chart representation published work on PBDTTT-EFT per year.

As can be seen from Figure 3.12, PBDTTT-EFT was not introduced to the scientific world until 2013, where very little work had been published. PBDTTT-EFT molecule has different names such as PTB7-Th and PCE10. The data used in Figure 3.12 has been obtained using ‘Google Scholar’ to count the number of publications. Over the past six years, there has been a great interest in this polymer. It is believed to be the next ideal candidate to be used as the Donor material for OSCs. For this reason, this polymer has been chosen to be the donor material in this project.

3.3 Acceptor Materials

Many organic compounds exhibited potential properties as an electron acceptor material, but electron acceptor materials can be used in highly efficient OSC devices are limited. Fullerene and its derivatives are the most successful electron acceptor materials [33].

3.3.1 PCBM derivatives

In 1992, Sariciftci et al. were the first group to use C_{61} as an electron acceptor and acknowledge the photo-induced ultrafast electron transfer between D-A [129]. Fullerene C_{61} has well-symmetric molecular structure and shows excellent electron mobility, and this is because one molecule of C_{61} can receive four electrons [86]. Hence, C_{61} and its derivatives are considered as suitable electron acceptor materials [33]. The solubility of C_{61} is very limited to selective solvents such as CB and ODCB. Therefore, to enhance the solubility of C_{61} in more organic solvents, derivative [6,6]-phenyl- C_{61} -butyric acid methyl ester ($PC_{61}BM$) was synthesised for OSC applications [86]. In the past decade, $PC_{61}BM$ and its modified version, $PC_{71}BM$ have been the primary acceptor material in the field of OSCs [86]. The molecular structure of $PC_{61}BM$ and $PC_{71}BM$ are illustrated in Figure 3.13. When comparing $PC_{61}BM$ to $PC_{71}BM$, one of the main distinctive difference between these molecules is their optical absorption, shown in Figure 3.14.

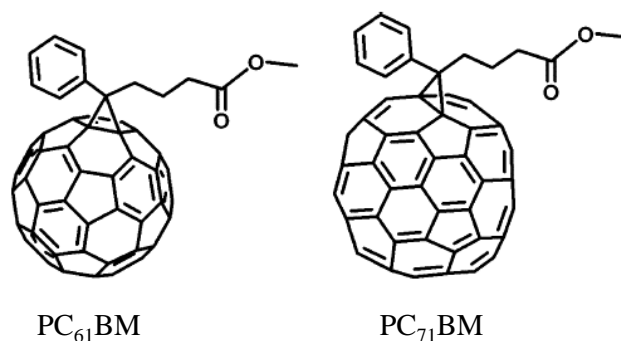


Figure 3.13: The molecular structure of $PC_{61}BM$ and $PC_{71}BM$.

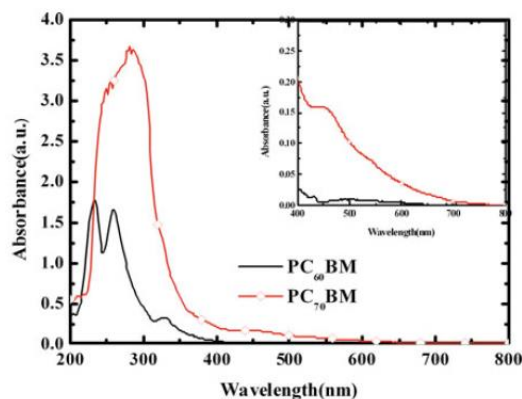


Figure 3.14: Optical absorption of PC₆₁BM and PC₇₁BM, inset: absorption in the 400 – 800 wavelength [86].

As can be seen from Figure 3.14, the absorption of both molecules is active in the ultraviolet (UV) region (200 – 400 nm). However, PC₇₁BM displays a stronger absorption in the visible region (400 – 700 nm) compared to PC₆₁BM. Therefore, OSC devices fabricated from PC₇₁BM blends, show higher device performance [130]. Although PC₇₁BM molecule has been attracting more interest as an electron acceptor material, it should be synthesising PC₇₁BM molecules are more expensive than PC₆₁BM, due to complex purification processes [86]. The energy levels of the acceptor materials play an essential role in the performance of OSCs since V_{oc} is directly proportional to the difference between HOMO of the donor and LUMO of the acceptor material in BHJ OSCs [69], [131].

Hence, the LUMO level of fullerene and its derivatives are a critical parameter for determining the performance of OSCs. The HOMO and LUMO levels of D-A materials are usually measured using Cyclic Voltammetry (CV) technique, described in *Chapter 4, section 4.8*. The C₆₁ molecule has a LUMO level ~ -4.2 eV [132]. Interestingly, the LUMO level of PC₆₁BM and PC₇₁BM are measured to be ~ -3.91 to -4.0 eV, respectively [133]. Therefore, it can be established that the LUMO level of the C₆₁ molecule can be altered or elevated by implementing substituents to make a PC₆₁BM or PC₇₁BM molecules [86]. It was mentioned previously that the LUMO level of the acceptor material plays a vital role in determining the V_{oc} for OSCs. Therefore, designing acceptor molecules with higher LUMO levels could enhance the V_{oc} value.

3.3.2 Indene- C_x Bisadduct derivatives

Indene- C_{61} Bisadduct and Indene- C_{71} Bisadduct are an example of Indene-fullerene adducts which are employed as electron acceptor materials in OPVs [1], [134]. This kind of compounds can be synthesised easily via a one-pot reaction [86]. The solution of indene and fullerene (C_{61} or C_{71}) in ODCB is heated to reflux for several hours, and a mixture of unreacted fullerene, indene-fullerene monoadduct (ICMA), indene-fullerene bisadduct (ICBA), and indene-fullerene multi adduct are obtained, which can be separated readily through column chromatography [86]. The molecular structures of $IC_{61(71)}MA$ and $IC_{61(71)}BA$ are represented in Figure 3.15.

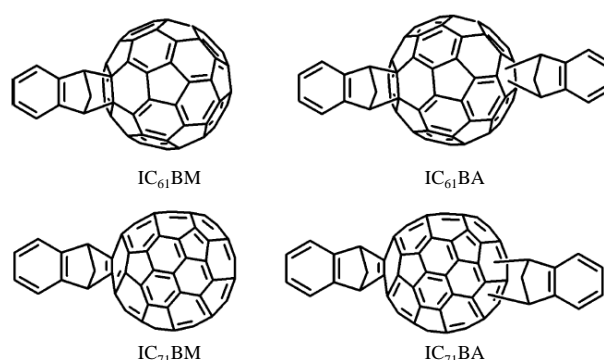


Figure 3.15: Molecular structure of $IC_{61(71)}BM$ and $IC_{61(71)}BA$.

The LUMO levels of $IC_{61}MA$ and $IC_{61}BA$ are -3.86 eV and -3.74 eV, respectively [1]. These levels are both higher than $PC_{61}BM$, therefore OSC composed of a blend of P3HT: $IC_{61}BM$ or P3HT: $IC_{61}BA$ will demonstrate a higher V_{oc} compared to a blend of P3HT: $PC_{61}BM$ [86]. $IC_{61}MA$ has poor solubility in CB and ODCB, and thus, the application of this material as a photovoltaic material is limited [86]. In contrast, $IC_{61}BA$ can be dissolved in CB or ODCB easier [86]. On average the V_{oc} of OSC devices composed of P3HT: $PC_{61}BM$ blend, yield to ~ 0.6 V. However, an OSC device successfully fabricated from a blend of P3HT: $IC_{61}BA$ will generate an average $V_{oc} \sim 0.84$ V without any losses to other parameters [135]. Table 3.4 presents the extracted electrical characteristics for OSC devices fabricated from P3HT blended with $PC_{61}BM$, $IC_{61}BM$, and $IC_{61(71)}BA$ as well as devices blended from PBDTTT-C-T: $IC_{61}BA$ or $PC_{61}BM$ and PBDTTT-EF: $IC_{61}BA$ or $PC_{61}BM$.

Table 3.4: Electrical characteristic parameters extracted from different polymer acceptor materials.

Donor:Acceptor	J_{sc} (mA cm ⁻²)	V_{oc} (V)	FF	PCE (%)	Refs
P3HT:PC ₆₁ BM	10.80	0.58	0.62	3.88	[1]
P3HT:IC ₆₁ BM	9.66	0.63	0.64	3.89	[1]
P3HT:IC ₆₁ BA	10.61	0.84	0.73	6.48	[135]
P3HT:IC ₇₁ BA	9.73	0.84	0.69	5.64	[134]
PBDTTT-C-T:PC ₆₁ BM	13.20	0.81	0.59	6.20	[2]
PBDTTT-C-T:IC ₆₁ BA	7.80	0.97	0.46	3.50	[2]
PBDTTT-EF:PC ₇₁ BM	14.99	0.70	0.69	7.23	[136]
PBDTTT-EF:IC ₆₁ BA	10.84	0.87	0.50	4.74	[136]

As it can be seen in Table 3.4, a significant increase in V_{oc} parameter can be observed by replacing PCBM with ICBA. However, depending on the type of polymer used in the blend, the overall performance of the OSC device seems to be dependent on the choice of the acceptor material. For example, devices fabricated from *BDT*-based polymers have shown a decrease in J_{sc} , FF and PCE parameters upon replacing PCBM with ICBA. In contrast devices based in P3HT have shown a significant overall enhancement when replacing PCBM with ICBA. Therefore, investigating the role of IC₆₁BA as an electron acceptor material is of interest in this research project and will be chosen as one of the fullerene derivative materials to be investigated when blended with PBDTTT-EFT polymer.

3.4 Buffer layers

Buffer layer materials are typically used in the fabrication process of OSCs to each the extraction of the corresponding charge as well as blockage of unwanted charge at the corresponding electrode. It is for these characteristics that they are also referred to as electrode interfacial layer [137]. One of the most common materials used as a buffer layer for hole extraction is *poly (3, 4-ethylene dioxythiophene) polystyrene sulfonate*. PEDOT: PSS is an aqua base solution which is sandwiched between a clean ITO surface and the active layer (for conventional architecture) [132].

Use of PEDOT: PSS as a buffer layer became noticeable when it was used in the fabrication of OLEDs in 1997, which resulted in enhancement performance and the stability of the OLED devices [138]. PEDOT: PSS was used as a buffer layer between the ITO and the active layer. The molecular structure of PEDOT: PSS is illustrated in Figure 3.16.

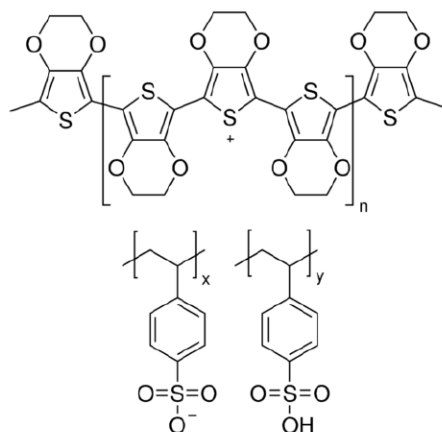


Figure 3.16: The molecular structure of PEDOT: PSS.

A thin transparent layer of PEDOT: PSS is fabricated onto an ITO coated substrate via a spin coating technique. Some of the important properties of PEDOT: PSS are high electrical conductivity and a smooth surface [132]. PEDOT: PSS as a hole conducting layer has the ability to reduce the surface roughness of the ITO collated substrate as well as stabilising the electrical contact between the active layer and electrode [139]. This is due to the matching work function of PEDOT: PSS with the ITO electrode.

As a result, the energy barrier between the anode electrode and the active layer can be reduced, and the collection of hole charges becomes more efficient [132]. Similarly, at the cathode electrode where electrons are collected, there are materials which are used as a buffer or interfacial layers. Examples of these include Calcium (Ca) and lithium fluoride (LiF) (for conventional architecture) [140], [141].

Due to their low work function, these materials provide similar stable electrical contact between the cathode and the active layer. Both Ca, and LiF are deposited via thermal deposition technique on top of the active layer prior to electrode deposition. To measure charge carrier mobilities, it is essential to fabricate a single charge carrier device similar to a diode configuration [142].

Such devices are fabricated with having the active layer sandwiched between two buffer layer materials which can block one type of charge (i.e. holes/electrons). As an example, PEDOT: PSS can only be used to fabricate a hole only device since it is a hole conducting material. For an electron only device, Caesium carbonate (Cs_2CO_3) is an ideal material to increase the energy barrier at the anode (ITO) electrode and block any injected hole [143].

3.5 Summary

In this chapter, a brief overview of donor, acceptor and buffer materials used for fabrication of OSC devices was presented. Donor materials from different categories such as polythiophenes, benzothiadiazole, pyrrolidinone (DPP) and benzodithiophene (BDT) were looked into, and based on their device performance in BHJ structure the best donor material with highest potential was chosen, it was decided that the ideal donor material for solution processable system in this project would be PBDTTT-EFT polymer and PC₇₁BM as the primary acceptor material.

Apart from using PC₇₁BM as the main acceptor material, PC₆₁BM and IC₆₁BA will also be employed as additional acceptor materials to be blended with PBDTTT-EFT. IC₆₁BA was chosen as one of the fullerene derivative acceptor material to be blended with PBDTTT-EFT due to its high LUMO level which would boost the device V_{oc} when blended with PBDTTT-EFT, as compared to PCBM molecules. It has been reported that replacing PC₆₁BM with IC₆₁BA for blends of P3HT, the device performance and efficiency has boosted from 3.84% to 6.48%, mainly due to increased FF and V_{oc} parameters when IC₆₁BA is used. P3HT:PC₆₁BM gives V_{oc} of 0.58 V, whereas P3HT:IC₆₁BA gives V_{oc} of 0.84 V [135]. The sample and solution preparation details are discussed in *Chapter 4*.

CHAPTER 4

Experimental Procedures & Methodology

4.1 Introduction

In this chapter, the experimental procedures and methodology for the work done in this project are discussed. Starting with an introduction to experimental procedures and sample preparation followed by, the operation mechanism and set up of equipment used for characterising thin film samples /devices.

4.2 Experimental Procedures

In this section, the experimental procedures and techniques for sample and device fabrication are described sequentially. Table 4.1 below provides a list of materials and chemicals used for fabricating thin film samples and devices in this project.

Table 4.1: Summation of materials and chemicals used in this project.

Materials / Chemicals	
Electrode contacts	<i>Cathode:</i> Aluminium (Al), <i>Anode:</i> Indium Tin Oxide (ITO), Gold (Au)
Active layers	Poly[4,8-bis(5-(2-ethylhexyl)thiophen-2-yl)benzo[1,2-b;4,5-b']dithiophene-2,6-diyl-alt-(4-(2-ethylhexyl)-3-fluorothieno[3,4-b]thiophene-)-2-carboxylate-2-6-diyl)] (PBDTTT-EFT / PTB7-Th), [6,6]-Phenyl-C61-butyric acid methyl ester (PC61BM), [6,6]-Phenyl-C71-butyric acid methyl ester (PC71BM), 1',1'',4',4''-tetrahydro-di[1,4]methanonaphthaleno[5,6]fullerene-C60 (ICBA)
Buffer layers	Hole transport layer: Poly(3,4-ethylenedioxythiophene)-poly(styrenesulfonate) (PEDOT:PSS), Electron transport layer: Calcium (Ca), Caesium carbonate (CsCO3)
Solvents	Chlorobenzene anhydrous, 99.8% (CB), 1,2-Dichlorobenzene anhydrous 99% (ODCB), Methanol, Ethanol, Acetone, 2-Propanol (Isopropanol) (IPA)

4.2.1 Device architecture

Organic Solar Cell devices are fabricated with the following architecture for I-V characteristics:

ITO → PEDOT: PSS → Active layer → Ca → Al

4.2.2 Substrates

Two types of substrates are going to be used in this project, which are described below:

- Indium Tin Oxide (ITO) coated glass substrates (25 mm × 25 mm) used for OSC device fabrication.
- Quartz substrates (25 mm × 25 mm) used for Optical / material characteristics.

The main reason for using Quartz substrates instead of glass for optical characteristics, is the difference in their optical absorption coefficient. Glass substrates are not suitable for collecting optical absorption data of thin films [144], [145]. Since ITO is electrically conducting and transparent material, it must be patterned to identify the cell size and prevent short-circuiting when fabricating devices [24], [146]. ITO is only coated on one side of the glass substrate, by using a multimeter (in ohmic mode) the conducting (ITO) side of the substrate can be determined. Once the coated side is determined, the patterning of the ITO can be achieved by ‘Etching’ process described in Figure 4.1.

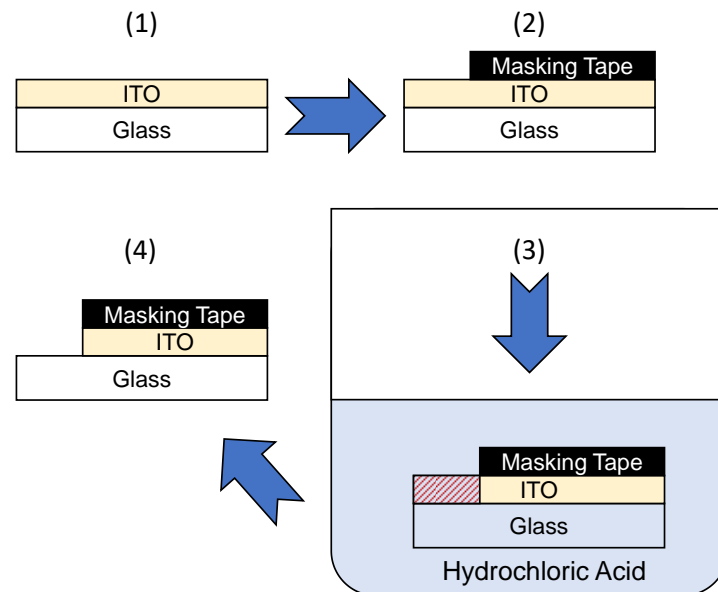


Figure 4.1: Schematic illustration of the ITO substrate Etching process.

The stages shown in Figure above are described below:

1. ITO coated substrate is covered with masking tape.
2. Masking tape should be cut to the selected length, leaving a portion of ITO exposed.
3. The masked substrate is submerged into a solution of Hydrochloric acid (HCL) for a period of 10 min. within this time, the HCL acid will dissolve the exposed ITO.
4. The substrate is extracted from the HCl solution, and the exposed ITO is now dissolved, leaving only the glass behind.

Once the ITO coated substrate is etched, it needs to go through the cleaning process. The cleaning process is identical for both types of substrates used here in this project. The cleaning process consists of three sequential stages using an ultrasonic bath. Each stage uses a different solvent sequentially which are as follows; Deionised water (DIO H₂O), Acetone, Isopropyl Alcohol (IPA).

Each stage is completed by submerging the substrate(s) into a beaker filled with the solvents mentioned above. The beaker is then placed inside the ultrasonic bath and sonicated for a period of 10 min. the substrate(s) are dried after each stage, after the final stage (IPA) the dried substrate(s) are placed in a Petri dish and transferred into Nitrogen (N₂) filled glove box as shown in Figure 4.2. The environmental condition of the N₂ glove box should always be < 1 ppm (parts per million) of O₂ and H₂O. All sample preparation and fabrications for this project are done inside the N₂ glove box.

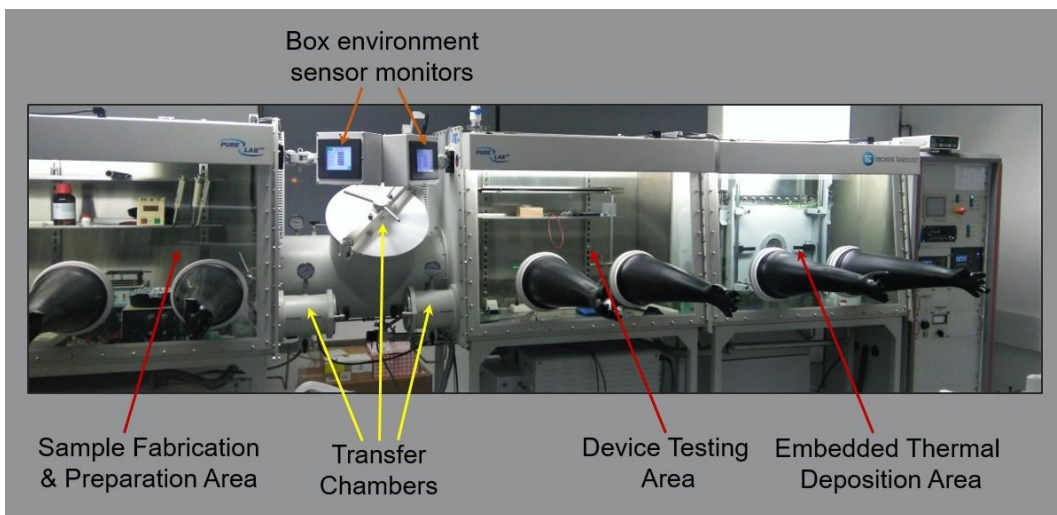


Figure 4.2: N₂ Glovebox system at R117 Thin Film Laboratory.

4.2.3 Sample preparation

All samples are prepared under the N₂ glove box condition mentioned above. In this section, the preparation of samples is described. Firstly, the materials used for the active layer of the OSCs need to be prepared into a solution form, which can then be used to fabricate. The active solution is made by dissolving the Donor-Acceptor material via a solvent which can be used to fabricate onto the substrate. This process is dependent on the following parameters:

- The concentration of the solution
- Solvent (single/mixed)
- D:A ratio

Active solutions are prepared with the weight, concentration, solvent(s) and D:A ratios presented in Table 4.2.

Table 4.2: Summary of solution preparation in this project.

Material(s)	D:A	weight (mg)	Solvent [mixing ratio]	Concentration (mg mL ⁻¹)
PBDTTT-EFT	n/a	10	ODCB	10
PC ₇₁ BM	n/a	10	ODCB	10
PC ₆₁ BM	n/a	10	ODCB	10
IC ₆₁ BA	n/a	10	ODCB	10
PBDTTT-EFT: PC ₇₁ BM	1:1.5	6: 9	ODCB	15
		10: 15	ODCB	25
		14: 21	ODCB	35
		10: 15	ODCB: CB [1:1]	25
		10: 15	ODCB: CB [2:1]	25
		10: 15	ODCB: CB [3:1]	25
PBDTTT-EFT: PC ₇₁ BM	1:0.5	16.7: 8.3	ODCB: CB [3:1]	25
		12.5: 12.5	ODCB: CB [3:1]	25
		10.0: 15.0	ODCB: CB [3:1]	25
		8.3: 16.7	ODCB: CB [3:1]	25
		6.3: 18.7	ODCB: CB [3:1]	25
PBDTTT-EFT: PC ₇₁ BM	1:2.0	8.3: 16.7	ODCB: CB [3:1]	25
PBDTTT-EFT: PC ₆₁ BM	1:2.0	8.3: 16.7	ODCB: CB [3:1]	25
PBDTTT-EFT: IC ₆₁ BA	1:2.0	8.3: 16.7	ODCB: CB [3:1]	25

To prepare each sample/solution, the desired weight of the material(s) was first weighted in a vial using a scale, and the vial was then transferred into the N₂ glove box. At this stage, the required amount of solvent(s) is added to the material(s) plus a

disposable permanent magnet. The vial is then placed onto a magnetic stirrer to ensure the solution is well dissolved. This is shown in Figure 4.3. Each active solution was stirred for a recorded time before being used for device fabrication. This timing before use of the active solution is labelled as an *Ageing process*, which is described in Chapter 5, section 5.3.3.

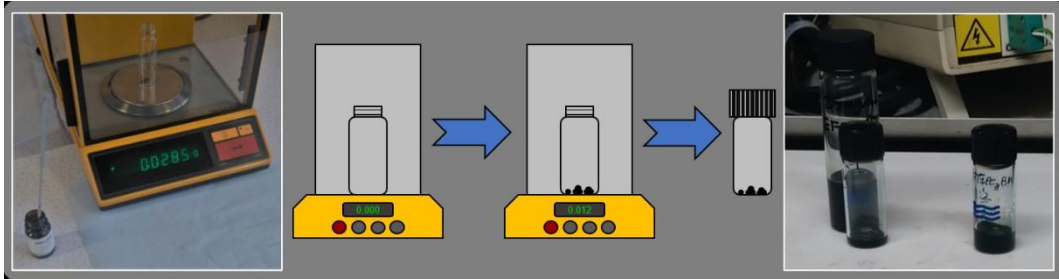


Figure 4.3: Pictures and diagram of Active solution preparation stages.

4.2.4 Sample Fabrication (Spin Coating)

Samples are fabricated onto the substrates (ITO / Quarts) via spin-casting technique. This technique has been the most used method for OSC fabrication [147]–[149]. This technique consists of applying the liquid onto the surface of a substrate which will spin at a set rotational speed, acceleration and period, as shown in Figure 4.4. Generally, this can be done either by applying the liquid to the substrate first or during the spinning process. The excess amount of the liquid will be ejected off the substrate due to the angular velocity of the substrate rotation, leaving the substrate with a thin film.

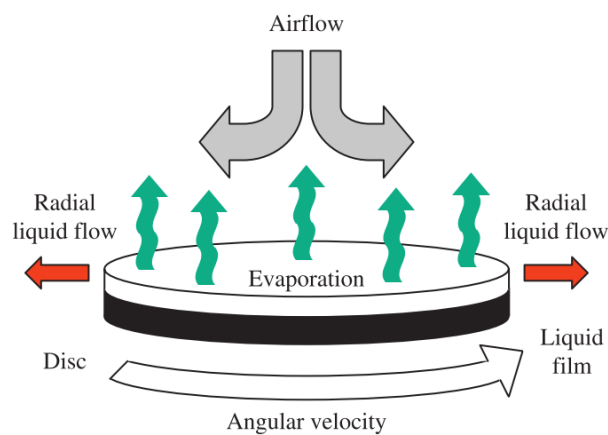


Figure 4.4: Schematic of Spin coating technique [149].

When using spin casting technique, the thickness and morphology of the film achieved for a particular concentration, material and solvent can be reproduced with minimal

changes [149]. The film thickness desired can be achieved by varying the spin rotation speed, acceleration and spin time, however it is important to note that the film thickness is limited by certain factors of the solution such as the viscosity, volatility and molecular weight of the material(s) used [149]. In general, the film thickness d obtained experimentally can be expressed mathematically by a power-law relationship:

$$d = k\omega^\alpha \dots \dots \dots (37)$$

where ω is the angular velocity, k and α are empirical constants. These constants are related to the physical properties of the solution itself, as mentioned above [149]. There have been thorough reviews on this topic, which can be found in the literature [147], [148]. By varying the spin speed, the film thickness will also change, and an example of this phenomena following the equation above is illustrated in Figure 4.5.

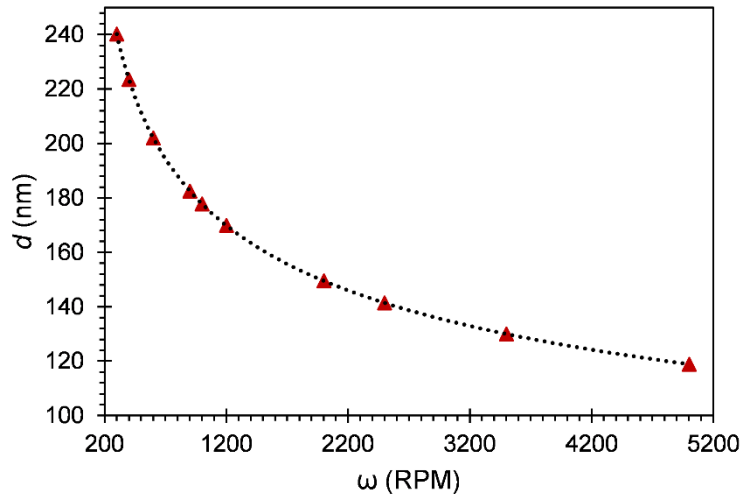


Figure 4.5: Plot of ω against d . Random Data generated using equation 39.

4.2.5 Thermal Vacuum deposition of Electrodes

The last stage of fabricating OSCs devices is the deposition of buffer material (such as Ca) and metal electrodes (Al, Ag). This is typically done using a thermal vacuum deposition system. For the work done in this project, AUTO-500 vacuum deposition system (HHV Ltd) has been used. The schematic diagram of this system is illustrated in Figure 4.6.

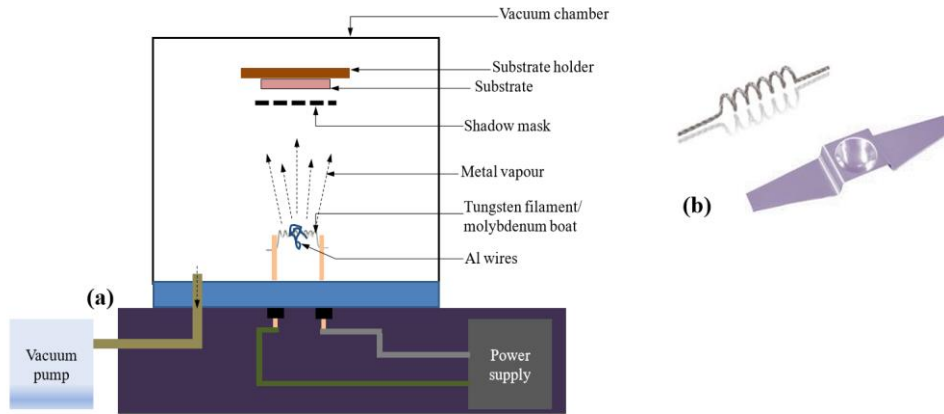


Figure 4.6: **(a)** schematic diagram of AUTO-500 thermal evaporation system used for electrode deposition. **(b)** Pictures of evaporation sources: Tungsten element and molybdenum dimple boat. [38].

Thermal deposition process requires the material(s), which needs deposition to be heated/melted under high vacuum levels ($\sim 10^{-7}$ mbar). Once the source material for deposition is heated to its melting point, it would evaporate. The vapours of the evaporated material will be deposited on the surface of the substrate after going through the Shadow/lithography mask. The substrate is placed at a distance away from the source with a lithography mask consisting of windows in between them. The mask will only allow specific areas of the film to be deposited with the evaporated vapour.

This lithography mask used for this project was designed, developed and manufactured by the author of this thesis. The evaporated vapour will dense to form a layer on top of the active layer film. To monitor the thickness of this layer, quartz crystal growth rate monitor IL-150 (Intellemetric) is used. IL-150 monitor operates based on observing changes in the resonance frequency of the crystal. The change in the resonance frequency of the crystal, due to the deposition rate of the source material(s) will decrease linearly with the thickness. This change can be used to determine the thickness of the deposited material on the film [150]. This information is fed to a computer module displayed in Figure 4.7. Intellemetric monitor computer will display the rate (nm / sec) and the total thickness of the deposited material. The deposition rate can be controlled by varying the electrical current supplied to the evaporation source.



Figure 4.7: Picture of Intellemetric IL-150 Quartz crystal growth monitor.

Based on the material that is going to be thermally deposited, the corresponding evaporation source shown in Figure 4.6b is going to be installed. For materials such as Al and Ca the Tungsten element is used, and for Ag, molybdenum dimple boats are installed as an evaporation source. The picture of fully fabricated devices with aluminium electrode is shown in Figure 4.8.



Figure 4.8: Photos of three different samples each with three devices fabricated (left: EFT: PC₇₁BM, middle: EFT: PC₆₁BM, right: EFT: IC₆₁BA).

4.2.6 Solar Simulator

To measure the performance of OSCs, fabricated devices need to be tested under illumination and dark conditions. When testing OSC devices under illumination conditions, the illumination power needs to be calibrated and standardised to match 1 sun power. Solar simulators are used to provide this illumination/light. For the work done in this project, LOT-LSO104 solar simulator with 1.5 AMG (air mass global) filter (LOT-LSZ189) is used. LOT-LSO104 solar simulator is shown in Figure 4.9.

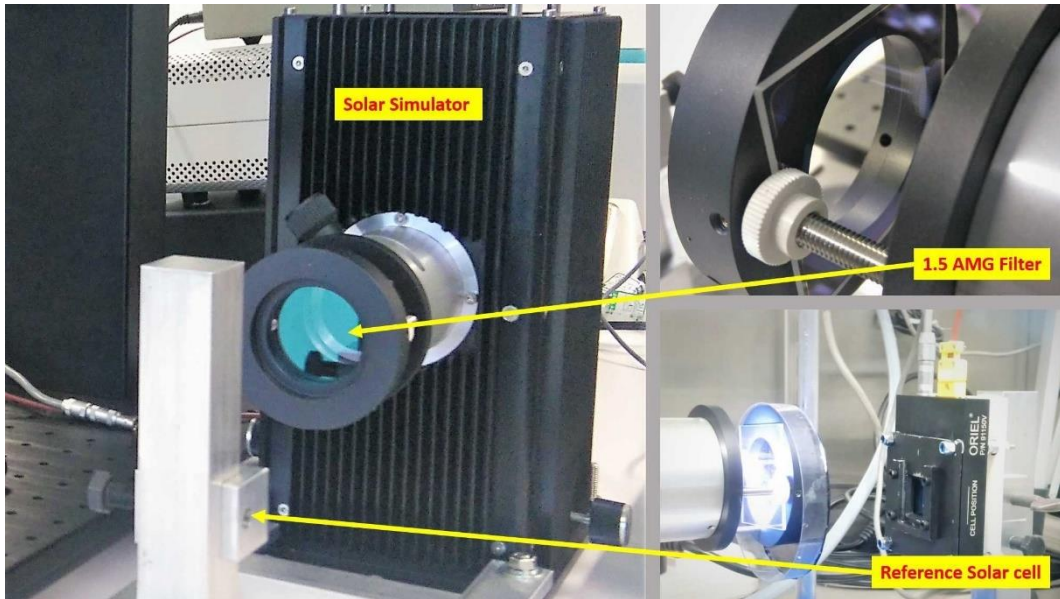


Figure 4.9: Pictures of Left: LOT-LSO104 Solar simulator, Top right: LOT-LSZ189 1.5 AMG filter, Bottom right: Silicone solar cell for reference.

The light from the solar simulator is used as the source of the input power to the fabricated OSC devices. The illumination light from the solar simulator is adjusted and calibrated to produce a power density of 1 sun under 1.5 AMG conditions. This would mean that its input power density should be calibrated to 100 mW cm^{-1} and its spectral irradiance to be regulated to 1.5 AMG, which is illustrated in Figure 4.10.

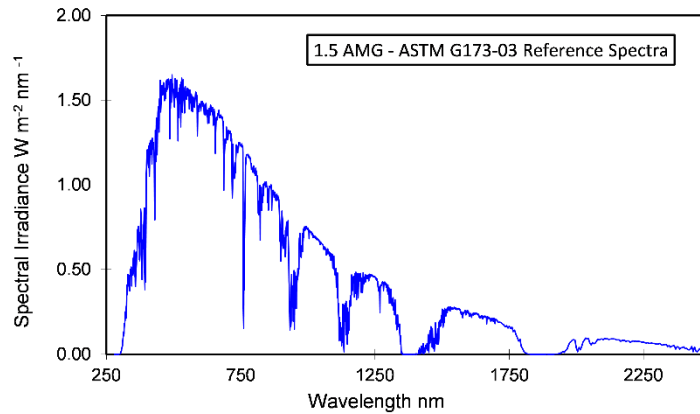


Figure 4.10. The plot of solar light against Spectral irradiance of 1.5 AMG with ASTM G173-03 standards.

To make sure the input power density is correctly calibrated to 1 sun, a calibrated silicon reference cell and a meter (Newport 91150V) is used to monitor and calibrate the solar simulator output power (see Figure 4.11). Light from the solar simulator shined onto the reference cell will be measured and displayed in terms of units of the

sun on the meter. The Solar simulator power can be adjusted by changing the electric current supplied to the solar simulator system.



Figure 4.11: Pictures of a) Newport 91150V reference cell, b) solar input power monitor, c) solar simulator power supply control.

Apart from adjusting the electric current supplied to the solar simulator, the light source power could also be adjusted by varying the distance away from the solar simulator and the reference cell / OSC device. For this purpose, an XYZ stage mount was designed and built by the author of this thesis.

4.3 DC – Characteristics

The DC current-voltage (I-V) characteristics of OSCs will be conducted using a source-meter unit (SMU). Keithley 2400 SMU, shown in Figure 4.12, has been used throughout this project for I-V data collection.



Figure 4.12: Picture of KEITHLEY 2400 source-meter.

LabTracer 2.0 software (LabView) was used to communicate and control Keithley 2400 SMU for data collection. The parameters of the data collection are set in the software prior to data collection. OSC devices were tested using a custom-built test

station, which is presented in Figure 4.13. This test station was used to collect I-V characteristics under dark and illumination conditions.

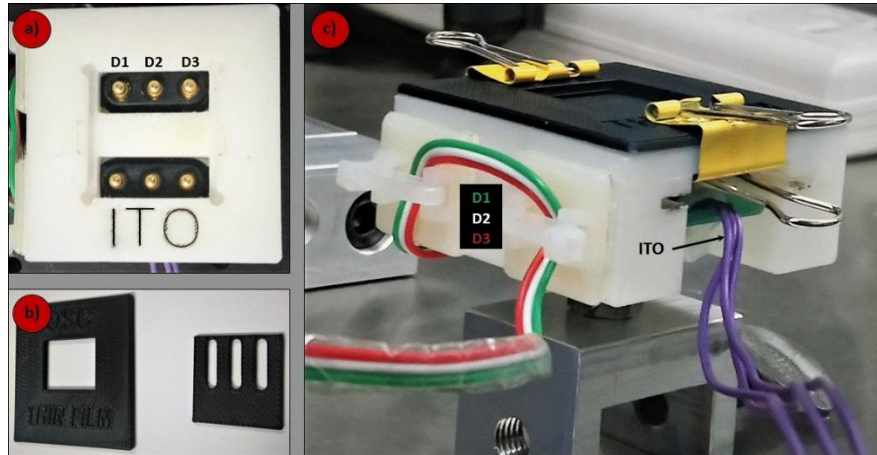


Figure 4.13. Pictures of the OSC device test station, **a)** top view of the substrate holder identifying the spring contact points, **b)** top lid and the shadow mask designed for the substrates, **c)** OSC device test station fully mounted, identifying each connection wire: D1, D2, D3 (Green, White, Red) respectively and ITO wires (Purple).

Device test station shown in Figure 4.13 was custom designed, developed and manufactured by the author of this project.

4.4 AC – Characteristics

AC impedance spectroscopy (IS) is a non-destructive tool generally used for the analysis of a wide range of electrical devices [38]. It has been reported that this tool can be used to determine charge carrier lifetime in dye-sensitized solar cells [151]–[153]. IS can also be a useful tool in providing insights for performance improvements of organic electronic devices [53], [154]. Several reports published on this technique have revealed that IS measurements can be used for characterisation of OSC devices [155]–[157]. IS measurements operation is done by applying an electrical AC signal to an electronic material sandwiched between electrodes, and the system response is observed accordingly [158]. The working principle is based on the change in the measured AC as a function of frequency. In an AC circuit, the opposing force to the flow of current at a given frequency is noted as impedance (Z) which is composed of two parts; a real and an imaginary (j) part [158]. This is mathematically expressed as:

$$Z = R + jX = |Z|\angle\theta^\circ \dots \dots \dots (38)$$

where R is the resistance in Ohms (real part), X is the reactance (j denoting the imaginary part) in Ohms, Z is the impedance magnitude in Ohms, and θ is the phase

angle (degrees or radians). Figure 4.14 illustrates a typical impedance plot (in vector formation) on an Argand diagram, and the instrumentation setup for IS measurements using HP4248.

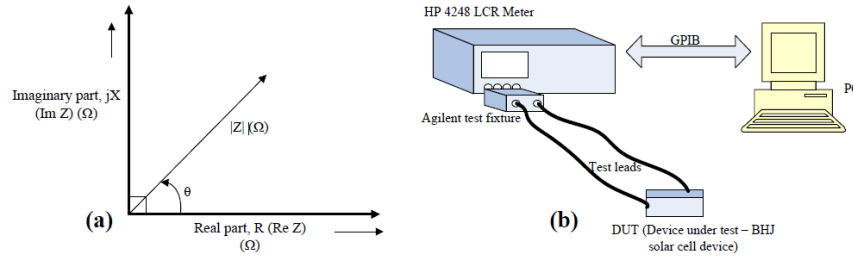


Figure 4.14. (a) Impedance plot (vector diagram representation), (b) schematic instrumentation setup for impedance spectroscopy measurement using HP 4248 LCR meter.

Using HP4248 LCR meter, IS measurement were performed in the frequency range of 20 Hz to 1 MHz, with an oscillation voltage of 50 mV. The machine generates results in the form of $|Z|$ in Ohms and $\angle\theta$ in degrees. The obtained results from the machine are then subsequently converted from *polar* to *rectangular*, and the calculated data are plotted in a Cole-Cole plot. Figure 4.15 illustrates an example of a typical Cole-Cole plot for impedance data obtained in a frequency range of 20 Hz – 1MHz.

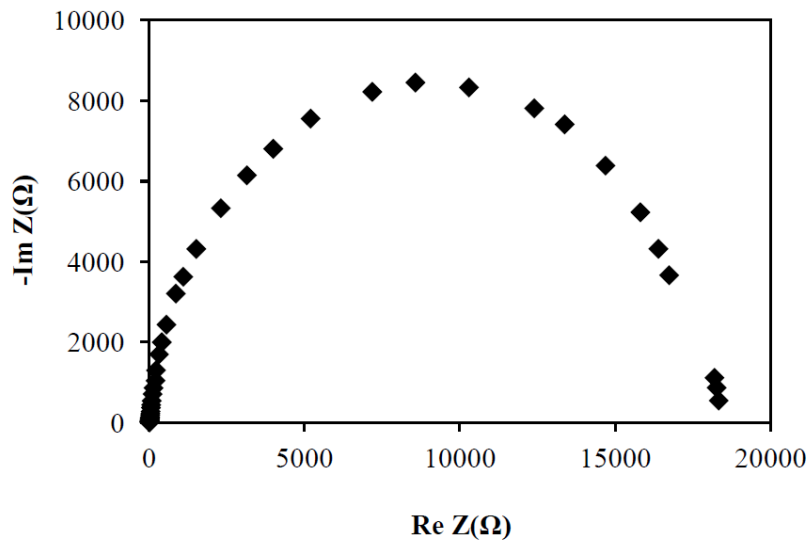


Figure 4.15. A typical Cole-Cole plot for IS data obtained in a frequency range of 20 Hz – 1 MHz.

4.5 Optical Absorption

The measurement of absorption spectra of thin films in the region of Ultraviolet-Visible (UV – Vis) wavelength is essential to characterise the energy absorption of the

thin films [159], [160]. By analysing the spectrum collected, numerous parameters from the material(s) within the thin film can be obtained. This information can then be used to interpret the characteristics of the material(s) [25]. From the UV – Vis spectra optoelectronic properties of the material(s) can be extracted. One of the most common parameters which are extracted from a thin film spectrum is its optical bandgap [26], [38], [161]. Optical absorption spectra are obtained based on Beer’s law [162]–[164].

$$A = \log_{10} \left(\frac{I_0}{I_T} \right) = -\log_{10} T \dots \dots \dots (39)$$

where **A** is the absorbance as a function of incident light intensity **I₀** and transmitted light intensity **I_T** ratio. Where this ratio **T** is the transmittance. Plotting **A** against the incident light wavelength would generate the absorption spectrum of the measured thin film sample. Varian Cary *bio* 50 UV – Vis spectrophotometer has been used to obtain the optical absorption spectra of all thin-film samples in this project. Figure 4.16 illustrates the operation of Varian Cary *bio* 50 in schematic format.

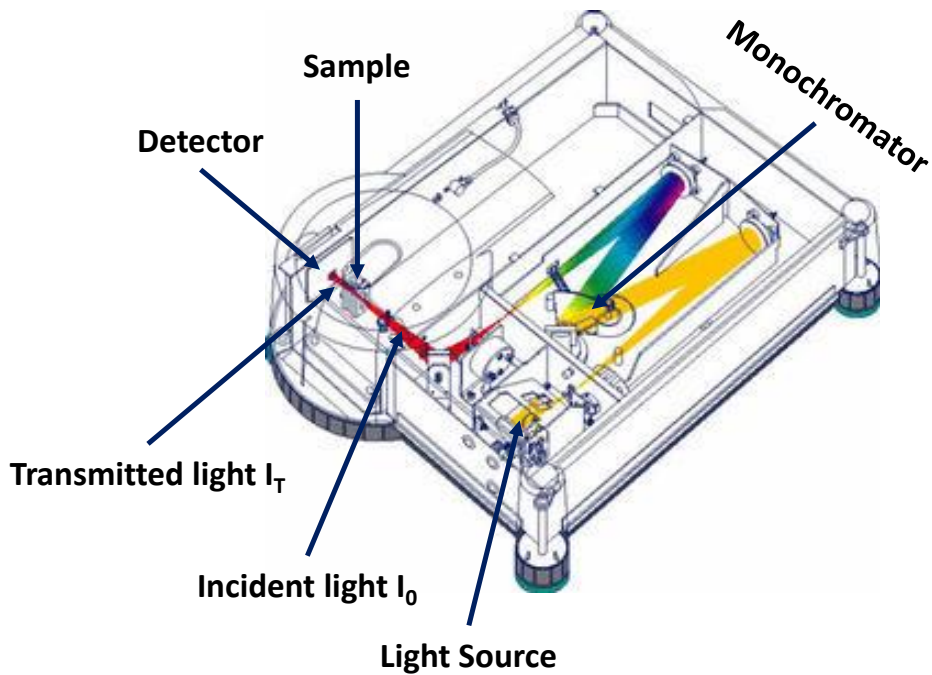


Figure 4.16. Schematic of Varian Cary *bio* 50 UV – Vis Spectrophotometer.

The light source in Varian Cary *bio* 50 will go through a monochromator to split the light into separate wavelengths. The light with a selected wavelength (Incident light) will go through the sample, and the transmitted light exiting the sample will be detected by a photo-sensor detector. This information is then fed to a computer system which will plot absorbance **A** against the wavelength of the incident light.

4.6 Raman & Photoluminescence Spectroscopy

Other Optical spectroscopic techniques used to characterise thin film samples are Raman and Photoluminescence (PL) spectroscopy. These techniques are an effective way to characterise the molecular structure of materials within thin films and OSCs [38], [78], [165]–[167]. Raman Spectroscopy was named after its inventor C. V.

Raman an Indian scientist who invented the technique followed by PL [168]–[171]. Raman spectroscopy is a technique which is used to identify the chemical bond properties of materials. Raman spectroscopy can be used to do a qualitative and quantitative investigation of the thin film. Measuring the frequency scattered from the sample will lead to qualitative analysis, and measuring the intensity of the sample will lead to quantitative analysis [168]. The principle of Raman spectroscopy operation is established on measuring the shift in frequency of the scattered light with respect to the incidence (monochromatic) light on the thin film sample [38], [172], [173].

Figure 4.17 illustrates the interception of incident monochromatic light with the thin film medium. When electromagnetic waves interact with molecules of a material they scatter. Majority of the scattered wave will have a similar frequency to the incident light. However, there is a fraction of this scattered light/wave which has a different frequency to the incident light. This change in frequency is referred to as ‘*Raman Scattering / Raman Shift*’ [173], [174].

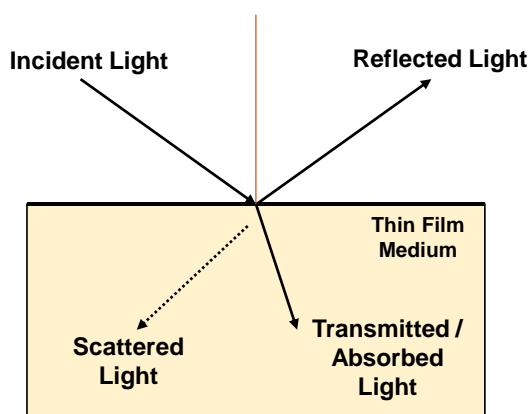


Figure 4.17. Schematic diagram of incident light and its paths after entering thin film medium.

When a thin film sample of a specific material(s) is investigated under Raman spectrometer, it will produce unique “fingerprints” specific to the molecular structure.

By analysing the produced Raman spectrum, important qualitative and quantitative information can be obtained. When investigating composite organic electronic materials in their pristine / blend form, specific characteristics can be identified, which will provide an in-depth understanding of the molecular structure of the material. The plot of Raman spectra consists of Raman shift on the x -axis and intensity on the y -axis. A material would produce a scattered line profile which is specific to its molecular structure. If there is going to be any changes in the molecular structure of a material (i.e. chemical or physical) upon changing its condition, for example blending two materials; Raman spectroscopy would show these changes. Obtaining this knowledge is of importance in understanding the impact of the material(s) nanodomains on the performance of OSCs. Raman and PL spectroscopy studies in this project were done using the InVia Raman microscope (Renishaw).

This instrument comprises an optical microscope attached to a Raman system. Samples are illuminated through the microscope coupled with a Laser. Lasers with an excitation wavelength of 514 nm (Green) and 785 nm (Near IR) were used to obtain the Raman spectra in this project. The schematic diagram for the operation of a Raman microscope is shown in Figure 4.18.

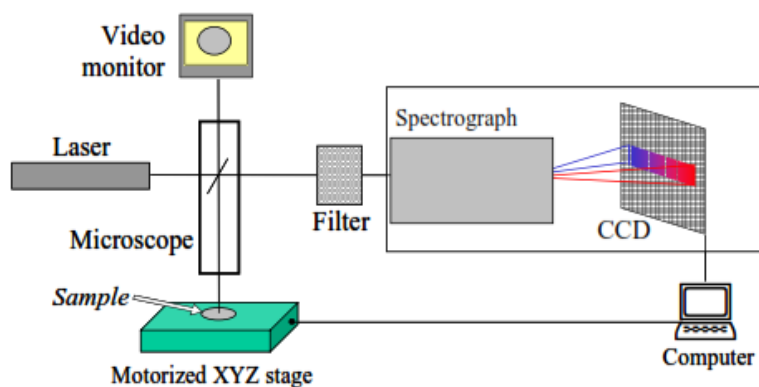


Figure 4.18. Schematic diagram of a Raman microscope.

PL spectroscopy is another technique which is used in conjunction with UV-Vis and Raman spectroscopy to probe material characteristics. PL operates based on the spontaneous emission of light after photon absorption by the material. This emission of light is due to the recombination process of excitons, which could not have been dissociated. When a sample is excited using a laser with a monochromatic wavelength (Excitation wavelength), it will emit a unique characteristic photoluminescence

signature which is measured using a spectrometer. Figure 4.19 illustrates typical experimental setup and operation of PL measurements.

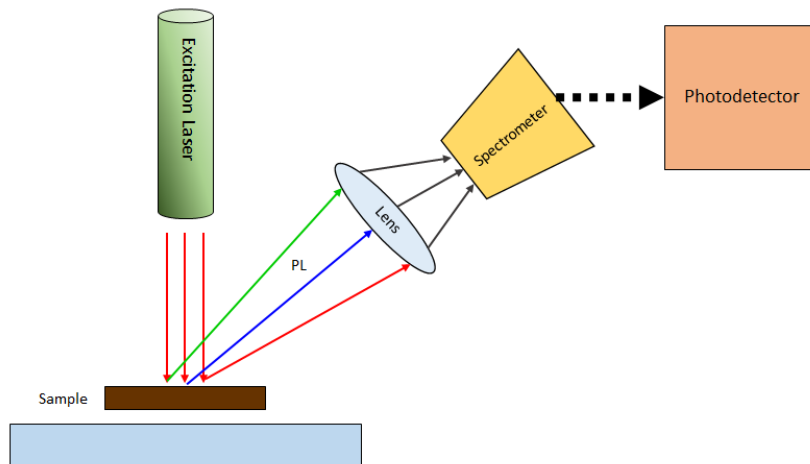


Figure 4.19: Schematic diagram of PL spectrometer setup.

The sample is excited with a laser of chosen excitation wavelength. The photon emission of the material(s) from the sample is condensed through an optical lens, which would be measured by a spectrometer and fed to a photodetector. This data is then transferred into the computer to produce PL spectra. PL spectra plot is constructed of a number of emission counts (*y-axis*) against emission wavelength (*x-axis*).

PL mode uses different laser power density and longer exposure times in comparison to Raman measurements. PL spectra analysis in OSCs field comprises of comparing the emission counts of pristine polymer thin film with the blended thin film. Quenching of emission counts (intensity) should be observed in the spectra when comparing blended thin films to pristine thin film (polymer material). This observation is an indication of charge transfer from a donor material to the acceptor material. Ideally higher PL quenching would result in enhancement of OSCs performance [30], [78], [175], [176]. Other parameters which can be extracted from PL spectra profile are, evaluation of the intermixing level of the composite materials in blended samples (donor: acceptor) and information associated to recombination processes which take place in the thin film [59], [77], [177]–[179]. For numerical analysis, the PL quenching is calculated and presented as PL quenching efficiency (Q.E.), which is simply the ratio of the area under the pristine film to blended film.

4.7 Grazing incident X-ray diffraction

Grazing incident X-ray diffraction (GIXRD) method, is a technique used for characterising the molecular structuring of the material(s) in thin films. It provides insightful information regarding the crystallography of the material(s) within the thin film (Donor / Acceptor). OSCs performance is directly related to the molecular structure and configuration of the material within the BHJ active layer. A better-structured polymer and fullerene domain will result in the enhancement of their PCEs [41], [180], [181].

Therefore, it is essential to be able to probe into the molecular structuring of OSC devices which are fabricated in BHJ configuration. GIXRD technique is used widely in the field of OSCs for molecular structural characterisation [181], [182]. GIXRD system operates based on transmitting a collimated X-ray beam onto the surface of the sample; the beam is scattered accordingly to the structure of the material(s) within the film (active layer). The scattered beam(s) is detected by a detector. The collimated beam is at an angle θ with respect to the plane of the sample. This incident beam undergoes diffraction when interacting with the crystalline / micro-crystalline segments of the active layer. This phenomenon follows Bragg's law, which states [183], [184], [72]:

“The Intensity of the reflected beam will be maximum at certain incident angle when the path difference between the two-reflected wave from two different planes is an Integral multiple of X-ray wavelength $n\lambda$.”

where n is an integer 1, 2, 3, ... and λ is the source x-ray beam wavelength. To better visualise the statement above, Figure 4.20 is drawn to aid express this law mathematically. The collimated beam will travel towards the crystal structure; the beam will diffract at the same angle θ and travel towards the detector. When a monochromatic, collimated beam strikes on a crystal structure, the atoms in the crystal will behave as scattering radiation of the same wavelength. If we consider a parallel x-ray beam with wavelength λ , travelling towards the crystal planes m and n as \overline{AS} and \overline{CT} respectively, both with an equal grazing angle θ , then the X-ray striking atom S

will diffract away along \overrightarrow{SB} and the X-ray striking atom T will diffract away along \overrightarrow{TD} path.

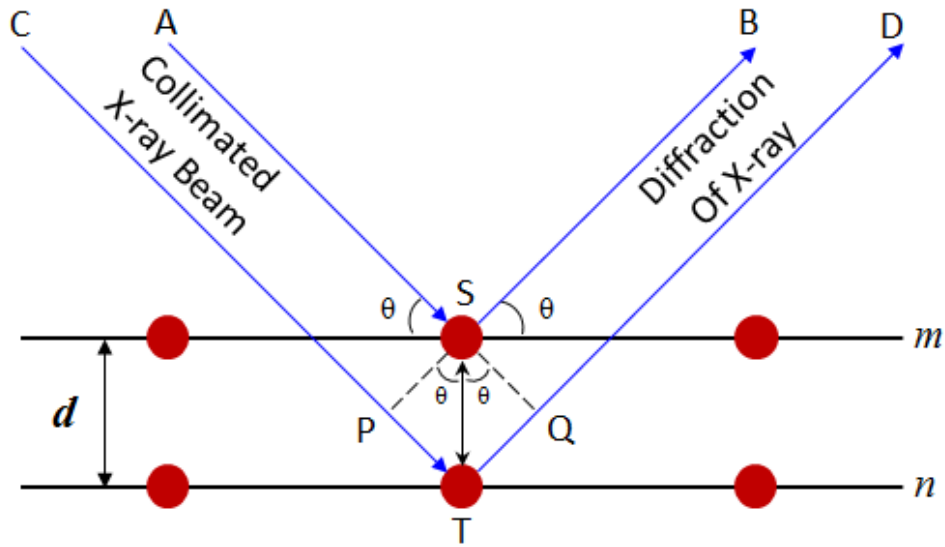


Figure 4.20: Schematic diagram of Bragg's law in vector form.

The path difference between \overrightarrow{ASB} and \overrightarrow{CTD} can be presented mathematically as:

$$\text{Path difference} = \overrightarrow{PT} + \overrightarrow{TQ}$$

But:

$$\overrightarrow{PT} = \overrightarrow{TQ} = \overrightarrow{ST} \sin \theta$$

\overrightarrow{ST} is also known as the inter-planer spacing d . Therefore, the maximum intensity will occur when:

$$n\lambda = 2d \sin \theta \dots \dots \dots (40)$$

where d is the intermolecular distance between the two paths and θ is the incident X-ray beam angle. The intensity of the measured X-rays is a function of the diffraction angle 2θ and crystalline orientation [38]. GIXRD machines operate in two modes/directions, which are illustrated in Figure 4.21.

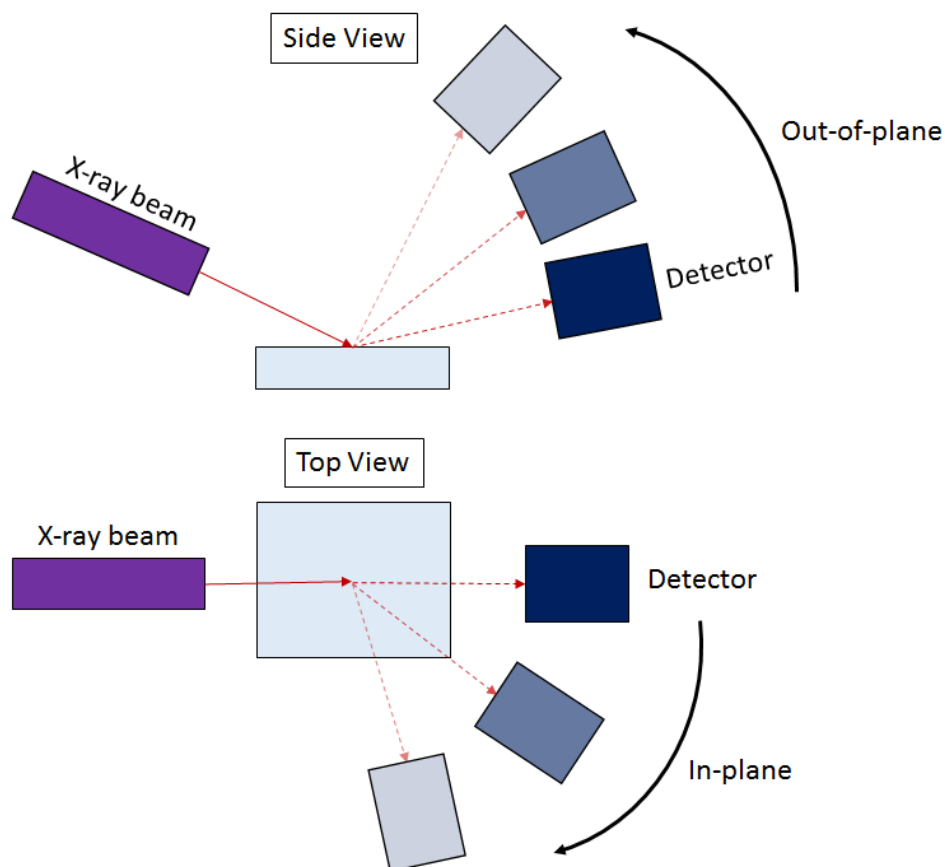


Figure 4.21: Schematics of Out-of-Plane (OOP) and In-Plane (IP) modes of operation of GIXRD.

GIXRD system setup in OOP mode would operate by having the detector moving in the out-of-plane (up / down) with respect to the sample plane. In contrast, IP mode operates by having the detector moving in the in-plane direction (same plane as the sample) as shown in the figure above. All the GIXRD data collected for this project is in the OOP mode using Bruker D8 Advance X-ray machine with an XYZ stage mount with X-ray source $\lambda = \text{Cu } \mathbf{k}\text{-}\alpha$ (0.15418 nm). This setup is shown in Figure 4.22.

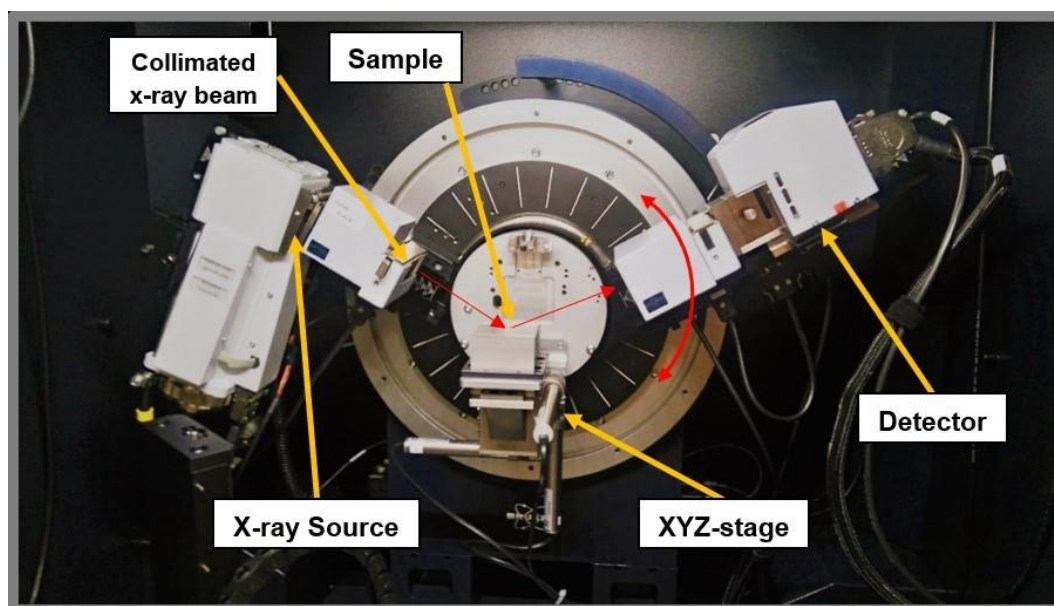


Figure 4.22: Picture of Bruker D8 Advance GIXRD with OOP XYZ stage mount.

The x-ray source generates x-ray beam which then collimates and travels towards the surface of the sample (red arrow) at an incident angle θ and the diffracted x-ray travels towards the detector. The incident x-ray beam will travel through the thin film, colliding with the crystalline phases of the molecules in the film.

This will create diffraction patterns depending on the structure and orientation of the molecules. By using Bragg's law, the spacing between the atoms of the molecules in a crystalline structure can be determined. It is crucial to obtain information about the inter-planer spacing and molecular structure of the thin films since would have an impact on the performance of OSCs [49], [185]. The GIXRD data can be used in supplement with Raman data to have a better understanding of molecular structuring of the active layer for OSCs. Highly crystalline polymers in the active layer would suggest a more regular structure, which would result in a better π orbitals overlaps [159], [184], [186]. Charge transport of holes is directly related to the π orbitals overlaps [42], [187].

Analyses of GIXRD data is dependent on the diffraction peak(s) detected by the (2θ) detector. From this data, the planetary orientation of the molecules can be determined using Miller indices [188]–[190]. Polymer (Donor) materials used for OSC applications would crystallise in different orientations. Most polymers have a preferred orientation with respect to the substrate they have been fabricated on [191]–[194]. Figure 4.23 illustrates an example of two possible primary orientation of a polymer molecule in its crystalline structure, which can be detected using IP or OOP mode

GIXRD. If the molecules are stacked on their edge, the orientation is referred to as ‘*Edge-on*’ and if the molecules are stacked on their backbone (laying parallel to the surface of the substrate) it is referred to as ‘*Face-on*’ orientation [195]. Since the data collected in this project is obtained using OOP mode, the collected XRD diffractogram d-spacing would imply that d_{100} is in the *Edge-on* orientation and d_{010} is in the *Face-on* orientation for PBDTTT-EFT polymer [195].

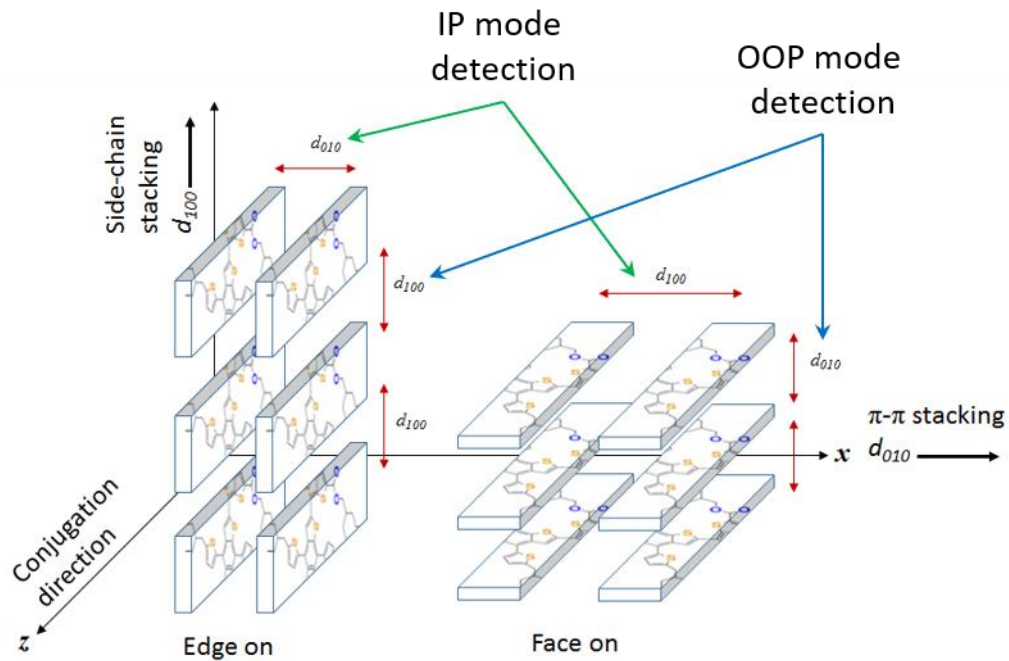


Figure 4.23: Schematic diagram of a polymer orientation, identifying planetary based on miller indices.

It is important to note, molecules with *Edge-on* / *Face-on* orientation could also have a parallel stack next to them, as shown in Figure 4.23. This parallel distance/spacing can only be detected by collecting data in IP mode GIXRD. In addition to the inter-planer spacing information, the crystal/grain size of a material can also be determined from the GIXRD data. such an analysis would be possible by using Scherrer’s equation [196]–[198]:

$$L_{hkl} = \frac{k\lambda}{\beta \cos \theta} \dots \dots \dots (41)$$

Where:

k = Scherrer’s constant ~ 0.9

λ = x-ray beam 0.15418 nm

β = Full width half maximum (FWHM) in radian of the peak

θ = Bragg’s angle (x-ray incident angle)

The parameters of data collection for GIXRD for this project were under the following conditions:

2θ detector range: **3 – 40°**

X-ray generating power: **1600 W** (40kV and 40 mA tube voltage and current)

4.8 Atomic Force Microscopy

Scanning probe microscopy (SPM) is a technique used in characterising of surface morphology. AFM provides the necessary tools to carry out the SPM technique for thin films in the field of organic electronics. In contrast to GIXRD, Atomic Force Microscopy (AFM) is a surface probing technique which is mechanically restricted to characterise the surface of the thin film. Surface morphology of thin films plays a vital role in affecting the electrical performance of BHJ OSCs [199]–[201]. Since the interface of the active layer with the cathode electrode has an impact on the overall electrical performance of OSC devices, it is essential to understand the surface morphology of the active layer. AFM operates based on the interaction of a cantilever tip and the film surface, as shown in Figure 4.24.

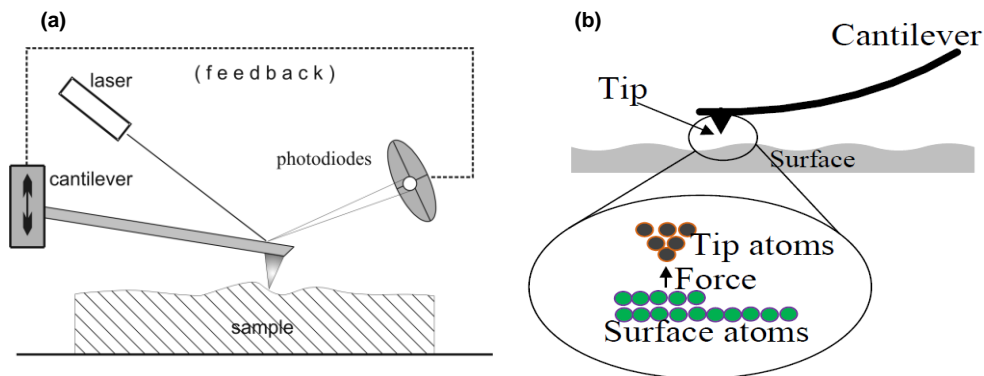


Figure 4.24: Surface composition detection schematic of AFM probe (a), AFM cantilever tip interacting with the film surface (b).

In general, AFM operates in two modes: contact and tapping modes. Each mode will be able to collect data from the surface by having an interaction of cantilever tip with the surface of the film/sample. A laser beam is shined on the back of the cantilever tip, its reflection is pointed towards a photo-diode detector, as shown in Figure 4.24a. Any dynamic changes caused by surface composition will be detected by the photodetector which is fed to a computer to generate it as a 2D/3D image. This interaction is described as the interatomic forces between the tip and the surface [38].

Agilent 5500 surface probing microscope AFM was used to collect all AFM images; all the AFM images obtained for this project were in tapping/acoustic mode (AC-AFM). Tapping mode AFM was used for all image collections because contact mode would damage the sample. Since the fabricated samples are made of polymeric/organic materials, they are soft, and this would mean that the film could get damaged if contact mode is used. However, in AC-AFM the cantilever is oscillated by a piezoelectric transducer capable of frequencies 100 – 400 kHz and amplitudes of around 20 nm.

Therefore, in AC-AFM, the tip is not making constant contact with the surface, and it is only tapping, hence ‘tapping mode’. AC-AFM operates by having a feedback system which controls and retains a constant amplitude of the cantilever interaction with the surface. Any changes in the oscillation because of cantilever interaction with the surface would be detected by the photo-diode. The photo-diode tracks these changes by measuring the reflected of the laser beam intensity, transmitted from the back of the cantilever tip. This signal from the photo-detector is then fed to a computer where topography and phase images are generated and presented. Figure 4.25 illustrates a schematic of AC-AFM operation.

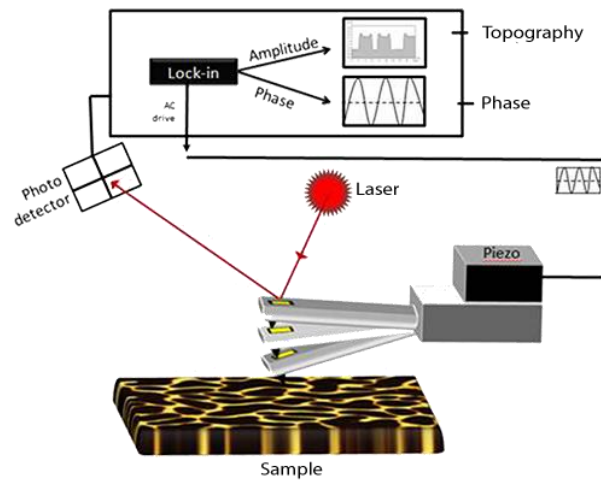


Figure 4.25: A schematic illustration of an AC-AFM operation.

The cantilever in tapping mode is oscillating close to its resonant frequency (f_0), which is driven by a piezoelectric transducer. The cantilever is in natural oscillation (before making any contact to the surface) would follow a classical homogenous forced oscillation driven by the piezoelectric transducer in classical mechanics. Hence this behaviour can be modelled mathematically:

$$F_c = A_0 \sin(\omega_0 t + \Phi) \dots \dots \dots (42)$$

where F_c is the cantilever force, A_0 is the waveform amplitude, $\omega_0 t$ oscillation frequency (rad) and Φ is the phase shift (rad). This function is illustrated in Figure 4.26.

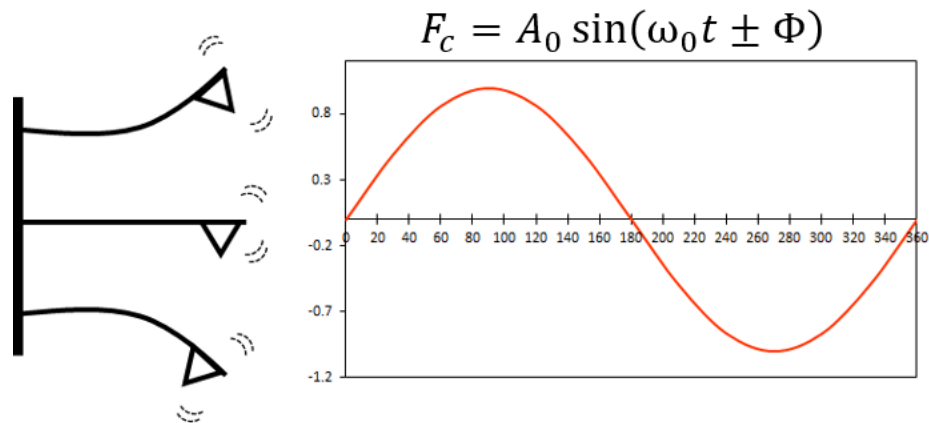


Figure 4.26: Cantilever under resonant oscillation, the physical movement of the cantilever on the left, one cycle waveform function of oscillation on the right.

Upon interaction of the tip with the sample surface, the oscillation of the cantilever will no longer be at f_0 . Depending on the nature of the material, which the tip is in contact with, there will be a phase shift. Factors such as the material, driving force of the cantilever (force constant), the distance between the tip and the sample, the speed of the scan and the feedback gains will have an effect on the phase shift value [202], [203]. When studying AC-AFM images, it is crucial to understand the nature of the material(s). For organic electronics applications, the nature of the materials and their geometry is the critical factor. When the tip is interacting with the surface of the film, depending on the material(s) structure, it would have a different dampening impact on the oscillation of the cantilever. An example of the tip interacting with two different materials is illustrated in Figure 4.27.

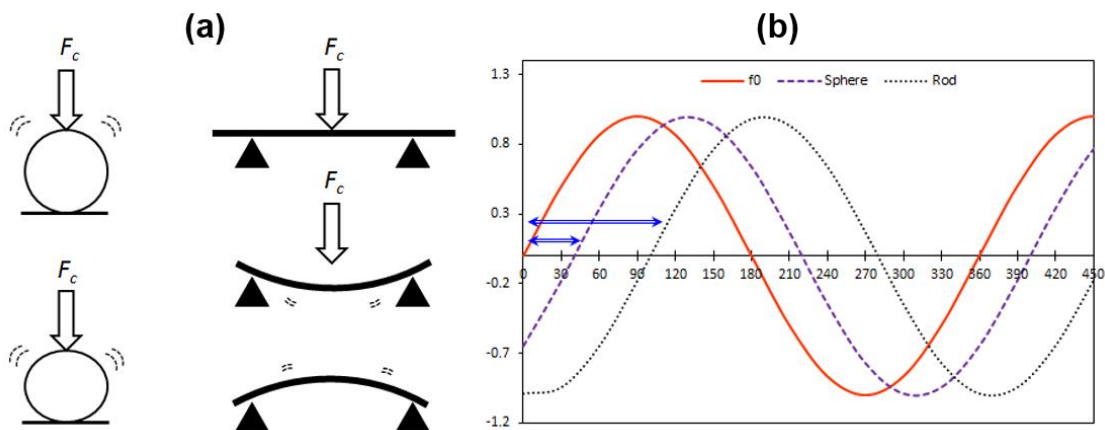


Figure 4.27: (a) Schematic of cantilever force F_c applied on different geometric shapes representing $PC_{71}BM$ and PBDTTT-EFT, (b) Effect of geometrical shape on Phase shift, based on mathematical modelling.

Figure 4.27a. illustrates the geometric schematic of two shapes (representing donor material PBDTTT-EFT and acceptor material $PC_{71}BM$) under a constant force, which represents the cantilever force once the tip is in contact with them. The spherical shape (fullerene) would have a higher stiffness in comparison to the bar-like (polymer) shape. Hence, different levels of stiffness will result in different levels of dampening, resulting in different Phase Shift (Φ).

This effect can be observed in the phase images collected by the AC-AFM. This phenomenon can also be represented as a mathematical model. Figure 4.27b. illustrates the output waveform from a mathematical model. The magnitude of the phase shift is directly correlated to the elasticity and stiffness of the material [202], [203]. In the example illustrated in Figure 4.27, spherical shapes are assumed to have a harder / stiffer property in comparison to bar-like shapes. This would result in different phase shift between the two materials. Such effects have been previously reported for P3HT: PCBM blends where it was highlighted that “softer and elastic regions of the sample dampens AFM cantilever vibrations more than that at harder regions, leading to higher phase difference from the reference drive signal” [204]. It was reported that by using this knowledge, it would be “possible to identify individual components of a heterogeneous mixture from the compositional mapping of the surface provided by the phase image” [204].

4.9 Cyclic Voltammetry Measurements

Cyclic Voltammetry (CV) measurements were performed in this project to determine the HOMO and LUMO energy levels of PBDTTT-EFT polymer. This technique has been previously used to determine the electrochemical p-doping (Φ_p) and n-doping (Φ_n) potentials of organic materials [38]. These electrochemical potentials are also referred to as reduction and oxidation potentials of material respectively. Most of the materials used for OSC application are identified as electroactive. Therefore CV measurements are proven to be an effective technique for estimating their HOMO / LUMO levels [38]. The CV measurement is based on an electrochemical process, which is illustrated in Figure 4.28.

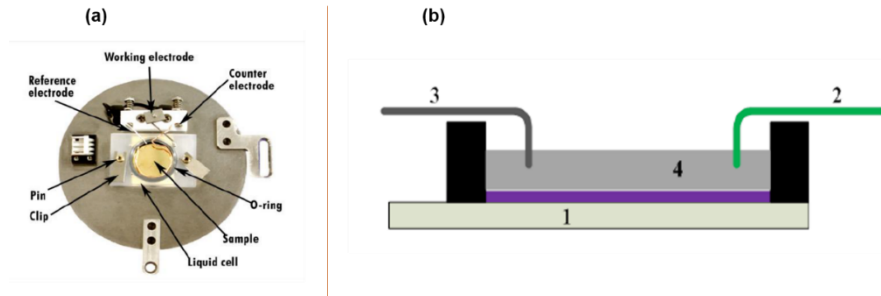


Figure 4.28: (a) Picture of Agilent 5500 AFM electrochemistry station, (b) Schematic of the electrochemistry (CV) experiment setup: (1) working electrode, (2) reference electrode, (3) counter electrode, (4) electrolyte solution.

CV measurements done for this project used, ITO coated substrate as working electrode, Ag wire as a quasi-reference electrode, platinum wire as a counter electrode and salts of lithium trifluoromethane sulfonate (Li triflate), tetrabutylammonium tetrafluoroborate (TBA BF₄), in acetonitrile at 0.01M as an electrolyte solution. Adopting a similar method as Oklobia (2013) and Heeger et al. (1999) the following equations were used to determine the HOMO and LUMO energy levels of PBDTTT-EFT [38], [205].

$$E_{HOMO} = -e(\Phi_p^{on} + 4.39) \dots \dots \dots (43)$$

$$E_{LUMO} = -e(\Phi_n^{on} + 4.39) \dots \dots \dots (44)$$

Where, Φ_p^{on} and Φ_n^{on} are the onset potentials of Oxidation and reduction, respectively.

4.10 Thin Film Thickness measurements

The DektakXT stylus surface profiler (BRUKER, Germany) is used in measuring the thicknesses of thin film samples. The instrument simply measures the thickness of thin films by a stylus tip in contact with the sample film surface. The stylus tip-surface contact force is as low as 30 nN, and this is required to access a film edge as it is traced across the sample surface. Figure 4.29 is a screenshot of a step height profile obtained using the DektakXT. As the tip makes its motion across the sample surface, a trace is collected, and converted by the analogue/digital converter electronics to a step profile. The DektakXT surface profiler is capable of providing a step height repeatability of $< 0.6 \mu\text{m}$.

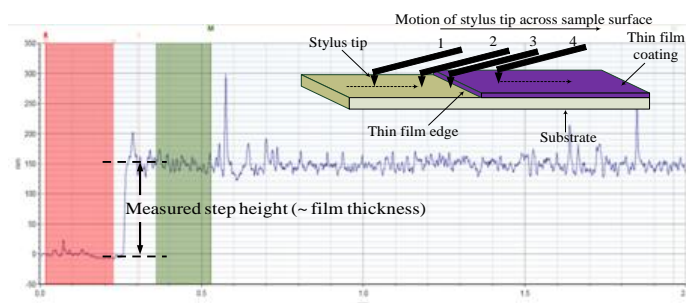


Figure 4.29: A measured step height profile of a thin film based on polymer/fullerene blend (Inset: a schematic illustration of stylus tip motion).

4.11 Mobility measurement of charge carriers

Measuring the charge carrier mobility of BHJ OSCs is an essential factor for determining the efficiency of the charge transport and collection within the active layer [143]. Improvement of charge transport properties would imply an increase in crystalline domains and optimised percolated pathways in the active layer for the donor and acceptor materials used. This would result in minimising the losses due to bimolecular recombination. Techniques employed for studying the transport properties of materials include:

- Time of Flight (TOF) [38].
- Photoinduced charge extraction by linearly increasing the voltage (Photo-CELIV) [132].
- Space charge limited current (SCLC) model fitting [38].

In this project, the charge carrier mobilities were determined by fitting the current density-voltage characteristics (in the dark) to the SCLC model (Mott-Gurney).

This method requires devices to be fabricated as a single charge carrier device (either electrons or holes). As such hole or electron-only devices are fabricated in a simple diode structure (e.g., anode/organic layer/cathode). Figure 4.30 illustrates the device architecture for a single charge carrier devices from which charge carrier mobilities were determined.

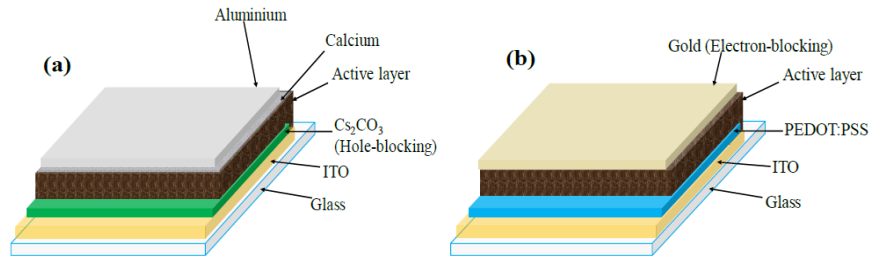


Figure 4.30: Example architecture configuration for a single charge carrier device, (a) Electron only device, (b) hole only device.

The device structure of hole only and electron only devices for EFT:IC₆₁BA, EFT:PC₆₁BM and EFT:PC₇₁BM were all identical and as follow respectively.

- ITO \ PEDOT:PSS \ EFT:Acceptor \ Au.
- ITO \ Cs₂CO₃ \ EFT:Acceptor \ calcium \ Al.

Each device/sample was tested using a SMU very similar to I-V characteristic methods, however the bias voltage range was in two stages, stage 1: 0-1 V with resolution of 0.05V. and 1-8V with resolution of 0.1V. The analysis of the collected data was fully explained in Chapter 2, section 2.3.2.

4.12 Summary

In this chapter, experimental procedures, operation, and setup of the equipment's used for fabricating and characterising OSC (devices and thin films) were briefly described. Experimental procedures such as device architecture, sample preparation and sample fabrication details for each set of samples was discussed exclusively. DC and AC characterisation methods of OSC devices were discussed and their importance for device performance extraction was described. Optical and structural characteristic methods were also discussed and its importance on revealing self-organisation and nanostructure formation of materials within the thin film has been highlighted. The importance of in-plane and out-of-plane in GIXRD was highlighted and correct miller indices plane assignment was identified.

CHAPTER 5

Results & Discussions

5.1 Introduction

In this chapter, all the experimental data obtained for this research are presented and discussed. The sample preparation was previously discussed in *Chapter 4, section 4.2.3*. The results collected from the experiments are categorised into two sections. Section 5.2, investigates the material characteristics such as potentiodynamic electrochemistry measurements (cyclic voltammetry), optical absorption, photoluminescence, Raman spectroscopy, molecular structuring (GIXRD) and Topography mapping (AFM). Section 5.3, will investigate device enhancement routes by applying numerous methods and techniques to optimise the device performance of OSC based on PBDTTT-EFT polymer. Methods such as film thickness optimisation, thermal annealing, solution ageing, concentration, drying techniques, solvent additives, surface washing, co-solvents, different D:A blend ratios and use of different fullerene acceptor materials are also presented.

5.2 Thin Film Material characteristics

In this section, pristine PBDTTT-EFT and fullerene derivative acceptor materials (PC₇₁BM, PC₆₁BM and IC₆₁BA) are investigated for their material characteristics. The optical absorption and Photoluminescence spectroscopy are also performed for blends of PBDTTT-EFT with different acceptor materials with D:A blend ratio of 1:2 respectively. The reason for the use of 1:2 blending ratio of D:A will be later explained in section 5.3.9.

5.2.1 Cyclic voltammetry

The highest occupied molecular orbital (HOMO) and lowest unoccupied molecular orbital (LUMO) levels of PBDTTT-EFT polymer in this research have been determined from electrochemistry methods. Agilent 5500 SPM workstation equipped with electrochemistry unit was used to perform the measurements in this section. The details of the cyclic voltammetry measurement and setup were previously discussed in Chapter 4, section 4.9. It was essential to obtain the HOMO and LUMO of PBDTTT-EFT material since at the time very few details were provided about these parameters. However, the HOMO and LUMO of acceptor materials, PC₇₁BM, PC₆₁BM and IC₆₁BA have already been provided by the manufacturer as well as reports in the literature. The electrochemical reduction-oxidation potentials of PBDTTT-EFT is presented in Figure 5.1, and the obtained HOMO and LUMO levels are presented in Table 5.1.

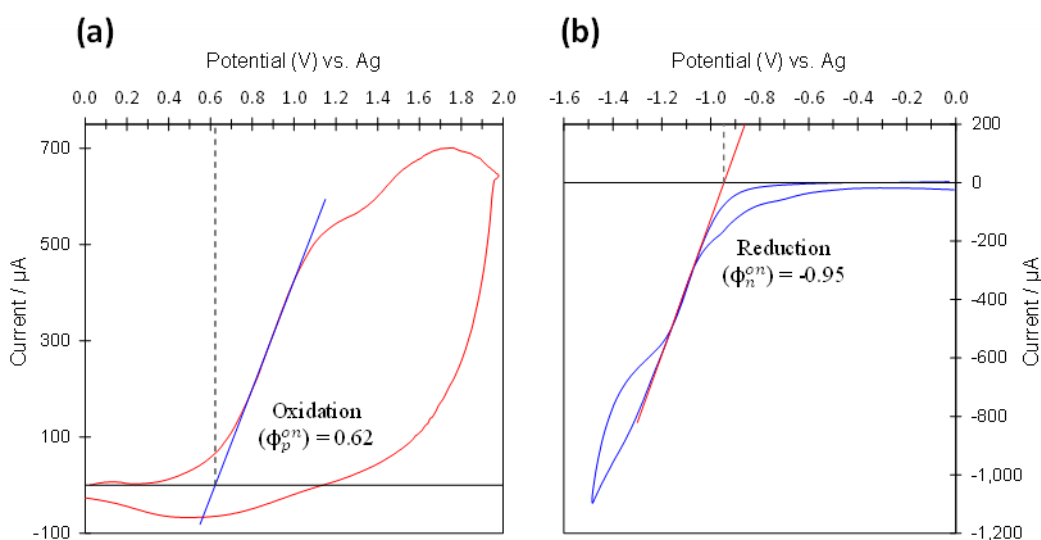


Figure 5.1: Cyclic voltammograms of pristine PBDTTT-EFT: (a) Oxidation potential of pristine PBDTTT-EFT, (b) Reduction potential of pristine PBDTTT-EFT.

Table 5.1: HOMO and LUMO parameters of materials.

Material	HOMO (eV)	LUMO (eV)	E_g (eV) [HOME – LUMO]
PBDTTT-EFT	-5.01	-3.44	-1.57
PC ₇₁ BM	-6.05	-4.00	-
PC ₆₁ BM	-6.10	-3.90	-
IC ₆₁ BA	-5.90	-3.67	-

The obtained HOMO and LUMO for PBDTTT-EFT and its calculated energy bandgap (E_g), corresponds well with what has been previously reported [42], [127], [130], [206]. The HOMO and LUMO levels of PC₇₁BM, PC₆₁BM and IC₆₁BA are taken from the manufacturer and reported literature [207]–[209].

5.2.2 Optical absorption

Optical absorption characteristics of the thin films can be extracted from their UV-Vis Spectrum. From which the optical energy band gap of PBDTTT-EFT is also calculated to be compared with the energy band gap obtained from electrochemistry experiment. The optical energy band gap (E_g^{opt}) can be calculated using Plank's equation:

$$E_g^{opt} (eV) = \frac{h \cdot c}{\lambda_{on}} \dots \dots \dots (7)$$

where, h is Plank's constant, c is the speed of light in a vacuum, and λ_{on} is the on-set wavelength obtained from the UV-Vis Spectrum. Optical absorbance spectrum of pristine PBDTTT-EFT, PC₇₁BM, PC₆₁BM, IC₆₁BA and spectral irradiance of 1.5 AMG (Air mass global) are presented in Figure 5.2.

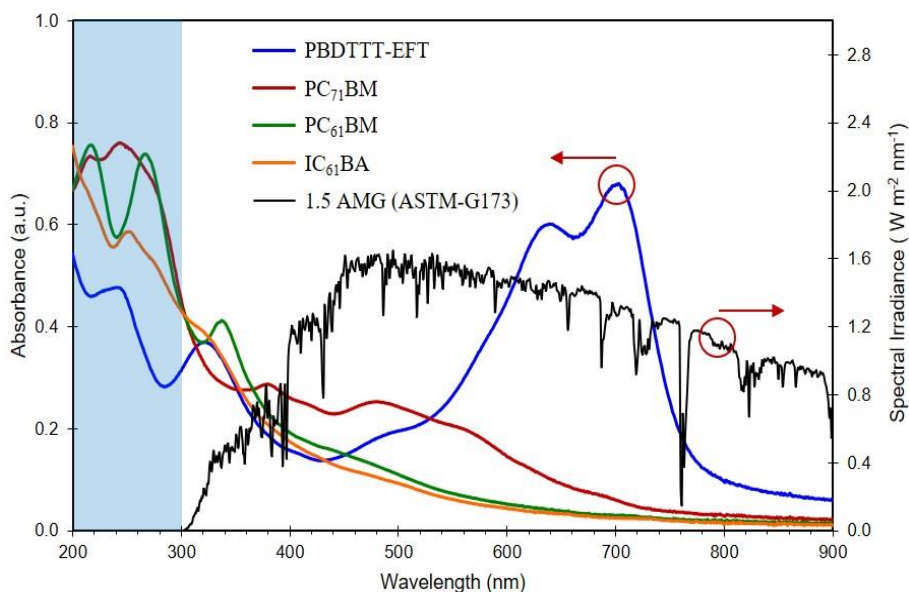


Figure 5.2: UV-Vis spectra of pristine PBDTTT-EFT, PC₇₁BM, PC₆₁BM, IC₆₁BA, and 1.5 AMG spectral irradiance.

The 1.5 AMG spectra irradiance is standardised by ‘American Society for Testing and Materials’ (ASTM) G-173 [210], [211]. This is the irradiance supplied by the solar simulator used throughout this project. As it can be seen from (ASTM-G173) spectrum, the irradiance power peaks around 450 – 500 nm and slowly decreases as the wavelength increases.

Therefore, to harvest most of this energy, the absorbance of an ideal donor material should cover regions of 450 – 800 nm. Since the solar simulator output irradiance is in the region of 300 – 900 nm any photocurrent generation analysis on the absorption spectrum has to be done for ≥ 300 nm. Figure 5.3 shows the absorption profile of pristine PBDTTT-EFT thin film with its two main peaks identified at 700 and 635 nm associated with backbone conjugation length and π - π stacking [212], [213]. It was also observed that the onset point of absorption is about 782 nm, which corresponds to 1.57 eV using Plank’s equation. Figure 5.4 illustrates the optical absorption for blend of PBDTTT-EFT polymer with different acceptor materials.

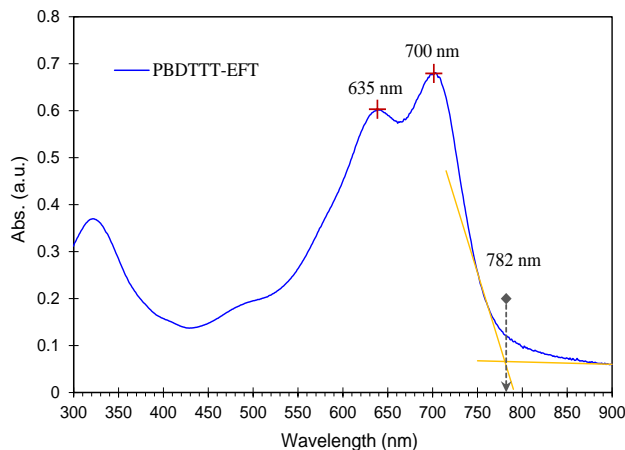


Figure 5.3: UV-Vis Spectrum of PBDTTT-EFT, illustrating its estimated optical absorption onset wavelength and its primary peak identifications.

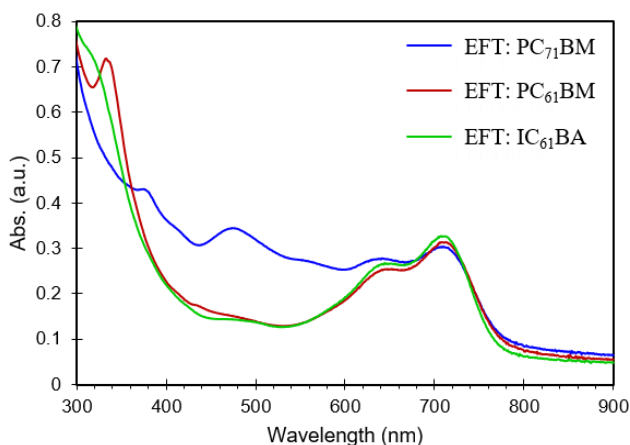


Figure 5.4: UV-Vis spectra of PBDTTT-EFT blended with PC₇₁BM, PC₆₁BM and IC₆₁BA.

As can be seen, the overall absorption area under EFT: PC₇₁BM spectrum is the highest compared to the other samples. This is due to the fact the PC₇₁BM has higher absorption 300 – 700 nm compared to PC₆₁BM and IC₆₁BA. It is also interesting to note that the peaks associated with PBDTTT-EFT at 635nm and 700nm have not shifted much, but their intensity is reduced depending on the acceptor material used. Thin film samples fabricated from EFT: IC₆₁BA show the least reduction in the peak intensities at 635 and 700 nm suggesting that IC₆₁BA had the least impact on the PBDTTT-EFT molecules backbone conjugation length and π - π structure. However, PC₇₁BM has had the most impact on the backbone structure of PBDTTT-EFT molecules. These observations and suggestions are discussed in detail in *section 5.3.10*, and crystallography data elucidate these suggestions.

5.2.3 Photoluminescence

In this section, PL spectra of the pristine materials, as well as their blend, were collected and characterised. The PL spectra were collected using a monochromatic excitation laser of 514 nm for surface probing. The spectra for pristine and their blend are illustrated in Figures 5.5 and 5.6. The process of PL spectroscopy was previously explained in Chapter 4, section 4.5.

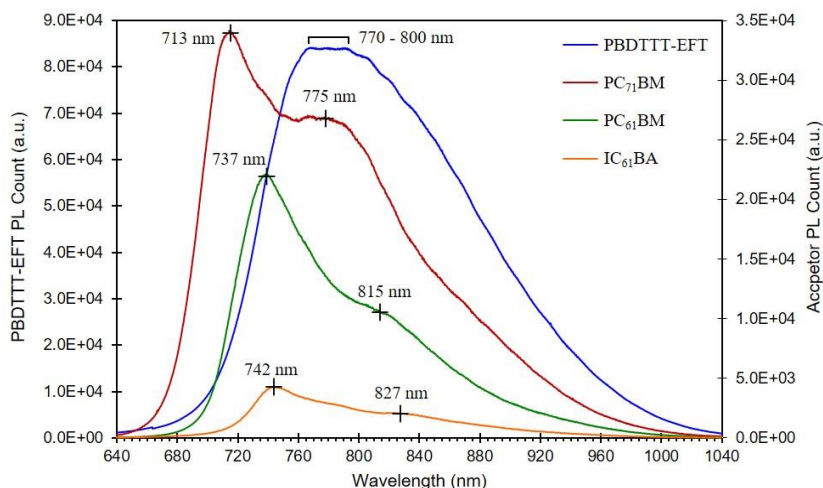


Figure 5.5: PL spectra of pristine PBDTTT-EFT, PC₇₁BM, PC₆₁BM, and IC₆₁BA under 514 nm excitation laser.

From Figure 5.5, it can be observed that the PL spectrum of PBDTTT-EFT has the highest PL count compared to the acceptor materials. This is expected since PBDTTT-EFT as the donor material is the absorbing layer. Photoluminescence phenomena occurs from recombination of generated excitons which do not dissociate. If the generated excitons are not dissociated, they will recombine and lead to a rise in the PL count. The PL spectrum profile of individual materials can be used to identify and characterise them. The spectrum profile of pristine PBDTTT-EFT has a broad peak with a flat PL emission in the region of 770 – 800 nm. On the contrary, PL spectrum profile of the fullerene derivative acceptor materials all shows a peak and a hump.

For PC₇₁BM peak and hump around 713 nm and 775 nm respectively, PC₆₁BM peak and hump around 737 nm and 815 nm and IC₆₁BA with a peak and hump around 742 and 827 nm respectively. Apart from the difference between the peak and hump position of each individual acceptor material, the PL emission levels are also different; With PC₇₁BM having the highest PL count amongst the three samples. This observation can be related to the fact that PC₇₁BM has the highest absorption amongst

the three acceptor materials at 514 nm wavelength, as is evident in Figure 5.4. To understand the impact of D:A blend and its importance for charge dissociation, the PL spectra profile for blends of PBDTTT-EFT with PC₇₁BM, PC₆₁BM and IC₆₁BA are collected and presented in Figure 5.6.

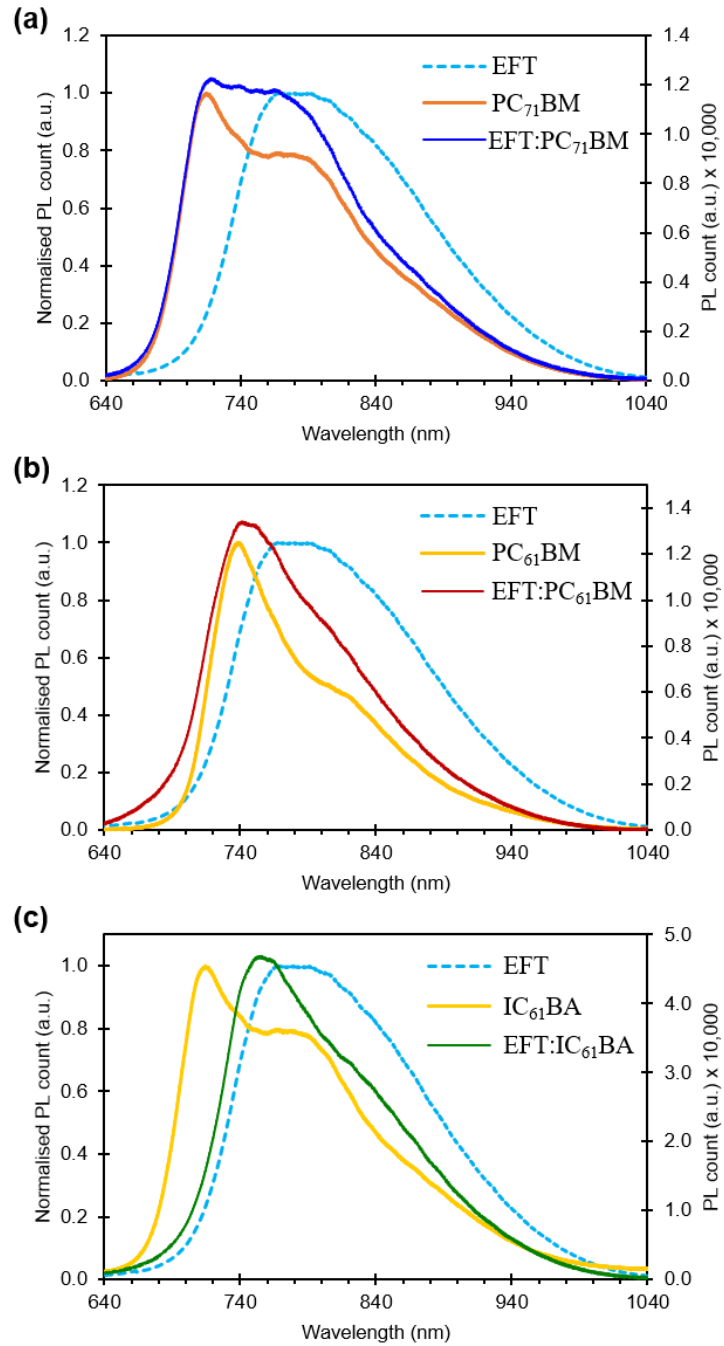


Figure 5.6: Normalised PL spectrum of pristine PBDTTT-EFT, PC₇₁BM, PC₆₁BM, IC₆₁BA and the PL intensity of (a) PBDTTT-EFT: PC₇₁BM, (b) PBDTTT-EFT: PC₆₁BM, (c) PBDTTT-EFT: IC₆₁BA.

The PL spectrum intensity of the pristine material is normalised in order to see the line profile overlap between the blend and pristine thin films. From all the blended PL spectra it can be seen that the PL count is reduced compared to their pristine films. Blend of PBDTTT-EFT: PC₆₁BM shows the most quenched PL spectrum profile amongst the three samples followed closely by PBDTTT-EFT: PC₇₁BM, suggesting a good donor/acceptor interface. However, PBDTTT-EFT: IC₆₁BA has not quenched as much, which could indicate that the donor/acceptor interface is not as good as the other samples.

When looking at the PL emission profile line of each blended thin film, it is noticed that PBDTTT-EFT: PC₆₁BM sample shows the most similarity to pristine PC₆₁BM emission profile (*see Figure 5.6b*). On the contrary, the spectrum profile of PBDTTT-EFT: IC₆₁BA sample shows similarity to pristine PBDTTT-EFT emission profile (*see Figure 5.6c*). However, the PL spectrum profile of PBDTTT-EFT: PC₇₁BM sample is in-between pristine PC₇₁BM and PBDTTT-EFT emission profiles with a flat region (720 – 770 nm) similar to pristine PBDTTT-EFT (*see Figure 5.6a*). Since PL spectroscopy is a surface probing technique, these observations suggest that PBDTTT-EFT: PC₆₁BM samples tend to have more of PC₆₁BM molecules present on the thin film surface. In contrast the PL spectrum profile of PBDTTT-EFT: IC₆₁BA samples it is suggested that there is more of PBDTTT-EFT molecules on the fabricated thin film surface; and the spectrum profile of PBDTTT-EFT: PC₇₁BM samples suggests that there is a balanced mixture of both PC₇₁BM and PBDTTT-EFT molecules on the thin film surface.

5.2.4 Raman Spectroscopy

In this section, the Raman spectra of each pristine material are investigated and characterised. It is important to note that in Raman spectroscopy the excitation laser and the laser intensity applied would have an impact on the collected results. In an ideal case, the material is analysed under resonant Raman spectroscopy. The simple definition of resonant Raman spectroscopy would mean that the excitation laser used for Raman spectroscopy should match with the maximum absorption of the material [214]–[216]. For example, PBDTTT-EFT has a maximum optical absorption peaking at 700 nm (see Figure 5.3); therefore, to obtain Raman data under resonant condition

an excitation laser with a wavelength of 700 nm should be employed. Unfortunately, the Raman microscope used for this project is only equipped with two sets of monochromatic excitation lasers of 514 nm and 785 nm. Figure 5.7 illustrates the position of the employed excitation lasers with respect to the materials absorbance spectrum.

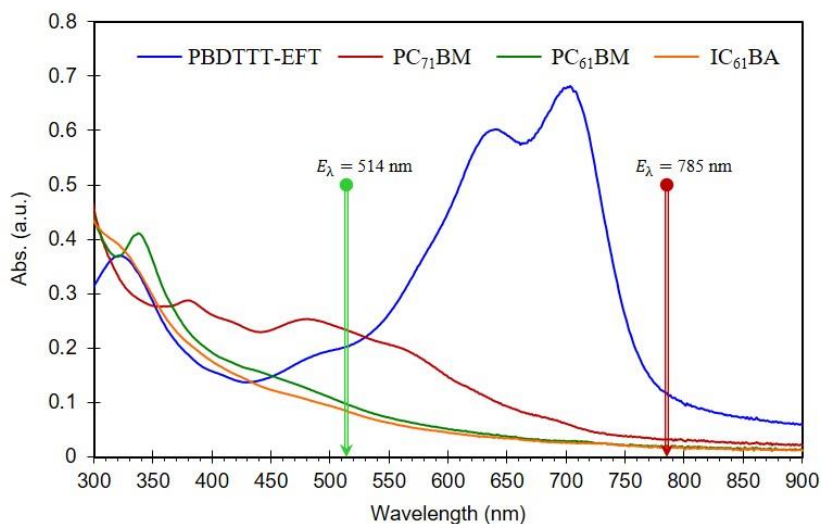


Figure 5.7: UV-Vis spectra of pristine materials with Raman excitation laser wavelengths indication.

As is evident in Figure 5.7, when using 785 nm excitation laser, only PBDTTT-EFT molecules would be excited (high laser power must be used), and the acceptor materials should not show any profile. However, if a 514 nm laser is used, both donor and acceptor materials should produce a Raman spectrum profile. It is important to note that the absorbance of PC₇₁BM at 514 nm is higher than PBDTTT-EFT, and this could have an impact when Raman spectrum of D:A blends are collected under the 514nm laser. The Raman spectrum of pristine PBDTTT-EFT collected under 514 nm, and 785 nm excitation laser is illustrated in Figure 5.8.

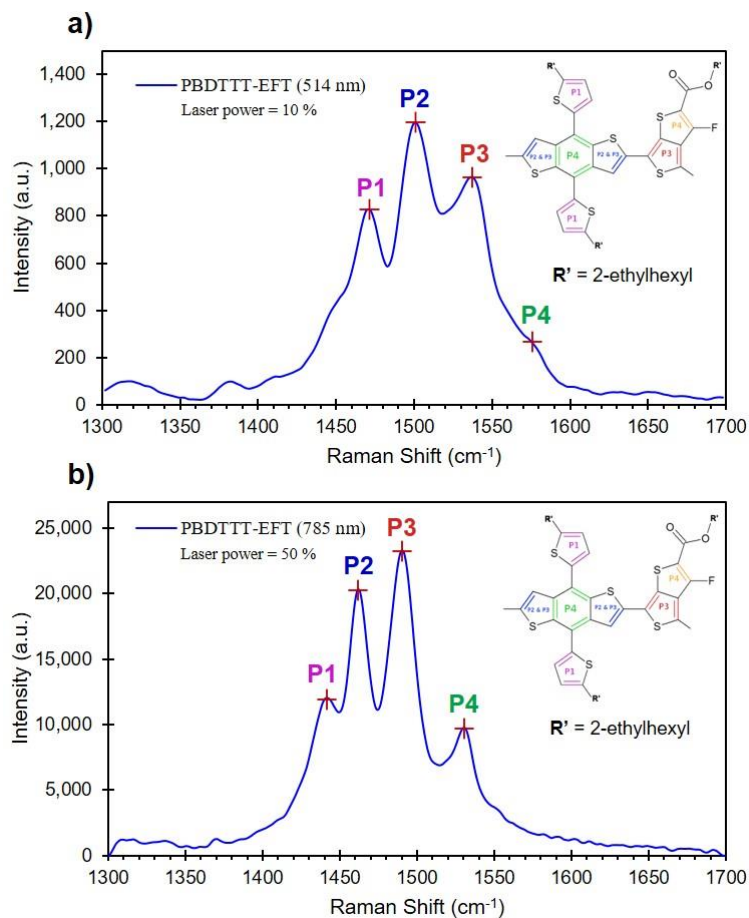


Figure 5.8: Raman spectrum of pristine PBDTTT-EFT under laser excitation wavelength of 514 nm (a) and 785 nm (b), with inset: PBDTTT-EFT molecular structure with bond vibrations numbered accordingly to the peaks in the spectrum profile.

As can be seen, PBDTTT-EFT has a unique “fingerprint” for both excitation wavelengths. It should be noted that when the excitation laser of 785 nm was used, the laser power intensity needed to be increased in order to obtain a spectrum. This is due to the fact that the absorption of PBDTTT-EFT at 785 nm is very low, therefore stronger laser intensity is required in comparison to 514 nm laser. The Raman peaks are assigned using numeric and colour coding system (P1 – P4). Using Raman vibration mode handbooks, the peaks were assigned to the nature of their chemical bonds, which are listed below [49], [217]:

- P1 at ~ 1440 cm^{-1} C=C stretching mode of thiophenes attached to BDT unit as a side chain (Purple).

- P2 at $\sim 1462 \text{ cm}^{-1}$ C=C stretching mode of the thiophenes fused to the benzene ring in the BDT unit (Blue).
- P3 at $\sim 1490 \text{ cm}^{-1}$ C=C stretching mode of (Blue) coupled to (Red) non-fluorinated thiophene in the TT unit.
- P4 at $\sim 1530 \text{ cm}^{-1}$ quadrant stretching mode of the Benzene ring in BDT (Green) coupled to the C=C stretching mode of the fluorinated thiophene in the TT unit (Orange).

Similarly, Raman spectra of fullerene derivative acceptor materials were collected for using both 514 nm and 785 nm excitation lasers and presented in Figure 5.9. However, as it can be seen from Figure 5.9b, there is no ‘fingerprint’ spectrum for any of the acceptor materials when a 785 nm laser is employed. This is because these materials do not absorb any energy at 785 nm wavelength, and therefore, they are not Raman active under 785 nm excitation laser. The main peak(s) observed for the pristine PC₇₁BM, PC₆₁BM and IC₆₁BA under 514 nm excitation laser are assigned as follow:

- PC₇₁BM peak at $\sim 1570 \text{ cm}^{-1}$ assigned to anti-symmetric C=C stretching mode [213], [218]–[220].
- PC₆₁BM peak at $\sim 1460 \text{ cm}^{-1}$ assigned to symmetric C=C stretching mode [221], [222].
- ICBA peak at $\sim 1460 \text{ cm}^{-1}$ assigned to symmetric C=C stretching mode [216], [221], [223].

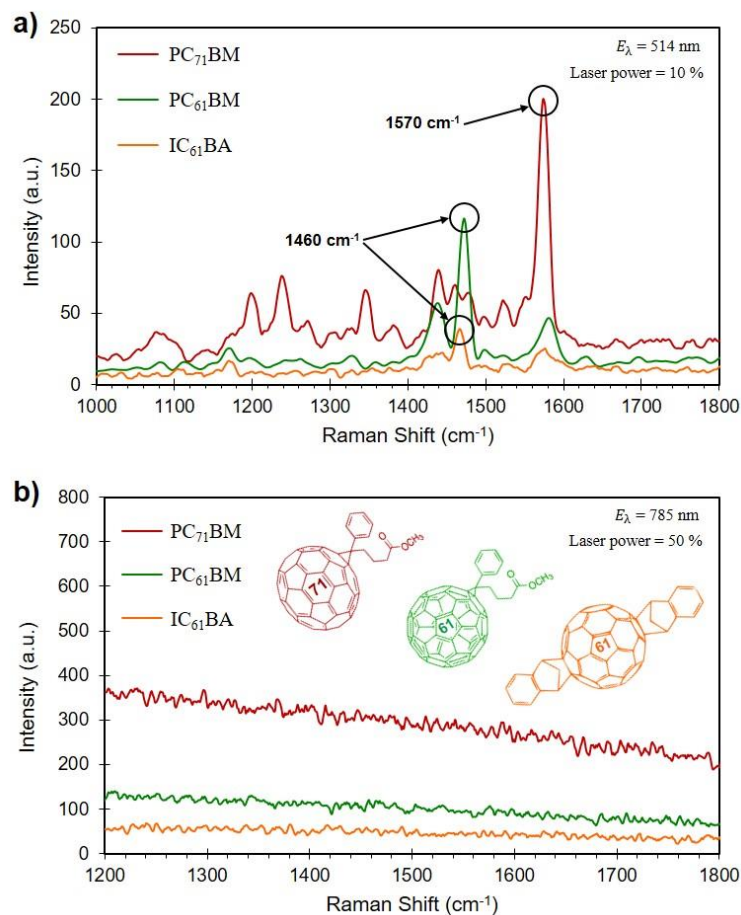


Figure 5.9: Raman spectra of pristine PC₇₁BM, PC₆₁BM, and IC₆₁BA under (a) 514 nm excitation laser, (b) 785 nm excitation laser, inset: 2D molecular structure of the acceptor materials.

5.2.5 Molecular structure (GIXRD)

OOP GIXRD diffractograms of pristine materials were collected by fabricating a thin film of pristine material from a solution of 10 mg mL⁻¹ onto a quartz substrate to give a film thickness of ~100 nm. To find the best incident angle of the X-ray beam, PC₇₁BM, which is a well-known material, was chosen as a pilot study. The different incident angle of the X-ray beam was applied to the thin film sample, and the obtained diffractograms are presented in Figure 5.10.

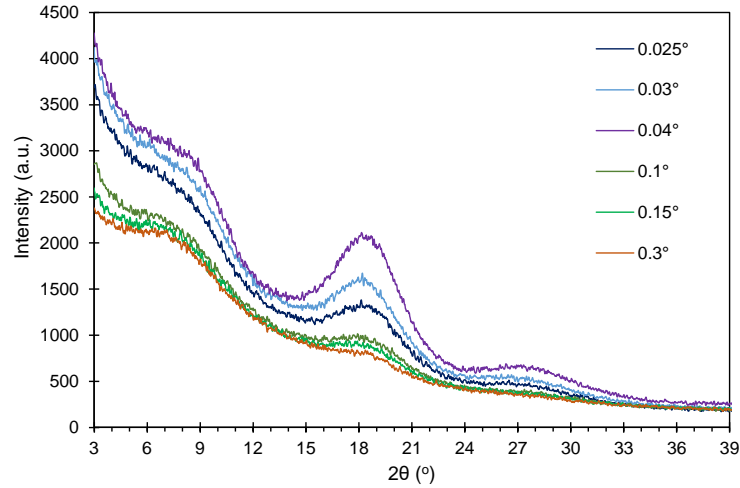


Figure 5.10: OOP GIXRD diffractograms of pristine PC₇₁BM film coated onto a quartz substrate, with the different incident angle of the X-ray beam.

As it can be seen from Figure 5.10, the best incident angle is at 0.04°. Based on this observation, all of the OOP GIXRD diffractograms collected in this project will have an X-ray incident angle of 0.04°. Since the prepared samples are fabricated onto the quartz substrate, OOP GIXRD of the clean quartz substrate is also collected at an incident angle of 0.04°. The obtained diffractograms for the clean quartz substrate and pristine PC₇₁BM film coated onto the quartz substrate, are illustrated in Figure 5.11.

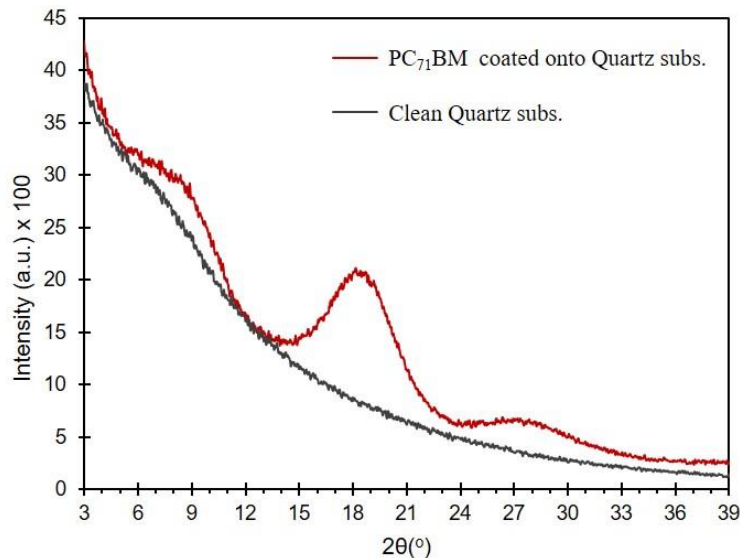


Figure 5.11: OOP GIXRD diffractograms of pristine PC₇₁BM film coated onto quartz substrate and clean quartz substrate at an incident angle of 0.04°.

By subtracting the diffractogram profile of the PC₇₁BM thin film coated onto the substrate from the profile of clean quartz substrate; just the profile of PC₇₁BM can be obtained. This is illustrated in Figure 5.12.

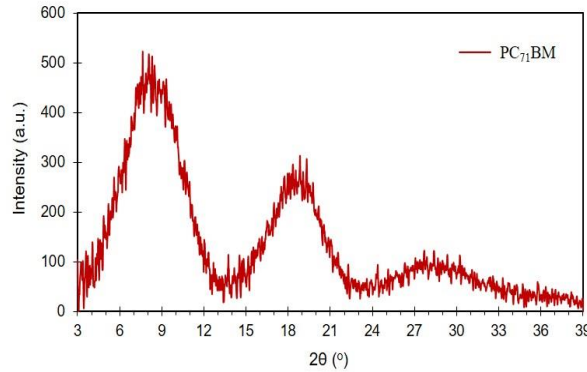


Figure 5.12: OOP GIXRD of the pristine PC₇₁BM thin film after background removal of the quartz substrate.

As it can be seen from Figure 5.12, the remaining diffractogram profile is purely the profile of the fabricated thin film, in this case thin film of pristine PC₇₁BM. The profile of the clean quartz substrate was added to the computer software used for GIXRD data acquisition, so all the obtained OOP GIXRD diffractogram profiles will be presented after subtraction of this profile. Computer-based software models were also used to provide the tools necessary to do a ‘curve-fit’ on the collected diffractogram profiles. *Gaussian* and *Lorentzian* curve fit methods were employed to generate a computer model of each diffractogram profile with the best curve-fit match. These computer-generated models, as well as the diffractogram data for pristine materials, are presented in the Figures 5.13 & 5.14.

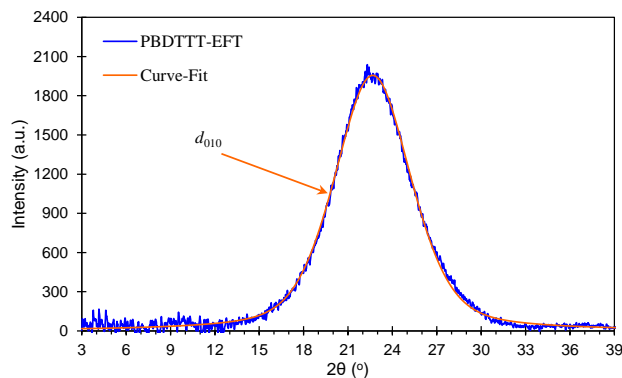


Figure 5.13: OOP GIXRD diffractogram of pristine PBDTTT-EFT films and its corresponding computer-generated a curve fit for the d_{010} plane.

Figure 5.14, illustrates the thin film diffractogram profile of pristine PBDTTT-EFT and the computer generated a curve fit corresponding to its d_{010} plane, indicating that PBDTTT-EFT is predominantly in a *Face-on* orientation [40], [42]. Similarly, diffractograms and curve fits of pristine acceptor materials are illustrated in Figure 5.14.

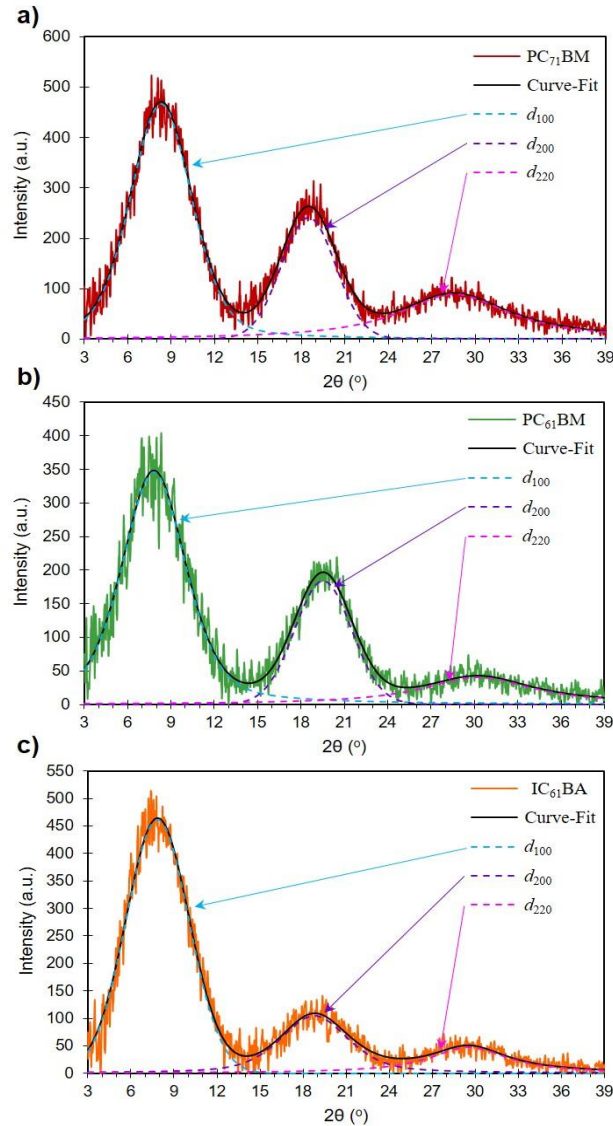


Figure 5.14: OOP GIXRD diffractogram of pristine acceptor material films and their corresponding computer generated curve fit (a) PC₇₁BM with its individual planes, (b) PC₆₁BM with its individual planes, (c) IC₆₁BA with its individual planes.

Table 5.2 presents the parameters extracted from computer-generated profiles, matching the collected diffractograms. The planes assigned for each material has been previously reported in the literature [40], [193], [195], [224]–[227].

Table 5.2: OOP GIXRD parameters extracted from the computer-generated curve-fits for pristine materials.

Material	Plane	2θ ($^\circ$)	d (\AA)	FWHM ($^\circ$)	L_c (\AA)	Intensity (a.u.)
PBDTTT-EFT	d_{010}	22.69	3.91	5.65	14.34	1955.5
PC ₇₁ BM	d_{100}	8.30	10.64	5.03	15.83	466.8
	d_{200}	18.49	4.79	4.42	18.20	240.6
	d_{220}	28.55	3.12	9.30	8.81	89.3
PC ₆₁ BM	d_{100}	7.81	11.31	5.21	15.28	346.0
	d_{200}	19.53	4.54	4.65	17.33	183.6
	d_{220}	30.25	2.95	9.32	8.83	40.8
IC ₆₁ BA	d_{100}	7.85	11.25	5.15	15.46	460.9
	d_{200}	18.78	4.72	5.61	14.35	104.9
	d_{220}	29.54	3.02	6.55	12.54	47.3

In the OOP mode, only the d_{010} plane can be observed for PBDTTT-EFT, which is assigned to the π - π stacking / Face-on orientation of the polymer [40]. The d-spacing between the molecules is calculated using *Bragg's Law*, and it is measured in angstrom (\AA), similarly, the coherence length (average crystal/grain size) is calculated using *Scherrer's equation* (Equation 41). The intensity values are correlated to the overall number of molecules in the selected plane [49], [50]. Figure 5.15 illustrates a schematic diagram in which the intensity is used as an indication of total molecules in a selected plane.

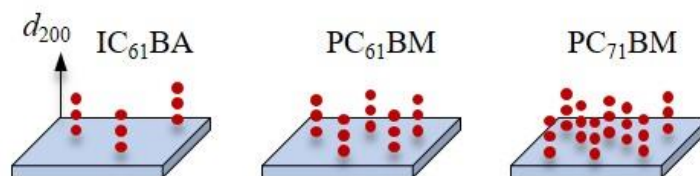


Figure 5.15: Schematic diagram of the d_{200} plane for pristine acceptor materials, illustrating the correlation of GIXRD intensity and the overall number of molecules in that plane.

The d_{200} plane for fullerene derivative materials is assigned as a measure of the vertical molecule segregation [49], [50]. As can be seen from the data in Table 5.2 and Figure 5.15, as the intensity associated with the d_{200} plane is increased, the number of acceptor molecules stacked in vertical direction would also increase. Therefore, by analysing

this parameter, important information about the nanostructure of each acceptor material can be obtained.

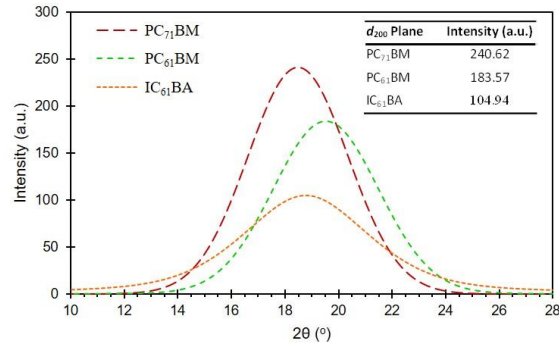


Figure 5.16: Extracted d_{200} curves from the computer-generated a fit model for different pristine acceptor materials, with intensity parameter as an inset.

As it can be seen from the data presented as the inset of Figure 5.16, PC₇₁BM has the highest vertical stacking/segregation along the d_{200} plane, followed by PC₆₁BM and IC₆₁BA.

5.3 Device Performance Enhancement

In this section, organic solar cell devices based on PBDTTT-EFT polymer are fabricated using various methods and techniques to enhance device performance. An overview of the different techniques/experimental studies applied, are shown as a flow chart diagram in Figure 5.17. Experimental studies 1 – 8 are the initial pilot studies to optimise sample / device preparation. Experiments 9 and 10 are more in-depth studies which are the main focus of this PhD thesis. The full detail of each experiment will be later discussed.

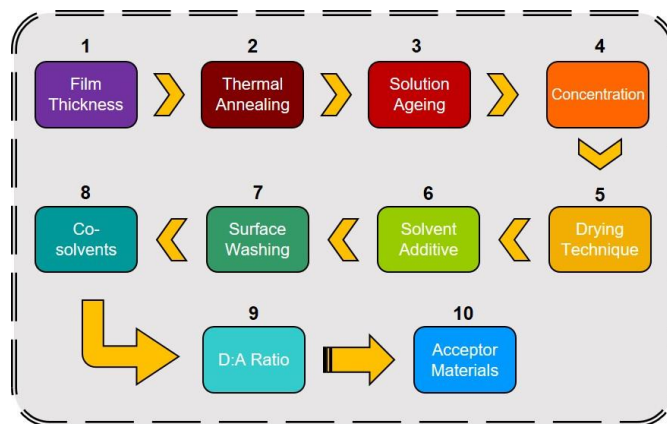


Figure 5.17: Schematic workflow diagram of experiments performed to identify the most optimised device generating the highest PCE.

5.3.1 Active Layer Film Thickness

The film thickness of the active layer for organic solar cell fabrication is an important parameter which needs to be tuned to obtain efficient charge dissociation and transport [53], [142]. The tuned film thickness is dependant on the materials used to form a D:A blend for the active layer. Therefore, a series of devices with different active layer film thickness were fabricated and tested to determine the optimum thickness. The sample preparation and fabrication procedures were previously discussed in *Chapter 4, section 4.2*. Different active layer film thickness was achieved by varying the spin-coating speed, and it was determined using the stylis profile meter. Table 5.3 presented the film thickness obtained for variable spin speeds. Each sample cooperates three devices and their averaged J-V characteristics under illumination are presented in Figure 5.18.

Table 5.3: Spin coating speeds corresponding to film thickness for a fixed period of time.

Spin speed (RPM)	Spin time (s)	Thickness (nm)
400	16	135
500	16	110
600	16	98
700	16	85
900	16	70

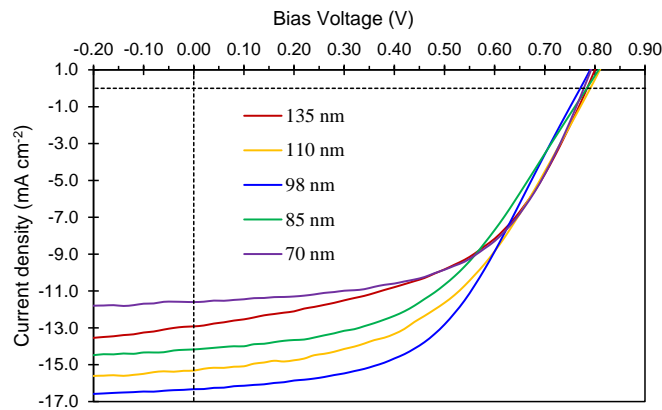


Figure 5.18: PBDTTT-EFT: PC₇₁BM J-V characteristics of averaged OSC devices of samples with different film thickness.

As can be seen from the J-V curves in Figure 5.18, the current density increases with a decrease in the active layer film thickness up to 98 nm. Any further reduction of the film thickness will also reduce the current density generated from the devices. In order

to understand the impact of active layer film thickness on the device performance, DC electrical parameters are extracted from the J-V curves and are presented in Table 5.4. Table 5.4: Electrical parameters extracted from averaged J-V curves for samples with different active layer film thickness.

Thickness (nm)	J_{sc} (mA cm ⁻²)	V_{oc} (V)	FF	PCE (%)	R_s (Ω cm ²)	R_{sh} (Ω cm ²)
135	12.91	0.78	0.50	5.03	16.70	252.66
110	15.29	0.79	0.48	5.84	19.68	366.44
98	16.34	0.78	0.51	6.41	19.63	470.15
85	14.17	0.78	0.48	5.33	23.57	419.87
70	11.59	0.78	0.56	5.08	15.04	719.96

As is evident from Table 5.4, the J_{sc} value increases as active layer film thickness decreases and reaches a maximum point at a film thickness of 98 nm. By further reducing the film thickness, J_{sc} value will also. In contrast, V_{oc} does not vary as the film thickness changes, indicating that the V_{oc} parameter is independent of this variation. However, the FF parameter is highest for devices with an active layer of 70 nm, suggesting that these devices provide good charge dissociation and transport as it can also be seen from the series (R_s) and shunt (R_{sh}) resistance values. Although the optimum FF value is for devices with an active layer of 70 nm, their PCEs are not. Instead, PCE follows the same trend as J_{sc} , with the highest PCE of 6.41 % for devices with an active layer film thickness of 98 nm. Therefore, from this study, it can be concluded that the most optimised device performance, are devices with an active layer film thickness of ~100 nm.

5.3.2 Post-thermal Annealing

It has been reported in the literature that post-thermal annealing technique enhances the performance of organic solar cells based on P3HT: PC₆₁BM [38]. Therefore, the impact of post-thermal annealing is investigated for OSC devices with an active layer of PBDTTT-EFT: PC₇₁BM. Fabricated devices were exposed to different post thermal annealing ranging from 50° – 150°C for a period of 10 min at steps of 25°C and after each step, their I-V characteristics under 1 sun illumination were collected. The initial test was for room temperature (25°C). The averaged J-V characteristic curves are

illustrated in Figure 5.19, and their extracted DC electrical parameters are presented in Table 5.5.

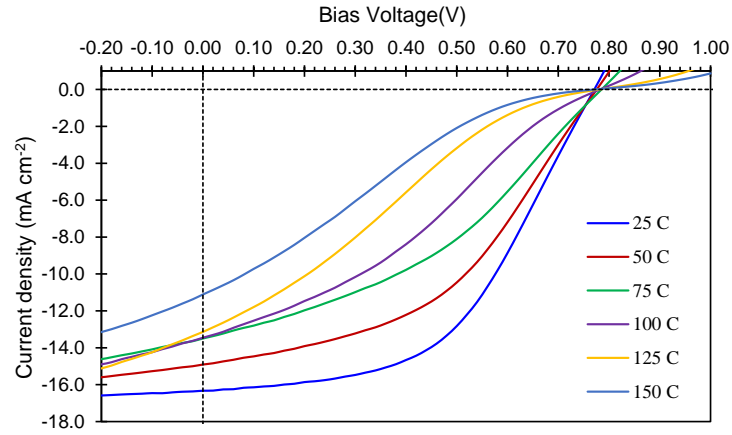


Figure 5.19: J-V characteristics of averaged OSC devices of PBDTTT-EFT: PC₇₁BM for post thermal annealing from 25°C – 150°C in steps of 25°C (10 min at each step).

Table 5.5: Electrical characteristic parameters extracted from averaged J-V curves for post thermal annealing ranging from 25°C – 150°C in steps of 25°C.

Temperature (°C)	J _{sc} (mA cm ⁻²)	V _{oc} (V)	FF	PCE (%)	R _s (Ω cm ²)	R _{sh} (Ω cm ²)
25	16.34	0.78	0.51	6.41	19.62	470.05
50	14.92	0.78	0.45	5.24	25.41	227.06
75	13.50	0.79	0.38	4.08	35.45	128.90
100	13.46	0.78	0.32	3.36	76.76	104.77
125	13.13	0.78	0.24	2.42	201.07	69.27
150	11.12	0.77	0.21	1.82	346.37	67.78

As can be seen in Figure 5.19, upon applying heat to the sample, the J_{sc} value starts to decrease, and it continues to decrease as the temperature of post-thermal annealing increases. It can also be seen that beyond 50°C, the J-V profile curve starts to form an S-shape, and it gets more profound at higher temperatures. As is evident from the data in Table 5.5, J_{sc} and FF are reduced significantly as the devices are exposed to thermal annealing. J_{sc} seems to negatively saturate between 75 – 125°C and further decrease significantly above 125°C. From Figure 5.19, the formation of S-shape can be observed on the J-V characteristic curves for temperatures >100°C. Although Oklobia, O, et al. [60] reported that post thermal annealing as a technique would enhance the device performance of P3HT: PC₆₁BM at 150°C, the formation of S-shape has also been observed when devices were annealed above 200°C.

It has been suggested that the formation of *S-shape* in J-V characteristic curve could rise from poor interface between the active layer surface and the cathode as a result of acceptor material aggregation [228]–[230].

From the reported studies on post thermal annealing, formation of PC₇₁BM molecular aggregation was detected from the optical absorption spectrum of the annealed samples, by associating the reduction in the absorption intensity of the PCBM region (200-300 nm) [231]. Using similar method as suggested in the literature, optical absorption of thermally annealed samples for blend of PBDTTT-EFT: PC₇₁BM were collected and illustrated in Figure 5.20.

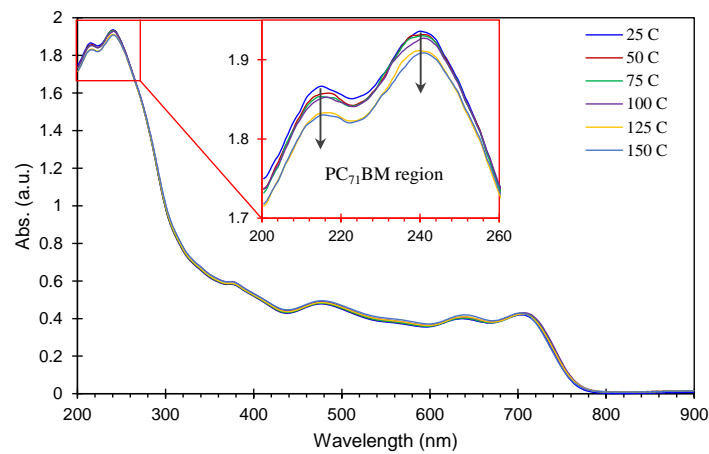


Figure 5.20: UV-Vis spectra of PBDTTT-EFT: PC₇₁BM upon post thermal annealing from 25 – 150°C in steps of 25°C, [inset: indicating the reduction of Abs. in the PC₇₁BM region (200 – 260 nm)].

As can be seen from Figure 5.20 inset, the absorption intensity in the region of 200 – 300 nm, associated with PC₇₁BM is reducing upon thermal annealing above >100°C. Suggesting the formation of PC₇₁BM cluster above 100°C, which matches with the initiation of *S-shape* formation of J-V curves in Figure 5.19. These observations are in good agreement with reported literature for fullerene derivative molecules undergoing post thermal annealing [38], [60], [83], [175].

From these observations it can be suggested that upon post thermal annealing of PBDTTT-EFT: PC₇₁BM devices, the PC₇₁BM molecules initiate a cluster formation and aggregate; leading to poor D:A interface which impacts the charge dissociation and transport. The shunt resistance (R_{sh}) is associated with the leakage current of the device; therefore, the reduction observed in this parameter is evidence of poor charge transport and collection (Table 5.5). Similarly FF and R_s parameters are also decreasing upon annealing, indicating that poor D:A interface and charge extraction

takes place for annealed devices. Therefore, post-thermal annealing has shown negative results in enhancing the device performance, and this method will not be further investigated nor used in this PhD project.

5.3.3 Solution Ageing

In this study, the impact of elapsed time from making an active blend solution of PBDTTT-EFT: PC₇₁BM on device performance is investigated. This experiment is referred to as ‘Solution Ageing’ in this work. Three samples (24hrs, 48hrs and 72hrs) are prepared to investigate the impact of blending time after mixing PBDTTT-EFT with PC₇₁BM on the device performance. Until now, the solution ageing time has been 24hrs. The averaged J-V characteristic curves are illustrated in Figure 5.21, and their corresponding extracted electrical parameters are presented in Table 5.6.

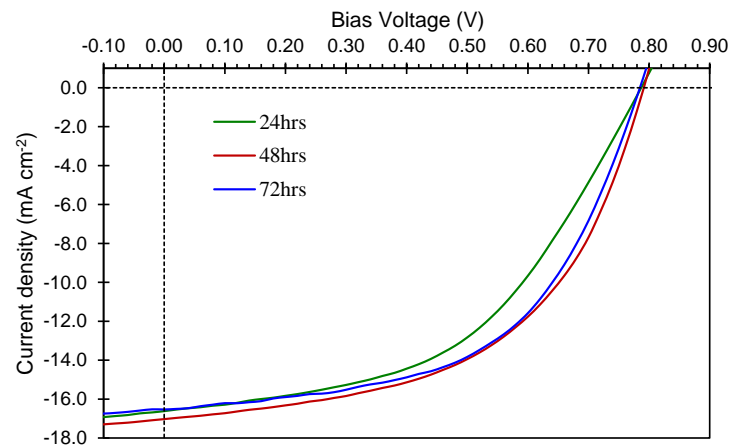


Figure 5.21: J-V characteristics of averaged PBDTTT-EFT: PC₇₁BM, indicating elapsed time for a blended active solution since it was made.

Table 5.6: Electrical characteristic parameters extracted from averaged J-V curves for different active solution ageing.

Blending Time	J _{sc} (mA cm ⁻²)	V _{oc} (V)	FF	PCE (%)	R _s (Ω cm ²)	R _{sh} (Ω cm ²)
24hrs	16.62	0.79	0.49	6.42	17.46	404.66
48hrs	17.03	0.79	0.53	7.17	10.36	357.88
72hrs	16.52	0.78	0.55	7.10	11.18	398.63

As is evident from Table 5.6, devices which had to be fabricated from samples of 48hrs ageing, show the best performance with improved PCE of 7.17 %. There is not

much of a difference in performance enhancement (PCE) between 48hrs and 72hrs aged solutions.

The improvement of device performance for 48hrs and 72hrs aged solutions compared to 24hrs is believed to be as a result of better dissolving of the materials in the solvent. From the extracted electrical parameters presented in Table 5.6, it is evident that the FF parameter is improving as the solution is aged. This suggests that the PBDTTT-EFT and PC₇₁BM molecules are well dissolving and intermixing. However, J_{sc} parameters peak for samples that are aged 48hrs, after which, start to deteriorate. This is believed to be due to the breakdown of PBDTTT-EFT molecule's conjugation length. The relationship between the conjugation length and J_{sc} for PBDTTT-EFT molecules has been reported in the literature [232]. Therefore, all the solution samples prepared from this study onwards will all be aged between 48hrs – 72hrs prior to being used for fabrication.

5.3.4 Solution Concentration

In this study, the impact of active solution concentration is investigated. All the OSC devices fabricated up to this study, were based on a concentration of 15 mg mL⁻¹. Therefore, it is crucial to find the optimum active solution concentration to possibly maximise the PCE of the OSC devices. Three different active solution concentrations are prepared to be investigated; 15mg mL⁻¹, 25mg mL⁻¹ and 35mg mL⁻¹. The collected average J-V characteristics curves are illustrated in Figure 5.22, and the extracted electrical parameters are presented in Table 5.7.

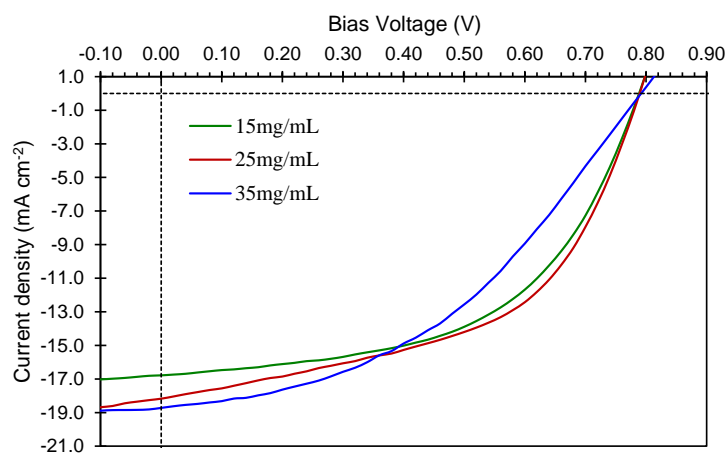


Figure 5.22: J-V characteristics of PBDTTT-EFT: PC₇₁BM with different active solution concentration.

Table 5.7: Electrical characteristic parameters extracted from averaged J-V curves for different active solution concentrations.

Concentration (mg mL ⁻¹)	J _{sc} (mA cm ⁻²)	V _{oc} (V)	FF	PCE (%)	R _s (Ω cm ²)	R _{sh} (Ω cm ²)
15	16.78	0.79	0.54	7.13	11.81	395.86
25	18.16	0.79	0.53	7.49	9.89	253.51
35	18.72	0.79	0.43	6.30	21.15	328.57

As can be seen from Figure 5.22, upon increasing the concentration of the active solution, the current density (J_{sc}) also increases accordingly. However, the curve profile shape starts to deviate from an ideal I-V characteristic curve. Electrical parameters presented in Table 5.7, confirms the observation made on the increase of J_{sc} value upon increasing the concentration of the active solution. This is due to an increase in the amount of donor and acceptor material present in the active layer.

Therefore, the higher the concentration, the more PBDTTT-EFT molecules, the higher the J_{sc}. However, the FF parameter does not follow the same trend, and it starts to decrease, resulting in a seesaw action with J_{sc}, which impacts the PCE. Reduction trend of FF parameter is believed to be due to the oversaturation of the sample as the concentration gets higher, and the dissolvability of the D/A material becomes more challenging at higher concentrations; leading to larger separated phase domains. For solutions with 25mg mL⁻¹, the increase in J_{sc} parameter compensates the reduction in FF, resulting in an overall device performance enhancement. Therefore, from this case study it can be concluded that the concentration of 25 mg mL⁻¹ is the most optimised concentration which will be used from now on in this PhD project.

5.3.5 Active layer drying technique

The structural formation of molecules within the active layer after fabrication would play an essential role in the overall performance of OSC devices. The solidification of the wet spin-cast film will directly govern the morphological and nanoscale domains within the active layer. Therefore, determining the optimum technique for drying the active layer is essential in device optimisation. In this study, the wet fabricated active layer will undergo different drying techniques to identify the most optimised technique

for PCE enhancement. Three setups have been designed to find the optimum technique for drying the active layer:

1. Natural drying under a N₂ environment for 30 min. (Currently employed).
2. Solvent vapour annealing (SVA) using ODCB for 5 min, prior to natural drying (N₂ for 30 min.).
3. Rapid drying of the wet film by placing the spin-cast film under vacuum pressure at -100 kPa for 5 min.

The experiment setup for each technique is illustrated a schematic diagram in Figure 5.23.

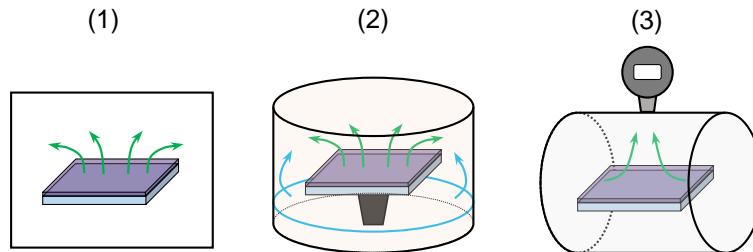


Figure 5.23: Schematic diagram of different active layer drying techniques: (1) Natural drying under N₂ environment for 30 min., (2) SVA under ODCB solvent (Blue lines) for 5 min. in closed chamber, (3) Rapid drying under a vacuum pressure of -100 kPa for 5 min. in a vacuum chamber.

Samples are dried accordingly (1 – 3) and then transferred into a thermal vacuum chamber for electrode deposition. The collected averaged J-V characteristic curves under illumination are illustrated in Figure 5.24, and their extracted electrical parameters are presented in Table 5.8.

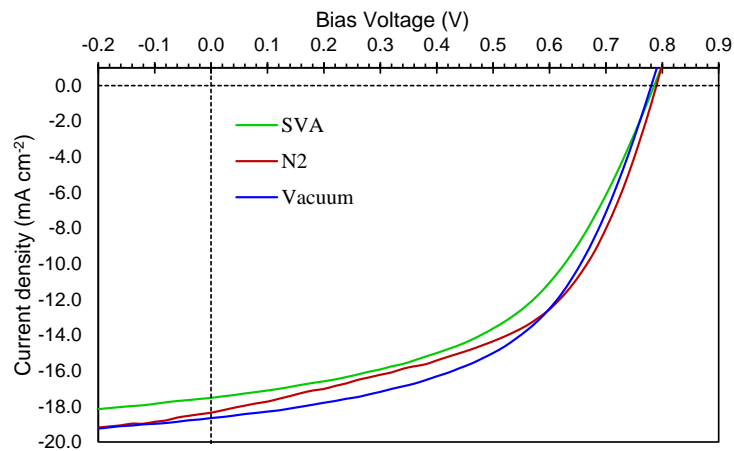


Figure 5.24: J-V characteristics of PBDTTT-EFT: PC₇₁BM devices with different drying techniques of the active layer.

Table 5.8: Electrical parameters extracted from averaged J-V curves for different active layer drying technique.

Drying Technique	J_{sc} (mA cm ⁻²)	V_{oc} (V)	FF	PCE (%)	R_s (Ω cm ²)	R_{sh} (Ω cm ²)
SVA	17.52	0.79	0.50	6.92	12.99	310.82
N ₂	18.34	0.79	0.52	7.56	10.82	251.91
Vacuum	18.67	0.79	0.53	7.69	10.23	304.96

As can be seen from Figure 5.24 and the extracted electrical parameters in Table 5.8, the performance of OSC devices is enhanced as the drying time of wet active layer is reduced, with vacuum drying technique achieving the highest PCE of 7.69 %. In order to determine the reason for this behaviour, the optical absorption spectrum of each sample is collected and illustrated in Figure 5.25.

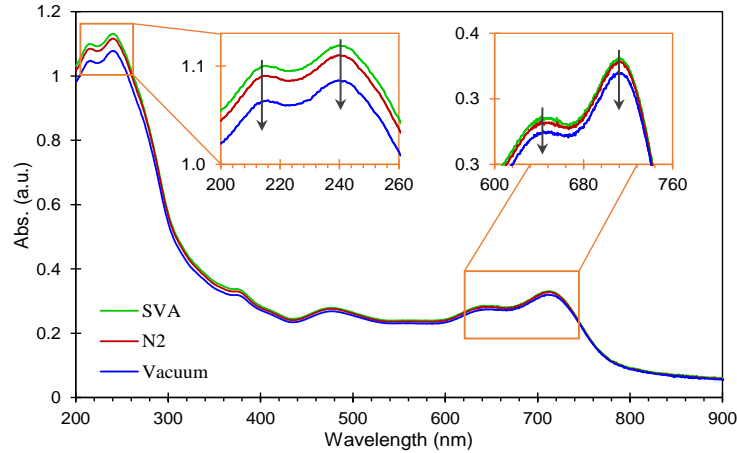


Figure 5.25: UV-Vis spectra of PBDTTT-EFT: PC₇₁BM active layer fabricated via different drying technique: SVA, N₂, Vacuum; Insets: PC₇₁BM region indicating a reduction of absorption, and PBDTTT-EFT region indicating a reduction of absorption.

It is well known that the optimised phase separation of donor/acceptor molecules is essential in charge dissociation and transport [32]. Numerous studies on polymer/fullerene OSCs suggest that optimal aggregated phase domain sizes for both donor and acceptor should be in regions tens of nanometers [233]–[238]. Therefore, it is crucial for an OSC system to be optimised with the best possible Nano-phase domain. From the absorption profiles, as the drying time is reduced the absorption of both PBDTTT-EFT and PC₇₁BM regions also decrease, suggesting that rapid drying of the active layer causes the molecules to crystallise and have a better phase-separated domain. Similar observations have been previously made for BDT-based polymers

(PBDTTT-C-T) [239]. From the crystallographic data reported in the literature, it has been suggested that PBDTTT-EFT and PC₇₁BM molecules aggregate and form their optimal conformation during the solvent evaporation process in thin films due to thermodynamic effects [240].

Therefore, the longer the active layer thin film is kept wet, the more chance donor and acceptor material will have to relax and unwind and lose their level of crystallinity. Also, the aggregation of fullerene acceptor materials to a degree has been proven to be beneficial for improving the device performance of OSCs [175], [231]. Therefore, from this study, it can be concluded that rapid drying of the active layer film under vacuum will lead to enhanced device performance, believed to be due to the formation better D:A phase domain as a result of tuned PC₇₁BM aggregation and PBDTTT-EFT crystallisation.

5.3.6 Solvent Additive

In this study, the impact of solvent additive is investigated. Numerous studies have shown that by controlling the selectivity of solubility for each material within the blend can play an essential role in the morphology and nanostructure formation within the thin films [43], [241]. Solvent additive 1,8-Diiodooctane (DIO) has been used in this study with the conjunction of the primary solvent. Foster et al. investigated the use of DIO as a solvent additive and reported its impact on OSC devices with PTB7: PC₇₁BM to be constructive for the enhancement of PCE [242].

Similarly, McNeil et al. group performed this investigation on PBDTTT-EFT: PC₇₁BM for ‘inverted’ solar cell structure by using 3% w:w ratio of DIO:o-DCB prior to device fabrication and they reported enhancement of both J_{sc} and FF for their devices [243]. In this study, similar experimental procedures to *McNeil’s* group was employed for the preparation of the active solution containing 3% w:w ratio of DIO:o-DCB. Upon addition of DIO to the solution, it was stirred for additional 2hrs prior to sample fabrication. Two sets of samples were prepared As-Cast (no additive), and DIO added. The averaged J-V characteristic curves under illumination are illustrated in Figure 5.26, and their extracted electrical parameters are presented in Table 5.9.

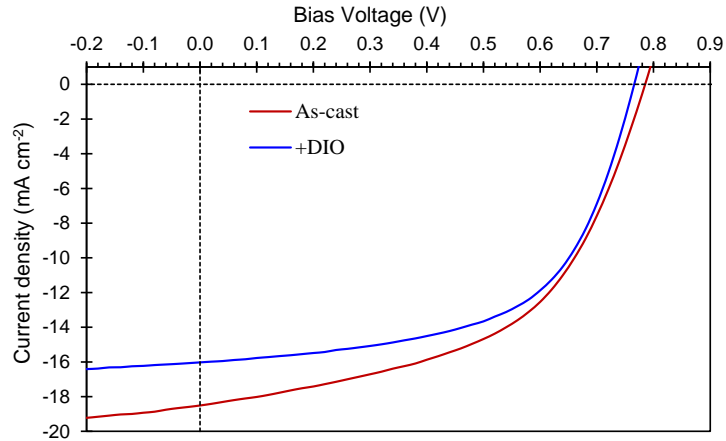


Figure 5.26: Average J-V characteristics curves of PBDTTT-EFT: PC₇₁BM blend, As-cast, and DIO added the active solution.

Table 5.9: Electrical parameters extracted from averaged J-V curves for As-Cast and DIO added samples.

Sample	J_{sc} (mA cm ⁻²)	V_{oc} (V)	FF	PCE (%)	R_s (Ω cm ²)	R_{sh} (Ω cm ²)
As-cast	18.50	0.78	0.52	7.61	10.87	256.11
+DIO	16.02	0.77	0.59	7.19	8.66	389.71

As from the J-V curves Figure 5.26 and the data in Table 5.9, devices with added DIO shows a reduction in J_{sc} and V_{oc} parameters. However, the FF value is significantly improved. The series and shunt resistance values indicate that there is a better charge transfer for devices containing a small amount of DIO [40]. Although this is beneficial, the trade-off between J_{sc} and FF has had a negative impact on the PCE of these devices, resulting in lower PCE of 7.19% in comparison to devices without DIO. The obtained results clearly show a contradiction to what was reported in literature upon employing DIO as an additive agent. It is important to note that in the reported literature, the architecture of devices fabricated was ‘inverted’ structure, and the architecture used throughout this project is based on a ‘conventional’ structure. Therefore, to understand the reason for such behaviour, the optical absorption spectrum of both samples is collected and illustrated in Figure 5.27.

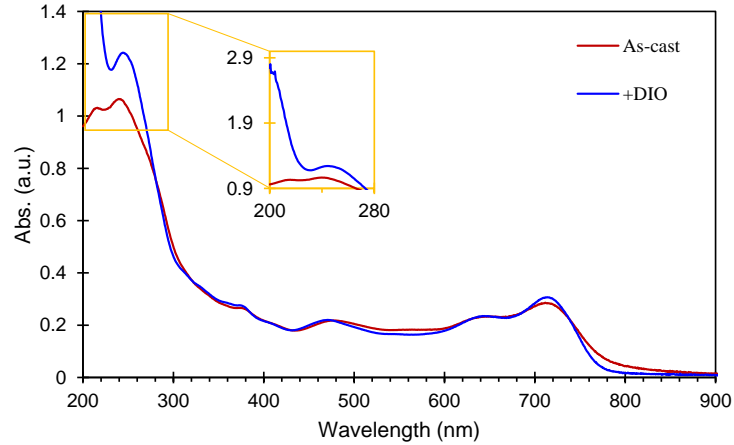


Figure 5.27: UV-Vis spectra of PBDTTT-EFT: PC₇₁BM, As-cast (red), and DIO added (blue) sample, Inset: illustrating that the absorbance of PC₇₁BM region being affected upon addition of DIO.

As it can be seen from Figure 5.27 inset, there is a significant change in the optical absorption profile and intensity of the PC₇₁BM region with the presence of DIO additive compared to As-casted sample. The absorbance intensity of DIO added sample is remarkably increased for the PC₇₁BM peak at ~210 nm, and its profile shape deviates from its As casted sample; suggesting dispersion of PC₇₁BM molecules.

The increase in FF parameter (*see Table 5.9*) also confirms the well distributed and intermixed PC₇₁BM with PBDTTT-EFT molecules. Since DIO solvent additive is selective only to PC₇₁BM, it will cause a dispersion of PC₇₁BM molecules as reported in literature [39], [40], [177], [237], [240]. Better dispersion of the acceptor molecules within the blend would result in better charge dissociation. However, this could also mean that there are less distinct phase domains that are beneficial for charge transport which also impacts charge extraction and hence, loss of J_{sc} . In addition, it can be observed that in the PBDTTT-EFT region, the absorbance profile is slightly more profound when compared to the As-casted sample, suggesting that PBDTTT-EFT molecules are more crystallised [39]. Therefore, from this case study it can be concluded that use of DIO as a solvent additive has a negative impact on the overall performance of fabricated devices and will not be further investigated nor used in this PhD project.

5.3.7 Active Layer Surface Washing

In this study, the impact of active layer surface washing with alcohol is investigated. It has been reported that washing the top surface of the active layer with alcohol-based solvents such as Methanol (CH_3OH) will enhance the performance of OSC devices for low bandgap BDT-based polymers [244], [245]. Therefore, three samples were prepared for this investigation, and their preparation is as follow:

- **As-cast:** Devices fabricated as standard.
- **Methanol washed:** After the active layer has been vacuum dried, it's surface is washed with 60 μL of Methanol (CH_3OH). Methanol is dropped cast onto the surface while spinning at 4,000 RPM; the sample is spun at this speed period of 30 sec. The sample is then transferred to the thermal deposition chamber for deposition of Ca and Al to complete the OSC devices.
- **Ethanol washed:** The washing procedure is identical to 'Methanol' washing, 60 μL of Ethanol ($\text{CH}_3\text{CH}_2\text{OH}$) is drop cast onto the surface.

The schematic of the alcohol surface washing technique is illustrated in Figure 5.28.

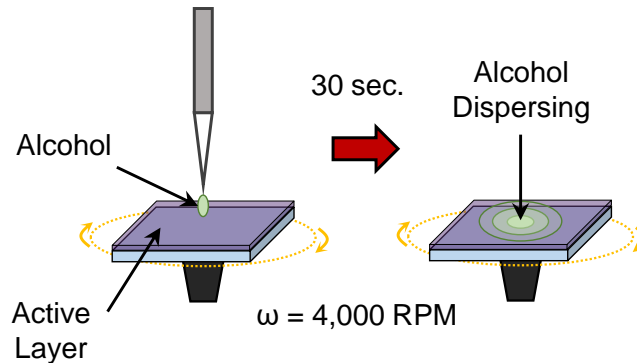


Figure 5.28: Schematic diagram of the active layer surface washing with selective alcohol drop-casting.

The schematic in Figure 5.28, shows the drop-casting of 60 μL of alcohol onto the active layer surface while spinning at 4,000 RPM for 30 sec. allowing the alcohol to disperse on the top surface and 'wash-off'. The averaged J-V characteristic curves for each sample under illumination is illustrated in Figure 5.29, and their corresponding extracted electrical parameters are presented in Table 5.10.

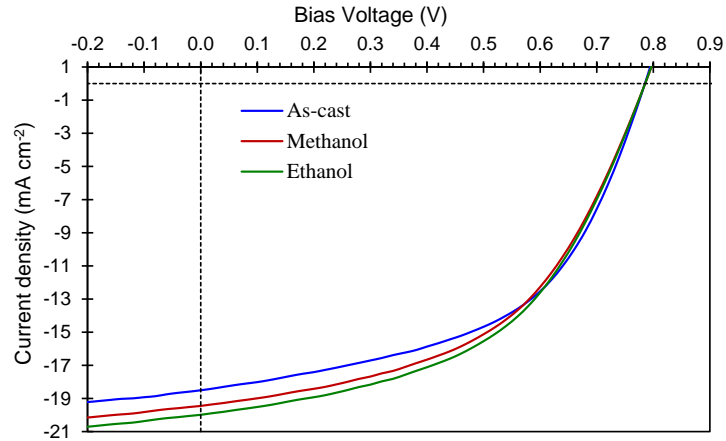


Figure 5.29: Averaged J-V characteristic curves for PBDTTT-EFT: PC₇₁BM. As-cast, Methanol and Ethanol surface washed.

Table 5.10: Electrical parameters extracted from the averaged J-V curves for As-cast, Methanol and Ethanol surface washed samples.

Sample	J _{sc} (mA cm ⁻²)	V _{oc} (V)	FF	PCE (%)	R _s (Ω cm ²)	R _{sh} (Ω cm ²)
As-cast	18.50	0.78	0.52	7.61	10.87	256.11
Methanol	19.44	0.79	0.50	7.69	12.32	202.49
Ethanol	19.98	0.79	0.50	7.90	11.99	198.08

As is evident from the data presented in Table 5.10, there is a trade-off between the J_{sc} and FF parameter upon washing the top surface of the active layer with alcohol. As the active layer surface is washed with alcohol, the J_{sc} value is increased at the cost of a reduction in FF value. Ethanol washing has had the most impact on the enhancement of the PCE amongst the two selected alcohols, with averaged PCE of 7.90% and J_{sc} value of ~20 mA cm⁻¹.

Such behaviour has been reported by Sun Q., et al. for PBDTTT-EFT: PC₇₁BM OSC devices upon soaking and washing the active layer with Methanol [244]. They attributed the increase of J_{sc} to increased vertical phase separation and migration of PC₇₁BM to the top surface, which is beneficial for charge transport. Similarly, this phase domain segregation will cause a reduction of FF value. To confirm that the results obtained in this study are also telling the same story as Sun Q., et al. group, Optical absorption spectrum of each sample is collected and presented in Figure 5.30.

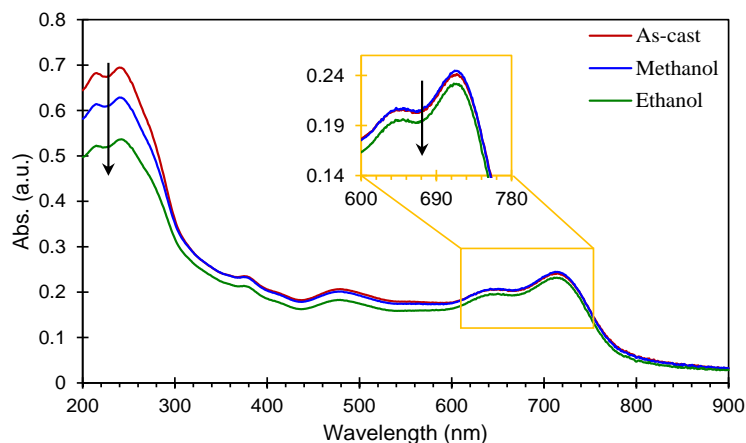


Figure 5.30: UV-Vis spectra of As-cast, Methanol, and Ethanol washed samples. Inset: PBDTTT-EFT region indicating a reduction in absorption.

As it can be seen from the absorption spectrum profiles, there is a significant reduction of intensity in the PC₇₁BM region, indicative of PC₇₁BM cluster formation. In addition, there is also a slight reduction of intensity for Ethanol treated sample in the PBDTTT-EFT region (Figure 5.30 inset), which is in good agreement with reported literature [246]. The subsequent reduction of absorbance in the PC₇₁BM region from As-cast to Ethanol washed shows a correlation with the increased J_{sc} values. Ethanol washed samples showing the highest J_{sc} and most cluster formed PC₇₁BM molecules.

The reason for the higher level of PC₇₁BM cluster formation in ethanol washed samples compared to methanol, is due to the nature of these alcohols. The boiling point of methanol and ethanol are 64.70°C and 78.37°C, respectively [247]. Since methanol evaporates quicker than ethanol, it will have less time to impact on the active layer surface and hence, less time to interact with the PC₇₁BM molecules to form a cluster and impact their phase separation. Therefore, from this case study, it can be concluded that surface washing of the active layer with alcohol will have a positive impact on the enhancement of PCE. Amongst the tested alcohols, ethanol has had the most significant improvement to the device performance.

5.3.8 Co-solvents

From experiences in the previous case studies of this PhD project, it was concluded that using a solvent additive selective to the acceptor material (PC₇₁BM) would enhance the FF parameter and reduce the J_{sc} parameter. This was suggested to be due

to the dispersion of PC₇₁BM molecules within the active layer. So far, all the existing solutions prepared in this project are based on a single solvent o-DCB. It has been reported that acceptor material PC₇₁BM has a higher solubility in CB than o-DCB [248], [249]. Therefore, a new method of sample preparation is designed to use co-solvents o-DCB:CB mixture instead of a single solvent for dissolving the active materials. In this study, the impact co-solvents [o-DCB:CB] mixing ratio is investigated on the overall device performance. The experimental setup and preparations are discussed in *Chapter 4, section 4.2.3*. The averaged J-V characteristic curves under illumination are illustrated in Figure 5.31 and their extracted electrical parameters in Table 5.11.

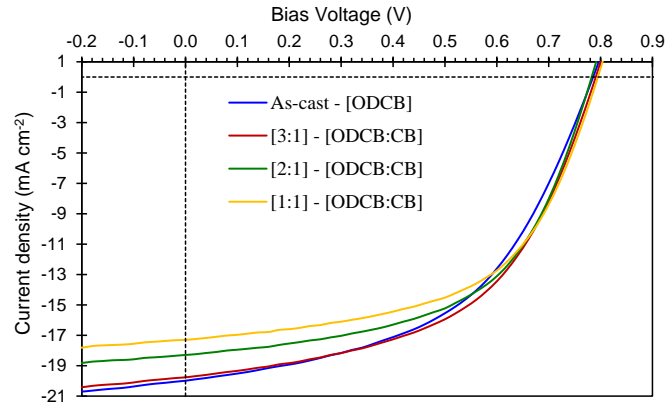


Figure 5.31: Averaged J-V characteristic curves for PBDTTT-EFT: PC₇₁BM samples fabricated from: As-cast, co-solvents [o-DCB:CB] mixture with ratios of [3:1] [2:1] and [1:1].

Table 5.11: Electrical parameters extracted from the averaged J-V curves in Figure 5.29.

Samples	J _{sc}	V _{oc}	FF	PCE	R _s	R _{sh}
[o-DCB:CB]	(mA cm ⁻²)	(V)		(%)	(Ω cm ²)	(Ω cm ²)
As-cast	19.98	0.79	0.50	7.90	11.99	198.08
[3:1]	19.37	0.79	0.53	8.06	11.08	229.84
[2:1]	18.29	0.79	0.55	7.93	10.87	279.86
[1:1]	17.29	0.78	0.56	7.65	9.98	300.32

From the results presented in Table 5.11, it is evident that use of co-solvent reduces J_{sc} parameter and enhances the FF. The highest obtained PCE belongs to the devices fabricated from co-solvent with a mixture ratio of [3:1] [o-DCB:CB] achieving efficiency of 8.06%. This behaviour of ‘seesaw’ action between J_{sc} and FF amongst As cast and co-solvent samples, is very similar to the study on DIO (*section 5.2.6*).

Which suggests that the use of a selective solvent (CB) for solubility of PC₇₁BM will cause higher levels of PC₇₁BM dispersion within the active layer as is evident by the FF values. As the presence of CB solvent increases in the solution, the higher the FF value gets at the cost of reduced J_{sc}. However, co-solvent containing only 25% CB [3:1] shows the most fine-tuned mixing ratio of co-solvent, where the reduction of J_{sc} and enhancement of FF had benefited the overall performance of the devices fabricated from this solution. Therefore, from this study, it can be concluded that the most optimised system for device fabrication will be the use of co-solvent of [o-DCB:CB] containing only 25% CB.

5.3.9 Optimising Donor: Acceptor ratio

In this section, the impact of donor: acceptor ratio within the blend is investigated. This is one of the most important investigations of this project as there is very little information on optimising the D:A blend ratio for PBDTTT-EFT: PC₇₁BM OSCs. So far, all the samples prepared are at D:A ratio of 1:1.5 respectively, which is what has been reported in literature for BDT-based polymers blended with PC₇₁BM (including PBDTTT-EFT: PC₇₁BM) [40], [42], [181], [182], [220], [224], [250], [251]. However, there is minimal information as to why this blend ratio is chosen, and if it is the most optimised blend ratio. Therefore, this study is designed to find the most optimised D:A blend ratio for PBDTTT-EFT: PC₇₁BM solar cells and provide an in-depth analysis of the optimisation of D:A ratio. Blend ratios [D:A] of 1:0.5, 1:1, 1:1.5, 1:2 and 1:3 are prepared for this investigation, and their preparation procedure is discussed in *Chapter 4, section 4.2.3*. The obtained average J-V characteristic curves are illustrated in Figure 5.32, and their extracted electrical parameters are presented in Table 5.12.

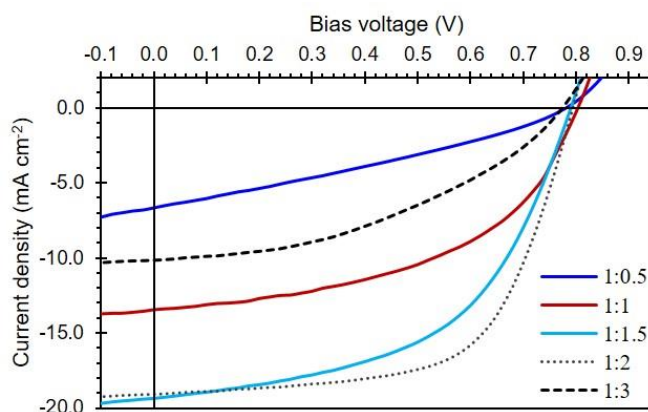


Figure 5.32: Averaged J-V characteristic curves for PBDTTT-EFT: PC₇₁BM samples fabricated from different D:A blend ratios.

Table 5.12: Electrical parameters extracted from the averaged J-V curves for different blend ratios of PBDTTT-EFT: PC₇₁BM.

D:A Ratio	J _{sc} (mA cm ⁻²)	V _{oc} (V)	FF	PCE (%)	R _s (Ω cm ²)	R _{sh} (Ω cm ²)
1:0.5	6.68	0.78	0.31	1.60	46.75	158.62
1:1	13.49	0.80	0.50	5.38	13.49	300.22
1:1.5	19.21	0.79	0.54	8.10	9.75	336.18
1:2	19.08	0.79	0.63	9.56	7.26	526.33
1:3	10.13	0.77	0.41	3.25	21.38	323.25

As it can be seen from the J-V characteristic curves and the extracted electrical parameters, as PC₇₁BM is loaded into the blend, the performance of the fabricated devices improves up to D:A blend ratio of 1:2. Any further increase of PC₇₁BM within the blend causes reduction of device performance and PCE. As can be seen, the J_{sc} is improving as the PC₇₁BM content in the blend is increased, and it peaks at a blend ratio of 1:1.5. Although, there is a slight reduction of J_{sc} for 1:2 blend ratio, the improved FF compensates for this and devices fabricated from 1:2 blend ratio achieves the highest PCE of 9.56%. To gain insight to the trend of the electrical parameters presented in Table 5.12 and explain the trade-off between short circuit current density and FF for 1:1.5 and 1:2 blend ratios, PL measurements were performed on thin film samples fabricated with the same blend ratios. The optical absorption and PL spectra for each sample is illustrated in Figure 5.33.

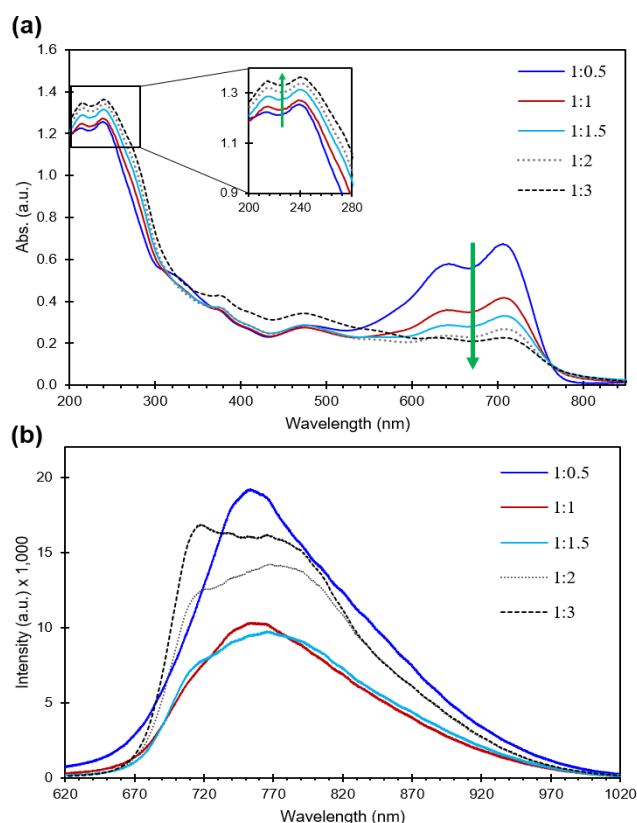


Figure 5.33: (a) UV-Vis spectra profile and (b) PL spectra for PBDTTT-EFT: PC₇₁BM at different blend ratios.

As it can be seen from Figure 5.33a, the absorbance of PBDTTT-EFT region is decreasing, and PC₇₁BM region is increasing upon the increase of PC₇₁BM content within the blend. This observation can be associated to the simple fact that the content of PBDTTT-EFT is reducing since the concentration of the blend is constant. Figure 5.33b illustrates the PL spectra profile for each active layer blend with different D:A ratio under 514nm excitation laser. An interesting observation from the PL spectra in Figure 5.33b is that above 1:1.5 blend ratio, the PL emission profile starts to look more like the line profile of pristine PC₇₁BM, this was previously discussed in *section 5.2.3*, where it was suggested that more PC₇₁BM are surfacing on the thin film active layer. In addition to the PL spectrum, the PL quenching percentage of each blend ratio with respect to PL of pristine PBDTTT-EFT is calculated and presented in Figure 5.34.

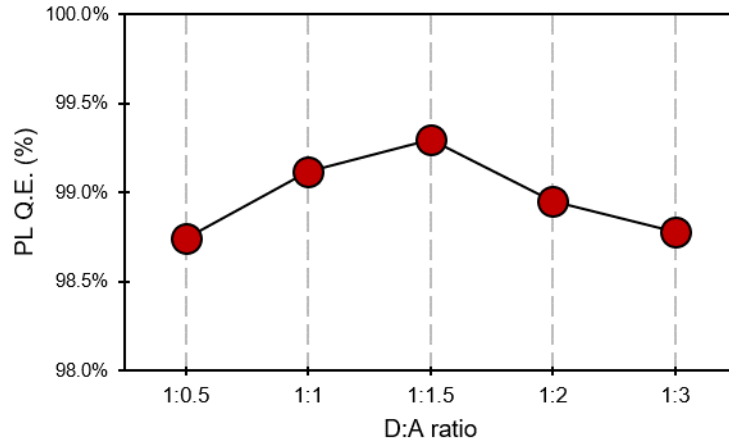


Figure 5.34: PL Quenching efficiency (Q.E.) as a function of D:A blend ratios with respect to pristine PBDTTT-EFT.

As it's evident, in Figure 5.34, the PL intensity quenches upon introducing PC₇₁BM, resulting from a fast charge transfer [67], [252]–[254]. Upon further increasing the PC₇₁BM content, the quenching efficiency improves and peaks at 1:1.5 ratio, which corresponds to the highest short circuit current density observed. From the PL results, it can be said that 1:1.5 blend ratio provides suitable domains for efficient exciton dissociation resulting in enhanced short circuit current density.

However, further increasing PC₇₁BM content above 1:1.5 ratio leads to higher PL intensity yielding lower short circuit current density also reported in the literature [255]. It can be suggested that upon increasing PC₇₁BM content above 1:1.5 ratio, could facilitate opposing processes, which may initiate lower exciton dissociations and at the same time as providing suitable networks for charge extractions, resulting in increased FF. It is important to note that the concentration of each sample (blend) is constant, therefore as the PC₇₁BM amount is increased within the blend, the amount of PBDTTT-EFT present in the blend is reduced, and this could be another explanation for the reduction for J_{sc} parameter for samples with 1:2 blend ratio. Figure 5.33 illustrates a correlation between the device fill factor (FF) and shunt resistance (R_{sh}) as a function of the blend ratio.

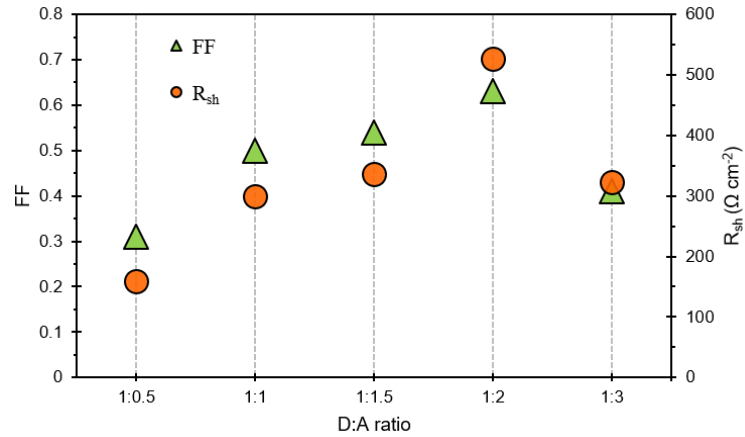


Figure 5.35: Correlation graph between FF and R_{sh} as a function D:A blend ratio.

As is evident from Figure 5.33, FF and R_{sh} parameters peak at 1:2 ratio. It is believed that the improved value of the fill factor is due to better charge carriers transport network and lower device leakage current indicated by the value of shunt resistance. Previous work reported by Foster et al. [253], suggests that the improved value of fill factor is initiated from increased PC₇₁BM content within the active layer blend, providing suitable network and consecutively leading to higher electron mobility. Further work on other polymers also suggests similar behaviour upon PC₇₁BM loading [256]. To further investigate the impact of PC₇₁BM loading on the device performance, the surface morphology of these samples is investigated. Atomic Force Microscopy (AFM) images could provide further insight into the morphological properties of PBDTTT-EFT: PC₇₁BM blend ratios, the topography, and phase images for pristine PBDTTT-EFT, PC₇₁BM and their blend at different ratios were collected. Figure 5.36 illustrates the AFM topography and phase images of PBDTTT-EFT: PC₇₁BM blend at different ratios.

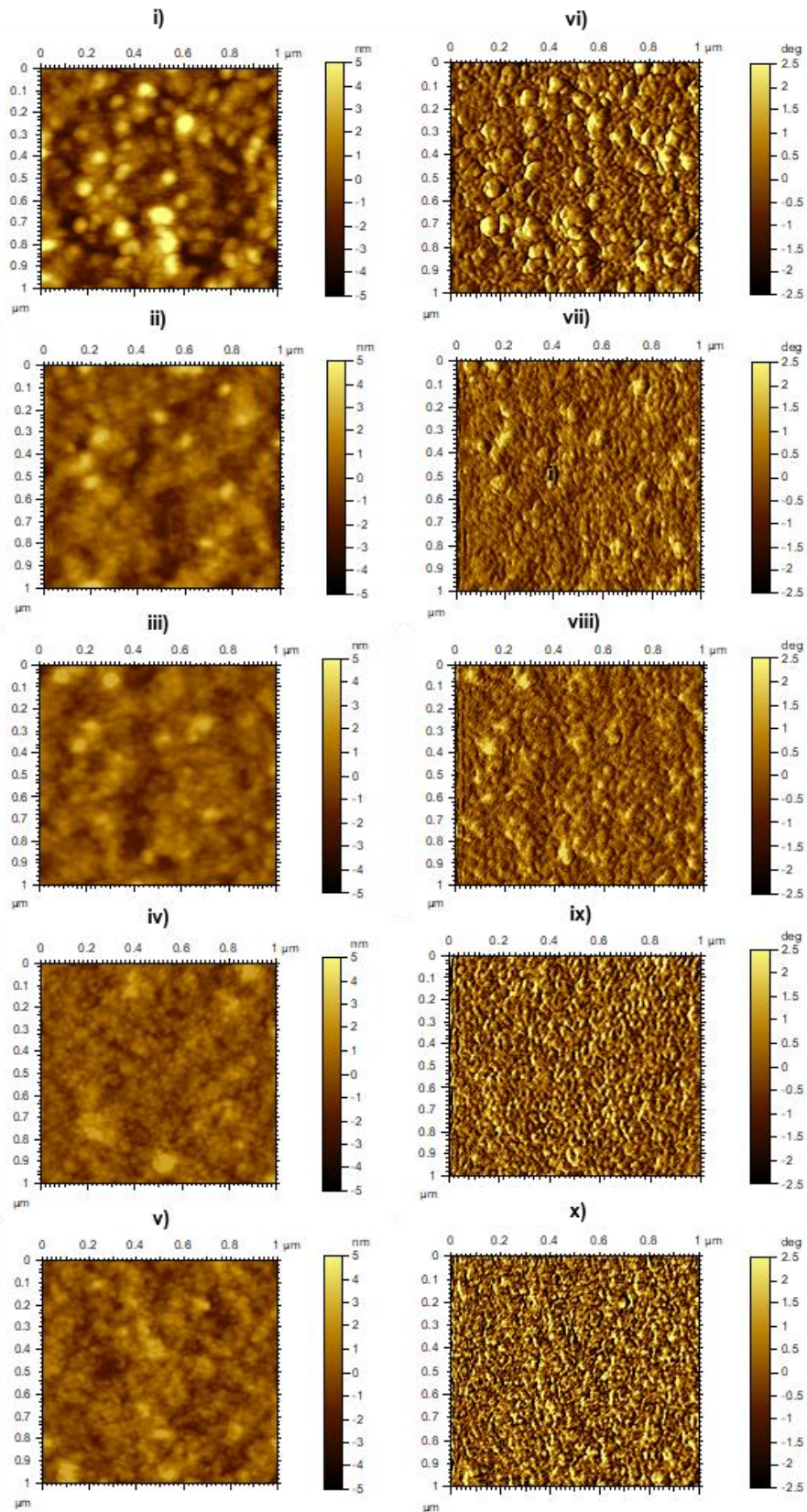


Figure 5.36: AFM morphology images for PBDTTT-EFT: PC₇₁BM corresponding to 1:0.5 – 1:3 blend ratios; (i – v) represents Topography images, and (vi – x) represents Phase images.

Surface roughness (S_q) was calculated from the topography images collected and are presented in Table 5.13. $|\Delta S_q|$ was calculated to be the absolute difference between the surface roughness of each blended sample and pristine PC₇₁BM. . Low values of $|\Delta S_q|$ are an indication of more PC₇₁BM on the surface of the thin film.

Table 5.13: Surface roughness (S_q), an absolute difference of surface roughness between S_q of blends and S_q of pristine PC₇₁BM $|\Delta S_q|$ and series resistance R_s for PBDTTT-EFT: PC₇₁BM blends at different D:A ratios. Note: (1:0 ratio is representing pristine PBDTTT-EFT and 0:1 represents pristine PC₇₁BM).

D:A Ratio	S_q (nm)	$ \Delta S_q $ (nm)	R_s (Ω cm ²)
1:0	2.234	-	-
1:0.5	1.650	0.862	46.75
1:1	1.050	0.262	13.49
1:1.5	0.871	0.083	9.50
1:2	0.769	0.019	6.50
1:3	0.887	0.099	21.38
0:1	0.788	-	-

As is evident from the values in Table 5.13, it appears that there is a correlation between this $|\Delta S_q|$ and R_s . As can be observed, the lowest series resistance (R_s) corresponds to the lowest value of $|\Delta S_q|$. Therefore, it is suggested that surfaces with more PC₇₁BM are beneficial for surface contact to the cathode. Hence, better contact resistance / series resistance (R_s). Similar trends between the quantitative presence of acceptor material on the film surface and contact resistance have been reported for other polymers: fullerene blended devices [257], [258]. Furthermore, when surface roughness for pristine PBDTTT-EFT, PC₇₁BM and all the blend ratios are investigated, it indicates that the surface roughness is influenced by the content of PC₇₁BM within the blend, showing that upon loading the sample with PC₇₁BM, more of this molecule appears at the top surface of the film. Similar observations have been previously reported on the formation of PC₆₁BM clusters on the top surface of the active layer film as its percentage is loaded onto P3HT blends [82]. It is interesting to note that for a sample of 1:3, S_q value is higher than pristine PC₇₁BM. This could be due to the amount of PC₇₁BM in the thin film. Pristine PC₇₁BM film was fabricated from a 10 mg mL⁻¹ solution; however, 1:3 sample consisted of 16.7 mg of PC₇₁BM.

Therefore, this could have impacted the cluster size of PC₇₁BM present at the film/air boundary. Figure 5.37 illustrates a schematic diagram to visualise this phenomenon.

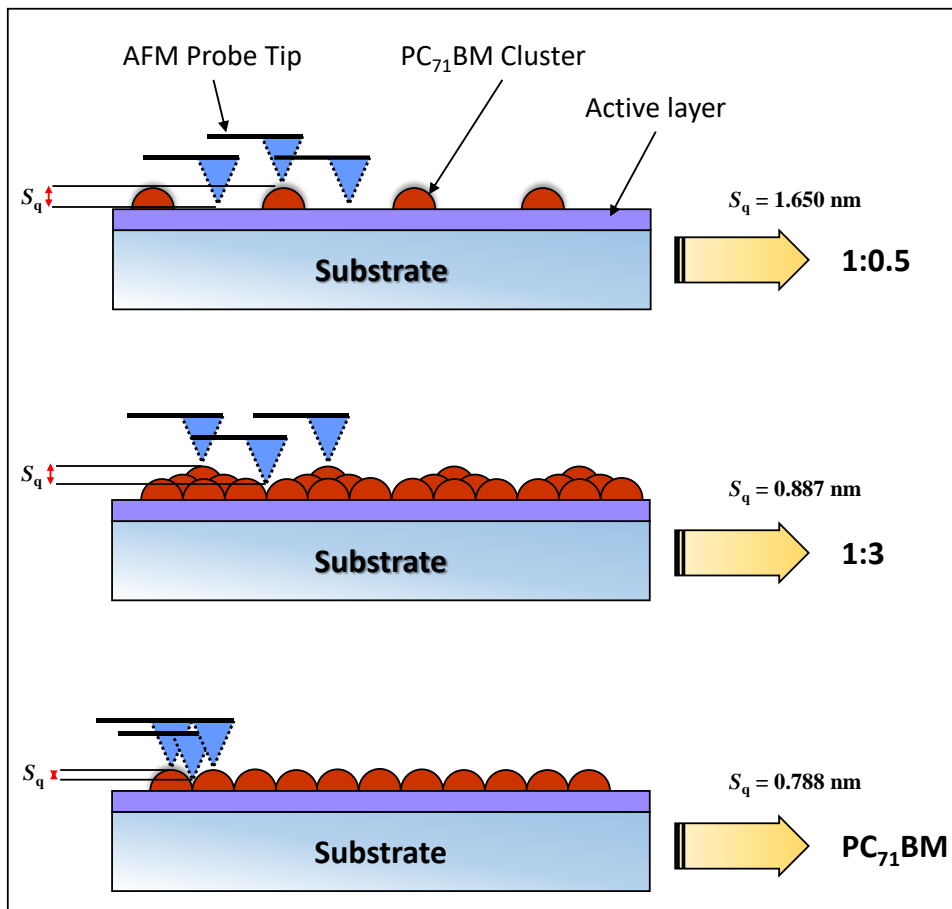


Figure 5.37: Schematic diagram of PC₇₁BM cluster formation on film/air boundary, representing three cases of 1:0.5, 1:3 blend ratio and pristine PC₇₁BM.

To understand the impact of PC₇₁BM content in the blend on PBDTTT-EFT molecules, the analysis of the structural properties of these blends becomes fundamental. Figure 5.38 illustrates the OOP GIXRD diffractogram pattern for thin films of pristine PBDTTT-EFT, pristine PC₇₁BM and blends of PBDTTT-EFT: PC₇₁BM with different D:A ratios.

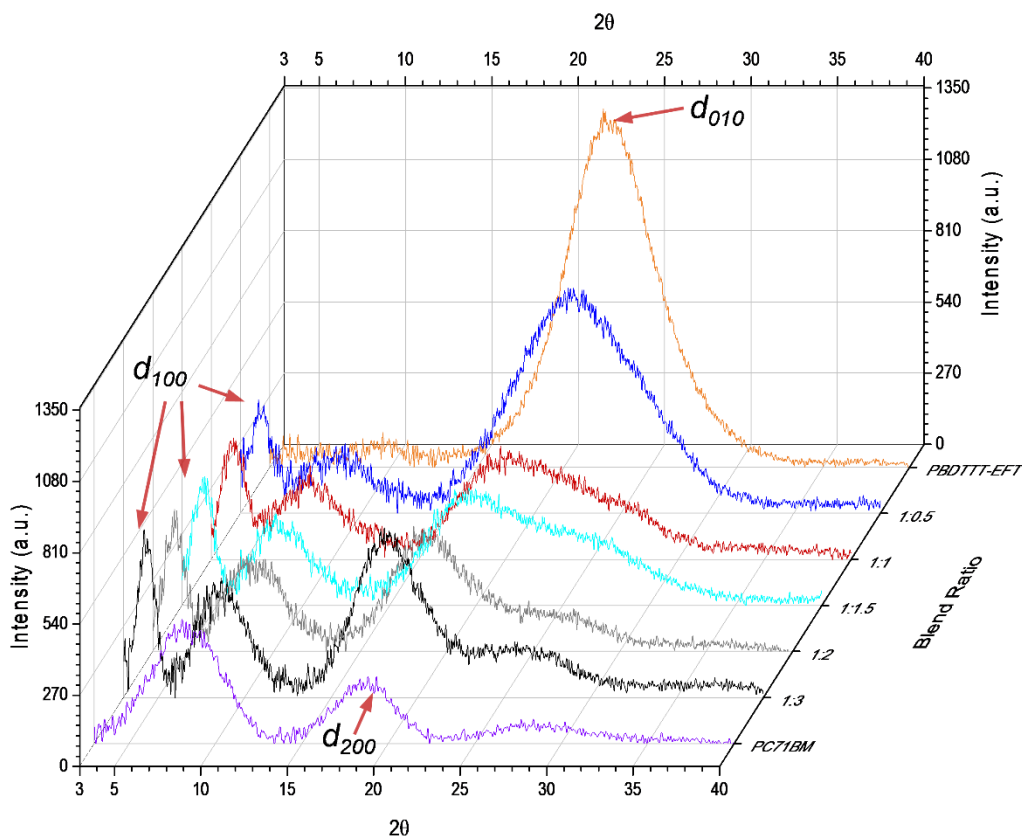


Figure 5.38: 3D representation of OOP GIXRD diffractograms for pristine PBDTTT-EFT, PC₇₁BM and their blends at different ratios respectively. Note: the peak assignments are indicated on the graph for PBDTTT-EFT d_{100} and d_{010} plane, and PC₇₁BM d_{200} plane.

As PC₇₁BM content in the blend is increased, a peak at $2\theta = 4.15^\circ$ associated with the alkyl side chain of PBDTTT-EFT molecule appears, and its intensity enhances with a further increase of PC₇₁BM. As is evident in Figure 5.38, pristine PBDTTT-EFT only reveals a substantial peak at $2\theta = 22.69^\circ$ which is associated with the d_{010} plane, indicative that the molecule has a preferred orientation in the *Face-on* orientation [243]. However, the peak arising at the region of $2\theta = 4.15^\circ$ is associated with the d_{100} plane of PBDTTT-EFT, indicative of *Edge-on* molecules [243]. To evaluate the impact of PC₇₁BM on PBDTTT-EFT structural parameters, a computer model based on Gaussian & Lorentzian curve fit was used to analyse each diffractogram presented in Figure 5.36, the extracted parameters are presented in Table 5.14.

Table 5.14: OOP GIXRD parameters extracted from the curve fits for PBDTTT-EFT: **(a)** d_{100} plane, **(b)** d_{010} plane, and for PC₇₁BM: **(c)** d_{200} plane.

	Blend ratio	2 θ ($^\circ$)	FWHM ($^\circ$)	d (Å)	L_c (Å)	Intensity (a.u.)	no. stacks
(a)	PBDTTT-EFT	-	-	-	-	-	-
	1:0.5	4.15	1.57	21.27	50.61	345	2.38
	1:1	4.24	1.49	20.82	53.37	367	2.56
	1:1.5	4.26	1.43	20.72	55.57	416	2.68
	1:2	4.28	1.40	20.62	56.76	450	2.75
	1:3	4.30	1.21	20.53	65.68	563	3.20
(b)	PBDTTT-EFT	22.69	5.65	3.91	14.34	1215	3.66
	1:0.5	21.69	5.77	4.09	14.01	685	3.42
	1:1	21.55	5.80	4.12	13.94	235	3.38
	1:1.5	21.10	5.95	4.21	13.58	195	3.23
	1:2	20.50	6.50	4.33	12.42	165	2.87
	1:3	-	-	-	-	-	-
(c)	1:0.5	18.64	3.95	4.75	20.37	117	4.29
	1:1	18.62	3.85	4.76	20.90	175	4.39
	1:1.5	18.58	3.79	4.78	21.23	194	4.44
	1:2	18.40	3.60	4.82	22.37	285	4.64
	1:3	18.19	3.59	4.87	22.40	565	4.60

The parameters presented in Table 5.14 **(a)** corresponds to the d_{100} *Edge-on* orientation of PBDTTT-EFT, **(b)** corresponds to the d_{010} *Face-on* orientation of PBDTTT-EFT and **(c)** corresponds to the d_{200} vertical segregation direction of PC₇₁BM. As it can be seen from Table 5.14**a**, upon increasing PC₇₁BM content within the blend, the d_{100} spacing is decreasing, and its intensity is increasing and indicating that more PBDTTT-EFT molecules are crystallising into *Edge-on* orientation. The average crystal size of PBDTTT-EFT molecules in *Edge-on* direction is increasing as more PC₇₁BM is loaded into the blend.

Similarly, from the data presented in Table 5.14**b**, it is evident that as the percentage loading of PC₇₁BM is increased, the peak intensity of d_{010} is reduced, and the peak position is shifted towards lower 2 θ values resulting in an increase in the spacing between the backbone (π - π stacking). In simple term, there seems to be a seesaw action between *Face-on* and *Edge-on* molecular orientation of PBDTTT-EFT molecules, initiated by PC₇₁BM loading. Although PBDTTT-EFT has preferred *Face-on*

orientation, randomly *Edge-on* orientated molecules may also be formed during the fabrication processes [243]. It appears that presence and increase of PC₇₁BM content within the blend, initiate a change in preferred orientation of PBDTTT-EFT polymer, revealing the *Edge-on* orientation line profile which otherwise could not have been detected in OOP.

The change in preferred orientation could facilitate vertical segregation of PC₇₁BM molecules towards the film surface. Table 5.14c presents data for the d_{200} plane associated with PC₇₁BM vertical segregation [49]. From the extracted data it is evident that the intensity and coherent length (L_c) of d_{200} are increased as PC₇₁BM content is increased within the blend, initiating a system of bi-continuous network assisting electron transport, which would lead to higher electron mobility and better charge transport [254]. Furthermore, data presented in Table 5.14(a) reveals that the increase of PC₇₁BM loading results in a reduction of d_{100} spacing. Suggesting that side chains are intercalating, leading to the dihedral angle change of thiophene rings attached to BDT units. S. Zhang et al. [127], reported that using Density Function Theory (DFT) modelling shows that narrow bandgap polymers (PBDTTT-) with three different side chains namely EFF, EFT, and EFS have different dihedral angles (ψ) between their side-chain and backbone (34° , 60° and 60°) respectively. The spacing between the π - π backbone is shown to increase accordingly with the dihedral angle; this is presented in Table 5.15 [127].

Table 5.15: Dihedral angle ψ and d_{010} spacing for PBDTTT- based polymer.

Side chain	ψ ($^\circ$)	d_{010} (Å)
Furan (EFF)	34	3.63
Thiophene (EFT)	60	3.94
Selenophene (EFS)	60	3.94

The π - π stacking distance (d_{010} spacing) in Table 5.14b is increased upon increasing PC₇₁BM content. Therefore, there must be a mechanism which causes the change in the dihedral angle of the thiophene rings attached as a side chain, which subsequently changes the π - π backbone spacing. From the reduction of d_{100} spacing in Table 5.14a as a function of PC₇₁BM, it was clear that there is intercalation between the side chains of PBDTTT-EFT molecules. The intercalation of the alkyl side chains would cause

compression on the thiophene rings attached to the backbone as part of the side chains, causing the thiophene side-chain rings to rotate to have a larger dihedral angle and subsequently increase the π - π spacing. To support the above statement, Raman spectroscopy was performed on the thin film samples for different D:A blend ratios. The collected Raman spectrum under 785nm excitation laser is presented in Figure 5.39, with the four main peaks of PBDTTT-EFT identified.

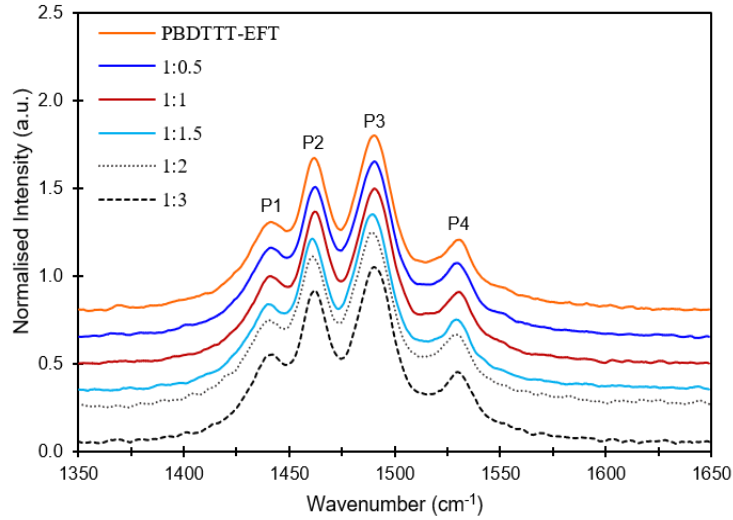


Figure 5.39: Raman spectrum of pristine PBDTTT-EFT and its blend ratios with PC₇₁BM with appropriately designated peaks under 785 nm excitation laser. Inset: molecular structure of PBDTTT-EFT molecule with peak assignments.

Detailed analysis of the individual peaks from the Raman spectrum profiles using Gaussian and Lorentzian curve fits indicates that there is no significant Raman shift of these peaks. Table 5.16 presents the extracted parameters from the curve fit analysis of P1 – P4 for each sample, where the Raman shift is noted as (f cm⁻¹).

Table 5.16: Raman spectrum profile peak analysis for samples with different D:A ratios.

D:A Ratio	P1		P2		P3		P4	
	f (cm ⁻¹)	FWHM (cm ⁻¹)						
1:0 (EFT)	1439	8.0	1462	10.7	1491	15.6	1530	10.8
1:0.5	1440	8.1	1462	10.6	1491	15.6	1530	12.0
1:1	1441	9.4	1462	10.7	1491	15.7	1530	12.8
1:1.5	1441	15.4	1461	10.8	1490	15.8	1530	14.0
1:2	1441	17.8	1461	10.8	1490	15.8	1530	14.7
1:3	1441	18.7	1462	10.7	1491	15.6	1530	15.5

From the extracted FWHM parameters in Table 5.16, it is evident that there is no significant change for peaks 2 and 3. However, there is an increase in FWHM for both peak 1 and 4. The FWHM of each peak as a function of PC₇₁BM loading is illustrated in Figure 5.40.

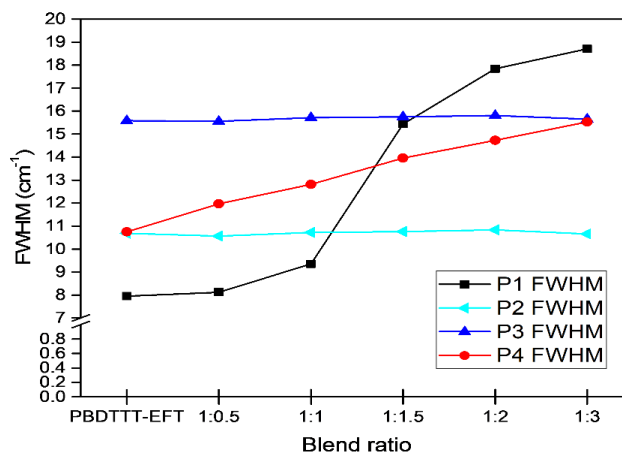


Figure 5.40: The FWHM for P1 – P4 assigned on the Raman spectrum as a function of the blend ratio.

Since P2 and P3 are associated to the backbone vibration modes of the PBDTTT-EFT, no significant change in their FWHM correlates well with the FWHM parameters extracted from GIXRD diffractograms for the d_{010} plane (Table 5.14(b)) associated to the backbone of PBDTTT-EFT. Indicating that there are no significant changes in the backbone of PBDTTT-EFT molecule, further supporting that PC₇₁BM does not compromise the integrity of the backbone structure. Similarly, the noticeable increase in FWHM in P1 and P4 as PC₇₁BM content is increased within the blend confirms the hypothesis of PBDTTT-EFT side-chain intercalation and causing structural deformation of the side chain thiophene rings influencing the π - π spacing between the backbone of PBDTTT-EFT and as a result of an increase in dihedral angle and d_{010} spacing. Evidentially this further supports the statement that an increase in the π - π spacing of the PBDTTT-EFT molecules is caused by side-chain intercalation of PBDTTT-EFT molecules.

To summarise this section, it is concluded that upon increasing PC₇₁BM content within the blend the overall device performance is enhanced and peaks at D:A blend ratio of 1:2, and any further loading of PC₇₁BM into the blend would have an adverse effect. It is identified that PC₇₁BM, as well as its well-known role for exciton dissociations, can facilitate electron transport networks.

The ΔS_q values presented in Table 5.13 revealed a direct correlation between surface roughness and series resistance as a function of D:A blend ratio. The S_q values of pristine PC₇₁BM, PBDTTT-EFT and blended films indicate that the film morphology is dependent on blend ratio, and at higher PC₇₁BM contents; the S_q value is predominantly closer to that of PC₇₁BM. This could, therefore, be used as an indicator for PC₇₁BM presence at the film surface. The GIXRD line profile data, suggests that PC₇₁BM loading influences the PBDTTT-EFT molecules. It is causing disruption of π - π stacking and side-chain intercalations; leading to a change in the preferred orientation (*Face-on* \rightarrow *Edge-on*) as PC₇₁BM content is increased.

Subsequently, this could remove the obstruction of PC₇₁BM vertical segregation and enhance its quantity at the surface. Furthermore, a longer coherent length associated with the d_{200} plane for PC₇₁BM is generated from increased content within the blend, creating a system of bi-continuous network suitable for electron transport (see Figure 5.41). The Raman signal also supports the suggestions for PBDTTT-EFT intercalations leading to change of dihedral angle and the increase in π - π spacing. Finally, the correlation between fill factor and shunt resistance as a function of blend ratio provides sufficient information to suggest, that the charge carriers transport network can be influenced by the quantitative presence of PC₇₁BM leading to lower leakage current. Most importantly that the best optimised D:A ratio for PBDTTT-EFT: PC₇₁BM is 1:2 respectively.

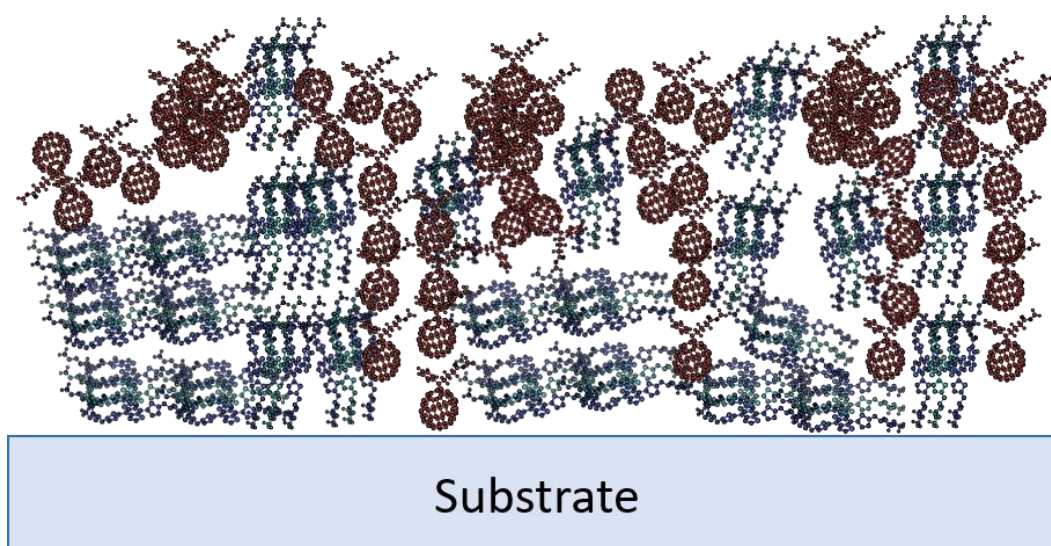


Figure 5.41: Schematic diagram of PBDTTT-EFT: PC₇₁BM blend illustrating the bi-continuous network formation of PC₇₁BM (red) and PBDTTT-EFT (blue) molecules.

5.3.10 Fullerene Derivative Acceptor Materials

In this section, the influence of different fullerene derivative acceptor materials (PC₇₁BM, PC₆₁BM and IC₆₁BA) on PBDTTT-EFT polymer in blended BHJ system is investigated. PBDTTT-EFT blended with different acceptor materials were fabricated for either optical and structural investigations or electrical characterisations. The sample preparation and fabrication techniques are described in *section 4.1.3*.

The optical absorption spectrum and the impact of different acceptor materials in the blend are fundamentally important for this investigation. The averaged J-V characteristic curves, and optical absorption profile of the blended samples are presented in Figure 5.42. J-V characteristic curves under illumination illustrate (*Figure 5.42a*) that the active layer containing PC₇₁BM shows the highest J_{sc} and lowest V_{oc}. Devices fabricated from EFT: IC₆₁BA blends show the opposite; highest V_{oc} and lowest J_{sc}. The electrical parameters extracted from the J-V characteristic curves are presented in Table 5.17. From Figure 5.42b, it is evident that PBDTTT-EFT: PC₇₁BM thin film has higher absorption in 350 – 700 nm range compared to the other samples. This is due to the fact that PC₇₁BM has greater absorption in that region compared to PC₆₁BM and IC₆₁BA (see Figure 5.2), This can also be seen from the figure's inset which shows the darker film for samples blended with PC₇₁BM.

Table 5.17: Extracted electrical parameters from the averaged J-V characteristic curves for EFT: PC₇₁BM, EFT: PC₆₁BM, and EFT: IC₆₁BA as well as the total absorption for each sample in the range of 350 – 850 nm wavelength.

Samples	J _{sc} (mA cm ⁻²)	V _{oc} (V)	FF	PCE (%)	R _s (Ω cm ²)	R _{sh} (Ω cm ²)	UV-Vis Area (nm) (350 – 800)
PBDTTT-EFT: PC ₇₁ BM	19.08	0.79	0.63	9.56	7.26	526.33	412.07
PBDTTT-EFT: PC ₆₁ BM	15.87	0.81	0.65	8.44	8.11	963.17	260.83
PBDTTT-EFT: IC ₆₁ BA	13.06	0.99	0.45	5.86	17.43	285.58	245.86

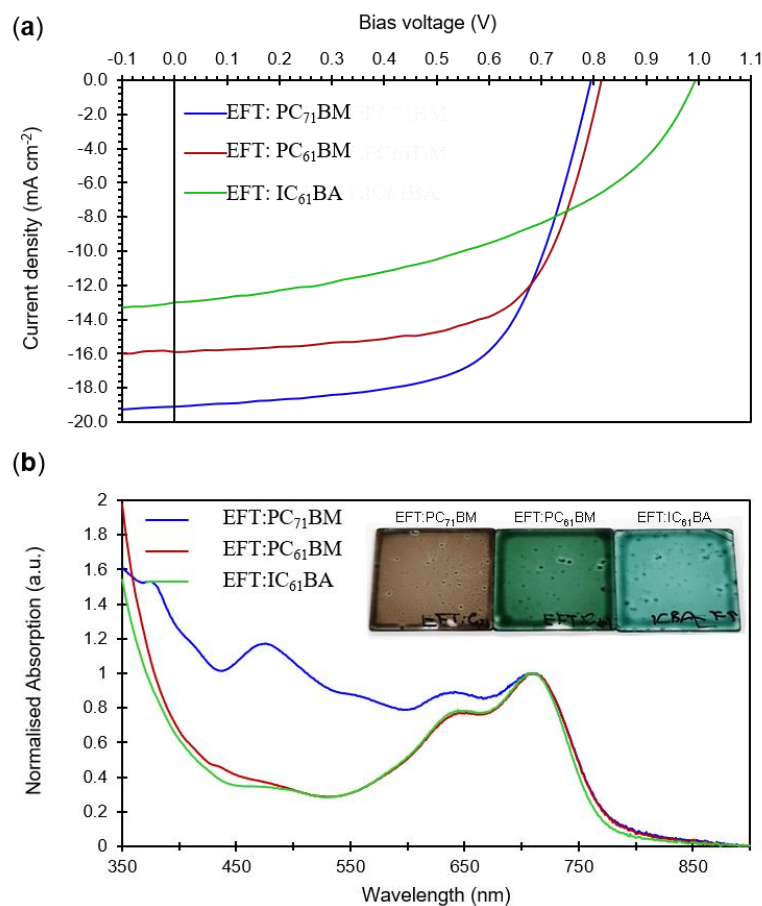


Figure 5.42: J-V characteristic curves of PBDTTT-EFT: PC₇₁BM, PBDTTT-EFT: PC₆₁BM and PBDTTT-EFT: IC₆₁BA (a) Averaged J-V curves, (b) UV-Vis spectra profile, inset: images of the thin films.

As it can be seen from Table 5.17, the highest PCE belongs to devices fabricated from active layer composed of EFT: PC₇₁BM with average PCE of 9.56 %, followed by 8.44% and 5.86% for EFT: PC₆₁BM and EFT: IC₆₁BA respectively. Although EFT: IC₆₁BA sample has the highest V_{oc} parameter, it also has the lowest J_{sc} and FF parameter. Such observations have been previously reported, and the reason for high V_{oc} value is due to a more substantial difference between HOMO of the EFT and LUMO of IC₆₁BA [218].

Although, to a degree, the reduction in J_{sc} for PBDTTT-EFT blended with PC₆₁BM and IC₆₁BA can be related to their absorption profile, the massive decrease of J_{sc} and FF for PBDTTT-EFT: IC₆₁BA cannot be entirely due to lack of absorption since the absorption profile of PBDTTT-EFT: IC₆₁BA and PBDTTT-EFT: PC₆₁BM are very close. As it can be seen from Table 5.17, the reduction in total absorption (integration of spectrum) in the range of 350 – 800 nm doesn't follow the trend of J_{sc} parameter. It

has been reported that blending IC₆₁BA (instead of PC₆₁BM) with P3HT enhances the device performance. However, using IC₆₁BA with low bandgap BDT-based polymers results in poor device performances. Yan et al. investigated the device performance of PBDTTT-C-T blended with PC₆₁BM and IC₆₁BA, and they reported that using IC₆₁BA instead of PC₆₁BM as an acceptor material has reduced the PCE from 6.2% to 3.5%.

Although they have reported high V_{oc} for PBDTTT-C-T: IC₆₁BA, the J_{sc} and FF were low compared to a device composed of PBDTTT-C-T: PC₆₁BM [2]. They proposed that such reduction in PCE is due to poor structural network formation of the polymer and fullerene domains and their miscibility [2], [259]. To investigate this, Photoluminescence (PL) spectroscopy is employed to collect a spectrum of the three samples using 514 nm excitation laser. The collected spectra for blended and pristine films are presented in Figure 5.41. The PL quenching efficiency (Q.E.) of each blended spectrum (with respect to pristine PBDTTT-EFT) is also presented in Figure 5.43.

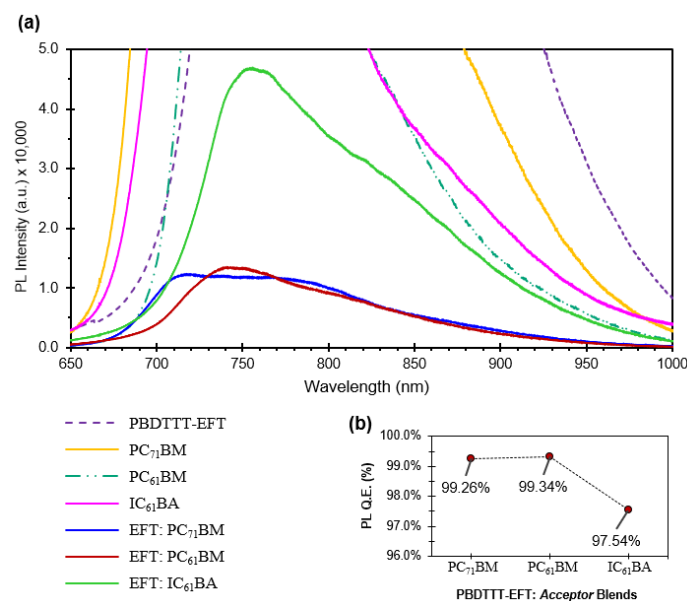


Figure 5.43: (a) PL spectra profile of pristine EFT, PC₇₁BM, PC₆₁BM, IC₆₁BA and blend of EFT: PC₇₁BM, EFT: PC₆₁BM, EFT: IC₆₁BA. (b) PL Q.E. with respect to pristine EFT.

As is evident from, Figure 5.43b, blended samples composed of PCBM (C₆₁ or C₇₁) have the highest Q.E., with PBDTTT-EFT: PC₆₁BM having the higher Q.E. In order to understand the impact of the D/A interface on the electrical performance of the device, Q.E. and FF parameters are plotted as a function of different acceptor blends in Figure 5.44.

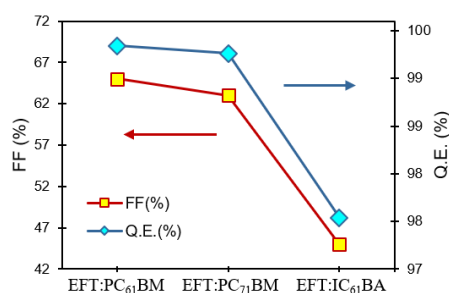


Figure 5.44: Correlation graph between Q.E. and FF as a function of blends with different acceptors.

As can be seen, FF and Q.E. are strongly correlated to each other and follow the same trend. Therefore, the lack of D/A interface in PBDTTT-EFT: IC₆₁BA sample explains the poor FF value obtained. These observations are in good agreement with Yan et al. [2], suggestions.

However, relying only on optoelectronic analysis does not fully explain the lack of IC₆₁BA performance with BDT-based polymers. Therefore, further investigations on the PBDTTT-EFT: IC₆₁BA samples are needed to elucidate the reason for lack of device performance and incompatibility of IC₆₁BA with PBDTTT-EFT. The morphological properties of these samples are investigated using AFM technique and the collected topography, and phase images are presented in Figure 5.45.

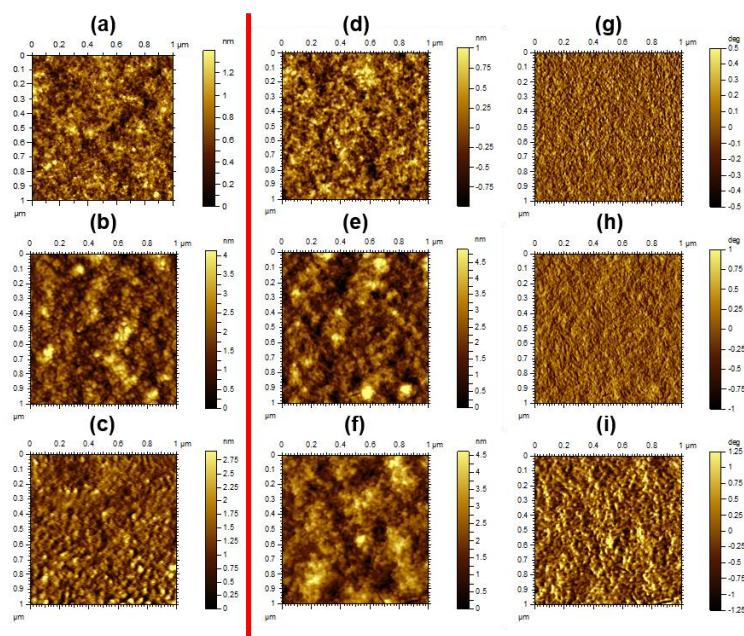


Figure 5.45: AFM images: (a–c) Topography images of pristine PC₆₁BM, PC₇₁BM, IC₆₁BA; (d–f) Topography images of EFT: PC₆₁BM, EFT: PC₇₁BM, EFT: IC₆₁BA; (g–i) Phase images of EFT: PC₆₁BM, EFT: PC₇₁BM, EFT: IC₆₁BA. Redline distinguishes Topography images between pristine and blended films.

From the topography images, the surface roughness of each sample was determined and is presented in Table 5.18. $|\Delta S_q|$ is the absolute difference between the S_q of the blended sample and its corresponding pristine acceptor.

Table 5.18: Surface roughness of blended films and pristine acceptor materials (S_q), the absolute difference between pristine and blend surface roughness $|\Delta S_q|$, and series resistance (R_s).

Sample	S_q (nm)	$ \Delta S_q $ (nm)	R_s ($\Omega \text{ cm}^2$)
EFT:PC ₇₁ BM	0.795	0.017	7.26
EFT:PC ₆₁ BM	0.276	0.032	8.11
EFT:IC ₆₁ BA	0.915	0.450	17.43
PC ₇₁ BM	0.778	-	-
PC ₆₁ BM	0.244	-	-
IC ₆₁ BA	0.465	-	-

From the $\Delta|S_q|$ and R_s parameters, they follow the same trend. Indicating the active layer which has the lowest R_s value correlates to the sample which has the lowest $\Delta|S_q|$. PBDTTT-EFT: IC₆₁BA has the poorest R_s and highest $|\Delta S_q|$, indicating that in this blended sample, least amount of IC₆₁BA is on the top surface of the film, which is beneficial for electron charge collection. From these results, it seems that IC₆₁BA has the least migration to the top surface. To fully understand this, molecular structuring techniques such as GIXRD is required to investigate these samples. Therefore, OOP GIXRD diffractogram pattern of PBDTTT-EFT: PC₇₁BM, PBDTTT-EFT: PC₆₁BM and PBDTTT-EFT: IC₆₁BA are collected and presented in Figure 5.46.

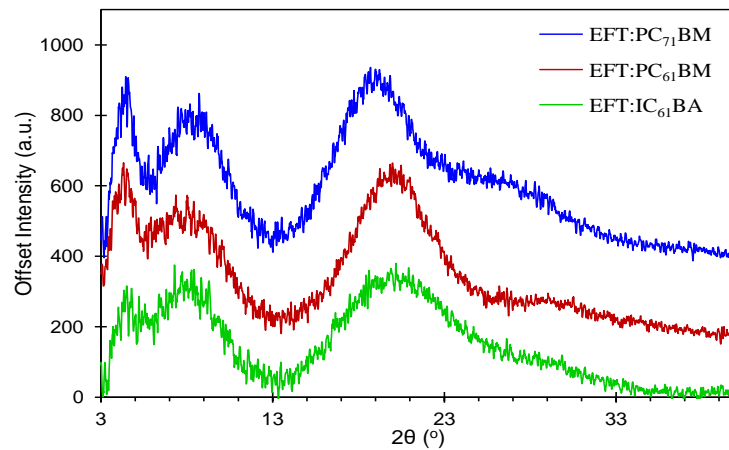


Figure 5.46: OOP GIXRD diffractograms of PBDTTT-EFT: PC₇₁BM, PBDTTT-EFT: PC₆₁BM and PBDTTT-EFT: IC₆₁BA. The intensity has been offset for clearer representation.

In sections 5.2.5 & 5.3.9, the peaks in OOP GIXRD were identified and associated with each material at various 2θ . To evaluate the impact of different acceptor materials on PBDTTT-EFT structural parameters as well as the vertical segregation of the acceptor molecules, computer curve fits based on Gaussian & Lorentzian curve fit were used to analyse each diffractogram profile. The extracted parameters are presented in Table 5.19.

Table 5.19: Extracted parameters from GIXRD computer model curve fits (a) d_{100} plane of PBDTTT-EFT, (b) d_{010} plane of PBDTTT-EFT, and (c) d_{200} plane of acceptor materials within the blend.

	Sample	2θ ($^\circ$)	d (Å)	FWHM ($^\circ$)	L_c (Å)	no. Stacks	Intensity (a.u.)
(a)	PBDTTT-EFT	-	-	-	-	-	-
	d_{100} EFT:IC ₆₁ BA	4.28	20.63	1.48	53.71	2.60	195
	EFT:PC ₆₁ BM	4.30	20.52	1.42	55.99	2.73	380
	EFT:PC ₇₁ BM	4.36	20.24	1.43	55.63	2.75	401
(b)	PBDTTT-EFT	22.69	3.91	5.65	14.34	3.67	1215
	d_{010} EFT:IC ₆₁ BA	20.99	4.23	7.41	10.91	2.58	280
	EFT:PC ₆₁ BM	20.50	4.33	6.05	13.34	2.55	116
	EFT:PC ₇₁ BM	19.25	4.61	5.74	14.05	3.05	188
(c)	d_{200} EFT:IC ₆₁ BA	18.17	4.88	5.93	15.57	2.78	103
	EFT:PC ₆₁ BM	19.83	4.47	5.03	16.03	3.59	314
	EFT:PC ₇₁ BM	18.25	4.86	4.68	17.19	3.54	274

As it can be seen from the extracted parameters in Table 5.19, the active layer composed of EFT: PC₇₁BM has the highest quantity of EFT molecules in *Edge-on* orientation (d_{100} plane) followed by EFT: PC₆₁BM and EFT: IC₆₁BA. It can also be seen that EFT: PC₇₁BM samples show the most EFT intercalated alkyl side chains with d_{100} spacing of 20.24 Å. It is evident that PC₇₁BM presence in the blend has had the most influence on changing the preferred molecular orientation of EFT.

However, it had the least distortion of EFT π - π stacking, which is beneficial for charge transport. In contrast, EFT: IC₆₁BA sample shows the most distortion for the EFT molecule for both π - π stacking in *Face-on* and alkyl *Edge-on* orientation. This is evident from the peak's FWHM, L_c and number of stacks in d_{100} and d_{010} plane. Although the total number of EFT *Face-on* molecules is the highest for EFT: IC₆₁BA samples, but their stacking number is the lowest amongst the three samples. Similar

observation for distortion of EFT molecules upon introduction of IC₆₁BA into the blend has also been reported by McNeil et al. [218]. In *section 5.2.9*, it was established that the introduction of PC₇₁BM initiates a change in the preferred molecular orientation in EFT molecules. In this study, similar behaviour can be observed. However, the degree of change in preferred orientation of EFT molecule seems to be dependent on the acceptor material used in the blend.

Table 5.19c presents the d_{200} plane parameters belonging to the acceptor materials within the blend. In the previous section, it was established that parameters of the d_{200} plane could be used to measure the level of vertical segregation of the PC₇₁BM molecules. From the intensity values in Table 5.19c, the highest value belongs to the blended sample containing PC₆₁BM and the lowest value to IC₆₁BA. The number of stacks in the d_{200} direction also follows the same trend. These results will indicate that in samples of EFT: IC₆₁BA, the acceptor molecules (IC₆₁BA) have the least vertical segregation, hence poor charge extraction at the cathode interface.

In order to support the analysis comments made on the OOP GIXRD, Raman spectroscopy is employed to elucidate the possible changes in the molecular structuring of different active layer blends. The importance and application of Raman spectroscopy have been previously discussed. The data collection and analysis are similar to *section 5.2.9*. The collected spectra are illustrated in Figure 5.47. Using computer curve-fitting models, FWHM parameters were extracted for each identified peak. The obtained data are presented in Table 5.20.

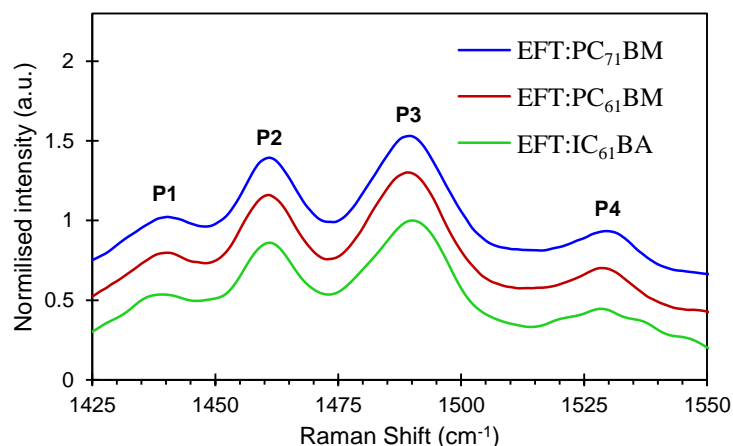


Figure 5.47: (a) Raman spectra profile for PBDTTT-EFT: acceptor blends under 785 nm excitation laser with peak identification (P1 – P4).

Table 5.20: FWHM parameters for identified Raman peaks (P1 – P4).

	FWHM (cm ⁻¹)			
	P1	P2	P3	P4
EFT:IC ₆₁ BA	20.19	15.54	20.92	19.61
EFT:PC ₆₁ BM	15.46	15.60	20.82	15.80
EFT:PC ₇₁ BM	16.26	15.70	20.78	15.14

As is evident from the FWHM parameters in Table 5.20, the FWHM for P2 and P3 belonging to the backbone of PBDTTT-EFT molecule do not show significant change, indicative that the backbone structure of PBDTTT-EFT is not altered regardless of the acceptor material used in the blend. However, P1 and P4 show significant changes in FWHM, which are dependent on the acceptor material used in the blend. In order to identify the impact of acceptor material on the molecular structure of PBDTTT-EFT, correlation graphs between Raman FWHM and OOP GIXRD FWHM have been plotted in Figure 5.48. Figure 5.48a illustrates the correlation of FWHM between P1 and d_{100} plane. Figure 5.48b the correlation of FWHM between P4 and d_{010} plane.

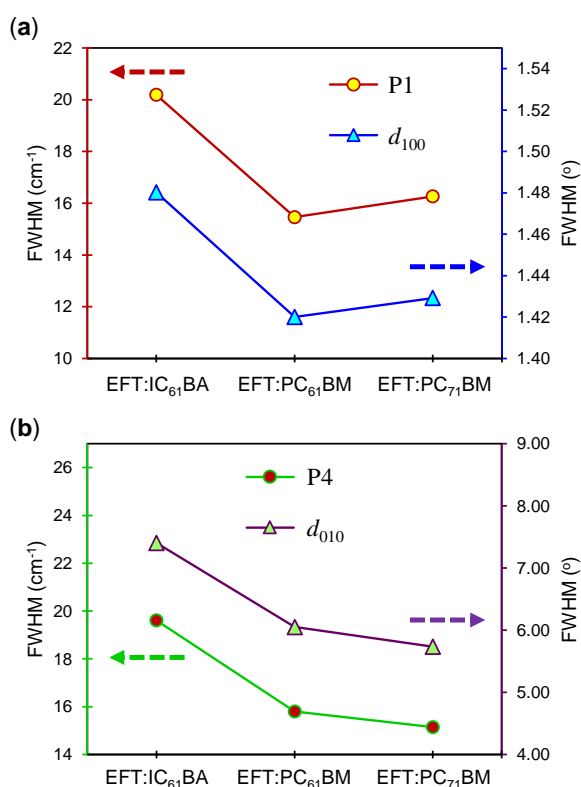


Figure 5.48: Correlation graph between FWHM of Raman peaks and d-spacing for each blended thin film. (a) Raman P1 FWHM and d_{100} FWHM, (b) Raman P4 FWHM and d_{010} FWHM.

As can be seen from the plots in Figure 5.48, there is a strong correlation between Raman and GIXRD FWHM data. Supporting the suggestions made for the change in the molecular orientation of PBDTTT-EFT observed in GIXRD diffractograms.

To understand the influence of different acceptor materials on the device performance, it is essential to investigate the charge carrier mobility for each sample composed of the different active layer. Therefore, single charge carrier devices, i.e., electron / hole – only devices were fabricated, similar device fabrication process (using charge blocking layers accordingly). Fabrication details of these devices are described in *Chapter 4, section 4.10* and the device architecture is shown in Figure 4.29.

The averaged dark J-V characteristics of the electron / hole – only devices for each sample are shown in Figure 5.49 and Figure 5.50, respectively. Upon applying a bias voltage across the single charge carrier devices, it was noted that at low voltages (0.1 – 1.0 V), J-V property obeys Ohm's law. At higher voltages (2 – 5 V), J-V behaviour deviates from Ohm's law and follows the SCLC relationship. At even higher voltages (>5 V), it was noted that the J-V relationship indicates trap-filling states associated with exponents greater than 2 known as *Power Law* (Equation 6) [260].

For all the active layer blend films, the dielectric constant of the active layer was assumed to be ~3.4, and the film thickness of the active layer was measured to be ~170 nm. Using the equations stated in *Chapter 2, section 2.2.2*, charge mobility parameters are calculated from the plots in Figures 5.49 and 5.50. The extracted parameters are presented in Table 5.21.

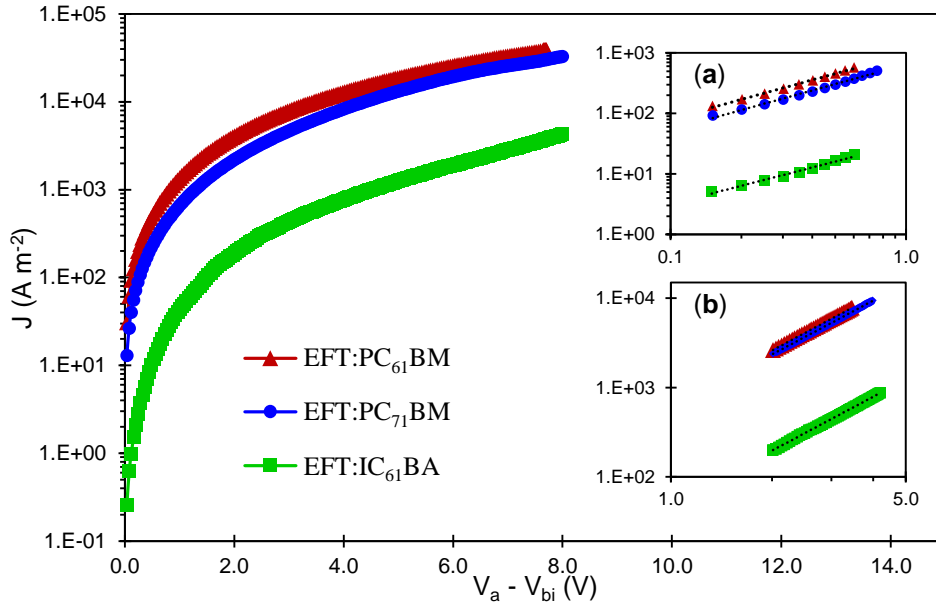


Figure 5.49: Dark J-V plot of electron-only devices for PBDTTT-EFT blended with PC₆₁BM, PC₇₁BM and IC₆₁BA; Inset: (a) Ohmic region, (b) SCLC region.

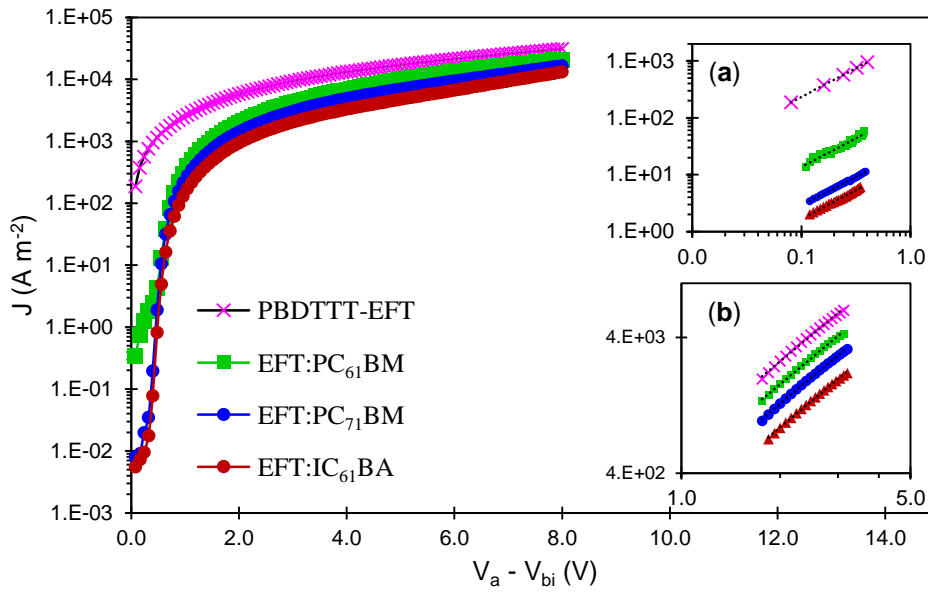


Figure 5.50: Dark J-V plot of the hole only devices for pristine PBDTTT-EFT and its blended films with PC₆₁BM, PC₇₁BM and IC₆₁BA; Inset: (a) Ohmic region, (b) SCLC region.

Table 5.21: Charge mobility measurement parameters extracted from each sample.

	PBDTTT-EFT	EFT:IC ₆₁ BA	EFT:PC ₇₁ BM	EFT:PC ₆₁ BM
μ_e (m ² V ⁻¹ s ⁻¹)	-	7.16×10^{-9}	8.53×10^{-8}	9.49×10^{-8}
μ_h (m ² V ⁻¹ s ⁻¹)	9.59×10^{-8}	6.50×10^{-8}	4.67×10^{-8}	3.13×10^{-8}
μ_e / μ_h	-	0.11	1.79	3.03
n (m ⁻³)	-	5.12×10^{21}	7.64×10^{21}	1.06×10^{22}
p (m ⁻³)	2.64×10^{22}	2.26×10^{21}	6.55×10^{20}	5.70×10^{20}
N_{Te} (m ⁻³)	-	6.57×10^{24}	3.74×10^{24}	2.70×10^{24}
N_{Th} (m ⁻³)	-	4.20×10^{26}	3.27×10^{26}	3.31×10^{25}
Ohmic Region [†] (V)	-	0.15 - 0.6	0.1 - 0.6	0.1 - 0.75
SCLC Region [†] (V)	-	2.0 - 4.2	2.0 - 4.0	2.0 - 3.5
Trap-limited Region [†] (V)	-	7.2 - 7.8	7.2 - 7.8	7.2 - 7.8
Ohmic Region* (V)	0.1 - 0.4	0.1 - 0.4	0.1 - 0.4	0.1 - 0.4
SCLC Region* (V)	1.8 - 3.2	1.8 - 3.2	1.8 - 3.2	1.8 - 3.2
Trap-limited Region *(V)	-	7.4 - 7.8	7.4 - 7.8	7.4 - 7.8
Voltage range: [†] Electron only devices, * Hole only devices				

Table 5.21 shows that the hole-mobility of pristine PBDTTT-EFT is calculated to be 9.59×10^{-8} m² V⁻¹ s⁻¹. Reduction of this parameter is seen upon introducing acceptor material into the system. The highest hole-mobility amongst the three different samples belongs to EFT: IC₆₁BA; followed by EFT: PC₇₁BM and EFT: PC₆₁BM.

In contrast, the electron mobility of EFT: IC₆₁BA blend is the lowest amongst the three samples. It has been previously reported that IC₆₁BA has much lower electron mobility than PC₆₁BM, or PC₇₁BM [193], [261]. It is known that the charge transport mobility is dependent on the molecular structuring of the materials. From literature, it was reported that hole-mobility for BDT-based polymers takes place along the backbone of the polymer in π - π direction and having more *Face-on* configuration of the polymer would be beneficial for hole mobility [40].

Therefore, the fact that EFT: IC₆₁BA active layer has higher hole-mobility can be confirmed by the GIXRD results indicating that this blend has the highest amount of

EFT molecules in *Face-on* orientation. Similarly, EFT: PC₆₁BM with the lowest hole-mobility, has the least amount of *Face-on* EFT molecules within the blend.

In addition, the electron-mobility parameters follow the same trend as the level of acceptor molecules stacked in a vertical direction. It has been reported that ‘electron’ transport undergoes a ‘hopping’ mechanism via the acceptor material in the vertical direction [25], [262]. Hence, the highest electron mobility belongs to EFT: PC₆₁BM which has the highest amount of acceptor molecules arrayed in the vertical direction (d_{200} plane intensity) and the lowest electron mobility belongs to EFT: IC₆₁BA which has the lowest amount of acceptor molecules arrayed in the vertical direction.

In order to visualise such statements, a series of correlation graphs between mobility parameters and the GIXRD parameters are plotted in Figure 5.51. These plots illustrate the correlation between mobility and crystallography parameters as a function of different active layers. The calculated *Pearson’s* correlation coefficient r is also included as an inset for each corresponding graph.

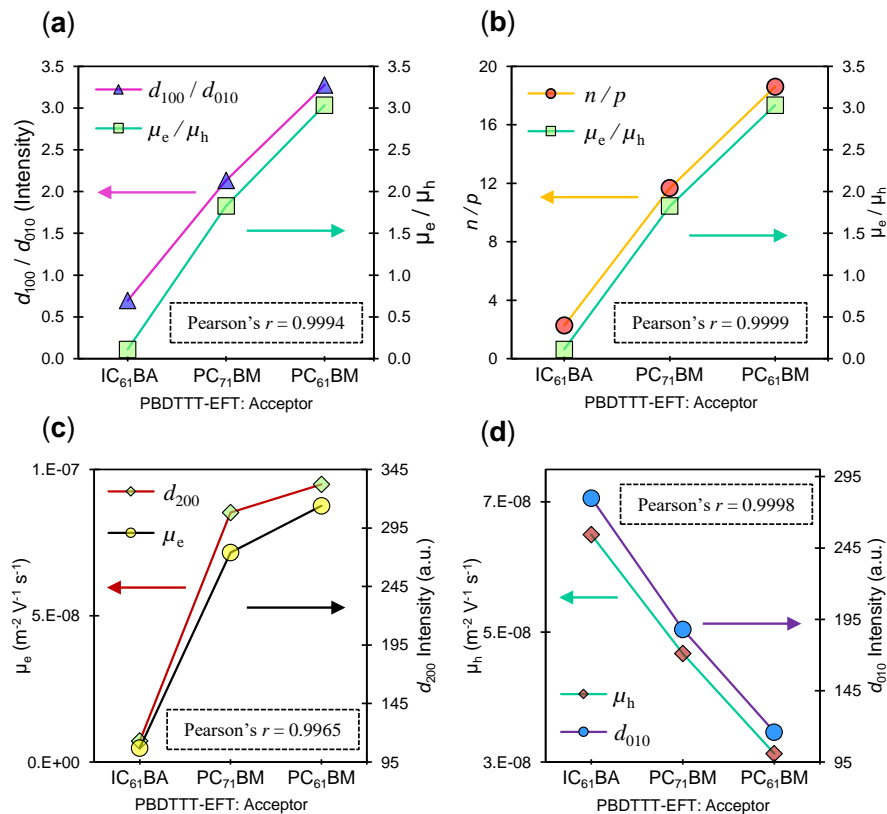


Figure 5.51: Correlation plots between (a) d_{100}/d_{010} intensity and μ_e/μ_h , (b) n/p and μ_e/μ_h , (c) μ_e and d_{200} intensity, (d) μ_h and d_{010} intensity as function of PBDTTT-EFT blended with different acceptors (IC₆₁BA, PC₇₁BM, and PC₆₁BM). Inset: Pearson's correlation coefficient (r).

Figure 5.51a shows the correlation between the ratio of *Edge-on* to *Face-on* EFT molecules and the ratio of electron / hole mobility. As is evident, there is a direct correlation between these parameters, which indicates that the ideal electron/hole ratio, which is beneficial for good charge transport depends on the orientation ratio of the EFT molecules. Figure 5.51b shows the correlation between the ratio of electron / hole density and the ratio of electron / hole mobility.

It can be seen that these parameters are strongly dependent on each other, and this is expected since the charge density is directly proportional to the mobility. Figure 5.51c illustrates the correlation between the intensity of the d_{200} plane (a quantitative indication of vertically segregated acceptor molecules) and electron mobility. As is evident, these parameters correlate with each other and follow the same trend. To simply explain this phenomenon, it can be said that the more acceptor materials stack in the vertical direction (within the bulk of the active layer) result in higher electron mobility.

Similarly, Figure 5.51d illustrates the correlation between the intensity of d_{010} for PBDTTT-EFT molecules (a quantitative indication of *Face-on* molecules) and the hole mobility. A strong correlation between these parameters can be observed, which would mean that the hole mobility is strongly dependent on the level of *Face-on* PBDTTT-EFT molecules.

To further investigate the impact of charge mobility and the molecular structure formation of donor and acceptor material on the device performance, the photocurrent generation and recombination mechanisms of each sample are investigated. The process of photocurrent generation has previously been discussed. It is known that the photocurrent generated for any OSC device is dependent on some factors such as; optical absorption of the active material(s), successful dissociation of excitons in charge transfer (CT) state and extraction of the free charges [32], [38].

Photocurrent generation measurement is a very useful tool for studying the effects of varying the acceptor material blended with PBDTTT-EFT on device performance. To study this effect within the active layer on the photocurrent generation in the PBDTTT-EFT based BHJ device (composed of different acceptor material used to form the active layer), J-V properties were measured under 1 sun, 1.5 AMG solar simulator conditions. The architecture of fabricated devices is the same as those described in previous section (standard device). In this section, all device fabrication

and characterisations were done under the N₂ glove box. A log-log graph of photocurrent ($J_{ph} = J_{light} - J_{dark}$) against the effective applied voltage ($V_{effe} = V_0 - V_{app}$) is illustrated in Figure 5.52, where V_0 is the bias voltage when $J_{light} = J_{dark}$.

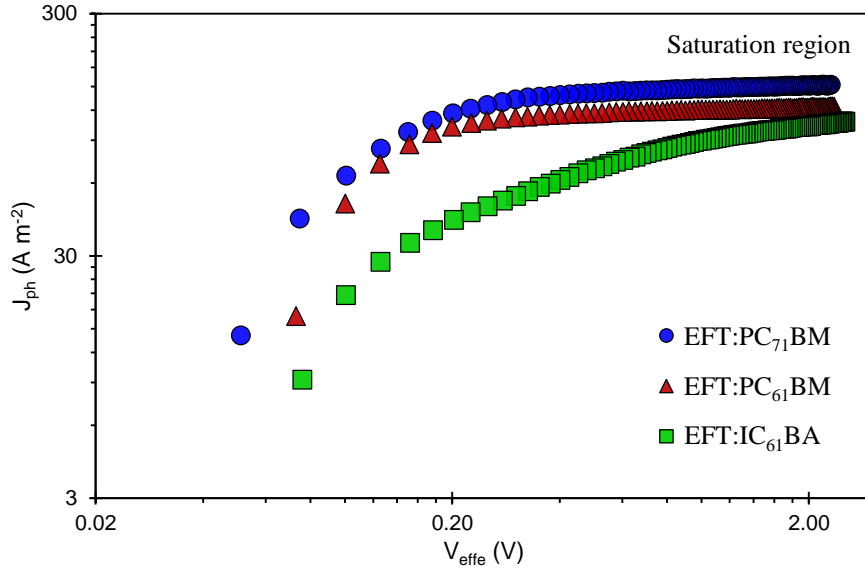


Figure 5.52: Log-Log graph of photocurrent (J_{ph}) against effective applied voltage (V_{effe}) for PBDTTT-EFT based devices blended with PC₇₁BM, PC₆₁BM and IC₆₁BA (active layer thickness ~ 170 nm).

As is evident from the data presented in Figure 5.52, an effective voltage of above 1V, J_{ph} begins to saturate for EFT: PC₇₁BM and EFT: PC₆₁BM samples. However, for EFT: IC₆₁BA samples, J_{ph} saturates at a higher effective voltage ($V_0 - V_{app} > 1.6$ V). This is denoted as the ‘*Saturation region*’ in Figure 5.50. Important to note that only a certain fraction of photo-generated excitons will dissociate into free charges with the probability $P(E,T)$, at any given electric field and temperature [143]. Generation of free charge carriers $G(E,T)$ is very much dependent on electric field and temperature and is mathematically expressed as [176]:

$$G(E, T) = G_{max}P(E, T) \dots \dots \dots (46)$$

where G_{max} is the maximum generation rate and is mathematically expressed as:

$$J_{sat} = qG_{max}l \dots \dots \dots (47)$$

where J_{sat} is the saturation current density, q is the electron charge, and l is the device active layer film thickness (for this study the active layer of the devices were ~ 170 nm thick). Since there is no temperature change for the samples, and they are all under identical temperature condition, the T factor is removed from the probability and generation representations. The probability of exciton dissociation can also be expressed as:

$$J_{ph} = qG_{max}P(E)l \dots \dots \dots (48)$$

Which can be further simplified to:

$$P(E) = \frac{J_{ph}}{J_{sat}} \dots \dots \dots (49)$$

Using the equations above, G_{max} and $P(E)$ were calculated using experimental data shown in Figure 5.50. Summary of the photovoltaic parameters for PBDTTT-EFT based devices blended with different acceptor materials (PC₇₁BM, PC₆₁BM and IC₆₁BA) are presented in Table 5.22. Probability of exciton dissociation [$P(E)$] is calculated at different electric fields: $V_{effe} = V_0$, $V_{effe} = V_{max}$ and $V_{effe} = V_{oc}$.

Table 5.22: Summary of PV parameters for PBDTTT-EFT based devices blended with acceptor materials (PC₇₁BM, PC₆₁BM and IC₆₁BA) with an active layer film thickness of ~ 170 nm.

	EFT:PC ₇₁ BM	EFT:PC ₆₁ BM	EFT:IC ₆₁ BA
J_{sc} (A m ⁻²)	190.80	158.70	130.60
V_{oc} (V)	0.79	0.81	0.99
FF	0.63	0.65	0.45
PCE (%)	9.56	8.44	5.86
G_{max} (m ⁻³ s ⁻¹)	5.59×10^{27}	4.52×10^{27}	3.67×10^{27}
$P(E)$ @ V_0	0.940	0.974	0.906
$P(E)$ @ V_{max}	0.926	0.963	0.772
$P(E)$ @ V_{oc}	0.995	0.992	0.990

As can be seen from the calculated parameters in Table 5.22, the probability of exciton dissociation is very much dependent on the effective electric field across the device. In order to understand the relationship between the photocurrent generation, the probability of exciton dissociation and the device performance, correlation graphs between J_{sc} against G_{max} and FF against $P(E)$ are plotted and presented in Figure 5.53.

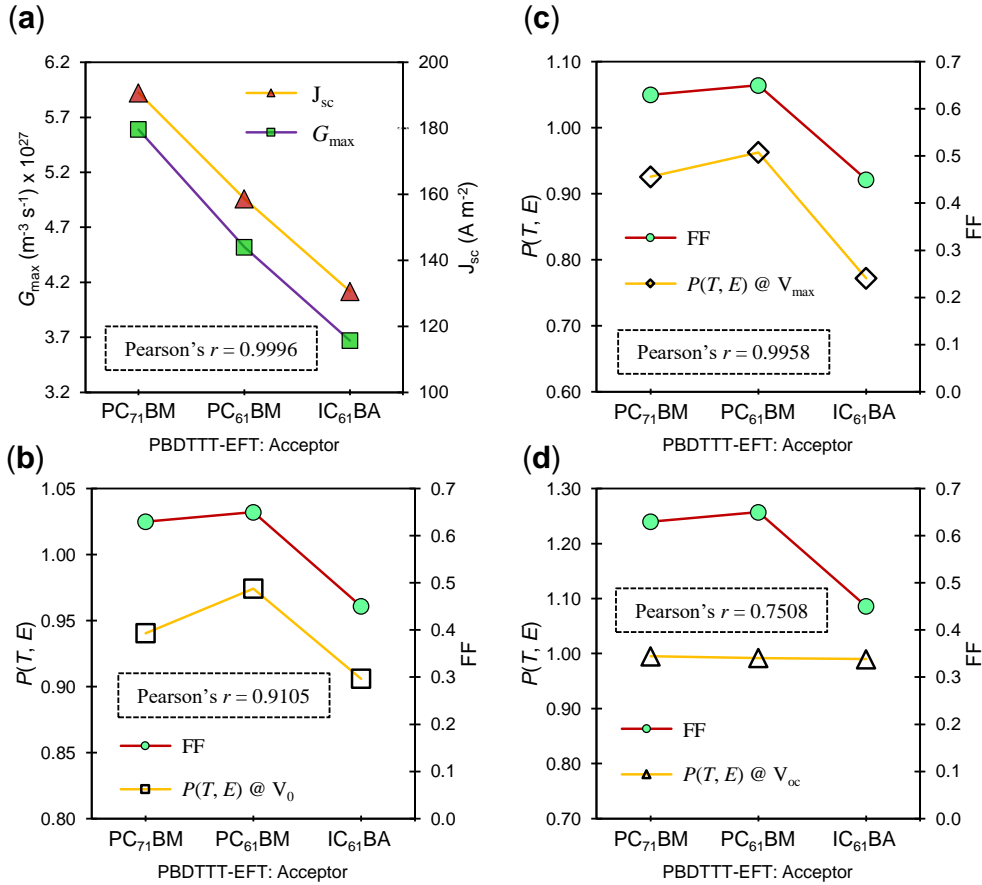


Figure 5.53: Correlation graphs for PBDTTT-EFT based devices blended with PC₇₁BM, PC₆₁BM and IC₆₁BA (a) G_{\max} and J_{sc} , (b) FF and $P(E) @ V_0$, (c) FF and $P(E) @ V_{\max}$, (d) FF and $P(E) @ V_{oc}$. Inset: Pearson's correlation coefficient.

As it can be seen from Figure 5.53a, there is a direct correlation between maximum generation rate of free charges (G_{\max}) and the short circuit current density (J_{sc}) with its r value calculated to be 0.9996 indicative that there is a strong correlation between these parameters. However, in the case of FF parameter and the calculated probability of exciton dissociation [$P(E)$] at given electric field; it can be seen that the strongest correlation (determined by r coefficient) belongs to FF and $P(E)$ at V_{\max} (Figure 5.53c). Therefore, it can be concluded that the fill factor is governed by the probability of exciton dissociation at V_{\max} .

To understand the reason for lack of performance in PBDTTT-EFT: IC₆₁BA based OSC devices fabricated in this work, the exciton dissociation and recombination mechanisms for the three samples are investigated. In an ideal solar cell, every incident photon would successfully dissociate into free electron and hole charges; which is then extracted at the corresponding electrodes. However, in fabricated OSCs, this does not

happen, and the performance of the cell is dependent on the dissociation and recombination mechanisms.

Usually, the generated excitons have only a few nanoseconds to reach the heterojunction to entering CT state before returning to the ground state. If the phase domain size between the donor and acceptor material is greater than the diffusion length (~ 10 nm), the exciton will likely recombine before entering CT state [32], [75], [263]. Excitons that do reach the heterojunction interface and enter CT state will only dissociate with a probability factor, and some of them will recombine. The recombination mechanism taking place during the CT state is referred to as ‘*Geminate recombination*’ [32].

This type of recombination occurs when the electron-hole pairs (excitons) generated from a single photon recombine at the D/A interface. Electron-hole pairs that do dissociate successfully at the D/A interface, still have a chance to recombine. This type of recombination is known as ‘*Non-geminate recombination*’. Non-geminate recombination is categorised into two mechanisms: ‘*Bimolecular*’ and ‘*Trap assisted*’ recombination [72], [73], [79]. Using the equations stated in *Chapter 2, section 2.3.2 & 2.3.3*; recombination parameters for EFT: PC₇₁BM, EFT: PC₆₁BM and EFT: IC₆₁BA devices are calculated and presented in Table 5.23.

Table 5.23: Recombination parameters calculated for EFT: PC₇₁BM, EFT: PC₆₁BM and EFT: IC₆₁BA devices.

	EFT:PC ₇₁ BM	EFT:PC ₆₁ BM	EFT:IC ₆₁ BA
μ_e (m ² V ⁻¹ s ⁻¹)	8.53×10^{-8}	9.49×10^{-8}	7.16×10^{-9}
μ_h (m ² V ⁻¹ s ⁻¹)	4.67×10^{-8}	3.13×10^{-8}	6.50×10^{-8}
n (m ⁻³)	7.64×10^{21}	1.06×10^{22}	5.12×10^{21}
p (m ⁻³)	6.55×10^{20}	5.70×10^{20}	2.26×10^{21}
N_{Te} (m ⁻³)	3.74×10^{24}	2.70×10^{24}	6.57×10^{24}
N_{Th} (m ⁻³)	3.27×10^{26}	3.31×10^{25}	4.20×10^{26}
B_L (m ³ s ⁻¹)	3.51×10^{-16}	3.36×10^{-16}	3.81×10^{-17}
R_B (m ⁻³ s ⁻¹)	1.76×10^{27}	2.03×10^{27}	4.41×10^{26}
C_n (m ³ s ⁻¹)	4.54×10^{-16}	5.05×10^{-16}	3.81×10^{-17}
C_p (m ³ s ⁻¹)	2.49×10^{-16}	1.67×10^{-16}	3.46×10^{-16}
B_{SRH} (m ³ s ⁻¹)	1.16×10^{-13}	4.17×10^{-14}	1.65×10^{-13}
R_{SRH} (m ⁻³ s ⁻¹)	5.82×10^{29}	2.52×10^{29}	1.91×10^{30}

As is evident from the parameters presented in Table 5.23, the μ_e and μ_h are within the same magnitude of order for EFT: PC₇₁BM and EFT: PC₆₁BM.

Therefore, when it comes to calculating the bimolecular recombination constant, the spatial average of the charge carrier mobility method is used. However, for devices composed of EFT: IC₆₁BA blend, the $\mu_e \ll \mu_h$, therefore the bimolecular recombination constant is calculated using ‘ $\min(\mu_e, \mu_h)$ ’ method. From the data presented in Table 5.23, EFT: IC₆₁BA has the lowest bimolecular recombination rate per unit volume ($B_L = 4.41 \times 10^{26} \text{ m}^{-3}\text{s}^{-1}$) and the highest trap-assisted SRH recombination rate per unit volume ($R_{\text{SHR}} = 1.91 \times 10^{30} \text{ m}^{-3}\text{s}^{-1}$).

This is indicative that most of the recombination process within EFT: IC₆₁BA samples is due to the trapped assisted mechanism. In contrast, EFT: PC₆₁BM has a different recombination mechanism. In Braun’s model, the probability of a bounded electron-hole pair to dissociate into free charge carriers at a given electric field is mathematically expressed as [30]:

$$P(E) = \frac{k_D(E)}{k_D(E) + k_F} \dots \dots \dots (20)$$

where, $P(E)$ is the probability of bound electron-hole pair to dissociate into free charge carriers at a given electric field E , $k_D(E)$ is electric field dependent decay rate constant of separated free charge carriers (decay rate constant of bimolecular recombination), k_F is geminate decay rate constant of electron-hole pairs back to ground state [263]. Therefore, k_D can be calculated from the following equation:

$$k_D(E) = [\max(n, p) \text{ or } \langle n + p \rangle] \times B_L \dots \dots \dots (50)$$

where, $\max(n, p)$ is the higher parameter of electron density n (m^{-3}) or hole density h (m^{-3}), $\langle n + p \rangle$ is a spatial average of electron and hole density, and B_L is the bimolecular recombination constant ($\text{m}^3 \text{ s}^{-1}$). By knowing $P(E)$ and k_D , the geminate decay rate constant can also be calculated using the following equation:

$$k_F = \left(\frac{k_D(E)}{P(E)} \right) - k_D(E) \dots \dots \dots (51)$$

$P(E)$ is taken at V_{max} since it has the highest correlation to the FF. Using the equations above, k_D and k_F parameters were calculated and tabulated in Table 5.24. It should be noted that k_D values calculated for EFT: PC₇₁BM and EFT: PC₆₁BM samples are based on the following equation since ($n \gg p$):

$$k_D(E) = \max(n, p) \times B_L \dots \dots \dots (52)$$

k_D value calculated for EFT: IC₆₁BA is based on the following equation since $n \sim p$:

$$k_D(E) = \langle n + p \rangle \times B_L \dots \dots \dots (53)$$

Table 5.24: Recombination decay constant rate parameters calculated for PBDTTT-EFT blended with PC₇₁BM, PC₆₁BM and IC₆₁BA.

	EFT:PC ₇₁ BM	EFT:PC ₆₁ BM	EFT:IC ₆₁ BA
$P(E) @ V_{\max}$	0.926	0.963	0.772
k_D (s ⁻¹)	2.68×10^6	3.56×10^6	1.41×10^5
$1 / k_D$ (μs)	0.37	0.28	7.11
k_F (s ⁻¹)	2.14×10^5	1.37×10^5	4.15×10^4
$1 / k_F$ (μs)	4.66	7.31	24.08

As is evident from the data in Table 5.24, devices fabricated from EFT: PC₆₁BM blend indicates that bimolecular recombination phenomenon occurs faster than the other samples, with $1/k_D$ of 0.28 μs, followed by 0.37 μs and 7.11 μs for EFT: PC₇₁BM and EFT: IC₆₁BA respectively. This is in good agreement with the R_B results calculated in Table 5.23. Based on the data in Table 5.24, it is interesting to note that the highest geminate recombination rate (k_F) belongs to EFT: PC₇₁BM, and it is reduced for EFT: PC₆₁BM and EFT: IC₆₁BA. Therefore, to understand the implication of these recombination mechanisms on the device performance, a series of correlation graphs has been plotted in Figure 5.54, which elucidate the relationship between molecular structuring and recombination rate.

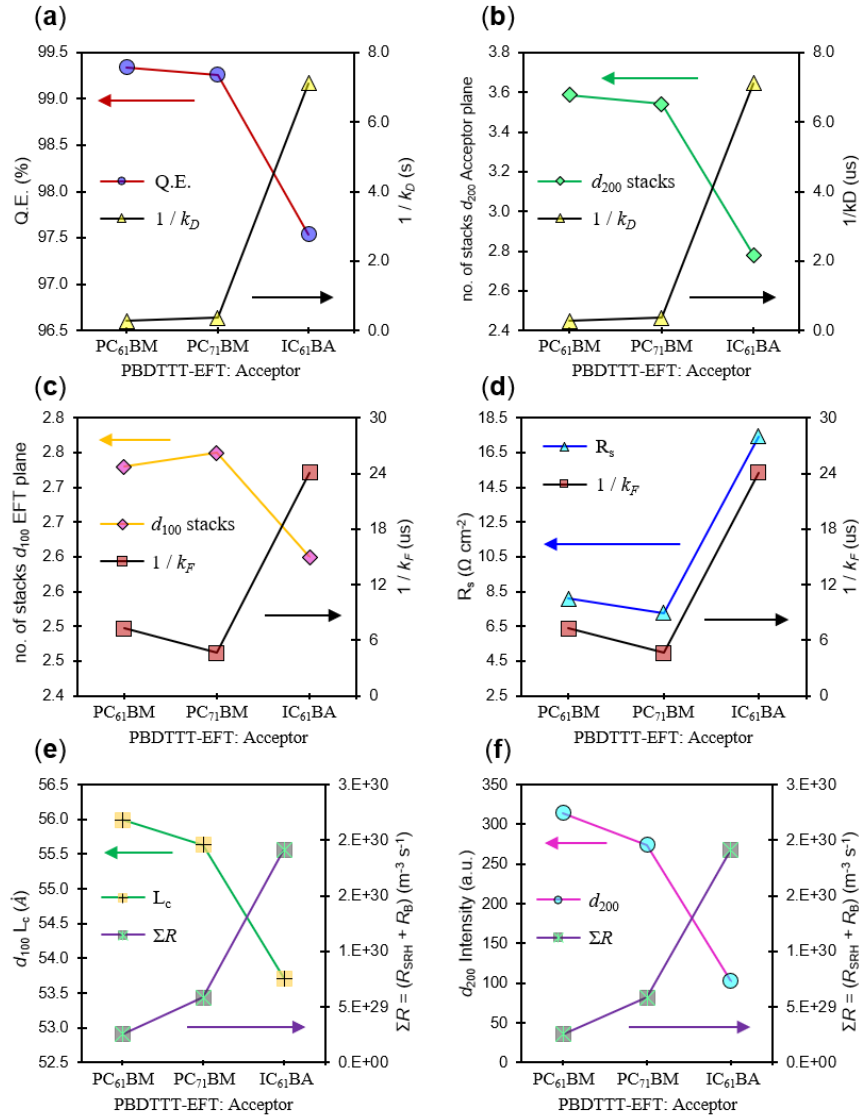


Figure 5.54: Correlation graphs for PBDTTT-EFT based OSC devices blended with PC₆₁BM, PC₇₁BM and IC₆₁BA: (a) PL Q.E. v.s. $1/k_D$, (b) Number of acceptor molecules stacked in d_{200} plane v.s. $1/k_D$, (c) Number of PBDTTT-EFT molecules stacked in d_{100} plane v.s. $1/k_F$, (d) Series resistance v.s. $1/k_F$, (e) Coherence length (crystal size) of PBDTTT-EFT molecules in d_{100} plane v.s. the sum of recombination rate per unit volume ($\Sigma R = R_{SRH} + R_B$) and (f) Acceptor molecules intensity in d_{200} plane (indicative of vertically segregated acceptor) v.s. the sum of recombination rate per unit volume ($\Sigma R = R_{SRH} + R_B$).

Figure 5.54a illustrates the relationship between quenching efficiency (Q.E.) and $1/k_D$ as a function of different active layers. As can be seen, these parameters are inversely proportional and follow the opposite trend. This suggests that the sample with the highest Q.E. has the highest bimolecular recombination rate. This would indicate that the PL quenching is governed by a bimolecular recombination mechanism. Figure

5.54b illustrates the relationship between the number of acceptor molecules stacked in the vertical direction (d_{200} plane) and the reciprocal of bimolecular recombination decay constant ($1/k_D$).

An inverse trend between these parameters can be seen, which would suggest that the higher the number of vertically stacked acceptor molecules, the higher bimolecular recombination rate of decay (k_D). An interesting observation to be made is that PL Q.E. and the number of acceptor materials vertically stacked are correlated. This indicates that in a blended system which has ‘good’ bi-continuous network of acceptor would have a higher chance of the bimolecular recombination mechanism in the CT state.

Interestingly, Figure 5.54c shows similar but opposite trend between the number of PBDTTT-EFT molecules stacked in *Edge-on* orientation and the reciprocal of geminate recombination decay constant $1/k_F$. This would suggest that the higher the quantity of PBDTTT-EFT molecules stacked in *Edge-on* orientation, the higher the rate of geminate recombination decay. Another interesting observation to be made is that by looking at the correlation graph (Figure 5.54d) between series resistance (R_s) and reciprocal of geminate recombination decay rate a similar pattern exists between these parameters when plotted as a function of PBDTTT-EFT blends with different acceptors.

From this graph, it can be concluded that devices with the lowest series resistance would have the higher geminate recombination decay rate. Figure 5.54e illustrates the correlation plot between the coherence length of PBDTTT-EFT molecules in an *Edge-on* orientation and the total sum of the recombination rate per unit volume of each active layer blend. As is evident, there is an opposing correlation between these two parameters. This would suggest that the longer the coherence length of PBDTTT-EFT molecules in d_{100} plane, the lower the overall recombination mechanisms and hence, better FF parameter of the device.

Figure 5.54f also shows the similar opposite trend between the quantitative presence of acceptor molecules vertically segregated (indicative via the intensity of the d_{200} plane) and the total sum of recombination rate per unit volume. Which would suggest that if more acceptor materials exist in the vertical direction, there will be less recombination for that device. From the comments made on Figures 5.54e and 5.54f, it can be suggested that there must be a direct relationship between the coherence

length of PBDTTT-EFT molecules (L_c) in d_{100} plane and the quantitative presence of the acceptor molecules in the vertical direction.

From Table 5.23, R_{SRH} values are more significant than R_B , which is a suggestion that the trap-assisted recombination is dominant in comparison to bimolecular recombination. The highest PCEs measured in the present work correspond PBDTTT-EFT: PC₇₁BM at 1:2 blend ratio. Therefore, it is expected that a lower recombination rate should be observed. However, this is not the case as the parameters in Tables 5.23, and 5.24 indicate. Devices with the highest PCE also have highest geminate recombination rate (k_f). In addition, it can be noticed that the trap concentrations (N_{Th} or N_{Te}) are for these devices EFT: PC₇₁BM is not the lowest.

Therefore, it can be concluded that devices with the lowest total sum of recombination rate per unit volume possess the best FF but not the best PCE. The fact that FET: PC₇₁BM has the best μ_e / μ_h ratio plays a vital role in charge transport to the respective electrodes, and therefore better PCE. What is interesting is that PBDTTT-EFT: IC₆₁BA, has the poorest PCE and μ_e / μ_h ratio as well as the highest sum of recombination rate per unit volume.

In order to provide further evidence for the domination of the recombination mechanism, the relationship between light intensity and open circuit voltage (V_{oc}) is explored (see *section 2.3.4* for details). It has been reported in the literature that studying the relationship between the variation of light intensity and V_{oc} would elucidate this matter [59], [264].

Therefore, the V_{oc} of these samples as a function of change in the illuminated light intensity are investigated. The variation of light intensity was achieved by using optical density filters. The following equation was presented to illustrate the relationship between V_{oc} and light intensity:

$$V_{oc} = \frac{E_g}{q} - \frac{k_B T}{q} \ln \left(\frac{[1 - P(E)] B_T N_{CV}^2}{P(E) G(E)} \right) \dots \dots \dots (29)$$

In a case that the bulk of the active layer in the OSC is free of traps, the equation above will have a slope of $S = k_B T/q$ (eV), when V_{oc} is plotted as a function of the logarithm of light intensity. It has been reported that S values higher than $k_B T/q$ are indicative of a trap-assisted recombination mechanism [79]. The plot of V_{oc} against the logarithm of light intensity is illustrated in Figure 5.55.

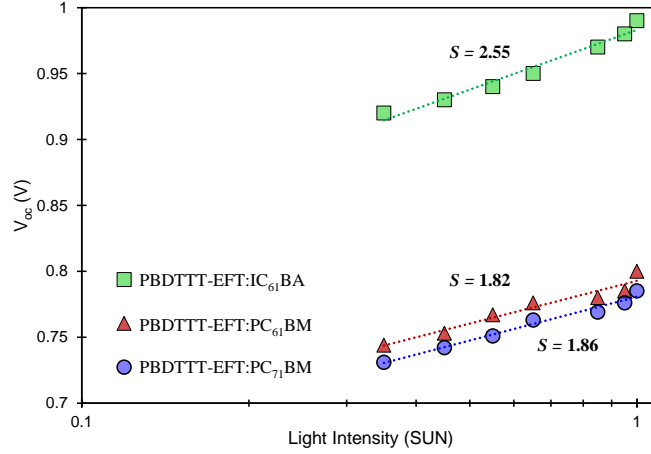


Figure 5.55: V_{oc} as a function of light intensity for PBDTTT-EFT blended with different acceptor materials (IC₆₁BA PC₆₁BM and PC₇₁BM). Dotted lines are linear fits used to determine the slope S .

As is evident from Figure 5.55, EFT: IC₆₁BA has a slope $S = 2.55$ ($k_B T/q$) indicates the highest trap-assisted recombination followed by EFT: PC₇₁BM, $S = 1.86$ ($k_B T/q$) and EFT: PC₆₁BM, $S = 1.82$ ($k_B T/q$). To further understand the impact of these trap-assisted recombination mechanisms on the device performance and charge transport, AC measurement (Impedance Spectroscopy, IS) study is employed.

As it was previously described in *Chapter 4, section 4.3*; Impedance Spectroscopy is known to be a useful tool for characterising the electrical properties of electronic devices and is primarily based on the measurement of the current response to an AC voltage applied to the OSC device as a function of frequency. Unlike DC methods, IS measurements, would evaluate the role of D:A interfaces within the bulk of the photoactive layer [265]. The IS measurements for PBDTTT-EFT blended with PC₇₁BM, PC₆₁BM and IC₆₁BA have been done under 1 sun illumination and no DC bias voltage. The obtained results are converted from *polar* to a *rectangular* format and are presented as a Cole-Cole plot in Figure 5.56.

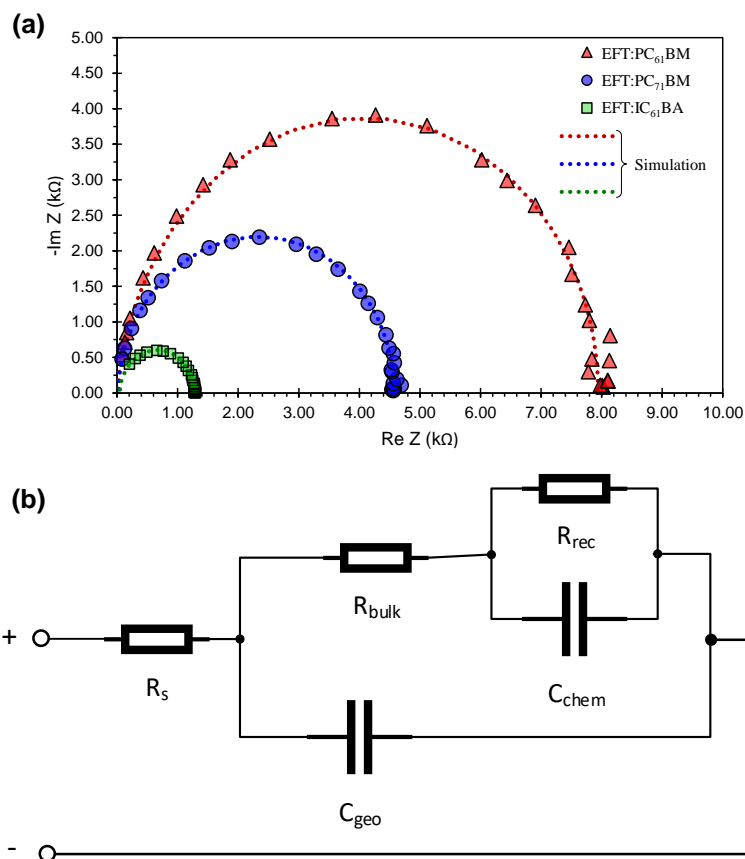


Figure 5.56: (a) Impedance spectra of PBDTTT-EFT blended with PC₆₁BM, PC₇₁BM and IC₆₁BA under 1 SUN illumination and no DC bias voltage (Simulated Dotted line are computer model fit based on simulation), (b) equivalent circuit model used to simulate the IS data.

It has been reported in the literature that parameters such as charge carrier lifetime, chemical capacitance and recombination resistance can be extracted from the IS measurements by developing an equivalent circuit model incorporating both resistive and capacitive elements [43]. Components used in the equivalent circuit model presented in Figure 5.56b are as follow; R_s is series resistance, R_{bulk} is bulk resistance, C_{geo} is geometrical capacitance, R_{rec} is the recombination resistance, and C_{chem} is the chemical capacitance of the active layer. Using EIS Spectrum analyser 1.0 software the IS obtained data for each sample were uploaded and by using the equivalent circuit model shown in Figure 5.56b, simulated data was generated (shown as dotted lines). From the computer model, the equivalent circuit model parameters were obtained and are presented in Table 5.25.

Table 5.25: Extracted parameters from the equivalent circuit models used to simulate the IS data

		EFT:PC ₇₁ BM	EFT:PC ₆₁ BM	EFT:IC ₆₁ BA
R _s	(Ω)	21.38	25.87	44.95
R _{bulk}	(kΩ)	3.23	4.80	1.06
R _{rec}	(kΩ)	2.56	3.12	0.66
C _{geo}	(nF)	3.22	2.80	3.25
C _{chem}	(nF)	3.59	2.54	9.57
τ _{avg}	(μs)	9.19	7.94	4.96

The average charge carrier lifetime was determined using the following equations [266]:

$$\tau_{avg} = R_{rec} C_{chem} \dots \dots \dots (54)$$

As is evident in Table 5.25, the most extended average charge carrier lifetime (τ_{avg}) belongs to EFT: PC₇₁BM devices, which possess the highest PCE and J_{sc}. Similarly, the poor performance of EFT: IC₆₁BA based OSC devices can be attributed to the fact that the charge carrier lifetime, which is the shortest amongst these samples.

This study can be summarised into the following achievements:

- Correlation between absorption levels of different active layers and the J_{sc} was demonstrated. Also, from the PL measurements, it was evident that the PL Q.E. correlates well with the FF parameter.
- From the AFM analysis, it was established that Δ|S_q| correlates well with R_s. Indicating that devices with the lowest Δ|S_q| have the lowest R_s.
- From GIXRD results, it was established that pristine IC₆₁BA has a less molecular ordering in comparison to the other fullerene derivative acceptor materials (PC₆₁BM & PC₇₁BM). This was also observed when the blend of EFT: IC₆₁BA was investigated. It was established that IC₆₁BA has the least impact on the preferred molecular orientation of PBDTTT-EFT, meaning in blends containing IC₆₁BA, more PBDTTT-EFT molecules remained in Face-on orientation in comparison to blends containing PC₆₁BM or PC₇₁BM. In fact, active layer blends containing PC₆₁BM showed the greatest change in preferred orientation of PBDTTT-EFT molecules. Based on the computer-generated

models, it was evident that PC₆₁BM molecules are more vertically segregated in comparison to PC₇₁BM and IC₆₁BA. Also, the side chain intercalation of the PBDTTT-EFT molecules and the increase in the π - π spacing were backed up with the results obtained from the Raman spectroscopy.

- From the mobility measurements, it was established that EFT: IC₆₁BA devices showed the highest hole mobility and the lowest electron mobility. In contrast EFT: PC₆₁BM devices had the highest electron mobility and the lowest hole mobility. This was expected since the transport of holes takes place on the backbone of BDT-based polymers (donors) which need PBDTTT-EFT molecules in Face-on orientation, and electron transport is directly related to the vertical segregation of the acceptor molecules. An important observation from the mobility measurements was the correlation between the μ_e/μ_h and d_{100}/d_{010} ratios.
- From the photocurrent generation and recombination analysis, it was established that the maximum generation rate and the J_{sc} are in good correlation as expected. The relationship between FF parameter and the probability of exciton dissociation was also agreed to be for $P(E) @ V_{max}$. Recombination analysis showed that the highest bimolecular recombination rate per unit volume belongs to EFT: PC₆₁BM, EFT: PC₇₁BM and EFT: IC₆₁BA, respectively. However, when trap-assisted recombination rate per unit volume is considered, EFT: IC₆₁BA has the highest rate, followed by EFT: PC₇₁BM and EFT: PC₆₁BM, respectively. When the total sum of the recombination was considered, it was established that EFT: PC₆₁BM has the lowest recombination rate per unit volume. The highest recombination rate per unit volume belonged to EFT: IC₆₁BA devices. Also, it was identified that the highest geminate recombination rate belongs to EFT: PC₇₁BM.
- From the study on the relationship between light intensity and V_{oc} , the recombination mechanism dominance in each sample was identified as trap-assisted, with EFT: IC₆₁BA having the highest trap-assisted recombination mechanism when compared to the other two samples.
- From the Impedance spectroscopy analysis, it was concluded that EFT: IC₆₁BA devices have the shortest charge carrier lifetime and EFT: PC₇₁BM have the highest lifetime, which correlates well with the obtained PCE values.

5.4 Summary

In this chapter, materials used for the active layer were characterised, and a series of studies were designed to optimise device performance for conventional architecture OSC with PBDTTT-EFT as the donor material and PC₇₁BM as the primary acceptor material, as well as other fullerene derivative acceptor materials. A systematic approach for enhancing the device performance was followed in this project, which was introduced in the introduction of this chapter, Figure 5.57 illustrates the summary of all the studies completed in this chapter.

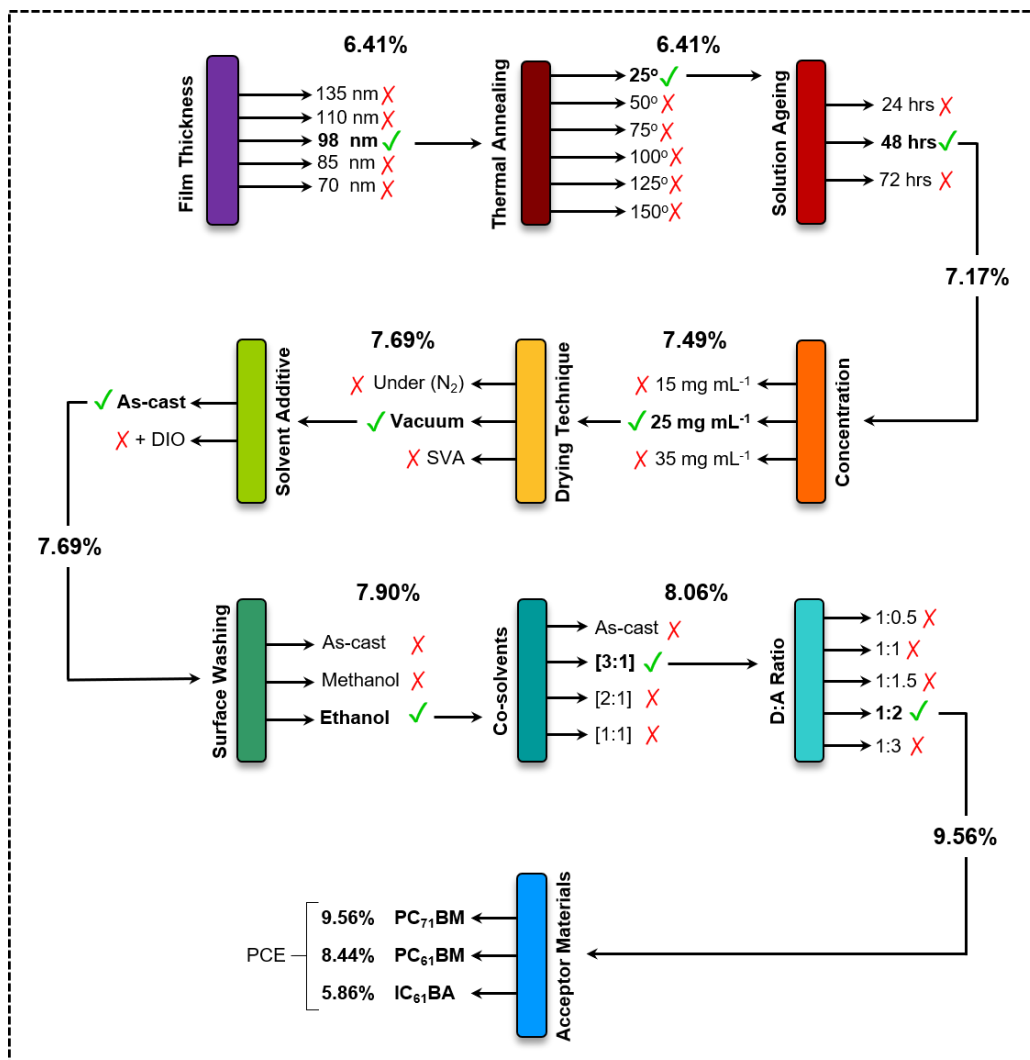


Figure 5.57: Workflow diagram for pilot study experiments in chapter 5, illustrating the success of each experiment and the highest PCE obtained from that process. [✓] marks represent the highest achieved PCE and [X] marks represent low-performance OSC devices.

CHAPTER 6

Conclusion & Future Work

In this chapter, conclusions are drawn from the experimental results and discussions which summarise the key points of this work. These summaries are bullet-pointed into relevant categories. Following the conclusion, a brief outlook of the future work in several significant areas for further improving the performance of OSCs are provided.

Conclusion:

- **Solution Ageing:** From *section 5.3.3*, it was concluded that as the active solution used to fabricate the active layer should be dissolved well prior to being spin cast. However, the time taken for the solution to dissolve is important; a fine-tuned time / ageing is required to achieve the desired blend mixture between donor and acceptor materials in the vial. If the ageing process is longer than the optimised timing, the D:A blend would be deteriorated and have a negative impact on device performance. Therefore, dissolving the D:A blend correctly is of importance. This was achieved by allowing the D:A blend solution to age in the vial prior to being used for active layer fabrication.

- **Thin Film Drying time, impacting the D:A phase domains:** From *section 5.3.5*, it was concluded that depending on how the fabricated active layer was dried, the D:A phase domain will be impacted. Fast-drying technique such as vacuum drying, straight after casting would result in the best separated D:A phase domains and formation of PC₇₁BM clusters which are beneficial for charge separation and transport.
- **GIXRD, change in molecular orientation of PBDTTT-EFT and acceptor migration to the thin film surface:** From the GIXRD results analysed in *sections 5.3.9 and 5.3.10*, for the first time, the existence of PBDTTT-EFT molecules in the *Edge-on* orientation was identified in the OOP mode upon blending with fullerene acceptor materials. This was achieved by correct background removal from the collected diffractograms. Based on this observation, as the percentage loading of PC₇₁BM in the blend was increased, the more PBDTTT-EFT molecules appeared in the *Edge-on* orientation as compared to their preferred *Face-on* molecular orientation. It was also noticed that as more PBDTTT-EFT molecules are becoming *Edge-on* oriented, the level of PC₇₁BM molecules stacking in the vertical direction increases. This is beneficial for electron charge transport and extraction. PBDTTT-EFT molecular orientation change from *Face-on* to *Edge-on* was very much dependent on the quantitative presence of and the type of the acceptor material in the blend. It was noticed that IC₆₁BA has the least impact on the molecular structure and orientation of PBDTTT-EFT compared to PC₇₁BM and PC₆₁BM when formed a blend. IC₆₁BA, in its pristine form, has the lowest vertical stacking, also when blended with PBDTTT-EFT, this acceptor material has the poorest vertical stacking. Since fewer acceptor materials are stacking vertically within the active layer blend of PBDTTT-EFT: IC₆₁BA, there will be fewer electrons being transported and extracted at the top surface. This can be clearly seen from the mobility data collected, indicating the lowest electron mobility belongs to samples fabricated from blends that contain IC₆₁BA as their acceptor material. From the mobility measurements it was established that PBDTTT-EFT: IC₆₁BA devices showed the highest hole mobility and the poorest electron mobility, in contrast PBDTTT-EFT: PC₆₁BM devices had shown the highest electron mobility and the poorest hole mobility. This was

expected since the transport of holes takes place on the backbone of BDT-based polymers (donors) and electron transport is directly related to the vertical segregation and stacking of the acceptor molecules. The recombination analysis showed that the highest bimolecular recombination rate per unit volume belongs to PBDTTT-EFT: PC₆₁BM followed by PBDTTT-EFT: PC₇₁BM and PBDTTT-EFT: IC₆₁BA, respectively. However, when trap-assisted recombination rate per unit volume is considered, PBDTTT-EFT: IC₆₁BA samples have the highest rate, followed by PBDTTT-EFT: PC₇₁BM and PBDTTT-EFT: PC₆₁BM, respectively, indicating that PBDTTT-EFT: IC₆₁BA samples have the poorest D:A network formation which is due to their molecular structure and orientation. Hence, most of the charges generated are trapped within the active layer and can't be extracted. When the total sum of the recombination was calculated, it was established that PBDTTT-EFT: PC₆₁BM has the lowest recombination rate per unit volume, which is why these samples have the highest FF and PL Q.E. parameters. Despite the V_{oc} enhancement for PBDTTT-EFT: IC₆₁BA devices, the overall performance is poor compared to using PC₆₁BM or PC₇₁BM as the acceptor material in the blend. Although it has been reported that IC₆₁BA enhances the device performance of some organic solar cells, it is not true for BDT based polymers. It seems that IC₆₁BA is incompatible with some polymers and to understand why the molecular structure of polymers which has shown signs of improvement must be investigated. OSCs that showed improved device performance upon using IC₆₁BA as their acceptor material was blended with polymers which all have a preferred *Edge-on* orientation. However, almost all of the BDT-based polymers have a *Face-on* orientation. Therefore, it can be concluded that one of the main reasons for the incompatibility of IC₆₁BA with BDT-based polymers for OSC application is due to lack of vertical stacking of IC₆₁BA and preferred molecular orientation of the polymers.

Future work

- **The solubility of materials for the active layer:** solubility of donor and acceptor materials is one of the critical factors for solution processed organic solar cell fabrication. Therefore, further investigating the role of solvent and how the donor / acceptor materials are dissolved is of importance. In order to commercialise OSC devices, environmentally friendly chemical / materials need to be used. Amongst which, solvents are one of them. Using green solvents such as toluene and o-Xylene as a replacement for CB and o-DCB could be the step forward in the future works.
- **Monitoring migration of acceptor material to film surface:** As it was mentioned in the conclusion section, vertical stacking and presence of acceptor material on the top surface of the active layer are crucial for charge transport and collection. Therefore, new techniques should be developed for faster monitoring of this phenomenon. Apart from GIXRD technique, Raman mapping is another useful technique which can be used to obtain visual pixelated images distinguishing the difference between materials on the film surface by colour coding. Developing such technique by writing image processing algorithms and data processing of scanned Raman mapped regions would also be the next step in the future works.

References

- [1] Y. He, H. Chen, J. Hou, and Y. Li, “Indene–C₆₀ Bisadduct: A New Acceptor for High-Performance Polymer Solar Cells,” *J. Am. Chem. Soc.*, vol. 132, no. 4, pp. 1377–1382, Feb. 2010.
- [2] H. Yan, D. Li, C. He, Z. Wei, Y. Yang, and Y. Li, “A material combination principle for highly efficient polymer solar cells investigated by mesoscopic phase heterogeneity,” *Nanoscale*, vol. 5, no. 23, p. 11649, 2013.
- [3] T. Fox, “Population: One Planet, Too Many People?,” *IMechE*, 2013. [Online]. Available: <http://www.sciencemediacentre.org/population-one-planet-too-many-people/>.
- [4] J. Tsao, N. Lewis, and G. Crabtree, “Solar FAQs,” 2006.
- [5] L. Dou *et al.*, “25th Anniversary Article: A Decade of Organic/Polymeric Photovoltaic Research,” *Adv. Mater.*, vol. 25, no. 46, pp. 6642–6671, Dec. 2013.
- [6] “Electricity Production Data | World Electricity Statistics | Enerdata.” [Online]. Available: <https://yearbook.enerdata.net/electricity/world-electricity-production-statistics.html>. [Accessed: 15-Feb-2018].
- [7] “World Power consumption | Electricity consumption | Enerdata.” [Online]. Available: <https://yearbook.enerdata.net/electricity/electricity-domestic-consumption-data.html>. [Accessed: 15-Feb-2018].
- [8] D. Hales, “Renewables 2018, Global Status Report,” 2018.
- [9] E. M. MRAK, “Advantages and Disadvantages of Pyrethrum,” in *Pyrethrum*, 2014, pp. 307–311.
- [10] “Research Cell Efficiency Records | Department of Energy.” [Online]. Available: <https://www.energy.gov/eere/solar/downloads/research-cell-efficiency-records>. [Accessed: 14-Mar-2018].
- [11] T. Schoder, “Monocrystalline Cells vs. Polycrystalline Cells | CivicSolar,” 2018. [Online]. Available: <https://www.civicsolar.com/support/installer/articles/monocrystalline-cells-vs-polycrystalline-cells-whats-difference>. [Accessed: 06-Jun-2019].
- [12] A. Sendy, “Pros and Cons of Monocrystalline vs Polycrystalline solar panels,” *Solar Reviews*, 2017. [Online]. Available: <https://www.solarreviews.com/blog/pros-and-cons-of-monocrystalline-vs-polycrystalline-solar-panels>. [Accessed: 06-Jun-2019].
- [13] F. Jay *et al.*, “Advanced process for n-type mono-like silicon a-Si:H/c-Si heterojunction solar cells with 21.5% efficiency,” *Sol. Energy Mater. Sol. Cells*, vol. 130, pp. 690–695, Nov. 2014.
- [14] P. Preis *et al.*, “Towards 20 % solar cell efficiency using silicon from metallurgical process route,” *Energy Procedia*, vol. 55, pp. 589–595, 2014.
- [15] K. M. Park, M. B. Lee, and S. Y. Choi, “Investigation of surface features for 17.2% efficiency multi-crystalline silicon solar cells,” *Sol. Energy Mater. Sol. Cells*, vol. 132, pp. 356–362, Jan. 2015.
- [16] W. Shockley and H. J. Queisser, “Detailed balance limit of efficiency of p-n junction solar cells,” *J. Appl. Phys.*, vol. 32, no. 3, pp. 510–519, 1961.
- [17] M. A. Green, K. Emery, Y. Hishikawa, W. Warta, and E. D. Dunlop, “Solar cell efficiency tables (version 41),” *Prog. Photovoltaics Res. Appl.*, vol. 21, no. 1, pp. 1–11, Jan. 2013.
- [18] S. E. Shaheen, D. S. Ginley, and G. E. Jabbour, “Organic-Based Photovoltaics: Toward Low-Cost Power Generation,” *MRS Bull.*, vol. 30, no. 01, pp. 10–19, Jan. 2005.
- [19] “Photovoltaic Research | NREL.” [Online]. Available: <https://www.nrel.gov/pv/>. [Accessed: 14-Mar-2018].
- [20] J. DeBloisblanc, “Synthesis and Characterization of P3HT : PCBM Organic Solar Cells,” 2010.
- [21] C. Meehan, “NREL Developing Improved Tech to Lower Costs for Multi-Junction Solar Cells,” *Solar Reviews*, 2018.
- [22] H. Spanggaard and F. C. Krebs, “A brief history of the development of organic and polymeric photovoltaics,” *Sol. Energy Mater. Sol. Cells*, vol. 83, no. 2–3, pp. 125–146, Jun. 2004.
- [23] W. C. H. (Wallace C. H. Choy, *Organic solar cells: materials and device physics*. Springer, 2013.
- [24] C. W. Tang, “Two-layer organic photovoltaic cell,” *Appl. Phys. Lett.*, vol. 48, no. 2, pp. 183–

- 185, Jan. 1986.
- [25] H. Hoppe and N. S. Sariciftci, "Organic solar cells: An overview," *J. Mater. Res.*, vol. 19, no. 07, pp. 1924–1945, Jul. 2004.
- [26] J. Nelson, "Organic photovoltaic films," *Curr. Opin. Solid State Mater. Sci.*, vol. 6, no. 1, pp. 87–95, Feb. 2002.
- [27] A. J. Heeger, "25th Anniversary Article: Bulk Heterojunction Solar Cells: Understanding the Mechanism of Operation," *Adv. Mater.*, vol. 26, no. 1, pp. 10–28, Jan. 2014.
- [28] J. Yu, Y. Zheng, and J. Huang, "Towards High Performance Organic Photovoltaic Cells: A Review of Recent Development in Organic Photovoltaics," *Polymers (Basel)*, vol. 6, no. 9, pp. 2473–2509, Sep. 2014.
- [29] O. V. Mikhnenko, R. Ruitter, P. W. M. Blom, and M. A. Loi, "Direct Measurement of the Triplet Exciton Diffusion Length in Organic Semiconductors," *Phys. Rev. Lett.*, vol. 108, no. 13, p. 137401, Mar. 2012.
- [30] V. D. Mihailetschi, L. J. A. Koster, J. C. Hummelen, and P. W. M. Blom, "Photocurrent Generation in Polymer-Fullerene Bulk Heterojunctions," *Phys. Rev. Lett.*, vol. 93, no. 21, p. 216601, Nov. 2004.
- [31] J.-M. Nunzi, "Organic photovoltaic materials and devices," *Comptes Rendus Phys.*, vol. 3, no. 4, pp. 523–542, Jan. 2002.
- [32] M. Kuik, G.-J. A. H. Wetzelaer, H. T. Nicolai, N. I. Craciun, D. M. De Leeuw, and P. W. M. Blom, "25th Anniversary Article: Charge Transport and Recombination in Polymer Light-Emitting Diodes," *Adv. Mater.*, vol. 26, no. 4, pp. 512–531, Jan. 2014.
- [33] J. Hou and X. Guo, "Active Layer Materials for Organic Solar Cells," in *Organic Solar Cells Materials and Device Physics*, 2013, pp. 17–42.
- [34] D. D. S. Fung and W. C. H. Choy, "Introduction to Organic Solar Cells," in *Organic Solar Cells Materials and Device Physics*, 2013, pp. 1–16.
- [35] S. Singh and Z. Vardeny, "Ultrafast Transient Spectroscopy of Polymer/Fullerene Blends for Organic Photovoltaic Applications," *Materials (Basel)*, vol. 6, no. 3, pp. 897–910, Mar. 2013.
- [36] C. Duan, C. Zhong, F. Huang, and Y. Cao, "Interface Engineering for High Performance Bulk-Heterojunction Polymeric Solar Cells," in *Organic Solar Cells Materials and Device Physics*, 2013, pp. 43–79.
- [37] F. Brunetti and T. Vergata, "Introduction to New Generation Solution Processable Solar Cells : Perspectives and Challenges International Travelling Summer Schools on Microwaves and Lightwaves (ITSS) 2014," 2014.
- [38] O. Oklobia, "Investigations of Thermally Induced Morphology in P3HT / PCBM Thin Films : Influence of Composition and Thermal Annealing on Photovoltaic Properties Ochai Oklobia A thesis submitted in partial fulfilment of the requirement of Staffordshire University for," 2016.
- [39] A. J. Pearson, P. E. Hopkinson, E. Couderc, K. Domanski, M. Abdi-Jalebi, and N. C. Greenham, "Critical light instability in CB/DIO processed PBDTTT-EFT:PC 71 BM organic photovoltaic devices," *Org. Electron.*, vol. 30, pp. 225–236, Mar. 2016.
- [40] W. Huang, E. Gann, L. Thomsen, C. Dong, Y.-B. Cheng, and C. R. McNeill, "Unraveling the Morphology of High Efficiency Polymer Solar Cells Based on the Donor Polymer PBDTTT-EFT," *Adv. Energy Mater.*, vol. 5, no. 7, p. 1401259, Apr. 2015.
- [41] W. Huang *et al.*, "Impact of Fullerene Mixing Behavior on the Microstructure, Photophysics, and Device Performance of Polymer/Fullerene Solar Cells," *ACS Appl. Mater. Interfaces*, vol. 8, pp. 29608–29618, 2016.
- [42] S. Zhang, L. Ye, W. Zhao, D. Liu, H. Yao, and J. Hou, "Side chain selection for designing highly efficient photovoltaic polymers with 2D-conjugated structure," *Macromolecules*, vol. 47, no. 14, pp. 4653–4659, 2014.
- [43] K. A. Luck *et al.*, "Correlated In Situ Low-Frequency Noise and Impedance Spectroscopy Reveal Recombination Dynamics in Organic Solar Cells Using Fullerene and Non-Fullerene Acceptors," *Adv. Funct. Mater.*, vol. 27, no. 48, p. 1703805, Dec. 2017.
- [44] R. Sharma *et al.*, "Photo-physics of PTB7, PCBM and ICBA based ternary solar cells," *Org. Electron.*, vol. 34, pp. 111–117, Jul. 2016.
- [45] C. Kittel, *Introduction To Solid State Physics 8Th Edition*. 2011.
- [46] C. R. Nave, "Band Theory for Solids," *hyperphysics.phy-astr.gsu.edu*, 1999. [Online]. Available: <http://hyperphysics.phy-astr.gsu.edu/hbase/Solids/band.html#c6>. [Accessed: 09-Jun-2018].
- [47] B. A. Gregg and M. C. Hanna, "Comparing organic to inorganic photovoltaic cells: Theory, experiment, and simulation," *J. Appl. Phys.*, vol. 93, no. 6, pp. 3605–3614, Mar. 2003.

- [48] J. L. Bredas, J. P. Calbert, D. A. da Silva Filho, and J. Cornil, "Organic semiconductors: A theoretical characterization of the basic parameters governing charge transport," *Proc. Natl. Acad. Sci.*, vol. 99, no. 9, pp. 5804–5809, Apr. 2002.
- [49] S. Komilian, O. Oklobia, and T. Sadat-Shafai, "Controlling intercalations of PBDTTT-EFT side chain to initiate suitable network for charge extraction in PBDTTT-EFT:PC71BM blended bulk heterojunction solar cell," *Sol. Energy Mater. Sol. Cells*, vol. 175, pp. 35–40, Feb. 2018.
- [50] S. Komilian, O. Oklobia, and T. Sadat-Shafai, "Data related to the PC 71 BM loading and its impact on nanostructuring for blend of PBDTTT-EFT:PC 71 BM bulk heterojunction solar cell," *Data Br.*, vol. 16, pp. 506–510, Feb. 2018.
- [51] Y. Sun, G. C. Welch, W. L. Leong, C. J. Takacs, G. C. Bazan, and A. J. Heeger, "Solution-processed small-molecule solar cells with 6.7% efficiency," *Nat. Mater.*, vol. 11, no. 1, pp. 44–48, Jan. 2012.
- [52] N. Espinosa, M. Hösel, M. Jørgensen, and F. C. Krebs, "Large scale deployment of polymer solar cells on land, on sea and in the air," *Energy Environ. Sci.*, vol. 7, no. 3, p. 855, 2014.
- [53] M. Jaiswal and R. Menon, "Polymer electronic materials: a review of charge transport," *Polym. Int.*, vol. 55, no. 12, pp. 1371–1384, Dec. 2006.
- [54] A. Heeger and A. Macdiarmid, "2 - Synthesis and Design of Conjugated Polymers for Organic Electronics," in *Polymer Materials for Energy and Electronic Applications*, Sciecn Direct, 2017, pp. 9–61.
- [55] W. Geens, T. Aernouts, J. Poortmans, and G. Hadziioannou, "Organic co-evaporated films of a PPV-pentamer and C60: model systems for donor/acceptor polymer blends," *Thin Solid Films*, vol. 403–404, pp. 438–443, Feb. 2002.
- [56] W. Ma, C. Yang, X. Gong, K. Lee, and A. J. Heeger, "Thermally Stable, Efficient Polymer Solar Cells with Nanoscale Control of the Interpenetrating Network Morphology," *Adv. Funct. Mater.*, vol. 15, no. 10, pp. 1617–1622, Oct. 2005.
- [57] S. O. Kasap and S. M. Sze, *Semiconductor Devices: Physics and Technology*. 2002.
- [58] P. A. Leighton, "Electronic Processes in Ionic Crystals (Mott, N. F.; Gurney, R. W.)," *J. Chem. Educ.*, vol. 18, no. 5, p. 249, May 1941.
- [59] O. Oklobia and T. S. Shafai, "Correlation between charge carriers mobility and nanomorphology in a blend of P3HT/PCBM bulk heterojunction solar cell: Impact on recombination mechanisms," *Sol. Energy Mater. Sol. Cells*, vol. 122, pp. 158–163, Mar. 2014.
- [60] T. S. Shafai and O. Oklobia, "Effects of PCBM Loading and Thermal Annealing on Nanomorphology of Blend of Polymer/Fullerene Thin Films Solar Cells: Impact on Charge Carrier Mobility and Efficiency," *Appl. Mech. Mater.*, vol. 467, pp. 160–165, Dec. 2013.
- [61] J. Nelson, *The Physics of Solar Cells*. PUBLISHED BY IMPERIAL COLLEGE PRESS AND DISTRIBUTED BY WORLD SCIENTIFIC PUBLISHING CO., 2003.
- [62] Priyanka, M. Lal, and S. N. Singh, "A new method of determination of series and shunt resistances of silicon solar cells," *Sol. Energy Mater. Sol. Cells*, vol. 91, no. 2–3, pp. 137–142, 2007.
- [63] K. Bouzidi, M. Chegaar, and A. Bouhemadou, "Solar cells parameters evaluation considering the series and shunt resistance," *Sol. Energy Mater. Sol. Cells*, vol. 91, no. 18, pp. 1647–1651, 2007.
- [64] D. Pysch, A. Mette, and S. W. Glunz, "A review and comparison of different methods to determine the series resistance of solar cells," *Sol. Energy Mater. Sol. Cells*, vol. 91, no. 18, pp. 1698–1706, 2007.
- [65] J. L. Bredas, R. Silbey, D. S. Boudreaux, and R. R. Chance, "Chain-length dependence of electronic and electrochemical properties of conjugated systems: polyacetylene, polyphenylene, polythiophene, and polypyrrole," *J. Am. Chem. Soc.*, vol. 105, no. 22, pp. 6555–6559, Oct. 1983.
- [66] M. Universal, V. a C. Connecting, and B. N. C. Adapter, "Dielectric constant of different materials LEP 4.2.06," *Physics (College. Park. Md.)*, pp. 4–7.
- [67] T. M. Clarke and J. R. Durrant, "Charge Photogeneration in Organic Solar Cells," *Chem. Rev.*, vol. 110, no. 11, pp. 6736–6767, Nov. 2010.
- [68] L. Onsager, "Deviations from Ohm's Law in Weak Electrolytes," *J. Chem. Phys.*, vol. 2, no. 9, pp. 599–615, Sep. 1934.
- [69] M. C. Scharber *et al.*, "Design Rules for Donors in Bulk-Heterojunction Solar Cells—Towards 10 % Energy-Conversion Efficiency," *Adv. Mater.*, vol. 18, no. 6, pp. 789–794, Mar. 2006.
- [70] M. Tachiya, "Breakdown of the Onsager theory of geminate ion recombination," *J. Chem. Phys.*, vol. 89, no. 11, pp. 6929–6935, Dec. 1988.

- [71] C. L. Braun, "Electric field assisted dissociation of charge transfer states as a mechanism of photocarrier production," *J. Chem. Phys.*, vol. 80, no. 9, pp. 4157–4161, May 1984.
- [72] M. M. Mandoc, F. B. Kooistra, J. C. Hummelen, B. de Boer, and P. W. M. Blom, "Effect of traps on the performance of bulk heterojunction organic solar cells," *Appl. Phys. Lett.*, vol. 91, no. 26, p. 263505, Dec. 2007.
- [73] L. J. A. Koster, V. D. Mihailetschi, and P. W. M. Blom, "Bimolecular recombination in polymer/fullerene bulk heterojunction solar cells," *Appl. Phys. Lett.*, vol. 88, no. 5, p. 052104, Jan. 2006.
- [74] S. O. Kasap, B. Fogal, M. Zahangir Kabir, R. E. Johanson, and S. K. O'Leary, "Recombination of drifting holes with trapped electrons in stabilized a -Se photoconductors: Langevin recombination," *Appl. Phys. Lett.*, vol. 84, no. 11, pp. 1991–1993, Mar. 2004.
- [75] L. J. A. Koster, V. D. Mihailetschi, and P. W. M. Blom, "Bimolecular recombination in polymer/fullerene bulk heterojunction solar cells," *Appl. Phys. Lett.*, vol. 88, no. 5, p. 052104, Jan. 2006.
- [76] W. Shockley and W. T. Read, "Statistics of the Recombinations of Holes and Electrons," *Phys. Rev.*, vol. 87, no. 5, pp. 835–842, Sep. 1952.
- [77] M. Kuik, L. J. A. Koster, G. A. H. Wetzelaer, and P. W. M. Blom, "Trap-Assisted Recombination in Disordered Organic Semiconductors," *Phys. Rev. Lett.*, vol. 107, no. 25, p. 256805, Dec. 2011.
- [78] K. S. Nalwa, H. K. Kodali, B. Ganapathysubramanian, and S. Chaudhary, "Dependence of recombination mechanisms and strength on processing conditions in polymer solar cells," *Appl. Phys. Lett.*, vol. 99, no. 26, p. 263301, Dec. 2011.
- [79] M. Kuik, L. J. A. Koster, G. A. H. Wetzelaer, and P. W. M. Blom, "Trap-Assisted Recombination in Disordered Organic Semiconductors," *Phys. Rev. Lett.*, vol. 107, no. 25, p. 256805, Dec. 2011.
- [80] G. Yu, J. Gao, J. C. Hummelen, F. Wudl, and A. J. Heeger, "Polymer Photovoltaic Cells: Enhanced Efficiencies via a Network of Internal Donor-Acceptor Heterojunctions," *Science (80-.)*, vol. 270, no. 5243, pp. 1789–1791, Dec. 1995.
- [81] B. Xu, G. Sai-Anand, A. I. Gopalan, Q. Qiao, and S. W. Kang, "Improving photovoltaic properties of P3HT:IC60BA through the incorporation of small molecules," *Polymers (Basel)*, vol. 10, no. 2, p. 121, Jan. 2018.
- [82] O. Oklobia and T. S. Shafai, "A quantitative study of the formation of PCBM clusters upon thermal annealing of P3HT/PCBM bulk heterojunction solar cell," *Sol. Energy Mater. Sol. Cells*, vol. 117, pp. 1–8, Oct. 2013.
- [83] O. Oklobia and T. S. Shafai, "A study of donor/acceptor interfaces in a blend of P3HT/PCBM solar cell: Effects of annealing and PCBM loading on optical and electrical properties," *Solid. State. Electron.*, vol. 87, pp. 64–68, Sep. 2013.
- [84] S. Cook, R. Katoh, and A. Furube, "Ultrafast Studies of Charge Generation in PCBM:P3HT Blend Films following Excitation of the Fullerene PCBM," *J. Phys. Chem. C*, vol. 113, no. 6, pp. 2547–2552, Feb. 2009.
- [85] B. G. Streetman and S. K. Banerjee, *Solid State Electronic Devices*. Prentice Hall, 2009.
- [86] J. Hou and X. Guo, "Active Layer Materials for Organic Solar Cells," in *Organic Solar Cells, Green Energy and Technology*, vol. 208, no. 12, London: Springer, 2013, pp. 17–42.
- [87] I. Osaka and R. D. McCullough, "Advances in molecular design and synthesis of regioregular polythiophenes," *Acc. Chem. Res.*, vol. 41, no. 9, pp. 1202–1214, Sep. 2008.
- [88] J. Hou, Z. Tan, Y. Yan, Y. He, C. Yang, and Y. Li, "Synthesis and Photovoltaic Properties of Two-Dimensional Conjugated Polythiophenes with Bi(thienylenevinylene) Side Chains," *J. Am. Chem. Soc.*, vol. 128, no. 14, pp. 4911–4916, Apr. 2006.
- [89] E. Zhou *et al.*, "Synthesis, Hole Mobility, and Photovoltaic Properties of Cross-Linked Polythiophenes with Vinylene-Terthiophene-Vinylene as Conjugated Bridge," *Macromolecules*, vol. 40, no. 6, pp. 1831–1837, Mar. 2007.
- [90] J. Hou, T. L. Chen, S. Zhang, L. Huo, S. Sista, and Y. Yang, "An Easy and Effective Method To Modulate Molecular Energy Level of Poly(3-alkylthiophene) for High- Voc Polymer Solar Cells," *Macromolecules*, vol. 42, no. 23, pp. 9217–9219, Dec. 2009.
- [91] A. M. Ballantyne *et al.*, "Studies of Highly Regioregular Poly(3-hexylselenophene) for Photovoltaic Applications," *Adv. Mater.*, vol. 19, no. 24, pp. 4544–4547, Dec. 2007.
- [92] D. Mühlbacher *et al.*, "High Photovoltaic Performance of a Low-Bandgap Polymer," *Adv. Mater.*, vol. 18, no. 21, pp. 2884–2889, Nov. 2006.
- [93] Z. Zhu *et al.*, "Panchromatic Conjugated Polymers Containing Alternating Donor/Acceptor

- Units for Photovoltaic Applications,” *Macromolecules*, vol. 40, no. 6, pp. 1981–1986, Mar. 2007.
- [94] H. N. Tsao *et al.*, “The Influence of Morphology on High-Performance Polymer Field-Effect Transistors,” *Adv. Mater.*, vol. 21, no. 2, pp. 209–212, Jan. 2009.
- [95] J. Peet *et al.*, “Efficiency enhancement in low-bandgap polymer solar cells by processing with alkane dithiols,” *Nat. Mater.*, vol. 6, no. 7, pp. 497–500, Jul. 2007.
- [96] M.-S. Su, C.-Y. Kuo, M.-C. Yuan, U.-S. Jeng, C.-J. Su, and K.-H. Wei, “Improving Device Efficiency of Polymer/Fullerene Bulk Heterojunction Solar Cells Through Enhanced Crystallinity and Reduced Grain Boundaries Induced by Solvent Additives,” *Adv. Mater.*, vol. 23, no. 29, pp. 3315–3319, Aug. 2011.
- [97] R. C. Coffin, J. Peet, J. Rogers, and G. C. Bazan, “Streamlined microwave-assisted preparation of narrow-bandgap conjugated polymers for high-performance bulk heterojunction solar cells,” *Nat. Chem.*, vol. 1, no. 8, pp. 657–661, Nov. 2009.
- [98] W. Yue *et al.*, “Novel NIR-absorbing conjugated polymers for efficient polymer solar cells: effect of alkyl chain length on device performance,” *J. Mater. Chem.*, vol. 19, no. 15, p. 2199, 2009.
- [99] M.-H. Chen *et al.*, “Efficient Polymer Solar Cells with Thin Active Layers Based on Alternating Polyfluorene Copolymer/Fullerene Bulk Heterojunctions,” *Adv. Mater.*, vol. 21, no. 42, pp. 4238–4242, Nov. 2009.
- [100] E. Wang *et al.*, “High-performance polymer heterojunction solar cells of a polysilafluorene derivative,” *Appl. Phys. Lett.*, vol. 92, no. 3, p. 033307, Jan. 2008.
- [101] N. Blouin *et al.*, “Toward a Rational Design of Poly(2,7-Carbazole) Derivatives for Solar Cells,” *J. Am. Chem. Soc.*, vol. 130, no. 2, pp. 732–742, Jan. 2008.
- [102] E. Zhou *et al.*, “Synthesis and Photovoltaic Properties of a Novel Low Band Gap Polymer Based on N-Substituted Dithieno[3,2-b:2',3'-d]pyrrole,” *Macromolecules*, vol. 41, no. 22, pp. 8302–8305, Nov. 2008.
- [103] A. J. Moulé *et al.*, “Two Novel Cyclopentadithiophene-Based Alternating Copolymers as Potential Donor Components for High-Efficiency Bulk-Heterojunction-Type Solar Cells,” *Chem. Mater.*, vol. 20, no. 12, pp. 4045–4050, Jun. 2008.
- [104] L. Huo, J. Hou, S. Zhang, H.-Y. Chen, and Y. Yang, “A Polybenzo[1,2-b:4,5-b']dithiophene Derivative with Deep HOMO Level and Its Application in High-Performance Polymer Solar Cells,” *Angew. Chemie Int. Ed.*, vol. 49, no. 8, pp. 1500–1503, Feb. 2010.
- [105] L. Huo, X. Guo, Y. Li, and J. Hou, “Synthesis of a polythieno[3,4-b]thiophene derivative with a low-lying HOMO level and its application in polymer solar cells,” *Chem. Commun.*, vol. 47, no. 31, p. 8850, 2011.
- [106] L. Bürgi, M. Turbiez, R. Pfeiffer, F. Bienewald, H.-J. Kirner, and C. Winnewisser, “High-Mobility Ambipolar Near-Infrared Light-Emitting Polymer Field-Effect Transistors,” *Adv. Mater.*, vol. 20, no. 11, pp. 2217–2224, Jun. 2008.
- [107] J. C. Bijleveld *et al.*, “Poly(diketopyrrolopyrrole-terthiophene) for Ambipolar Logic and Photovoltaics,” *J. Am. Chem. Soc.*, vol. 131, no. 46, pp. 16616–16617, Nov. 2009.
- [108] A. P. Zoombelt, S. G. J. Mathijssen, M. G. R. Turbiez, M. M. Wienk, and R. A. J. Janssen, “Small band gap polymers based on diketopyrrolopyrrole,” *J. Mater. Chem.*, vol. 20, no. 11, p. 2240, 2010.
- [109] M. M. Wienk, M. Turbiez, J. Gilot, and R. A. J. Janssen, “Narrow-Bandgap Diketo-Pyrrolo-Pyrrole Polymer Solar Cells: The Effect of Processing on the Performance,” *Adv. Mater.*, vol. 20, no. 13, pp. 2556–2560, Jul. 2008.
- [110] J. C. Bijleveld *et al.*, “Efficient Solar Cells Based on an Easily Accessible Diketopyrrolopyrrole Polymer,” *Adv. Mater.*, vol. 22, no. 35, pp. E242–E246, Sep. 2010.
- [111] H. Duran, A. Gitsas, G. Floudas, M. Mondeshki, M. Steinhart, and W. Knoll, “Poly(γ -benzyl-L-glutamate) Peptides Confined to Nanoporous Alumina: Pore Diameter Dependence of Self-Assembly and Segmental Dynamics,” *Macromolecules*, vol. 42, no. 8, pp. 2881–2885, Apr. 2009.
- [112] N. Allard *et al.*, “Germafluorenes: New Heterocycles for Plastic Electronics,” *Macromolecules*, vol. 43, no. 5, pp. 2328–2333, Mar. 2010.
- [113] E. Zhou *et al.*, “Diketopyrrolopyrrole-Based Semiconducting Polymer for Photovoltaic Device with Photocurrent Response Wavelengths up to 1.1 μm ,” *Macromolecules*, vol. 43, no. 2, pp. 821–826, Jan. 2010.
- [114] C. Kanimozhi, P. Balraju, G. D. Sharma, and S. Patil, “Synthesis of Diketopyrrolopyrrole Containing Copolymers: A Study of Their Optical and Photovoltaic Properties,” *J. Phys. Chem.*

- B*, vol. 114, no. 9, pp. 3095–3103, Mar. 2010.
- [115] A. P. Zoombelt, M. Fonrodona, M. G. R. Turbiez, M. M. Wienk, and R. A. J. Janssen, “Synthesis and photovoltaic performance of a series of small band gap polymers,” *J. Mater. Chem.*, vol. 19, no. 30, p. 5336, 2009.
- [116] J. Hou *et al.*, “Bandgap and Molecular Energy Level Control of Conjugated Polymer Photovoltaic Materials Based on Benzo[1,2-*b*:4,5-*b'*]dithiophene,” *Macromolecules*, vol. 41, no. 16, pp. 6012–6018, Aug. 2008.
- [117] H. Pan *et al.*, “Synthesis and Thin-Film Transistor Performance of Poly(4,8-didodecylbenzo[1,2-*b*:4,5-*b'*]dithiophene),” *Chem. Mater.*, vol. 18, no. 14, pp. 3237–3241, Jul. 2006.
- [118] H. Pan *et al.*, “Low-Temperature, Solution-Processed, High-Mobility Polymer Semiconductors for Thin-Film Transistors,” *J. Am. Chem. Soc.*, vol. 129, no. 14, pp. 4112–4113, Apr. 2007.
- [119] J. Hou *et al.*, “Synthesis of a Low Band Gap Polymer and Its Application in Highly Efficient Polymer Solar Cells,” *J. Am. Chem. Soc.*, vol. 131, no. 43, pp. 15586–15587, Nov. 2009.
- [120] L. Huo, S. Zhang, X. Guo, F. Xu, Y. Li, and J. Hou, “Replacing Alkoxy Groups with Alkylthienyl Groups: A Feasible Approach To Improve the Properties of Photovoltaic Polymers,” *Angew. Chemie Int. Ed.*, vol. 50, no. 41, pp. 9697–9702, Oct. 2011.
- [121] H.-Y. Chen *et al.*, “Polymer solar cells with enhanced open-circuit voltage and efficiency,” *Nat. Photonics*, vol. 3, no. 11, pp. 649–653, Nov. 2009.
- [122] Y. Liang and L. Yu, “A New Class of Semiconducting Polymers for Bulk Heterojunction Solar Cells with Exceptionally High Performance,” *Acc. Chem. Res.*, vol. 43, no. 9, pp. 1227–1236, Sep. 2010.
- [123] W. Zhao, L. Ye, S. Zhang, B. Fan, M. Sun, and J. Hou, “Ultrathin Polyaniline-based Buffer Layer for Highly Efficient Polymer Solar Cells with Wide Applicability,” *Sci. Rep.*, vol. 4, p. 6570, 2014.
- [124] E. D. Peterson, G. M. Smith, M. Fu, R. C. Coffin, R. D. Adams, and D. L. Carroll, “Increased photon absorption and conversion in ternary bulk heterojunction systems of CdSe/CdS core-shell nanoparticles/methyl viologen composites, conjugated polymers, and fullerenes,” in *2010 35th IEEE Photovoltaic Specialists Conference*, 2010, pp. 001643–001647.
- [125] S. C. Price, A. C. Stuart, L. Yang, H. Zhou, and W. You, “Fluorine Substituted Conjugated Polymer of Medium Band Gap Yields 7% Efficiency in Polymer–Fullerene Solar Cells,” *J. Am. Chem. Soc.*, vol. 133, no. 12, pp. 4625–4631, Mar. 2011.
- [126] H. Zhou, L. Yang, A. C. Stuart, S. C. Price, S. Liu, and W. You, “Development of Fluorinated Benzothiadiazole as a Structural Unit for a Polymer Solar Cell of 7 % Efficiency,” *Angew. Chemie Int. Ed.*, vol. 50, no. 13, pp. 2995–2998, Mar. 2011.
- [127] S. Zhang, L. Ye, W. Zhao, D. Liu, H. Yao, and J. Hou, “Side Chain Selection for Designing Highly Efficient Photovoltaic Polymers with 2D-Conjugated Structure,” *Macromolecules*, vol. 47, no. 14, pp. 4653–4659, Jul. 2014.
- [128] W. Huang, E. Gann, L. Thomsen, C. Dong, Y.-B. Cheng, and C. R. McNeill, “Unraveling the Morphology of High Efficiency Polymer Solar Cells Based on the Donor Polymer PBDTTT-EFT,” *Adv. Energy Mater.*, vol. 5, no. 7, p. 1401259, Apr. 2015.
- [129] N. S. Sariciftci, L. Smilowitz, A. J. Heeger, and F. Wudl, “Photoinduced Electron Transfer from a Conducting Polymer to Buckminsterfullerene,” *Science (80-.)*, vol. 258, no. 5087, pp. 1474–1476, Nov. 1992.
- [130] F. Zhang *et al.*, “Influence of PC60BM or PC70BM as electron acceptor on the performance of polymer solar cells,” *Sol. Energy Mater. Sol. Cells*, vol. 97, pp. 71–77, Feb. 2012.
- [131] C. J. Brabec, N. S. Sariciftci, and J. C. Hummelen, “Plastic Solar Cells,” *Adv. Funct. Mater.*, vol. 11, no. 1, pp. 15–26, Feb. 2001.
- [132] N. S. Sariciftci *et al.*, “Semiconducting polymer-buckminsterfullerene heterojunctions: Diodes, photodiodes, and photovoltaic cells,” *Appl. Phys. Lett.*, vol. 62, no. 6, pp. 585–587, Feb. 1993.
- [133] Y. He and Y. Li, “Fullerene derivative acceptors for high performance polymer solar cells,” *Phys. Chem. Chem. Phys.*, vol. 13, no. 6, pp. 1970–1983, 2011.
- [134] Y. He, G. Zhao, B. Peng, and Y. Li, “High-Yield Synthesis and Electrochemical and Photovoltaic Properties of Indene-C70 Bisadduct,” *Adv. Funct. Mater.*, vol. 20, no. 19, pp. 3383–3389, Oct. 2010.
- [135] G. Zhao, Y. He, and Y. Li, “6.5% Efficiency of Polymer Solar Cells Based on poly(3-hexylthiophene) and Indene-C60 Bisadduct by Device Optimization,” *Adv. Mater.*, vol. 22, no. 39, pp. 4355–4358, Oct. 2010.
- [136] P. Cheng, Y. Li, and X. Zhan, “Efficient ternary blend polymer solar cells with indene-C60

- bisadduct as an electron-cascade acceptor,” *Energy Environ. Sci.*, vol. 7, no. 6, p. 2005, 2014.
- [137] Z. Yin, J. Wei, and Q. Zheng, “Interfacial Materials for Organic Solar Cells: Recent Advances and Perspectives,” *Adv. Sci.*, vol. 3, no. 8, p. 1500362, Aug. 2016.
- [138] S. A. Carter, M. Angelopoulos, S. Karg, P. J. Brock, and J. C. Scott, “Polymeric anodes for improved polymer light-emitting diode performance,” *Appl. Phys. Lett.*, vol. 70, no. 16, pp. 2067–2069, Apr. 1997.
- [139] F. C. Krebs *et al.*, *Polymer Photovoltaics: A Practical Approach*. Society of Photo-Optical Instrumentation Engineers, 2008.
- [140] Y. Li, G. Vamvounis, and S. Holdcroft, “Tuning Optical Properties and Enhancing Solid-State Emission of Poly(thiophene)s by Molecular Control: A Postfunctionalization Approach,” *Macromolecules*, vol. 35, no. 18, pp. 6900–6906, Aug. 2002.
- [141] M. Wang *et al.*, “Limit of Voc in polymeric bulk heterojunction solar cells predicted by a double-junction model,” *Sol. Energy Mater. Sol. Cells*, vol. 108, pp. 17–21, 2013.
- [142] V. Coropceanu *et al.*, “Charge transport in organic semiconductors,” *Chem. Rev.*, vol. 107, no. 4, pp. 926–52, 2007.
- [143] V. Shrotriya, Y. Yao, G. Li, and Y. Yang, “Effect of self-organization in polymer/fullerene bulk heterojunctions on solar cell performance,” *Appl. Phys. Lett.*, vol. 89, no. 6, p. 063505, Aug. 2006.
- [144] G. D. Cody, C. R. Wronski, B. Abeles, R. B. Stephens, and B. Brooks, “Optical characterization of amorphous silicon hydride films,” *Sol. Cells*, vol. 2, no. 3, pp. 227–243, Nov. 1980.
- [145] H. R. Philipp, “Optical properties of non-crystalline Si, SiO, SiO_x and SiO₂,” *J. Phys. Chem. Solids*, vol. 32, no. 8, pp. 1935–1945, Jan. 1971.
- [146] Z. Wu, “Transparent, Conductive Carbon Nanotube Films,” *Science (80-.)*, vol. 305, no. 5688, pp. 1273–1276, Aug. 2004.
- [147] F. C. Krebs *et al.*, “A complete process for production of flexible large area polymer solar cells entirely using screen printing—First public demonstration,” *Sol. Energy Mater. Sol. Cells*, vol. 93, no. 4, pp. 422–441, Apr. 2009.
- [148] K. Norrman, A. Ghanbari-Siahkali, and N. B. Larsen, “6 Studies of spin-coated polymer films,” *Annu. Reports Sect. “C” (Physical Chem.)*, vol. 101, p. 174, 2005.
- [149] F. C. Krebs, “Fabrication and processing of polymer solar cells: A review of printing and coating techniques,” *Sol. Energy Mater. Sol. Cells*, vol. 93, no. 4, pp. 394–412, Apr. 2009.
- [150] C. Buzea and K. Robbie, “State of the art in thin film thickness and deposition rate monitoring sensors,” *Reports Prog. Phys.*, vol. 68, no. 2, pp. 385–409, Feb. 2005.
- [151] J. Bisquert, F. Fabregat-Santiago, I. Mora-Seró, G. Garcia-Belmonte, and S. Giménez, “Electron Lifetime in Dye-Sensitized Solar Cells: Theory and Interpretation of Measurements,” *J. Phys. Chem. C*, vol. 113, no. 40, pp. 17278–17290, Oct. 2009.
- [152] C. Longo, A. F. Nogueira, M.-A. De Paoli, and H. Cachet, “Solid-State and Flexible Dye-Sensitized TiO₂ Solar Cells: a Study by Electrochemical Impedance Spectroscopy,” *J. Phys. Chem. B*, vol. 106, no. 23, pp. 5925–5930, Jun. 2002.
- [153] Q. Wang, J.-E. Moser, and M. Grätzel, “Electrochemical Impedance Spectroscopic Analysis of Dye-Sensitized Solar Cells,” *J. Phys. Chem. B*, vol. 109, no. 31, pp. 14945–14953, Aug. 2005.
- [154] C.-C. Hsiao, A.-E. Hsiao, and S.-A. Chen, “Design of Hole Blocking Layer with Electron Transport Channels for High Performance Polymer Light-Emitting Diodes,” *Adv. Mater.*, vol. 20, no. 10, pp. 1982–1988, May 2008.
- [155] G. Garcia-Belmonte, P. P. Boix, J. Bisquert, M. Sessolo, and H. J. Bolink, “Simultaneous determination of carrier lifetime and electron density-of-states in P3HT:PCBM organic solar cells under illumination by impedance spectroscopy,” *Sol. Energy Mater. Sol. Cells*, vol. 94, no. 2, pp. 366–375, Feb. 2010.
- [156] G. Garcia-Belmonte, A. Munar, E. M. Barea, J. Bisquert, I. Ugarte, and R. Pacios, “Charge carrier mobility and lifetime of organic bulk heterojunctions analyzed by impedance spectroscopy,” *Org. Electron.*, vol. 9, no. 5, pp. 847–851, Oct. 2008.
- [157] G. del Pozo, B. Arredondo, B. Romero, G. Susanna, and F. Brunetti, “Degradation of PEIE interlayer in PTB7:[70]PCBM based solar cells characterized by impedance spectroscopy,” *Sol. Energy*, vol. 144, pp. 105–110, Mar. 2017.
- [158] J. K. Macdonald and E. Barsoukov, *Impedance Spectroscopy*. Hoboken, NJ, USA: John Wiley & Sons, Inc., 2005.
- [159] T. Erb *et al.*, “Correlation Between Structural and Optical Properties of Composite Polymer/Fullerene Films for Organic Solar Cells,” *Adv. Funct. Mater.*, vol. 15, no. 7, pp. 1193–1196, Jul. 2005.

- [160] H. Hoppe, N. Arnold, N. S. Sariciftci, and D. Meissner, "Modeling the optical absorption within conjugated polymer/fullerene-based bulk-heterojunction organic solar cells," *Sol. Energy Mater. Sol. Cells*, vol. 80, no. 1, pp. 105–113, Oct. 2003.
- [161] A. Goetzberger, C. Hebling, and H.-W. Schock, "Photovoltaic materials, history, status and outlook," *Mater. Sci. Eng. R Reports*, vol. 40, no. 1, pp. 1–46, Jan. 2003.
- [162] D. F. Swinehart, "The Beer-Lambert Law," *J. Chem. Educ.*, vol. 39, no. 7, p. 333, Jul. 1962.
- [163] D. Calloway, "Beer-Lambert Law," *J. Chem. Educ.*, vol. 74, no. 7, p. 744, Jul. 1997.
- [164] N. Tams, C.; Enjalbert, "The Use of UV/Vis/NIR Spectroscopy in the Development of Photovoltaic Cells," Waltham, Feb. 2007.
- [165] M. Campoy-Quiles *et al.*, "Morphology evolution via self-organization and lateral and vertical diffusion in polymer:fullerene solar cell blends," *Nat. Mater.*, vol. 7, no. 2, pp. 158–164, Feb. 2008.
- [166] T.-F. Guo *et al.*, "Effects of film treatment on the performance of poly(3-hexylthiophene)/soluble fullerene-based organic solar cells," *Thin Solid Films*, vol. 516, no. 10, pp. 3138–3142, Mar. 2008.
- [167] K. S. Nalwa, R. C. Mahadevapuram, and S. Chaudhary, "Growth rate dependent trap density in polythiophene-fullerene solar cells and its implications," *Appl. Phys. Lett.*, vol. 98, no. 9, p. 093306, Feb. 2011.
- [168] C. V Raman and N. S. N. Nathe, "The diffraction of light by high frequency sound waves: Part I," *Proc. Indian Acad. Sci. - Sect. A*, vol. 2, no. 4, pp. 406–412, 1935.
- [169] C. V Raman, "The diffraction of light by sound waves of high frequency: Part II," *Proc. Indian Acad. Sci. - Sect. A*, vol. 2, no. 4, pp. 413–420, 1935.
- [170] C. V Raman, "The diffraction of light by high frequency sound waves: Part III," *Proc. Indian Acad. Sci. - Sect. A*, vol. 3, no. 1, pp. 75–84, 1936.
- [171] C. V Raman and N. S. N. Nathe, "The diffraction of light by high frequency sound waves: Part V," *Proc. Indian Acad. Sci. - Sect. A*, vol. 3, no. 5, pp. 459–465, 1936.
- [172] F. B. Laun, K. H. Fritzsche, T. A. Kuder, and B. Stieltjes, "Semiconductor Materials: an Introduction to Basic Principles," vol. 51, no. 3, p. 228, 2011.
- [173] B. G. Yacobi, "Interatomic Bonding, Crystal Structure, and Defects in Solids," in *Semiconductor Materials*, Boston: Kluwer Academic Publishers, 2003, pp. 5–32.
- [174] B. G. Yacobi, "Characterization of Semiconductors," in *Semiconductor Materials*, Boston: Kluwer Academic Publishers, 2003, pp. 171–215.
- [175] O. Oklobia and T. S. Shafai, "A quantitative study of the formation of PCBM clusters upon thermal annealing of P3HT/PCBM bulk heterojunction solar cell," *Sol. Energy Mater. Sol. Cells*, 2013.
- [176] V. D. Mihailetschi, H. X. Xie, B. de Boer, L. J. A. Koster, and P. W. M. Blom, "Charge Transport and Photocurrent Generation in Poly(3-hexylthiophene): Methanofullerene Bulk-Heterojunction Solar Cells," *Adv. Funct. Mater.*, vol. 16, no. 5, pp. 699–708, Mar. 2006.
- [177] L. F. Hernández-García, O. Ramírez-Sánchez, V. Cabrera-Arenas, and L. M. Reséndiz-Mendoza, "A Gaussian model for recombination via carrier-trap distributions in organic solar cells," *J. Comput. Electron.*, vol. 15, no. 3, pp. 1103–1109, Sep. 2016.
- [178] C. M. Proctor, M. Kuik, and T.-Q. Nguyen, "Charge carrier recombination in organic solar cells," *Prog. Polym. Sci.*, vol. 38, no. 12, pp. 1941–1960, Dec. 2013.
- [179] G.-J. A. H. Wetzelaer, M. Kuik, and P. W. M. Blom, "Identifying the Nature of Charge Recombination in Organic Solar Cells from Charge-Transfer State Electroluminescence," *Adv. Energy Mater.*, vol. 2, no. 10, pp. 1232–1237, Oct. 2012.
- [180] S. D. Oosterhout *et al.*, "Mixing Behavior in Small Molecule:Fullerene Organic Photovoltaics," *Chem. Mater.*, vol. 29, no. 7, pp. 3062–3069, Apr. 2017.
- [181] L. Ye, S. Zhang, W. Zhao, H. Yao, and J. Hou, "Highly Efficient 2D-Conjugated Benzodithiophene-Based Photovoltaic Polymer with Linear Alkylthio Side Chain," *Chem. Mater.*, 2014.
- [182] H. Zhong *et al.*, "Regioregular conjugated polymer for high performance thick-film organic solar cells without processing additive," *J. Mater. Chem. A*, 2017.
- [183] W. H. Bragg, "The Reflection of X-rays by Crystals. (II.)," *Proc. R. Soc. A Math. Phys. Eng. Sci.*, vol. 89, no. 610, pp. 246–248, 1913.
- [184] C. G. Pope, "X-Ray Diffraction and the Bragg Equation," *J. Chem. Educ.*, vol. 74, no. 1, p. 129, Jan. 1997.
- [185] J. Kacher, C. Landon, B. L. Adams, and D. Fullwood, "Bragg's Law diffraction simulations for electron backscatter diffraction analysis," *Ultramicroscopy*, vol. 109, no. 9, pp. 1148–1156,

Aug. 2009.

- [186] L. A. Perez *et al.*, “Effect of backbone regioregularity on the structure and orientation of a donor-acceptor semiconducting copolymer,” *Macromolecules*, 2014.
- [187] H. Sirringhaus *et al.*, “Two-dimensional charge transport in self-organized, high-mobility conjugated polymers,” *Nature*, vol. 401, no. 6754, pp. 685–688, 1999.
- [188] F. C. Frank, “On Miller–Bravais indices and four-dimensional vectors,” *Acta Crystallogr.*, vol. 18, no. 5, pp. 862–866, May 1965.
- [189] W. T. C. Chien, C. O. Chang, Y. C. Lo, Z. W. Li, and C. S. Chou, “On the Miller-indices determination of Si {1 0 0} convex corner undercut planes,” *J. Micromechanics Microengineering*, vol. 15, no. 4, pp. 833–842, Apr. 2005.
- [190] C. Hammond, “The Basics of Crystallography and Diffraction (2nd edn),” *Meas. Sci. Technol.*, vol. 13, no. 2, pp. 232–232, Feb. 2002.
- [191] G. Zhang *et al.*, “Crystallinity Effects in Sequentially Processed and Blend-Cast Bulk-Heterojunction Polymer / Fullerene Photovoltaics,” 2014.
- [192] B. A. Collins *et al.*, “Polarized X-ray scattering reveals non-crystalline orientational ordering in organic films,” *Nat. Mater.*, vol. 11, no. 6, pp. 536–543, Jun. 2012.
- [193] N. C. Miller *et al.*, “Molecular Packing and Solar Cell Performance in Blends of Polymers with a Bisadduct Fullerene,” *Nano Lett.*, vol. 12, no. 3, pp. 1566–1570, Mar. 2012.
- [194] B. A. Collins, E. Gann, L. Guignard, X. He, C. R. McNeill, and H. Ade, “Molecular Miscibility of Polymer–Fullerene Blends,” *J. Phys. Chem. Lett.*, vol. 1, no. 21, pp. 3160–3166, Nov. 2010.
- [195] J. A. Bartelt *et al.*, “The Importance of Fullerene Percolation in the Mixed Regions of Polymer-Fullerene Bulk Heterojunction Solar Cells,” *Adv. Energy Mater.*, vol. 3, no. 3, pp. 364–374, Mar. 2013.
- [196] J. I. Langford and A. J. C. Wilson, “Scherrer after sixty years: A survey and some new results in the determination of crystallite size,” *J. Appl. Crystallogr.*, vol. 11, no. 2, pp. 102–113, Apr. 1978.
- [197] A. Monshi, M. R. Foroughi, and M. R. Monshi, “Modified Scherrer Equation to Estimate More Accurately Nano-Crystallite Size Using XRD,” *World J. Nano Sci. Eng.*, vol. 02, no. 03, pp. 154–160, 2012.
- [198] A. L. Patterson, “The scherrer formula for X-ray particle size determination,” *Phys. Rev.*, vol. 56, no. 10, pp. 978–982, 1939.
- [199] B. Agyei-Tuffour *et al.*, “Pressure effects on interfacial surface contacts and performance of organic solar cells,” *J. Appl. Phys.*, vol. 122, no. 20, p. 205501, Nov. 2017.
- [200] C. N. Hoth, S. A. Choulis, P. Schilinsky, and C. J. Brabec, “On the effect of poly(3-hexylthiophene) regioregularity on inkjet printed organic solar cells,” *J. Mater. Chem.*, vol. 19, no. 30, p. 5398, 2009.
- [201] C. V. Hoven, X.-D. Dang, R. C. Coffin, J. Peet, T.-Q. Nguyen, and G. C. Bazan, “Improved Performance of Polymer Bulk Heterojunction Solar Cells Through the Reduction of Phase Separation via Solvent Additives,” *Adv. Mater.*, vol. 22, no. 8, pp. E63–E66, Feb. 2010.
- [202] S. N. Magonov, V. Elings, and M.-H. Whangbo, “Phase imaging and stiffness in tapping-mode atomic force microscopy,” *Surf. Sci.*, vol. 375, no. 2–3, pp. L385–L391, Apr. 1997.
- [203] I. Schmitz, M. Schreiner, G. Friedbacher, and M. Grasserbauer, “Phase imaging as an extension to tapping mode AFM for the identification of material properties on humidity-sensitive surfaces,” *Appl. Surf. Sci.*, vol. 115, no. 2, pp. 190–198, Jun. 1997.
- [204] P. Dutta, “Connecting physical properties of spin-casting solvents with morphology, nanoscale charge transport, and device performance of poly(3-hexylthiophene):phenyl-C₆₁-butyric acid methyl ester bulk heterojunction solar cells,” *J. Photonics Energy*, vol. 1, no. 1, p. 011124, Jan. 2011.
- [205] Y. Li, Y. Cao, J. Gao, D. Wang, G. Yu, and A. J. Heeger, “Electrochemical properties of luminescent polymers and polymer light-emitting electrochemical cells,” *Synth. Met.*, vol. 99, no. 3, pp. 243–248, Feb. 1999.
- [206] D. Baran *et al.*, “Reducing the efficiency–stability–cost gap of organic photovoltaics with highly efficient and stable small molecule acceptor ternary solar cells,” *Nat. Mater.*, vol. 16, no. 3, pp. 363–369, Mar. 2017.
- [207] G. L. Schulz *et al.*, “Optimization of solution-processed oligothiophene: Fullerene based organic solar cells by using solvent additives,” *Beilstein J. Nanotechnol.*, vol. 4, no. 1, pp. 680–689, Oct. 2013.
- [208] P. P. Khlyabich, B. Burkhart, A. E. Rudenko, and B. C. Thompson, “Optimization and simplification of polymer-fullerene solar cells through polymer and active layer design,”

- Polymer*, vol. 54, no. 20. Elsevier Ltd, pp. 5267–5298, 06-Sep-2013.
- [209] H. Seon, B. Kim, and J. Kang, “Characteristic of an Organic Photodetector Fabricated with P3HT:ICBA Blending Materials for Indirect X-Ray Detection,” *IEEE Trans. Nucl. Sci.*, vol. 64, no. 7, pp. 1739–1743, Jul. 2017.
- [210] A. Marzo, F. Beiza, P. Ferrada, J. Alonso, and R. Roman, “Comparison of Atacama Desert Solar Spectrum vs. ASTM G173-03 Reference Spectra for Solar Energy Applications,” in *Proceedings of EuroSun2016*, 2017, pp. 1–13.
- [211] Astm and Astm, “References Solar Spectral Irradiance at Air Mass 1.5: Direct Normal and Hemispherical for a 37° Tilted Surface 1,” *Policy*, vol. 14, pp. 1–10, 2004.
- [212] B. Tang *et al.*, “Restricting the liquid–liquid phase separation of PTB7-Th:PF12TBT:PC 71 BM by enhanced PTB7-Th solution aggregation to optimize the interpenetrating network,” *RSC Adv.*, vol. 7, no. 29, pp. 17913–17922, 2017.
- [213] F. Bencheikh, D. Duché, C. M. Ruiz, J.-J. Simon, and L. Escoubas, “Study of Optical Properties and Molecular Aggregation of Conjugated Low Band Gap Copolymers: PTB7 and PTB7-Th,” *J. Phys. Chem. C*, vol. 119, no. 43, pp. 24643–24648, Oct. 2015.
- [214] J. Wade *et al.*, “Operational electrochemical stability of thiophene-thiazole copolymers probed by resonant Raman spectroscopy,” *J. Chem. Phys.*, vol. 142, no. 24, p. 244904, Jun. 2015.
- [215] J. Gao and J. K. Grey, “Resonance Raman overtones reveal vibrational displacements and dynamics of crystalline and amorphous poly(3-hexylthiophene) chains in fullerene blends,” *J. Chem. Phys.*, vol. 139, no. 4, p. 044903, Jul. 2013.
- [216] A. B. Myers, “Resonance Raman Intensities and Charge-Transfer Reorganization Energies,” *Chem. Rev.*, vol. 96, no. 3, pp. 911–926, Jan. 1996.
- [217] J. Razzell-Hollis, J. Wade, W. C. Tsoi, Y. Soon, J. Durrant, and J.-S. Kim, “Photochemical stability of high efficiency PTB7:PC 70 BM solar cell blends,” *J. Mater. Chem. A*, vol. 2, no. 47, pp. 20189–20195, Oct. 2014.
- [218] W. Huang *et al.*, “Influence of Fullerene Acceptor on the Performance, Microstructure, and Photophysics of Low Bandgap Polymer Solar Cells,” *Adv. Energy Mater.*, p. 1602197, 2017.
- [219] M. Jaiswal and R. Menon, “Equivalent circuit for an organic field-effect transistor from impedance measurements under dc bias,” *Appl. Phys. Lett.*, vol. 88, no. 12, p. 123504, Mar. 2006.
- [220] Z. He *et al.*, “Single-junction polymer solar cells with high efficiency and photovoltage,” *Nat. Photonics*, vol. 9, no. 3, pp. 174–179, 2015.
- [221] W. C. Tsoi *et al.*, “In-situ monitoring of molecular vibrations of two organic semiconductors in photovoltaic blends and their impact on thin film morphology,” *Appl. Phys. Lett.*, vol. 102, no. 17, p. 173302, Apr. 2013.
- [222] J. Razzell-Hollis, J. Wade, W. C. Tsoi, Y. Soon, J. Durrant, and J.-S. Kim, “Photochemical stability of high efficiency PTB7:PC 70 BM solar cell blends,” *J. Mater. Chem. A*, vol. 2, no. 47, pp. 20189–20195, Oct. 2014.
- [223] S. Baniya, S. R. Vardeny, E. Lafalce, N. Peygambarian, and Z. V. Vardeny, “Amplitude-Mode Spectroscopy of Charge Excitations in PTB7 π -Conjugated Donor-Acceptor Copolymer for Photovoltaic Applications,” *Phys. Rev. Appl.*, vol. 7, no. 6, p. 064031, Jun. 2017.
- [224] S.-H. Liao, H.-J. Jhuo, Y.-S. Cheng, and S.-A. Chen, “Fullerene Derivative-Doped Zinc Oxide Nanofilm as the Cathode of Inverted Polymer Solar Cells with Low-Bandgap Polymer (PTB7-Th) for High Performance,” *Adv. Mater.*, vol. 25, no. 34, pp. 4766–4771, Sep. 2013.
- [225] Q. V. Hoang *et al.*, “Asymmetric Electron-Donating 4-Alkyl-8-alkoxybenzo[1,2- b :4,5- b 'd]thiophene Unit for Use in High-Efficiency Bulk Heterojunction Polymer Solar Cells,” *Macromolecules*, vol. 48, no. 12, pp. 3918–3927, Jun. 2015.
- [226] B. A. Collins, Z. Li, J. R. Tumbleston, E. Gann, C. R. Mcneill, and H. Ade, “Absolute measurement of domain composition and nanoscale size distribution explains performance in PTB7:PC71bm solar cells,” *Adv. Energy Mater.*, vol. 3, no. 1, pp. 65–74, Jan. 2013.
- [227] H. Yang, L. Wang, J. Zhang, X. Yu, and Y. Geng, “Molecular Packing and Orientation Transition of Crystalline Poly(2,5-dihexyloxy-p-phenylene),” pp. 405–411.
- [228] J. C. Wang, X. C. Ren, S. Q. Shi, C. W. Leung, and P. K. L. Chan, “Charge accumulation induced S-shape J?V curves in bilayer heterojunction organic solar cells,” *Org. Electron.*, vol. 12, no. 6, pp. 880–885, Jun. 2011.
- [229] Y. Ho Huh, B. Park, and I. Hwang, “Investigating the origin of S-shaped photocurrent-voltage characteristics of polymer:fullerene bulk-heterojunction organic solar cells,” *J. Appl. Phys.*, vol. 115, no. 12, p. 124504, Mar. 2014.
- [230] L. Zuo, J. Yao, H. Li, and H. Chen, “Assessing the origin of the S-shaped I–V curve in organic

- solar cells: An improved equivalent circuit model,” *Sol. Energy Mater. Sol. Cells*, vol. 122, pp. 88–93, Mar. 2014.
- [231] O. Oklobia and T. S. Shafai, “A quantitative study of the formation of PCBM clusters upon thermal annealing of P3HT/PCBM bulk heterojunction solar cell,” *Sol. Energy Mater. Sol. Cells*, 2013.
- [232] S. F. Hoefler *et al.*, “The effect of polymer molecular weight on the performance of PTB7-Th:O-IDTBR non-fullerene organic solar cells,” *J. Mater. Chem. A*, vol. 6, no. 20, pp. 9506–9516, 2018.
- [233] S. J. Lou, J. M. Szarko, T. Xu, L. Yu, T. J. Marks, and L. X. Chen, “Effects of Additives on the Morphology of Solution Phase Aggregates.pdf,” *J. Am. Chem. Soc.*, vol. 133, pp. 20661–20663, 2011.
- [234] B. Walker *et al.*, “Nanoscale Phase Separation and High Photovoltaic Efficiency in Solution-Processed, Small-Molecule Bulk Heterojunction Solar Cells,” *Adv. Funct. Mater.*, vol. 19, no. 19, pp. 3063–3069, Oct. 2009.
- [235] W. Chen *et al.*, “Hierarchical Nanomorphologies Promote Exciton Dissociation in Polymer/Fullerene Bulk Heterojunction Solar Cells,” *Nano Lett.*, vol. 11, no. 9, pp. 3707–3713, Sep. 2011.
- [236] G. Li, Y. Yao, H. Yang, V. Shrotriya, G. Yang, and Y. Yang, “‘Solvent Annealing’ Effect in Polymer Solar Cells Based on Poly(3-hexylthiophene) and Methanofullerenes,” *Adv. Funct. Mater.*, vol. 17, no. 10, pp. 1636–1644, Jul. 2007.
- [237] M. Babics *et al.*, “Solvent Vapor Annealing-Mediated Crystallization Directs Charge Generation, Recombination and Extraction in BHJ Solar Cells,” *Chem. Mater.*, vol. 30, no. 3, pp. 789–798, Feb. 2018.
- [238] V. Fauzia, A. A. Umar, M. M. Salleh, and M. Yahaya, “The effect of solvent on the morphology of an inkjet printed active layer of bulk heterojunction solar cells,” *Adv. Nat. Sci. Nanosci. Nanotechnol.*, vol. 2, no. 1, p. 015014, Mar. 2011.
- [239] Z. Xiao *et al.*, “Universal Formation of Compositionally Graded Bulk Heterojunction for Efficiency Enhancement in Organic Photovoltaics,” *Adv. Mater.*, vol. 26, no. 19, pp. 3068–3075, May 2014.
- [240] T. Fukuda, A. Toda, K. Takahira, D. Kuzuhara, and N. Yoshimoto, “Improved performance of organic photovoltaic cells with PTB7-Th:PC 71 BM by optimized solvent evaporation time in electrospray deposition,” *Org. Electron.*, vol. 48, pp. 96–105, Sep. 2017.
- [241] J. Kniepert *et al.*, “Effect of Solvent Additive on Generation, Recombination, and Extraction in PTB7:PCBM Solar Cells: A Conclusive Experimental and Numerical Simulation Study,” *J. Phys. Chem. C*, vol. 119, no. 15, pp. 8310–8320, Apr. 2015.
- [242] S. Foster *et al.*, “Electron Collection as a Limit to Polymer:PCBM Solar Cell Efficiency: Effect of Blend Microstructure on Carrier Mobility and Device Performance in PTB7:PCBM,” *Adv. Energy Mater.*, vol. 4, no. 14, p. 1400311, Oct. 2014.
- [243] W. Huang, E. Gann, L. Thomsen, C. Dong, Y. B. Cheng, and C. R. McNeill, “Unraveling the morphology of high efficiency polymer solar cells based on the donor polymer PBDTTT-EFT,” *Adv. Energy Mater.*, vol. 5, no. 7, 2015.
- [244] Q. Sun *et al.*, “A two-step strategy to clarify the roles of a solution processed PFN interfacial layer in highly efficient polymer solar cells,” *J. Mater. Chem. A*, vol. 3, no. 36, pp. 18432–18441, 2015.
- [245] T. M. Khan, Y. Zhou, A. Dindar, J. W. Shim, C. Fuentes-Hernandez, and B. Kippelen, “Organic Photovoltaic Cells with Stable Top Metal Electrodes Modified with Polyethylenimine,” *ACS Appl. Mater. Interfaces*, vol. 6, pp. 6202–6207, 2014.
- [246] S. Guo, B. Cao, W. Wang, J.-F. O. Moulin, and P. Mü Ller-Buschbaum, “Effect of Alcohol Treatment on the Performance of PTB7:PC 71 BM Bulk Heterojunction Solar Cells,” *Appl. Mater. interfaces*, 2016.
- [247] H. H. Amer, R. R. Paxton, and M. Van Winkle, “Methanol-Ethanol-Acetone,” *Ind. Eng. Chem.*, vol. 48, no. 1, pp. 142–146, Jan. 1956.
- [248] B. A. Miller-Chou and J. L. Koenig, “A review of polymer dissolution,” *Prog. Polym. Sci.*, vol. 28, no. 8, pp. 1223–1270, Aug. 2003.
- [249] S. Parameters, “Reference : Polymer Properties,” pp. 46–49, 1999.
- [250] Q. Wan *et al.*, “10.8% Efficiency Polymer Solar Cells Based on PTB7-Th and PC 71 BM via Binary Solvent Additives Treatment,” *Adv. Funct. Mater.*, vol. 26, pp. 6635–6640, 2016.
- [251] K. Zhang *et al.*, “High-Performance Polymer Solar Cells with Electrostatic Layer-by-Layer Self-Assembled Conjugated Polyelectrolytes as the Cathode Interlayer,” *Adv. Mater.*, vol. 27,

- no. 24, pp. 3607–3613, Jun. 2015.
- [252] T. M. Clarke, A. M. Ballantyne, J. Nelson, D. D. C. Bradley, and J. R. Durrant, “Free Energy Control of Charge Photogeneration in Polythiophene/Fullerene Solar Cells: The Influence of Thermal Annealing on P3HT/PCBM Blends,” *Adv. Funct. Mater.*, vol. 18, no. 24, pp. 4029–4035, Dec. 2008.
- [253] Y. Kanai and J. C. Grossman, “Insights on Interfacial Charge Transfer Across P3HT/Fullerene Photovoltaic Heterojunction from Ab Initio Calculations,” *Nano Lett.*, vol. 7, no. 7, pp. 1967–1972, Jul. 2007.
- [254] T. Clarke, A. Ballantyne, F. Jamieson, C. Brabec, J. Nelson, and J. Durrant, “Transient absorption spectroscopy of charge photogeneration yields and lifetimes in a low bandgap polymer/fullerene film,” *Chem. Commun.*, vol. 7345, no. 1, pp. 89–91, 2008.
- [255] W. Huang *et al.*, “Influence of Fullerene Acceptor on the Performance, Microstructure, and Photophysics of Low Bandgap Polymer Solar Cells,” *Adv. Energy Mater.*, vol. 7, no. 11, 2017.
- [256] V. Pranculis, A. Ruseckas, D. A. Vithanage, G. J. Hedley, I. D. W. Samuel, and V. Gulbinas, “Influence of Blend Ratio and Processing Additive on Free Carrier Yield and Mobility in PTB7:PC71BM Photovoltaic Solar Cells,” *J. Phys. Chem. C*, vol. 120, no. 18, pp. 9588–9594, May 2016.
- [257] A. R. Bin Mohd Yusoff, H. P. Kim, and J. Jang, “High performance organic photovoltaics with zinc oxide and graphene oxide buffer layers,” *Nanoscale*, vol. 6, no. 3, pp. 1537–1544, 2014.
- [258] S. Rafique, S. M. Abdullah, H. Alhummiyany, M. S. Abdel-wahab, J. Iqbal, and K. Sulaiman, “Bulk Heterojunction Organic Solar Cells with Graphene Oxide Hole Transport Layer: Effect of Varied Concentration on Photovoltaic Performance,” *J. Phys. Chem. C*, vol. 121, no. 1, pp. 140–146, Jan. 2017.
- [259] T. E. Kang *et al.*, “Photoinduced charge transfer in donor-acceptor (DA) copolymer: Fullerene bis-adduct polymer solar cells,” *ACS Appl. Mater. Interfaces*, vol. 5, no. 3, pp. 861–868, Feb. 2013.
- [260] M. A. Lampert and R. B. Schilling, “Chapter 1 Current Injection in Solids: The Regional Approximation Method,” in *Semiconductors and Semimetals*, vol. 6, no. C, 1970, pp. 1–96.
- [261] P. W. Liang, C. C. Chueh, S. T. Williams, and A. K. Y. Jen, “Roles of fullerene-based interlayers in enhancing the performance of organometal perovskite thin-film solar cells,” *Adv. Energy Mater.*, 2015.
- [262] B. Ebenhoch, S. A. J. Thomson, K. Genevičius, G. Juška, and I. D. W. Samuel, “Charge carrier mobility of the organic photovoltaic materials PTB7 and PC71BM and its influence on device performance,” *Org. Electron.*, vol. 22, pp. 62–68, Jul. 2015.
- [263] P. W. M. Blom, V. D. Mihailetchi, L. J. A. Koster, and D. E. Markov, “Device Physics of Polymer:Fullerene Bulk Heterojunction Solar Cells,” *Adv. Mater.*, vol. 19, no. 12, pp. 1551–1566, Jun. 2007.
- [264] L. J. A. Koster, V. D. Mihailetchi, R. Ramaker, and P. W. M. Blom, “Light intensity dependence of open-circuit voltage of polymer:fullerene solar cells,” *Appl. Phys. Lett.*, vol. 86, no. 12, p. 123509, Mar. 2005.
- [265] B. J. Leever, C. A. Bailey, T. J. Marks, M. C. Hersam, and M. F. Durstock, “In Situ Characterization of Lifetime and Morphology in Operating Bulk Heterojunction Organic Photovoltaic Devices by Impedance Spectroscopy,” *Adv. Energy Mater.*, vol. 2, no. 1, pp. 120–128, Jan. 2012.
- [266] O. Oklobia, S. Komilian, and T. Sadat-Shafai, “Impedance spectroscopy and capacitance – voltage measurements analysis: Impact of charge carrier lifetimes and mapping vertical segregation in bulk heterojunction P3HT: PCBM solar cells,” *Org. Electron.*, vol. 61, no. June, pp. 276–281, Oct. 2018.